Investigation of neutron production by pyroelectric ion acceleration.

Dissertation

der Mathematisch-Naturwissenschaftlichen Fakultät
der Eberhard Karls Universität Tübingen
zur Erlangung des Grades eines
Doktors der Naturwissenschaften
(Dr. rer. nat.)

vorgelegt von
Dipl.-Phys. Gerhard Deuter
aus Tübingen

Tübingen
2012

Tag der mündlichen Qualifikation:	02.10.2012
Dekan:	Prof. Dr. Wolfgang Rosenstiel
Berichterstatter 1:	Prof. Dr. Josef Jochum
Berichterstatter 2:	Prof. Dr. Heinz Clement

Ich versichere an Eides statt, dass ich diese Arbeit ohne unerlaubte Hilfe und nur mit den angegebenen Hilfsmitteln angefertigt habe. Desweiteren habe ich bis jetzt noch keinen Promotionsversuch unternommen.

Tübingen, den November 14, 2012 .....

(Gerhard Deuter)

Abstracts

Untersuchung der Neutronenerzeugung durch pyroelektrische Ionenbeschleunigung.

Hochsensible Experimente zur direkten Suche nach Dunkler Materie wie zum Beispiel CRESST werden mit Neutronen kalibriert. Dafür verwendet man bislang radioaktive Isotope oder kleine Linearbeschleuniger. Beide Möglichkeiten sind unvorteilhaft für ein Experiment wie CRESST, da radioaktive Substanzen die Gefahr einer Kontamination bergen und normalerweise die Erzeugung der notwendigen Hochspannung für herkömmliche Kleinstbeschleuniger die Elektronik so stört, dass eine Messung unmöglich wird.
Abhilfe schafft die Hochspannungserzeugung mit Hilfe eines pyroelektrischen Kristalls, beispielsweise Lithiumtantalat. In dieser Arbeit wurde gezeigt, dass man die Temperaturabhängigkeit der spontanen Polarisierung von Lithiumtantalat ausnutzen kann, um Spannungen von mehr als 120.000 Volt zu erzeugen. Mit dieser Hochspannung kann nun durch Feldüberhöhung an Nanospitzen eine Feldstärke generiert werden, die Tunnel- und Feldionisation von Deuteriummolekülen in der Nähe der Spitze ermöglicht. Hat die Hochspannung die benötigte Polarität, kann ein entstandenes Ion auf Material beschleunigt werden, welches bereits weiteres Deuterium enthält, zum Beispiel deuteriertes Polyethylen (CD_2). Dort findet mit energieabhängiger Wahrscheinlichkeit eine Kernfusionsreaktion statt, bei der monoenergetische Neutronen mit einer kinetischen Energie von 2,45 MeV durch die Reaktion D(D,n)^{3}He erzeugt werden. Die im hier verwendenten Aufbau theoretisch maximal erreichbare Neutronenrate für eine Beschleunigungsspannung von 100 kV liegt bei ca. 200 Neutronen pro Sekunde, eine realistische Berechnung ergab jedoch ca. 1-10 Neutronen pro Sekunde.
Im Rahmen dieser Arbeit wurde ein Prototyp eines solchen pyroelektrischen Ionenbeschleunigers aufgebaut und charakterisiert. Es wurde gezeigt, dass eine pyroelektrische Hochspannung verlässlich und reproduzierbar generiert werden kann. Es wurden Wolframspitzen und Kohlenstoffnanoröhrchen auf ihre Ionisationseigenschaften hin untersucht. Ein Ionenstrom von bis zu 1.2 nA wurde auf dem Zielmaterial nachgewiesen. Es wurde ein Neutronendetektorsystem aufgebaut, welches in der Lage ist, selbst kleinste Neutronenflüsse, die mit dem Beschleuniger produziert werden, nachzuweisen. Die absolute Neutronennachweiswahrscheinlichkeit für Neutronen aus der Fusionsreaktion beträgt derzeit ca. 2.5%.
Durch eine geschickte Analyse kann die Nachweisgrenze für den Neutronenfluss weiter gesenkt werden. Geeignete Analysemethoden wurden entwickelt und werden in dieser Arbeit diskutiert. Es konnte eine mittlere erzeugte Neutronenrate von etwa 0.5 n/s nachgewiesen werden.

Investigation of neutron production by pyroelectric ion acceleration.

Highly sensitive experiments for direct Dark Matter searches, for example the CRESST experiment, are calibrated using neutrons. For this purpose one usually uses radioactive isotopes or tabletop linear accelerators. Both methods are not desirable in a CRESST-like experiment, because a radioactive source could cause contamination and the high voltage power supplies necessary for small accelerators disturb the detectors and electronics because of which measuring is no longer possible.
A solution would be the high voltage generation using a pyroelectric crystal such as Lithiumtantalate. In this work it has been shown, that Lithiumtantalate generates high voltages of above 120,000 volt. Using this high voltage for field enhancement on nanotips, a sufficiently high field strength can be generated to allow field and tunneling ionization of deuterium molecules near the tip. If the high voltage has the correct polarity, the ions can be accelerated towards a deuterated target, for example deuterated polyethylene (CD_2). On the target D(D,n)^{3}He fusion is expected to take place with an energy dependent probability, producing monoenergetic neutrons with a kinetic energy of 2.45 MeV. The theoretical limit for neutrons produced with 100 kV acceleration voltage is almost 200 per second, however a realistic calculation resulted in about 1-10 neutrons per second.
During this work a prototype of a pyroelectric accelerator was built and characterized. It was shown that a pyroelectric high voltage could be generated reliably with high reproducibility. Tungsten nanotips and carbon nanotubes were investigated with respect to their ionization properties. An ion current up to 1.2 nA was measured on target. A neutron detector system has been set up allowing to detect extremely low neutron fluxes generated in the accelerator. The absolute detection efficiency for neutrons created by the fusion reaction is presently at 2.5%.
With suitable analysis tools which were developed during this work, the detection threshold for neutrons could be lowered further. These tools are also discussed during this work.
A mean generated neutron rate of approximately 0.5 n/s has been detected.

Contents

Introduction: Dark Matter(s)

"Anybody who has been seriously engaged in scientific work of any kind realizes that over the entrance to the gates of the temple of science are written the words: »Ye must have faith.« "

- Max Planck

Search for Dark Matter

Understanding the nature of the universe is one of the most important issues currently being investigated. Cold, heavy dark matter by which rotation curves of galaxies (Volders, 1959 [49]) and the structure of the bullet cluster (Clowe, 2006 [13]) can be explained, is of special interest since theory provides a large parameter space for possible new fundamental particles. A number of experiments were built to clarify the existence of such proposed particles in the universe. The most popular dark matter candidate is the lightest supersymmetric particle, called the neutralino. In this work, neutralinos or similar particles will be referred from this point on as weakly interacting massive particles or WIMPs. Amongst a range of dark matter experiments, CRESST (**C**ryogenic **R**are **E**vent **S**earch with **S**uperconducting **T**hermometers) is a direct dark matter search experiment with a good discovery potential. Using several cooled target crystals as reported by the collaboration in 2003 [6], CRESST is able to discriminate electromagnetic from nuclear recoils and can even distinguish between different types of nuclear recoils as shown in the works of Coppi [14], Ciemniak [12] and Strauss [48]. Assuming coherent scattering off a nucleus, a heavy WIMP is expected to recoil most likely on heavier nuclei ($\sigma \propto A^2$ [6]), in comparison to neutrons which scatter more likely on lighter nuclei such as oxygen. This can yield important information on the neutron background.

Techniques at CRESST

CRESST uses different scintillating crystals (for example $CaWO_4$, $ZnWO_4$) to measure phonon and light signals. The amount of light produced by different particle interactions is used to define a particle dependent quantity, the light yield. The light yield is the ratio between the light and phonon signal height. It is normalized to electromagnetic interactions caused by gammas and electrons.

Electromagnetic signals therefore can be discriminated from nuclear recoils with a different light yield compared to the deposited phonon energy. Those signals are measured with transition edge sensors for phonons and light which are read out by a SQUID (**S**uperconducting **QU**antum **I**nterference **D**evice) system. Both channels are bolometers, devices that measure energy by temperature change upon absorption of radiation. The phonon detector measures the deposited heat in the absorber crystal which is proportional to energy from the particle interaction. The light emitted by the scintillating absorber crystal heats up another bolometer, the light detector. Both detectors together form a single detector module. These detectors are operated at around 15 mK and below. The detector scheme and the readout circuit are shown in figs. 1 and 2. Details are shown in most

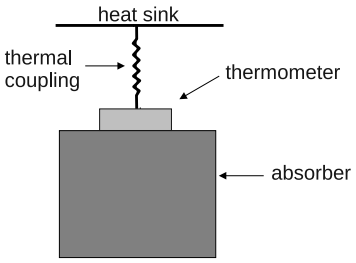

***Fig.** 1: CRESST detector scheme*

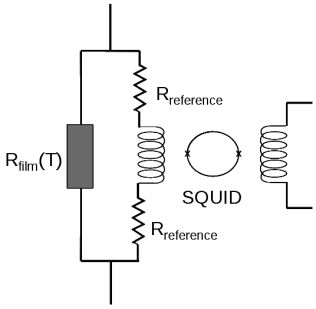

***Fig.** 2: CRESST readout circuit*

CRESST publications (e.g. [6], [43]). This detector type is disturbed by any high frequency transmitters. Therefore the whole setup was built in a large Faraday cage.

Shielding

CRESST is located in the Gran Sasso National Laboratory, Italy ("Laboratori Nazionali del Gran Sasso" further referred to as LNGS), where it is shielded with an average rock overburden of about 1500 m against cosmic radiation. This corresponds to 3500 m water equivalent and reduces the cosmic background at the place of the experiment by a factor of approx. $6 \cdot 10^5$ [15]. To suppress intrinsic material radioactivity and shield against muon induced background, there are several tons of lead, copper, internal and external polyethylene inside the Faraday cage where the experiment is located. A detailed description of the shielding can be obtained from Pröbst [43], Angloher et al.(2009) [7] or the most recent CRESST publication by Angloher et al.(2011) [8]. Extensive Monte Carlo simulations of background radiation with the shielding and the detectors were performed by Scholl [46] and Wulandari [50].

Calibration

A neutron calibration is needed to determine the position of the nuclear recoil band within each detector module as well as measuring the neutron multiplicity characteristics of a contamination source in all modules [8]. From the neutron multiplicity, a neutron source can possibly be identified. Muon induced neutrons usually produce much higher multiplicities due to hadronic showers at much higher energies compared to neutrons from an isotope source. A WIMP signal is expected to produce only single detector hits. If enough statistics can be collected, this can be used as an argument for or against a possible WIMP signal.
A neutron calibration is performed during each run. Either fission neutrons can be used or $\alpha - n$ sources such as americium-beryllium (AmBe) or radium-beryllium (RaBe). Since every calibration carries the burden of a possible contamination, this method is not preferable. As proposed in previous work (see Deuter, 2007 [16]), a small pyroelectric neutron generator would be highly preferable for such purposes. A neutron calibration could be performed at any time by activating the generator however without the necessity of any modification to the setup such as a temporary removal of parts of the shielding as done for calibrations up to now. Since a neutron generator has to be operated inside the Faraday cage near the SQUID system, any other kind of fusion neutron source will not suffice because of the intrinsic high frequency noise of the necessary high voltage power supplies.

Aim of this work

This work studies the feasibility of a pyroelectric neutron generator to be used as a neutron calibration source in any kind of low background experiments sensitive to neutrons. The high voltage generation with a pyroelectric crystal, ion ionization from gas phase and ion acceleration towards a defined target are being investigated. The tracing of reaction particles and the applicability to low background experiments is also being studied.

1 A pyroelectric accelerator

"...remarkable in its power, and so is the lyngourion[1], for seals are cut from this too, and it is very hard, like real stone. It has the power of attraction, just as amber has, and some say that it not only attracts straws and bits of wood, but also copper and iron, if the pieces are thin, as Diokles used to explain. It is cold and very transparent, and..."

- Theophrastus, On Stones, ca. 315 B.C.

Requirements and working principle

A pyroelectric neutron generator is a compact, tabletop device whose designation is to produce fusion neutrons to calibrate dark matter experiments such as CRESST. This neutron generator produces its high voltage by heating or cooling a pyroelectric crystal. This high voltage is then used to ionize and accelerate particles towards a target which is enriched with target isotopes in order to allow fusion reactions emitting neutrons in the process.
The working principle of the accelerator discussed in this work is as follows: A pyroelectric crystal is charged to about 100 kV by application of thermal changes. The deuterium ions are being ionized and accelerated towards a deuterated target, producing fusion neutrons on impact. A sketch of this working principle is shown in fig.1.1. In order to drive a $D(D,n)^3He$ fusion reaction, acceleration energies of about 50-100 keV are necessary so that the reaction cross section is in the order of 5-10 mbarn (see fig.1.17). To ionize deuterium from the gas phase, an electrical field strength of about 3 V/nm is needed. By using field enhancement on a small tip, in the order of 50 nanometers tip radius, in a dilute deuterium atmosphere, gas phase tunneling ionization of deuterium becomes possible (See electrical field strength calculations 1.2.2). A small layer of deuterated polyethylene (CD_2) can be used as target.

Preview: optimal setup

The optimal setup for neutron production and detection as determined in this work uses a Lithiumtantalate (LT, $LiTaO_4$) crystal with the Z^- axis glued to a copper mount which can be heated or cooled, the Z^+ axis facing a grid and a

[1]Translation from greek by Caley and Richards (1958); The Translation by Hill (1774) used "lyncurium" and "of a fire color" for the word cool; lyncurium is tourmaline, quote via [36]

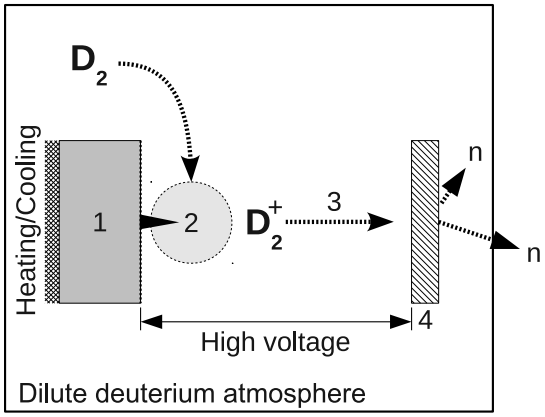

Fig. *1.1: Pyroelectric ion accelerator (PIA) function principle, 1: pyroelectric crystal which supplies high voltage, 2:ionization "area", 3: accelerated ions, 4: deuterated target where fusion reactions occur.*

target containing deuterium. Therefore the Z^+ face of the crystal will be charged positively upon heating. The tip is mounted on a copper plate which is glued to the exposed Z^+ LT crystal surface. Only in that configuration, the grid and the target can be biased to positive or negative voltages up to 100 V in order to suppress secondary electrons emitted by ions striking the target. The target is a thin layer of CD_2 on a metal backing where the bias voltage is applied and the ion current measured. The target is mounted directly onto a neutron detector which is flanged into the the experimental chamber to cover as much solid angle as possible.
It will be discussed in the following chapters, how the optimal setup was determined and which advantages is has compared to the other configurations.
All parts of the accelerator will be discussed in this chapter, starting with the pyroelectric crystal.

1.1 The pyroelectric crystal

The phenomenon "pyroelectricity" is known since ancient times, when people discovered, that tourmaline crystals, when laid into the sun, start sizzling. This was the reason why tourmaline was believed to have magical power, although the crystals were just discharging.
It took several centuries for mankind to understand the nature of this effect which is a manifestation of temperature dependance of the spontaneous polarization in specific crystal lattices. This effect is nowadays mainly used for thermal and infrared sensors. The application of high voltage generation is considered "exotic" compared to the standard applications. Especially LT ($LiTaO_3$) and LN ($LiNbO_3$) are mostly used in optics because the crystals are birefringent.

1.1.1 Pyroelectricity

In order to get a fundamental understanding of the effect, it is necessary to understand the basic thermodynamic models and the underlying crystal structure effects. It is recommended to read the "Sourcebook of pyroelectricity" by Sidney B. Lang (1974)[36] for a comprehensive description. A short summary of the book with extensive quotes is given in this section[1].
A crystal that changes its spontaneous polarization with temperature is called a pyroelectric. The crystal, whether it is a single crystal or a polycrystalline sample, accumulates space charge on its surfaces when temperature changes. This charge can be neutralized by charged particles from surrounding media or internal compensation currents. With a phenomenological approach to the macroscopic behavior of the crystal, the electrical, mechanical and thermal energy of a crystal are stored in quantities, each proportional to the product of an intensive and the differential of an extensive variable which is visualized in fig. 1.2:

Type	Extensive	Intensive
Thermal:	temperature	entropy
Mechanical:	elastic stress	strain
Electrical:	electric field	displacement

The intensive variables are specified at each point in the crystal. They are not additive and do not require any specification of quantity of the sample. The extensive variables are additive in the sense that the value of the variable for the whole crystal is the sum of the values of the constituent parts. As used in the mathematical treatment which follows, the extensive variables represent a quantity per unit volume or area of the crystal. The used variables are shown in the table of symbols 1.1.
The properties can be written by using the Einstein summation convention with the following tensor equations:

$$\mathrm{dS_{ij}} = \left(\frac{\partial \mathrm{S_{ij}}}{\partial \theta_{\mathrm{kl}}}\right)_{\mathrm{E,T}} \mathrm{d}\theta_{\mathrm{kl}} + \left(\frac{\partial \mathrm{S_{ij}}}{\partial \mathrm{E_k}}\right)_{\theta,\mathrm{T}} \mathrm{dE_k} + \left(\frac{\partial \mathrm{S_{ij}}}{\partial_{\mathrm{T}}}\right)_{\theta,\mathrm{E}} \mathrm{dT} \tag{1.1}$$

$$\mathrm{dD_i} = \left(\frac{\partial \mathrm{D_i}}{\partial \theta_{\mathrm{jk}}}\right)_{\mathrm{E,T}} \mathrm{d}\theta_{\mathrm{jk}} + \left(\frac{\partial \mathrm{D_i}}{\partial \mathrm{E_j}}\right)_{\theta,\mathrm{T}} \mathrm{dE_j} + \left(\frac{\partial \mathrm{D_i}}{\partial_{\mathrm{T}}}\right)_{\theta,\mathrm{E}} \mathrm{dT} \tag{1.2}$$

[1]Within the country of Baden-Württemberg, the book is only available at the Karlsruhe Intitute of Technology or the University of Konstanz. The quotes will not be marked separately, so the whole section,1.1.1 must be considered as quote.

Table 1.1: Table of symbols for chapter 1.1

A	Area, m^2
α	Thermal expansion coefficient, $1/K$
C	Capacitance, F
c	Heat capacity, $J/m^3/K$
D	Electric displacement, C/m^2
d	Piezoelectric constant, C/N
E	Electric field, V/m
e	Eulers constant
ϵ	Electrical permittivity, F/m
P_s	Spontaneous polarization, C/m^2
p	Pyroelectric coefficient, $C/m^2/K$
Q	Electric charge, C
q	Electrocaloric coefficient, Km/V
S	Elastic strain, dimensionless
s	Elastic compliance coefficient, m^2/N
σ	Entropy per unit volume, $J/m^3/K$
θ	Elastic stress, $\frac{N}{m^2}$
t	Time, s
T	Temperature, K
U	Electric potential, V
$\boldsymbol{\mu}$	Bold symbols indicate vectors.

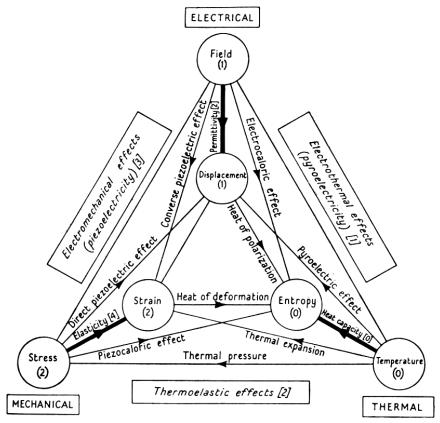

***Fig.** 1.2: Thermodynamical relations from Nye [32]*

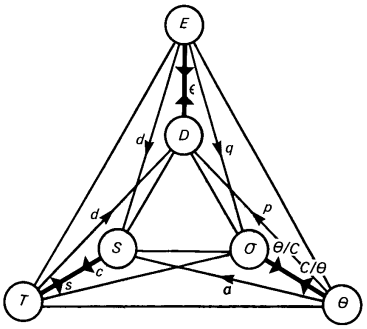

***Fig.** 1.3: Corresponding parameters from Lang[36]*

$$\mathrm{d}\sigma = \left(\frac{\partial\sigma}{\partial\theta_{\mathrm{ij}}}\right)_{\mathrm{E,T}} \mathrm{d}\theta_{\mathrm{ij}} + \left(\frac{\partial\sigma}{\partial\mathrm{E_i}}\right)_{\theta,\mathrm{T}} \mathrm{dE_i} + \left(\frac{\partial\sigma}{\partial_{\mathrm{T}}}\right)_{\theta,\mathrm{E}} \mathrm{dT} \tag{1.3}$$

The subscripts on the bracketed terms indicate variables held constant during partial differentiation.
From these equations one can derive a Gibbs function (done by Nye (1957) [32] and Mason (1966)) for the elastic, electrical and thermal variables and derive a set of Maxwell relations. All the partial derivatives are replaced by the properties they define.

$$\mathrm{dS_{ij}} = \underbrace{s^{E,T}_{ijkl}\mathrm{d}\theta_{\mathrm{kl}}}_{\text{elasticity}} + \underbrace{d^{T}_{kij}\mathrm{dE_k}}_{\substack{\text{converse}\\ \text{piezo-}\\ \text{electricity}}} + \underbrace{\alpha^{E}_{ij}\mathrm{dT}}_{\substack{\text{thermal}\\ \text{expansion}}} \tag{1.4}$$

$$\mathrm{dD_i} = \underbrace{d^{T}_{ijk}\mathrm{d}\theta_{\mathrm{jk}}}_{\substack{\text{direct}\\ \text{piezo-}\\ \text{electricity}}} + \underbrace{\epsilon^{\theta,T}_{ij}\mathrm{dE_j}}_{\substack{\text{permit-}\\ \text{tivity}}} + \underbrace{p^{\theta}_{i}\mathrm{dT}}_{\substack{\text{pyroelec-}\\ \text{tritcity}}} \tag{1.5}$$

$$\mathrm{d}\sigma = \underbrace{\alpha^{E}_{ij}\mathrm{d}\theta_{\mathrm{ij}}}_{\substack{\text{piezo-}\\ \text{caloric}\\ \text{effect}}} + \underbrace{p^{\theta}_{i}\mathrm{dE_i}}_{\substack{\text{electro-}\\ \text{caloric}\\ \text{effect}}} + \underbrace{\frac{c^{\theta,E}}{T}\mathrm{dT}}_{\substack{\text{heat}\\ \text{capacity}}} \tag{1.6}$$

All parameters in eqs. 1.4 to 1.6 are tensor components. This means, that this set of eqations is actually a shorthand representation of $3^2+3+1=13$ eqs. with 13 terms each on the right hand side. This is also the case for eqs. 1.1 to 1.3.
These equations describe how the crystal behaves if the extensive variables are changed. For example, if energy is fed to the crystal by applying elastic stress to

the crystal by compressing it, the energy is converted to strain (eq. 1.4), displacement via direct piezoelectricity (eq. 1.5) and entropy by the piezocaloric effect (eq. 1.6). A temperature change will cause strain by thermal expansion (eq. 1.4), displacement by the pyroelectric effect (eq. 1.5) and entropy by the heat capacity (eq. 1.6).
Applying constant stress and constant electric field and looking only to the temperature change, eq. 1.5 simplifies to:

$$\mathrm{dD_i} = \mathrm{p_i^{\theta}dT}, \tag{1.7}$$

which is a tensor equation of first rank, namely a vector. The pyroelectric coefficient is a vector with three orthogonal components in three-dimensional space. It represents the proportionality constant between the polar vector, electric displacement, and the scalar, temperature. The unit of the pyroelectric coefficient is charge per unit area per temperature change ($C\,m^{-2}\,K^{-1}$).
A basic requirement for a pyroelectric material is the presence of an electric dipole in each fundamental cell. This dipole is caused by a shift in the centers of positive and negative charge. If these dipoles are aligned in a way that they do not cancel each other out statistically, the material has an electrical polarization, called *spontaneous polarization*. *Spontaneous* indicates that the polarization has a nonzero value in the absence of an external electric field which is different to materials which show *induced polarization*, for example a dielectric in a capacitor. Due to this nonzero value of electric polarization at a fixed temperature, surface charges will accumulate and mask the internal spontaneous polarization. By changing the temperature and therefore changing the relative position of atoms within the crystal structure, or by modifying the interatomic bindings, the spontaneous polarization changes.
This spontaneous polarization $\mathbf{P}$ can be expressed mathematically as the dipole moment per unit volume $\boldsymbol{\mu}$ averaged over the volume of the crystal. $\mathbf{P}$ and $\boldsymbol{\mu}$ are vectors.

$$\mathbf{P} = \frac{1}{v}\iiint \boldsymbol{\mu}\mathrm{dv}. \tag{1.8}$$

If the average $\mathbf{P}$ is nonzero, the material shows a spontaneous polarization in direction of $\mathbf{P}$. This is also true for polycrystalline aggregates where only the definition of unit volume is different. Its temperature derivative at constant stress and constant electric field is the pyroelectric coefficient in the direction $\mathbf{P}$:

$$p_i^{\theta}(T) = \left(\frac{\partial P_i}{\partial T}\right)_{\theta,E}. \tag{1.9}$$

The single polycrystalline subvolumes have different values depending on lattice orientation, lattice constants and ions in the lattice. The direction of interest

is denoted **z**. The pyroelectric coefficient in direction of **z**, $\tilde{p}$ can be obtained by projecting **p** onto **z**. For a given temperature change, $\tilde{p}$ yields a charge per unit area perpendicular to **z**. The accumulated change in spontaneous polarization, the accumulated charge ΔQ_{ac} since the last electrical equilibrium, can be calculated as

$$\Delta Q_{ac} = \tilde{p}(T) \cdot \Delta T \cdot A. \tag{1.10}$$

where ΔT is the temperature change actually applied from an equilibrium state of the crystal and A is the area perpendicular to **z**. In this work, a $LiTaO_3$ (LT) crystal is used where the face of the cylindrical crystal corresponds to A. The crystal is z-cut, which means the flat areas are perpendicular to the z-axis in the crystal. The pyroelectric coefficient of LT in z-direction is larger than those of the other axes. At 27^{o}C (300 K) the pyroelectric coefficient is 190 µC/m^{2}K. The temperature dependence of the pyroelectric coefficient for LT was investigated by M.Glass in 1968 [29] and is almost constant for the temperature range used in this work (-30^o to 100^o Celsius). Measuring the value of the pyroelectric coefficient below 0^{o}C (273 K) down to -272^{o}C (1 K) is currently being investigated and might be done in future (see chapter 6). The known temperature dependence is shown in fig. 1.4. The amount of charge does not depend on the crystal thickness as long as the crystal exceeds a height of one centimeter. This can be understood as result of internal charge compensation of electrically displaced unit cells with a compensation length of about the same order of magnitude.
This behavior was reported by Geuther and Danon in 2005 [28].

1.1.2 High voltage charge model

Using the relations discussed in the previous section, it is possible to calculate the expected high voltage on the crystal surface for a given temperature change applied over time according to equation 1.10. From the geometry as is shown in fig. 1.5 one can sketch a simplified circuit diagram (see fig. 1.6). With the electric capacity $C = \frac{\Delta Q}{\Delta U} = \epsilon_0 \cdot \epsilon_r \cdot \frac{A}{D}$, where ΔQ is the change in charge, ΔU is the voltage change, A the capacitors area and D the distance between the two plates, the voltage at the crystal surface can be calculated to

$$\Delta U(\Delta T) = \frac{\tilde{p}(T) \cdot \Delta T}{\epsilon_0 \cdot \frac{1}{D_{ABS}}(\epsilon_K \cdot \frac{D_{ABS}}{D_K} + 1)}. \tag{1.11}$$

where ΔT is the temperature change applied to the crystal in Kelvin. The permittivity of the crystal in z-direction is $\epsilon_K = 43$ ([2]). This model does not include corrections for any structure which is used later on to enhance the electric field,

[2]Value obtained from supplier datasheet. Roditi International Corporation Ltd, `http://www.roditi.com`

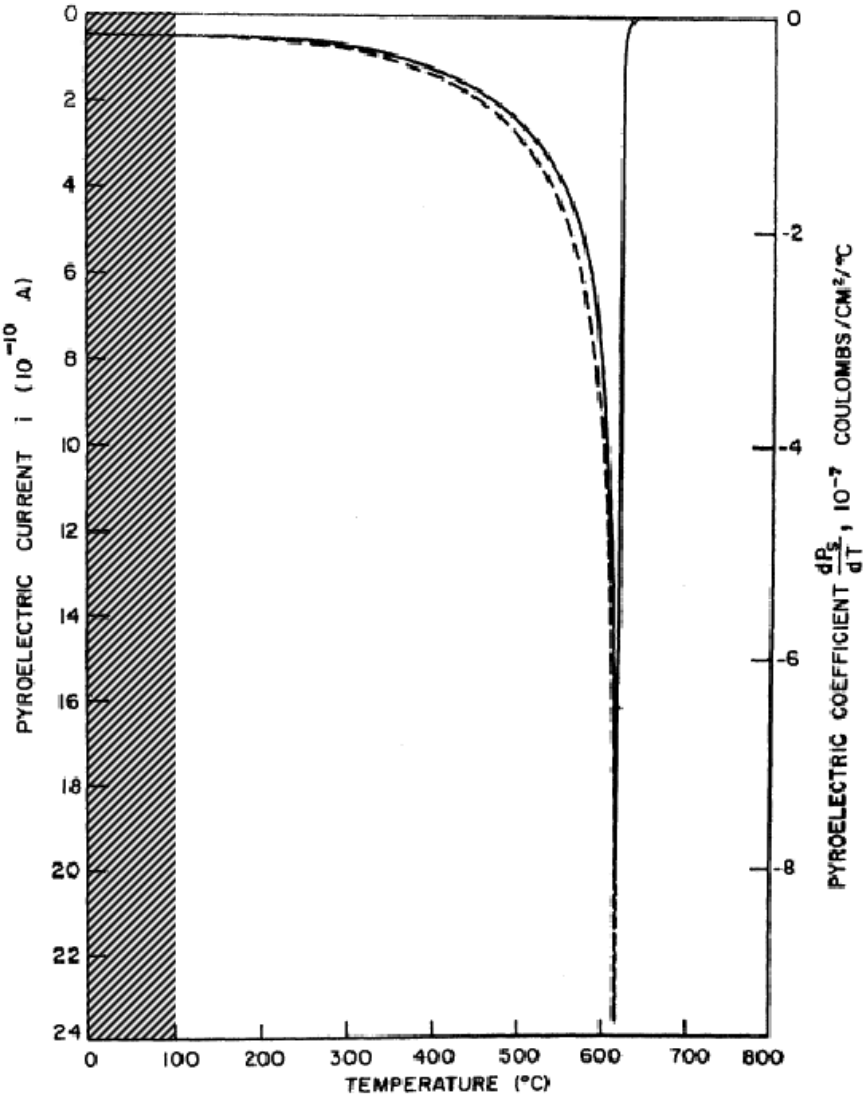

Fig. *1.4: Temperature dependence of the pyroelectric coefficient of $LiTaO_3$, temperature range used is shaded, modified picture from M.Glass (1968) [29].*

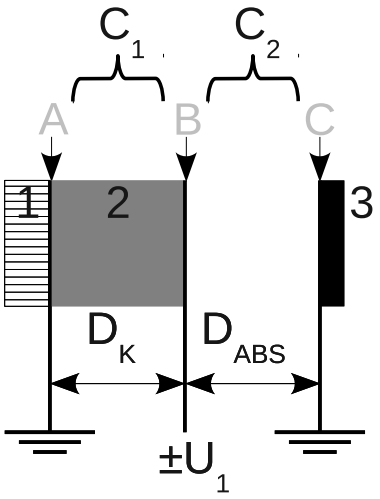

Fig. *1.5: Capacitor model scheme. 1: Crystal holder, 2: Crystal and 3: Target. D_K and D_{ABS} are the distances used for calculating the capacitance. U_1 is the voltage applied to the capacitor. A-C are reference points marked in the corresponding circuit diagram.*

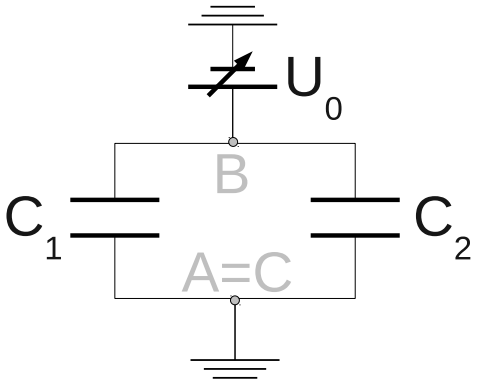

Fig. *1.6: Corresponding circuit diagram*

such as a tip or nanotube wafers (see chapter 2).
If a temperature change of 70 K is applied over a time of 1000 s, the change in charge is 94 μC accumulated in this 1000 seconds. The average change in charge per second is called pyroelectric current and has a value for this example of 9.4 nA. If no charge loss - intended or not - occurs, the crystal charges according to eq. 1.11 to 340 kV. In this calculation it was assumed that the crystals temperature and the charge accumulation follows the temperature change linearly, and that the temperature change is linear in time. The crystal follows the temperature linearly, however the charge accumulation depends on the time structure of the applied temperature change as there exist small hysteresis effects and surface charge losses. If the crystal is in electrical, thermal and mechanical equilibrium before any change of the extensive variables is applied, the changes of the charge and the voltage can be treated as absolute values: $\Delta Q = Q$ and $\Delta U = U$. In real world, heating and cooling is not linear so that it is necessary to parametrize the temperature curves in order to calculate the accumulated charge at a certain time. The temperature curves are parametrized by polynomial functions, where two examples are shown in fig. 1.7. With this parametrization it is possible to calculate the cumulative charge for a random time span within the cycle, for example after a discharge has occurred which resets the crystal to electrical equilibrium. For a given time t_x after the start of the cycle at t_0 or after a discharge

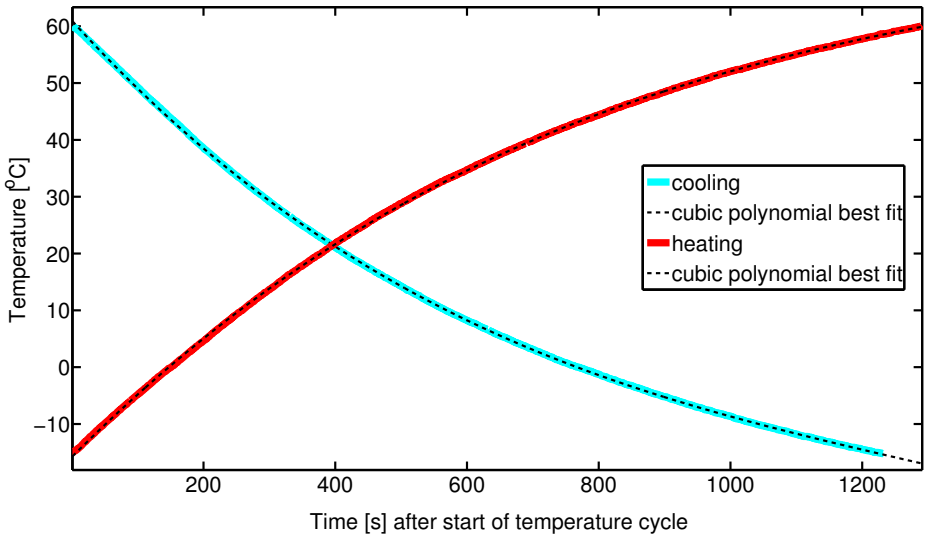

Fig. *1.7: Temperature curve parametrization by the black dashed polynomial fit, the red and blue curves are measured temperature values*

of the crystal at t_n, the voltage on the crystal surface can be calculated

$$U_{total} = \int_{t_0+t_n}^{t_x} \frac{\Delta U(\Delta T)}{dt}\,\mathrm{dt}. \tag{1.12}$$

In reality, deviations from this expected high voltage can be observed for voltages above 40 kV. Exemplary high voltage measurements compared to the expectation are shown in fig.1.8. There are several possible explanations for the observed lack

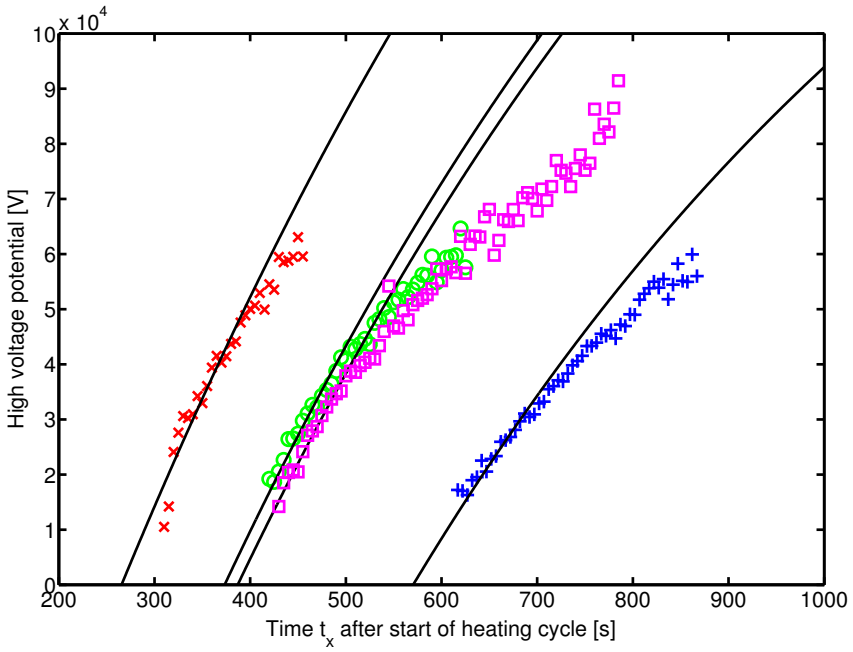

Fig. *1.8: High voltage charge model comparison to exemplary measurements. The high voltage is measured for different time period within the thermal cycle, but always from the last voltage breakdown.*

of high voltage:

- ionization processes and secondary charge loss.
- field electron emission.
- lack of X-ray detector efficiency at high voltages.
- geometric effects which change the charge model.

Ionization processes and secondary charge loss

Ionization processes triggered by large field strengths will accelerate ions according to the field geometry. For deuterium ions this is intended and desired, ionization of other gas types is a side-effect. Gas phase ionization will be discussed further in section 1.2. Ionization processes decrease the accumulated charge on the crystal until an electrical equilibrium is achieved or the ionization stops.
Secondary charge loss occurs, when ions are accelerated onto a surface and release secondary electrons. Those electrons will be accelerated according to the electric field, decreasing the charge on the crystal until electrical equilibrium is achieved or the ionization stops. This effect is further discussed in chapter 2.

Field electron emission

Field electron emission occurs, if the external field strength allows the electron to tunnel out of its binding potential. The necessary field strength is in the order of GV/m. The current density j(E) of the emission within an area can be calculated using the Fowler-Nordheim equation:

$$j(E) = K_1 \cdot \frac{|E|^2}{\Phi} \cdot e^{-(K_2 \cdot \Phi^{3/2})/|E|} \tag{1.13}$$

where K_1 and K_2 are material dependent constants, E is the electric field strength, and Φ is the work function. The work function for metals is in the order of some eV, around 4.5 eV for the metals used in this work (Cu, Fe, W).
The spot where vacuum, metal and dielectric meet is called a triple point. Such a triple point increases the yield of emitted electrons from the metal due to field enhancement. This may also cause a discharge by producing a secondary electron cascade when the discharge hits the dielectric (Or the adsorbed gas layers on its surface). This was investigated in the work of Jordan and others [39]. The triple point can be weakened by conical shapes and a homogenous surface finish which reduces the external field strength as well as coating the spot with CuO_2 or Cr_2O_3 to increase the work function. In this work, care was taken to have all edges as conical as possible, and every surface as clean as possible. A coating with such materials should be considered in future work.
Field electron emission is the main reason for a flash over event also called gas discharge or spark which instantaneously generates electrical equilibrium at the crystal surface. Since gas phase ionization is required for this experiment, gas discharges cannot be avoided.

Lack of detector efficiency at high voltages

The high voltage cannot be measured directly as such a measurement will instantaneously reset the crystal to electrical equilibrium. One uses the unavoidable

effects of electron emission and acceleration to measure the current high voltage by the endpoint of the Bremsstrahlung spectrum. The Bremsstrahlung radiation is detected by an silicon diode suitable for X-ray radiation. The size of the diode limits the sensitivity for high energetic X-rays, because the photoelectric cross-section within the detector volume becomes very small. If the high voltage rises, the endpoint of the Bremsstrahlung spectrum shifts to higher and higher energies until the detector can only see the lower part of the spectrum. Therefore the measured endpoint seems to be lower than in reality. This detector property will be further discussed in section 2.3.

Geometric effects which change the charge model

As can be seen by eq. 1.11, reducing the distance from the crystal to the target to be less than the thickness of the crystal, the maximum voltage drops.
Adding a grid in between the crystal and the target in order to suppress secondary electron emission from ions hitting the target, the overall charge model does not change significantly if the grid is connected to electric ground. However the effective distance from the crystal to the target is reduced.

1.2 Deuterium ionization

With the pyroelectric high voltage from the crystal, deuterium can be ionized and accelerated towards a deuterated target. Deuterium can be ionized by exposing it to strong field regimes where field and tunneling ionization are possible. A second option to ionize deuterium, however not realized in this experiment, would be the thermal collision ionization occurring at very high temperatures in the order of $3 \cdot 10^5\,\mathrm{K}$. Collision ionization is additionally suppressed by the low deuterium pressure. At a typical pressure in the range of $5 \cdot 10^{-4}\,\mathrm{mbar}$ to $5 \cdot 10^{-3}\,\mathrm{mbar}$ the mean free path of a deuterium molecule is roughly 5 m to 50 cm, details are shown in appendix A.

1.2.1 Field ionization

The remaining ionization mechanism is tunneling ionization in strong field regimes. Strong fields can be generated by field enhancement on very small structures. The required dimensions of the structure can be calculated by obtaining the necessary field strength for which tunneling ionization is probable.
Field ionization occurs, if the external field is greater than or equal to the internal electric field of the atom or molecule. To determine the field strength, the binding energies need to be known. The difference between the Hydrogen and the Deuterium molecule is negligible. Therefore all following values are calculated for the Hydrogen values and compared with literature values, if available. The atomic binding energy is 13.6 eV. However, deuterium gas does not consist of atoms under

normal conditions, it consists of molecules with a binding energy of 436 kJ/mol which equals 4.52 eV/molecule. The binding energy for a stable D_2^+-ion is 2.77 eV, which means that only 1.75 eV must be spent to remove one electron. As shown in a publication by Danon et al.[19], only D_2^+ is being produced by field enhancement on a nanotip as done in this work which will be shown is in agreement with the measurements and calculations derived during this work.
The classical approximation for the radius dependent critical field strength F_{crit} for an atom or molecule by Slater [47] and be rewritten as function of the binding energy W_{ion}

$$F_{crit} = \frac{4\pi\epsilon_0(2W_{ion})^2}{e^3}. \tag{1.14}$$

which gives a result of $F_{crit} = 8.5\,V/nm$ for D_2^+ and $514\,V/nm$ for D^+, with the electric charge e and the permittivity ϵ_0. However even for lower field strengths ions can be produced by tunneling ionization. The quantum mechanical calculation according to Grüner [10] gives the tunneling probability

$$P_{tunnel} = \exp\left\{-\sqrt{\frac{8m_eW_{ion}^3}{\hbar^2}}\frac{1}{2eF}\right\} \tag{1.15}$$

where m_e is the electron mass in kg, $\hbar$ is the reduced Planck constant, W_{ion} the ionization energy in eV, e the elementary charge in C and F the field strength in V/nm. The tunneling probability for a deuterium molecule to D^+ and D_2^+ as function of the field strength is shown in fig. 1.9. The frequency with which the

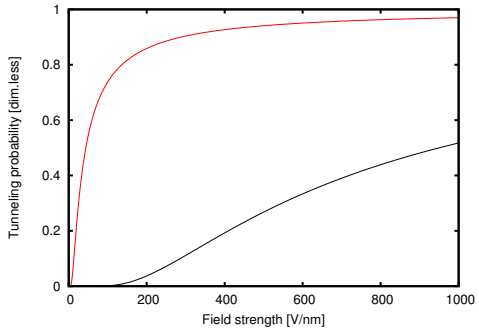

***Fig.** 1.9: Tunneling probability for a deuterium molecule resulting in D^+ (black) and D_2^+ (red) as function of the field strength.*

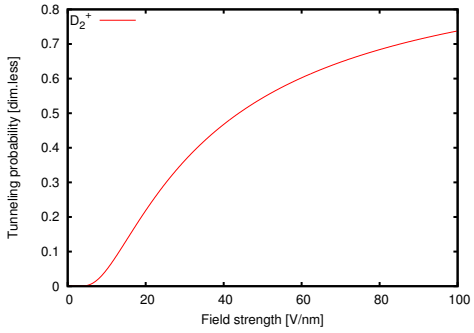

***Fig.** 1.10: Tunneling probability for deuterium molecule as function of field strength, fig.1.9 zoomed in.*

electron runs against the potential barrier is given by

$$\nu = \frac{W_{ion}}{h} \tag{1.16}$$

where h is the Planck constant. With the ionization rate

$$\eta = P_{tunnel} \cdot \nu \tag{1.17}$$

one can calculate the ionization probability $P_{ion}(t)$

$$P_{ion}(t) = 1 - e^{-\nu t P_{tunnel}}, \tag{1.18}$$

where t is the transition time of the particle in the strong field. To get the transition time one has to calculate the velocity of a deuterium molecule at T = 300 K as

$$v = \sqrt{\frac{3k_B T}{m}} \tag{1.19}$$

which yields 1368 m/s for a D_2 molecule. To get an idea for the typical distance a molecule can travel in the strong field near the tip, the electric field calculation for a tip with 50 nm tip radius, biased to 100 kV is shown in fig. 1.11. Since only

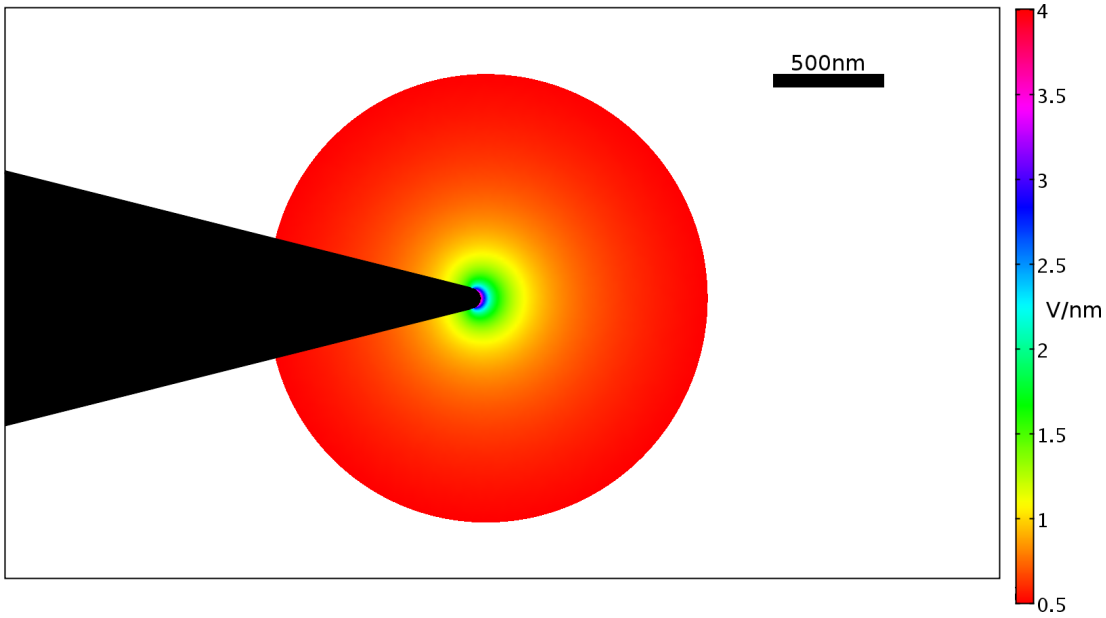

Fig. *1.11: Calculation of the electric field strength for a tip with radius 50 nm and a length of 2 mm which is charged to 100 kV. The electric field is only displayed for values larger than 0.5 V/nm.*

D_2^+ will be produced, the calculation will be done for D_2^+ however the values for D^+ will be given for comparison. The typical distance unless the electric field falls below 0.5 V/nm is in the order of 2 µm. The time the D_2 spents in a critical electric field above 0.5 V/nm is $1.5 \cdot 10^{-9}$ s. In fig. 1.12 the ionization probability

to get D_2^+ as function of the electric field is shown, to be compared with the ionization probability as a function of time for an electric field strength 2 V/nm and 4 V/nm in fig. 1.13. To conclude this calculation, the production of D_2^+ ions

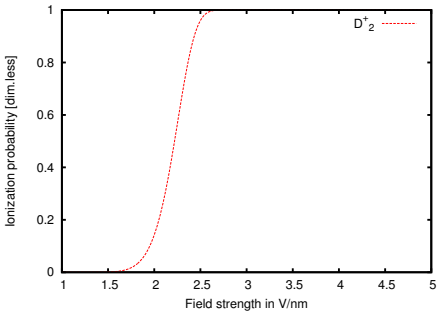

Fig. *1.12: Ionization probability for a deuterium molecule during the corresponding transition time as function of the field strength.*

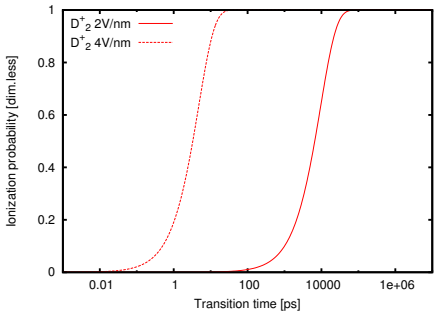

Fig. *1.13: Ionization probability for a deuterium molecule as function of transition time at different electric field strengths.*

from field ionization is possible the ionization of D^+ however not. The kinetic energy per nucleus in D_2^+ is half the acceleration energy which will reduce the fusion probability. As will be shown, this is consistent which the measurements. To achieve a field strength in the order of 5 V/nm from a homogenous field one needs a very small structure to enhance the field strength, for example a tip with small radius. The tip properties can now be determined.

1.2.2 Tip specifications and tip arrays

According to the theoretical field enhancement models presented by Edgcombe and Valdrè [21],[24], the field strength of a plate capacitor can be increased by a factor of 1 to 10^6, the so called field enhancement factor, by adding a small tip to the field. The tip is geometrically defined by the tip radius, the cone from etching, the base which has full wire thickness and the base length from the mount to the cone. A sketch of the tip properties with naming conventions is shown in fig. 1.14.

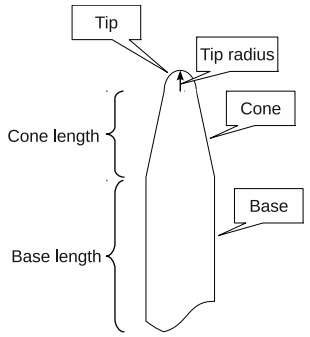

Fig. *1.14: Sketch of tip geometry with corresponding properties.*

If the ratio of the tip length to the tip radius is greater than 1000, the tip is called a "long" tip. Short tips have lower enhancement factors.
A naive estimation of the field strength for a long conductor being held at constant voltage U with a conical end of radius r has the form $E = U/r$. Depending on the real tip geometry in 3D there is no analytical solution to this problem. The real tip geometry does vary, of course. A real tip used within this work is shown in chapter 2, fig. 2.10.
Such tips can be produced by etching or mechanical deformation of a thin tungsten wire. Other common tip materials like gold are less resistant to thermal and mechanical stress. However, handling of a single tip is very challenging. The use of a tip array was considered. The necessary properties of tip arrays were investigated using finite element methods and will be discussed later in section 1.5.
A second approach follows the idea of the nanoscience community to use carbon nanotubes for gas phase ionization. Carbon nanotubes can be produced in large numbers with similar properties standing upright on a wafer. The nanotube parameters such as height and radius can be controlled very precisely, which may allow a good reproducibility of the wafers and high ionization yield.

1.2.3 Carbon nanotubes and carbon nanotube arrays

Quite recently the application of carbon nanotubes (also known as tube fullerene) as ion source was reported for fusion applications by Fink et al.[44]. A carbon nanotube consists of at least one rolled up graphene layer, with a single wall thickness of one carbon atom. A carbon nanotube can be open at the end or closed by half a spherical fullerene. Carbon nanotubes can be produced with different parameters, such as single walled or multi walled, lengths, diameters, closed and open. For this work only single walled nanotubes (SWNT) were considered as an option since multi walled nanotubes have larger radii and therefore less field enhancement. Typical diameters of nanotubes reach from less than one nanometer up to several tens of nanometers compared to a length of several micrometers.
According to the work of Grüner [10], closed nanotubes do withstand much higher field strengths than open ones. This can be understood due to the electron configuration at the edge of a open nanotube being weaker compared to half a spherical fullerene. There exist different types of carbon nanotubes depending on their

translation symmetry which is shown in fig. 1.15. Carbon nanotubes can be grown

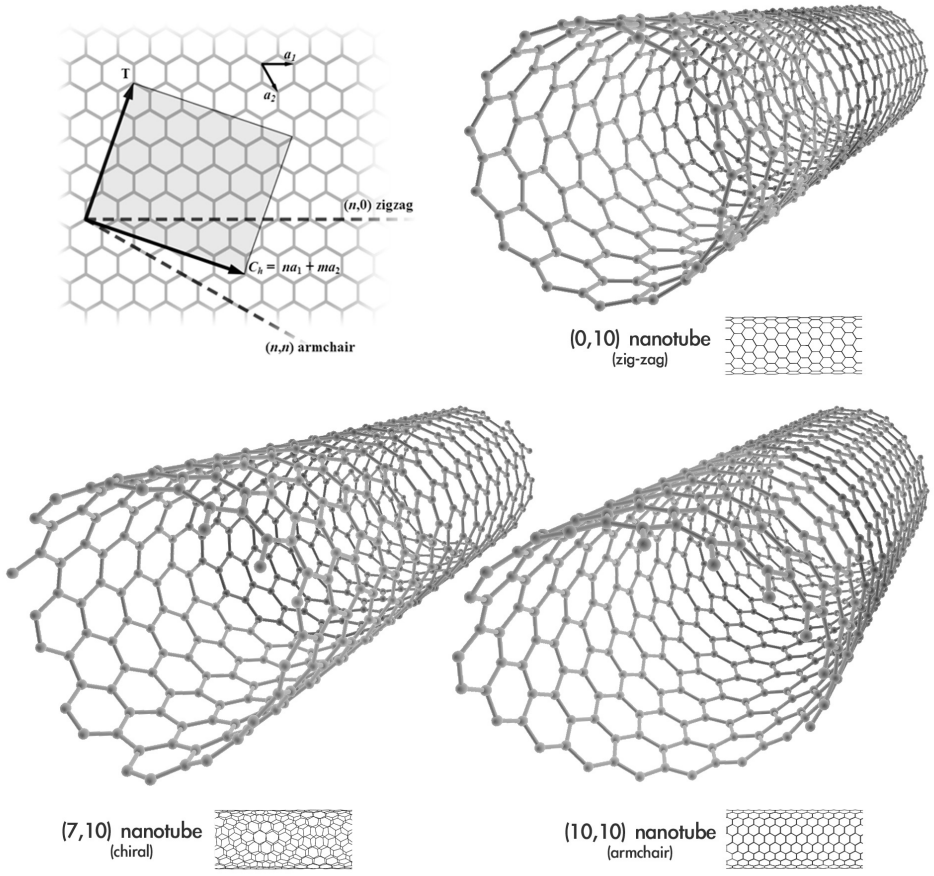

Fig. *1.15: A diagram showing the different types of carbon nanotubes. Created by Michael Ströck, 2006. Released under the GFDL.*

with different methods and on different substrates. Plasma-enhanced chemical vapor deposition (PECVD) is a common technique, where gaseous hydrocarbons are deposited on a surface using a metal catalyst. At high temperatures, the hydrocarbons disintegrate and the carbon diffuses into the metal creating a metastable carbon compound. If the metal is saturated with carbon, the exiting carbon atoms form into the energetically most favorable structure - a nanotube. Iron, nickel and cobalt can be used as a catalyst for this process. The plasma provides the energy to drive the disintegration reaction by heat and electron collisions. The electric field used to generate the plasma can be used to align the nanotube growth. PECVD grown nanotubes are straighter than without plasma support grown nanotubes. By changing the structure of the catalyst on the substrate, the properties of the nanotubes can be influenced. Covering a whole area

with catalyst will produce a forest of nanotubes, placing dots will produce single nanotubes. Nanotube forests used in this work were provided by the group of Prof. Kern at the University of Tübingen. SWNT-Arrays with single nanotubes and proper spacing should be considered on in future work. A SEM picture of one of the wafers used in this work is shown in fig. 1.16. The assumption was

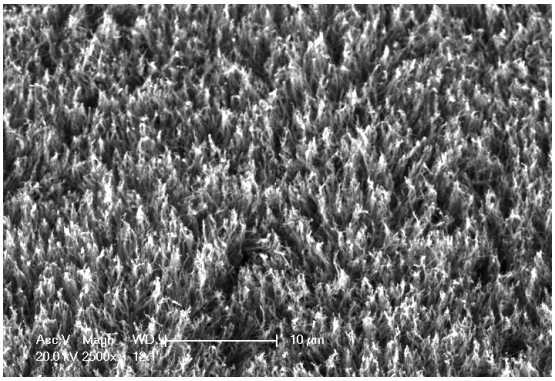

Fig. *1.16: SEM picture of nanotube forest.*

made, that there exist single tubes on the wafer which have larger height than surrounding tubes and that field enhancement will occur on those nanotubes. The ions will be accelerated along the field lines towards the deuterated target if placed correctly. The following section will discuss the fusion reaction as well as the expected neutron flux and discusses possible target materials.

1.3 Expected neutron flux

To drive a nuclear deuterium fusion at low ion currents and energies, a target containing deuterium has to be chosen. The allowed fusion reactions are

$$\begin{aligned} \mathrm{D} + \mathrm{D} &\longrightarrow {}^{3}\mathrm{He}\ (0.82\,\mathrm{MeV}) + \mathrm{n}\ (2.45\,\mathrm{MeV}) \\ \mathrm{D} + \mathrm{D} &\longrightarrow \mathrm{T}\ (1.01\,\mathrm{MeV}) + \mathrm{H}\ (3.02\,\mathrm{MeV}) \end{aligned}$$

which have about the same cross section at incident ion energies below 200 keV. In brackets, the shares of the released binding energy is given. The two reactions are often referred to as the n-branch and the p-branch. This is important because half of all ions will be lost for neutron production. During long runs, the tritium density at the target may rise and the D(T,n)He might become available.

$$\mathrm{D} + \mathrm{T} \longrightarrow {}^{4}\mathrm{He}\ (3.5\,\mathrm{MeV}) + \mathrm{n}\ (14.1\,\mathrm{MeV}) \tag{1.20}$$

However, the extremely low expected initial reaction rate will make the tritium fusion very unlikely within reasonable timescales. Tritium will cause dangerous

background if exposed directly to CRESST detector modules. Details on this topic will be discussed in section 4.6.1. A comparison of the nuclear cross sections for all dominant fusion reaction channels is shown in fig. 1.17.

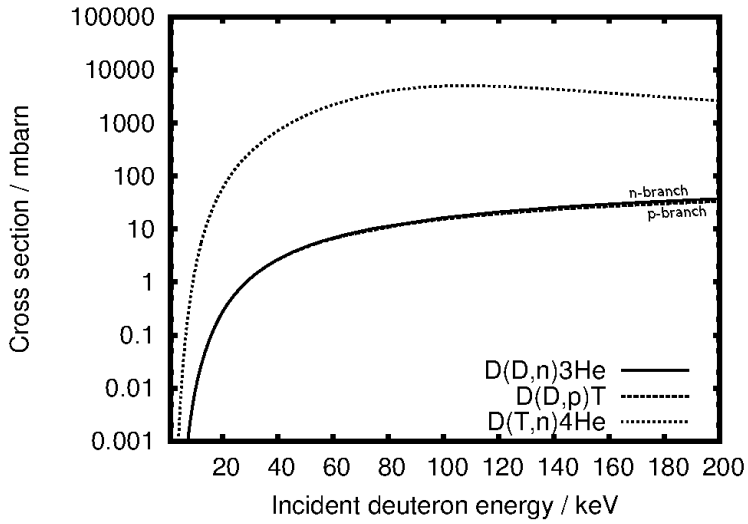

Fig. *1.17: Dominant fusion reaction cross sections. Data from the evaluated nuclear data files, ENDF.*
http://www.nndc.bnl.gov/exfor/endf00.jsp .

The crystal with a diameter of 30 mm provides an acceleration potential of 100 kV while accumulating a total charge of $Q = 1.01 \cdot 10^{-5}$ C during one heating cycle (75 K). As estimation of the maximum expected neutron flux, this charge will be considered as D^+ or D_2^+ ions striking the target. As explained in the last section, all of the ions produced are D_2^+ ions with half the acceleration energy per nucleus for which a realistic calculation of the expected flux is also performed.
With a kinetic energy of about 100 keV per D_2^+ ion, the range of the particle in matter is short. The active volume is defined as the range of the particle until the cross section for the nuclear reaction drops below reaction threshold due to the ions energy loss. The minimum fusion energy is given by the ions minimum energy to compensate the coulomb repulsion of the target nucleus. This energy is about 15 keV for the D(D,n)^{3}He reaction. The energy loss $\frac{dE}{dx}$ for D_2^+ and D^+ in different materials was calculated using SRIM[3] (see fig. 1.18), which gives the total penetration depth of the ions dependent on their incident energy. For example, a D^+ ion with 100 keV incident energy hitting a gold target has an energy loss dE/dx of approx. 0.17 keV per nm. A linear estimate gives a range of 590 nm in gold. This value is already in the right order of magnitude however, using the

[3]Stopping and Range of Ions in Matter, `http://www.srim.org/`

tabulated values will show that the projected range to full energy loss for this particle is roughly 480 nm. The material selection for which the energy loss and maximum range was determined depends on the target material characteristics which will be discussed later on. For the estimation of the expected fusion flux, only the values for deuterated polyethylene (CD_2) are being used. SRIM can calculate the energy loss also for anorganic and organic compound materials. The maximum ion range for selected materials is shown in fig. 1.19.

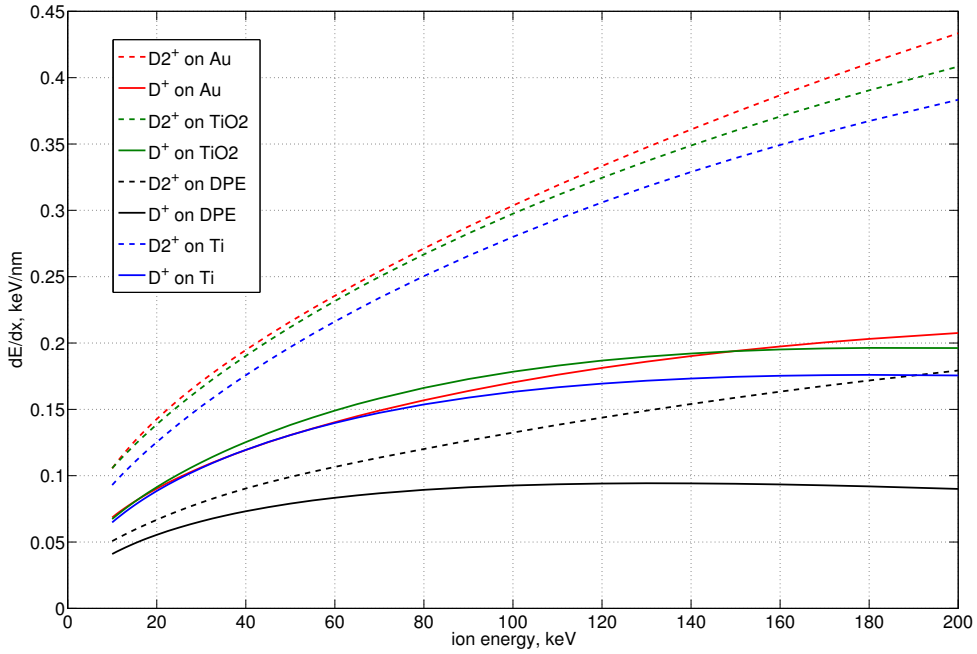

Fig. *1.18: dE/dx for ions in different target materials. Calculation done with SRIM code.*

In order to calculate the expected fusion rate for D^+ ions on a CD_2 target, the reaction cross section is integrated over the track of the ion in the target until the ions energy drops below the reaction threshold: The ion energy and dE/dx as function of depth in CD_2 is plotted in fig. 1.20. With the cross section data from the ENDF, plotted in fig. 1.17, the integrated cross section can be calculated:

$$\langle\sigma\rangle \cdot Range = \int_0^{Range} \sigma(E(x))dx. \tag{1.21}$$

For the parameters given above and using deuterated polyethylene as a target, the integrated cross section down to the threshold of 15 keV is $\langle\sigma\rangle \cdot Range = 1.01$ barn·nm for D_2^+ ions. Actually this is the integrated cross section for one of the two deuterium nucleii, with halft the energy of the whole ion. Therefore a factor two

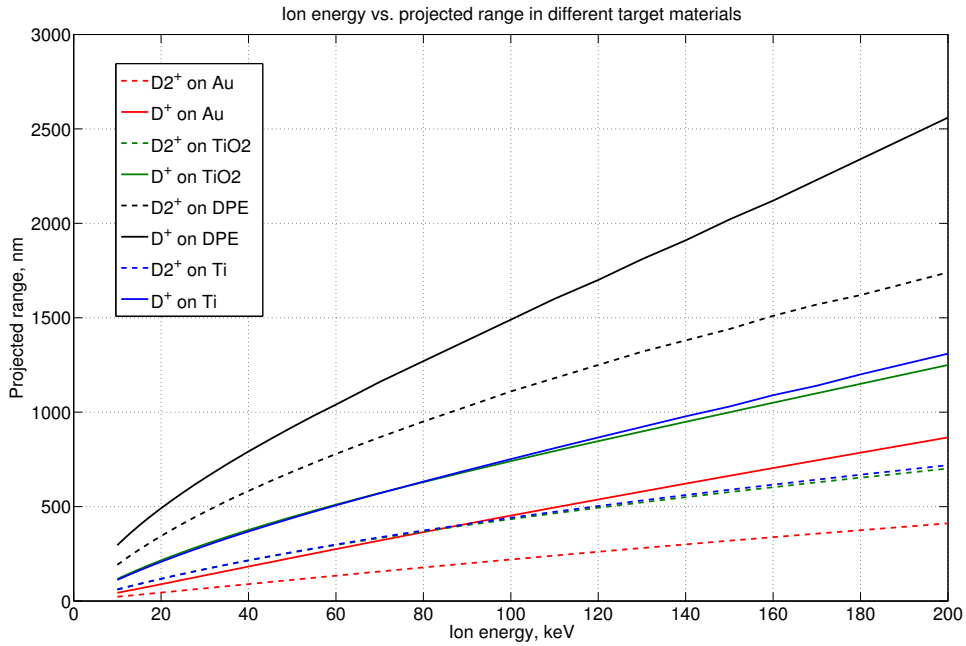

Fig. *1.19: Projected ion range in different target materials. Calculation done with SRIM code.*

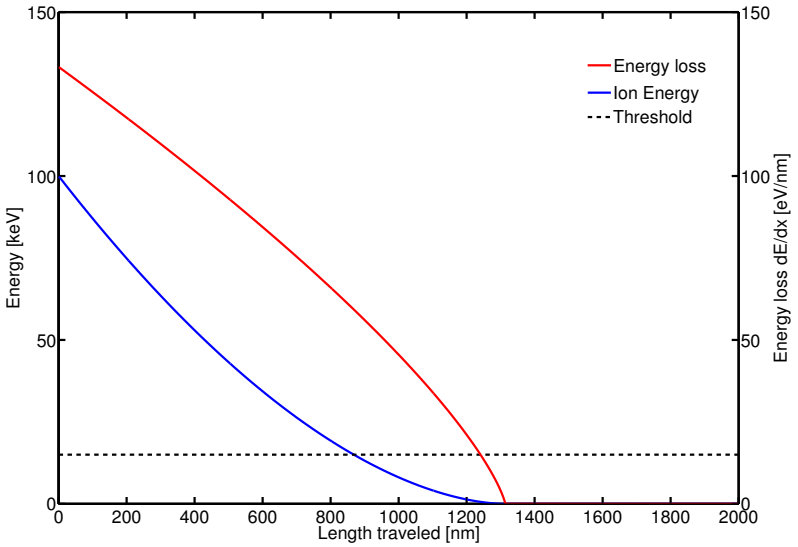

Fig. *1.20: SRIM: Range and dE/dx for 100 keV D_2^+ on CD_2, the 15 keV reaction threshold is also shown in plot.*

must be corrected. The expected number of fusions per thermal cycle is

$$N_{fusion} = 2 \cdot \phi \cdot N_D \cdot \langle \sigma \rangle \cdot Range \tag{1.22}$$

where ϕ is the number of ions per thermal cycle and N_D is the density of deuterium atoms in the target. At first, the number of ions is assumed to be equal to the total amount of charge available: $\phi = Q/e = 6.3 \cdot 10^{13}$ ions per thermal cycle. With the crystal charge Q and the elementary charge e. The number density of deuterium atoms in the target is

$$N_D = \frac{2\rho_{CD_2} N_A}{M_{CD_2}}. \tag{1.23}$$

The density of deuterated polyethylene is ρ_{CD_2}=1.06 g/cm^3, N_A is Avogadros constant and M_{CD_2} is the molar mass of CD_2. The factor of two has to be taken into account to correct for the amount of deuterium atoms per unit molecule. The number density is $N_D = 7.98 \cdot 10^{22}$ [1/cm^3]. For each incident D_2^+ ion there are two nuclei with half the energy of the ion. The expected number of fusions has a maximum of

$$D_2^+ : N_{fusion} = 1.0 \cdot 10^6 \tag{1.24}$$

per thermal cycle. But one has to keep in mind that half of the fusion reactions appear in the p-channel producing tritium. So the number of neutrons per thermal cycle has a maximum of

$$D_2^+ : R_{neutron} = 5.0 \cdot 10^5 \tag{1.25}$$

A typical temperature cycle duration, regardless of heating or cooling, is half an hour. Therefore the average number of neutrons produced per second is 280 for 100 keV D_2^+ ions. This calculation can now be performed for different incident energies. An energy dependent calculation of the expected maximum neutron number per thermal cycles is shown in fig. 1.21. Assuming that a minimum high voltage of 75 kV is necessary in order to drive the field ionization, only higher voltages contribute to the neutron flux and $1.8 \cdot 10^{13}$ charges are necessary to maintain this 75 kV, leaving $4.5 \cdot 10^{13}$ charges in every thermal cycle available for conversion into ions. This assumption decreases the maximum expected neutron flux to 200 n/s for D_2^+ ions. To derive a realistic expectation of the neutron flux, the time distribution of the high voltages must be determined so that a weighted average of the neutron flux can be determined.

1.3.1 Parameter acquisition for neutron flux estimation

A so called “run” is a series of subsequent thermal cycles recorded without any interception. The external parameters such as deuterium pressure and bias voltages are being held constant for each run. Bias voltages can be applied to modify

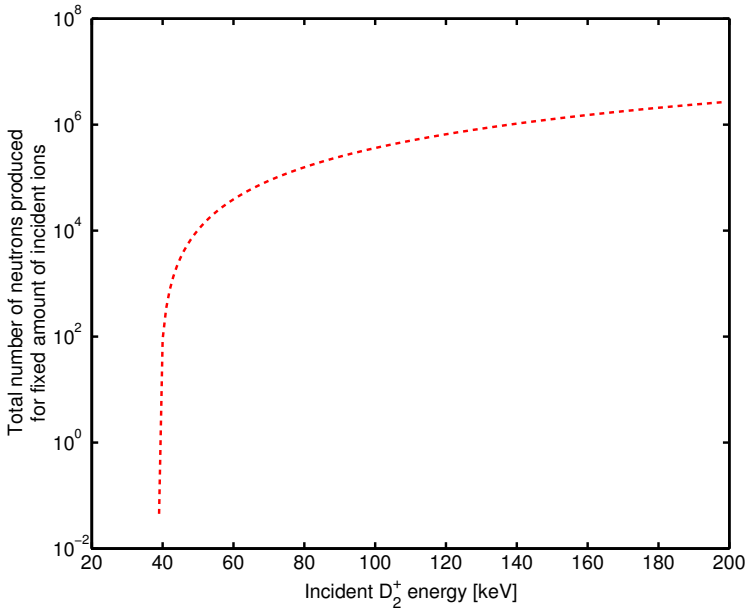

Fig. *1.21: Calculated energy dependent maximum neutron number per thermal cycle for D_2^+ ions hitting CD_2. This calculation uses a fixed amount of ions per energy: $4.5{\cdot}10^{13}$.*

the electrostatic field configuration in the setup. The internal parameters such as temperature, polarity, high voltage and available charge as discussed in this section vary within the run and must be recorded for the whole run time.

Temperature:

Each run is split into several heating and cooling cycles, whose length depends on the heater and cooler power settings and of the total heat capacity of the structure to be heated or cooled. A typical temperature difference which is used for heating and cooling covers 75 K, from -15^{o}C to 60^{o}C. A typical duration to achieve this temperature difference is in the order of half an hour.

Polarity:

Depending with which end of the polar axis the pyroelectric crystal points towards the target, the exposed crystal surface charges with different high voltage polarity if heated or cooled. It can be determined during a run (See section 2.3.4). Neutrons are only expected if the high voltage polarity allows the deuterium ions to be accelerated towards the target. This means that the exposed face of the crystal must be charged positive in order to drive a fusion reaction.

High voltage:

The high voltage at the crystal surface cannot be measured directly and must be determined by the unavoidable Bremsstrahlung which in addition can be used to determine the polarity. Bremsstrahlung must be reduced at all costs since the electrons also remove charge from the crystal, reducing the number of ions which can be accelerated towards the target. On the other hand, Bremsstrahlung is the only tool available to measure the high voltage and its polarity directly. The absence of Bremsstrahlung does not necessarily indicate the absence of high voltage. High voltage simply cannot be measured at all times.
An example where the relative time fraction for which the high voltage was measured for all high voltages is determined is shown in fig. 1.22. The integrated time fraction for all high voltages above 75 kV is in the order of 5-20% of the total run time, dependent on the optimization. The neutron flux is calculated for each ion

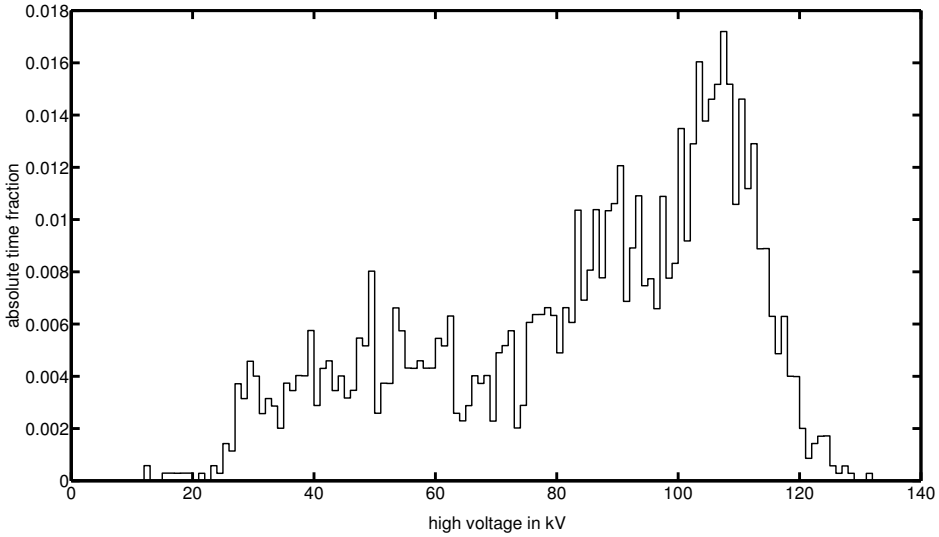

Fig. *1.22: Absolute high voltage heating time fraction from all heating cycles in an exemplary neutron run. If this fraction is integrated for high voltages above 75 kV, the total time fraction will be in the order of 5-20% of the total run time (In this plot: 32% of heating time which corresponds to 12% of the total run time).*

energy above 75 keV (see ionization limit) and weighted with the time fraction, then averaged for all heating cycles.

Charge loss:

All effects removing charge from the crystal which is no longer available for any neutron production decrease the expected neutron number, electrons being emit-

ted to or from the crystal, discharges and ions.

Ionization limits:

The majority of ions is expected to be produced at voltages above 75 kV where tunneling ionization of deuterium on the tip is allowed. This means, high voltages below 75 kV do not significantly contribute to the neutron yield even if the cross section allows it. Therefore, periods where the crystal is not charged to at least 75 kV have to be considered less or not productive. The charge necessary to maintain this high voltage is also not available for ions. Changes or damages of the tip also change its geometry, which can modify the ionization efficiency of the tip. The impact of this effect is not determined yet.

Ion loss:

Ions being produced and accelerated can also miss the target due to the geometry. Those ion losses will also decrease the expected number of neutrons.

1.3.2 A realistic expectation for the neutron flux

The following expectation is calculated using an exemplary real run averaging over all cycles of correct high voltage polarity. Considering all effects mentioned above, a realistic expectation of the approximate average neutron number produced per second during thermal cycles with correct polarity can be derived.
At first, the neutron rate is calculated as function of acceleration energy for a given number of ions per thermal cycle which can be determined from the integrated measured ion current or by the approximation described above. Then, the measured high voltage is sorted into bins to determine the absolute time fractions within that thermal cycle. Alternatively one can chose a reasonable average high voltage. The neutron rates are then weighted for each acceleration energy with the occurrence of the corresponding high voltage. A reasonable high voltage average of 75 kV and an typically measured integrated ion current of 350 nAs ($2.2{\cdot}10^{12}$ ions), occurring within 30% of the heating time of a single cycle (500 s) leads to the following prediction for the expected source neutron flux during high voltage is 10 n/s. By averaging over the complete polarity cycle of 1800 s, the average expected source neutron flux is only about 3 n/s. Due to the varying high voltage and ion current conditions, a realistic average flux is

$$\mathrm{D}_2^+\colon \Xi_{real,exp} \approx \text{1-10}\,\mathrm{n/s}$$

The ion current measured on the target is in the range of 0.5 to 1.2 nA, compared to the expectation of 4 nA. The "missing" ion current is covered by electrons from field electron emission.
For measurements where the ion current was measured, the expected fusion rates

can be calculated exactly. Data obtained by real cycles result in neutron rates of 1-10 n/s depending on each individual cycle settings.

1.3.3 Detection Capability

The neutron detector setup during the last phase of the experiment used for this work is able to detect one neutron out of 40 emitted by the source, at a background of approximately 0.03 neutrons per second. For a detailed description of the detectors solid angle, efficiency and energy response see chapter 2.
With this detector it should be possible to see a flux which is in the expected order of magnitude. For D_2^+ it will still be possible since the expected neutron flux seen by the detector flux is double the background rate. However to validate a signal, good statistics is necessary.

1.3.4 Summary

A realistic estimate of the number of neutrons that can be produced in this experiment is 1-10 n/s if the fusion is driven by D_2^+ ions.
This calculation can be performed for each possible target material. Materials considered as targets are metal hydride, adsorbed hydrogen on porous metal surfaces and plastics such as deuterated polystyrene, CD or deuterated polyethylene, CD_2. Their individual properties, advantages and disadvantages are being discussed in the following sections.
These calculations were done independently but in parallel by the group of Danon and others as well as during this work, however published first by Danon [20]. In contrary to this work, the published calculations and graphs contain several severe errors.

1.4 Targets

Deuterium fusion with a small accelerator needs a target of deuterium, of course. There are several possibilities to enrich deuterium in a material which then can be used as a target.

1.4.1 Metal hydride

A possible target material is a metal hydride where the deuterium[4] is embedded in the crystal structure. This target is electrically conductive and has a rather high deuterium area density. Electrical conductive targets make measurement of the ion current easier. Typical materials for these kinds of targets are titanium, palladium, copper and erbium. These targets are being used at accelerators and other groups researching pyroelectric fusion[38], but suffer from the dead layer energy loss.

[4]as stated before, processes are the same for deuterium as for hydrogen

Most metals oxidise if exposed to oxygen and a dead layer develops. Metal oxide cannot be hydrated and therefore does not contribute to the active (deuterated) volume of the target. The dead layer is usually several ten to hundreds of nanometers thick and has a similar dE/dx as the metal which can be obtained from the tabulated values.
A metal hydride is produced by heating a metal under a high pressure deuterium atmosphere. Typical process temperatures are in the range of 300-700°C while the starting pressure at normal conditions is 4-5 bar. This can be varied for different targets. The deuterium diffuses into the metals crystal lattice forming a metal-deuterium compound, a metal hydride. Metal hydrides are stable against ambient influences apart from heating which can cause the deuterium to be removed from the grid, allowing oxidation. By preparing the metal carrier under protective atmosphere such as nitrogen or argon, dead layers can be avoided. The dead layer can also be removed mechanically or chemically after the hydration process.
On porous metal surfaces such as sputtered titanium or palladium, hydrogen can also adsorb very well. A target which consists of sputtered titanium on a copper substrate was stored for three days under 4 bar deuterium atmosphere. Unfortunately, the target had already adsorbed ambient gas as well as being passivated due to storage under ambient conditions and therefore did not yield any neutrons during testing. The target testing at the Rosenau accelerator is described in section 2.5.
Using the self target effect on metal surfaces was also considered. The self target effect uses the beam ions deposited on the surface of a metal as target ions, the targets ion density increases with time unless the reaction rate equals the number of ions deposited per time. It can be shown that this effect requires much higher ion currents than those available in this experiment. Measurements are shown and discussed in the target testing section 2.5.

1.4.2 Deuterated plastics

Deuterated plastics such as deuterated polystyrene or deuterated polyethylene have very high deuterium densities, but can only be used in low ion current/low temperature environment. Having low melting temperatures, it is easy to get them into the desired shape, but this implies that the ion beam should be unfocused or weak - otherwise the target will melt. Since these materials are very good insulators, it is difficult to measure the current reaching the target unless the surface is metalized.
Thick targets were made by melting and shaping the thermoplast. Thin large area targets were prepared by dripping solved deuterated polyethylene on a polished metal disc. The solution was achieved with Xylene at the melting temperature of

deuterated polyethylene at around 135 °C. This common procedure is described in various sources, for example by Olivo and Bailey[41]. Several different metalized and pure plastic targets were tested upon their qualification as a target (see section 2.5).

1.4.3 Gaseous or liquid deuterium targets

Using gaseous or liquid targets is also possible, but was not considered in this work due to the difficult handling and maintenance. In addition it might be very challenging to develop a tritium-tight, high-vacuum target which has a nonzero transmission for low energetic deuterium ions ($E_{kin} \leq 100\,\mathrm{keV}$).

1.4.4 Target selection

Comparing the different targets, the metal hydride targets cannot be used unless the ion energy and the current are high enough to penetrate the oxygen layer. The deuterated polyethylene gives the highest expected neutron flux.

1.5 Finite element studies of field configuration

From the discussion of the field strengths necessary to ionize deuterium from the gas phase as discussed in section 1.2, a more detailed investigation of electric field strengths and the modification of the ionization rate by the internal geometry was necessary.
The influence on the electric field of the particular tip properties such as radius, surface structure, dimensions of the cone and tilting of the tip was studied. To get an idea how the geometry influences the field configuration and the high voltage on the crystal surface, finite element methods were used within the COMSOL[5] software package available to study such effects. COMSOL is used to model and solve finite element problems. Electric fields can be calculated using the maxwell equations, however they usually cannot be solved analytically for complex structures. By using finite element methods, the electric field can be calculated numerically. The area of interest is being divided into a finite number of elements, which can be described by a finite number of parameters. For each element an ansatz is made which is put into the partial differential equation system. With the geometrical limits and the boundary conditions for each element, the equation system can be solved. The complexity of the equation system and the number of degrees of freedom depends on the amount of elements the area is divided into. With these methods, approximations of electric fields can be calculated. The properties of tip arrays and the field geometry with only one tip were studied.
COMSOL provides several modules each with the corresponding set of differential equations for the problem. Calculations were done with the electrostatic mod-

[5]COMSOL multiphysics, `www.comsol.com`

ule for dielectric and conductive materials. COMSOL provides also a material library and a graphical interface where it is possible to draw the geometry even in 3D. However, a true sized calculation of the cylindrical symmetric setup exceeds, even in two dimensions, all available hardware limitations ($\mathcal{O}\,10^{16}$ elements) since the vacuum chamber structures are several centimeters in size, the ionization tip however has a radius of 50 nm. Therefore, only qualitative statements for the whole setup could be calculated.

1.5.1 Field geometry

The capacitor model does neither include effects of the tip, nor effects of the surrounding geometry such as the grid in between the crystal and the target, which in addition can be biased. The grid between crystal and target is being investigated.
With the grids open area and wire thickness one can calculate the field enhancement and estimate the effective ion transmittance. The field strength on the biased grid ranges from 10^2 to 10^6 V/m depending on the grids properties and bias voltages. For the grid with small wire diameter and large opening area of 88% the field strength can exceed 10^6 V/m. The radial field strength for two different grids and three different bias voltages is shown in figs. 1.23 and 1.24. The ions accelerated towards the grid do have kinetic energies of approximately

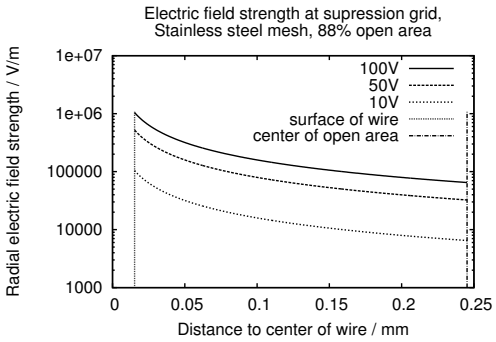

***Fig.** 1.23: Radial electric field strength as function of distance to wire center for different bias voltages. The mesh properties for the fine grid with 88% opening area are being used.*

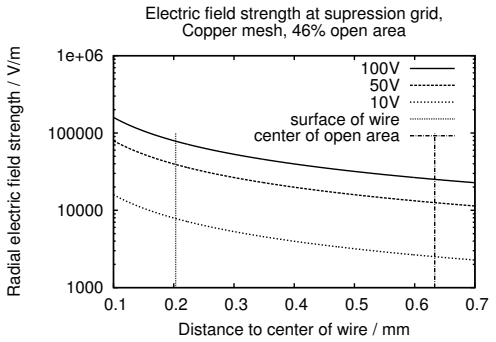

***Fig.** 1.24: Radial electric field strength as function of distance to wire center for different bias voltages. The mesh properties for the copper grid with 46% opening area are being used.*

100 keV. For a D_2^+ ion this corresponds to 1% speed of light. A calculation was performed to see the impact of a biased grid, compared to a target at ground potential and vice versa. With bias voltage of 100 V the calculation shows: the field configuration does not change enough to make an impact on the ion flux

compared to the unbiased case, however a grid at ground potential together with the vacuum chamber walls creates a Faraday cage around the target. A Faraday cage around the target prevents the electrons from field emission processes reaching the crystal, as well as suppressing secondary electron emission from the target. Accelerated ions may hit the grid which will then be lost for fusion processes. Ions transiting the grid extremely close to the wire surface where the field strength is large can be deflected and can miss the target. The deflection angle depends on the electric field strength and polarity of the bias voltage.
The target was biased to +100 V and the grid to ground potential, a configuration was found which does not have any impact on ion traces except for the ions hitting the grid directly. In order to make a possible ion deflection effect of the grid visible, the grid voltage in the simulation was increased to 10 kV and 100 kV. The ions were started near the tip with thermal velocity. The corresponding ion traces are shown in fig. 1.25. In the used COMSOL package there is no collision monitoring implemented so that the ion tracks always reach the boundary of the calculated volume, regardless of whether they strike a structure or not. It could

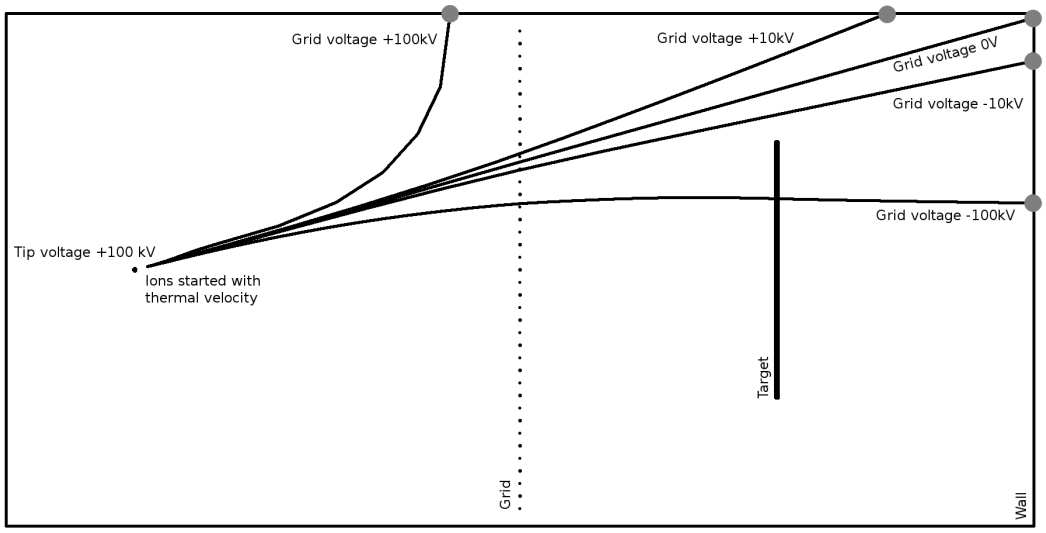

Fig. *1.25: A simplified model in 2D is being used for the calculation of the electric field. The point to the left corresponds to the tip charged to +100 kV, the outer border represents the vaccuum chamber at ground potential. The target on the right is biased to +100 V. The grids voltage is variable and was increased by a factor of 1000 to make any deflection effects visible.*

be shown that the grid bias' effect on ion traces is negligible. The default grid bias is ground potential while the target is biased positively.

1.5.2 Tip geometry

The influence of the tips geometry properties such as cone shape and surface structure on the field configuration have yet to be investigated. To study the effect of the cone shape, the electric field for a series of elliptical "tips" were calculated with COMSOL. The long axis of the ellipses were aligned perpendicular to the closest ground potential. The distance between the tips edge and the nearest ground potential was held constant, so was the tips potential. The relative field enhancement factor was determined by normalizing the field strength to the field strength of the non-elliptical tip. Again only relative values are given which are easier to compare. The field strength of a non-elliptical tip with 50 nm radius at a potential of 100 kV is approximately $5{\cdot}10^9$V/m.
The tip with the highest eccentricity of 0.0078 shows the highest relative field enhancement, a factor of 17 compared to an eccentricity of one which is expected since the effective tip radius decreases.
Tilting the tip from the axis does not change the results significantly if the tilting angle is smaller than 45 degrees. The field enhancement relative non-elliptical tip for different eccentricities is shown in fig. 1.26. The visualization of the calculated

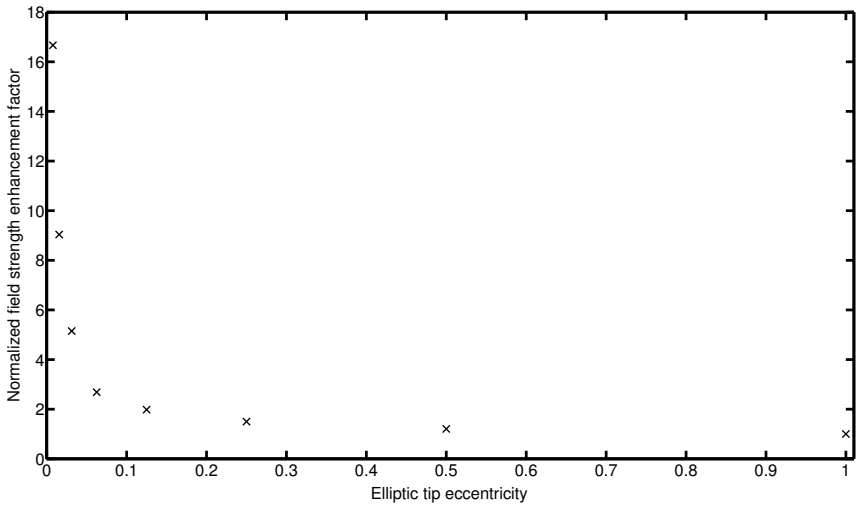

Fig. *1.26: Relative field enhancement factor as function of tip eccentricity. The long axis of the ellipse is perpendicular to the target.*

setups is shown in fig. 1.27.

1.5.3 Tip surface

It is expected that surface substructures on the tip which are smaller than the tip radius increase the field strength at the tip. The term substructure refers to any

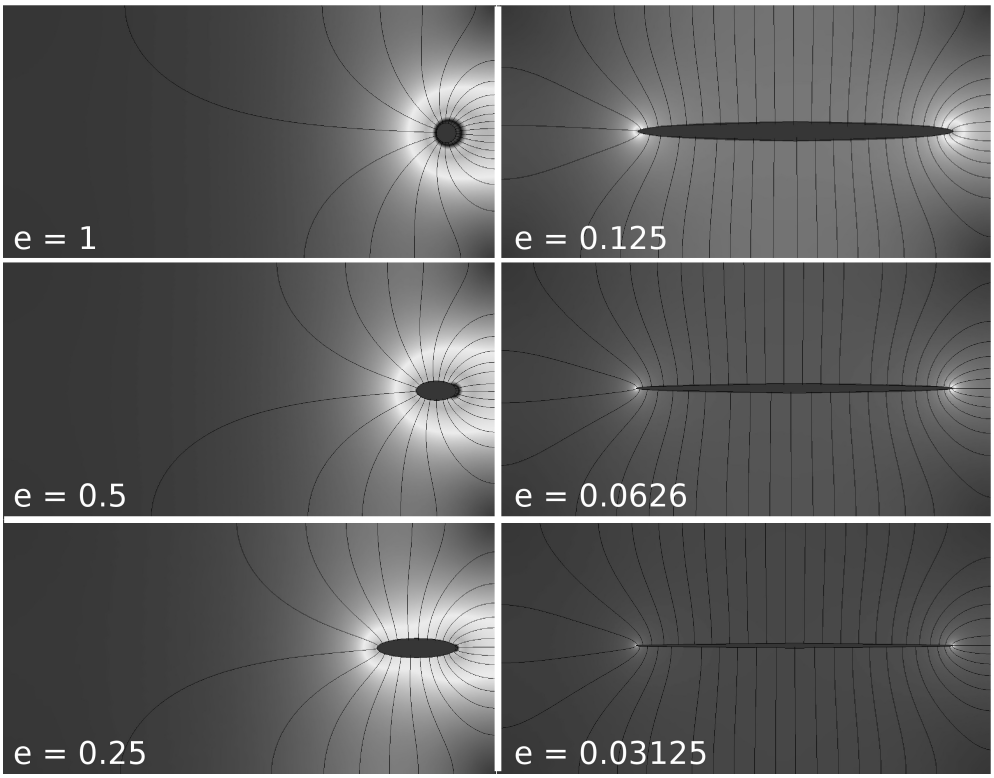

Fig. *1.27: Visualization of tip field strength as function of tip eccentricity*

smaller sized structures on the actual tip surface. The reason for such substructures can be an inhomogenity of the tip material exposed during etching of the tip as well as dirt particles attached to the tip or deformation due to mechanical and thermal damage.
A few calculations were performed to test the expectation of an increse in field strength for existing substructures. The used substructure was a sphere, placed on the tip edge at zero or 45 degree angle. The sphere radius was varied, calculations for 10, 25 and 50% of the tip radius were performed. The calculations show that substructures can enhance the field strength as expected. A 10% radius substructure placed at 45% angle increases the maximum field strength by a factor of about 1.6 compared to the tip without any substructure. A smaller structure will further increase the field strength.

Several substructures were added to the tips surface with different positions and sizes simulating an inhomogenous tip surface. Examples are being given with substructure and maximum field enhancement relative to a tip without structure. Two equal sized structures with 10% tip radius were added to the tip surface yielding an enhancement of ≈1.75, adding another two still increases the field strength by a factor of ≈1.65. By using differently sized substructures with 10 and 25% of the tip radius, the enhancement drops to ≈1.4, however still enhancing the field strength. As expected, structures smaller than the radius of the tip do increase the field strength no matter how they are aligned.

In comparison to a tip which has only the radius of the surface structure, the increase in field strength due to the substructure does not reach the values achieved for the small tip only. A substructure with 10% of the tip radius reaches only 29% of the field strength of a single tip with the same radius, a substructure with 25% of the tip radius reaches roughly 50% and a substructure with 50% of the tip radius reaches 75% of the field strength of a single tip with the radius of the substructure.
This means, if the substructures are small compared to the radius of the tip on which it is located, they do not increase the field strength as much as a tip of smaller radius will. The field strength for smaller tips rises faster than the reduction of the additional field strength gained with the substructure. The overall field strength gets larger.
The field strength relative to the field strength without substructure as function of the substructure size is shown in fig. 1.28.

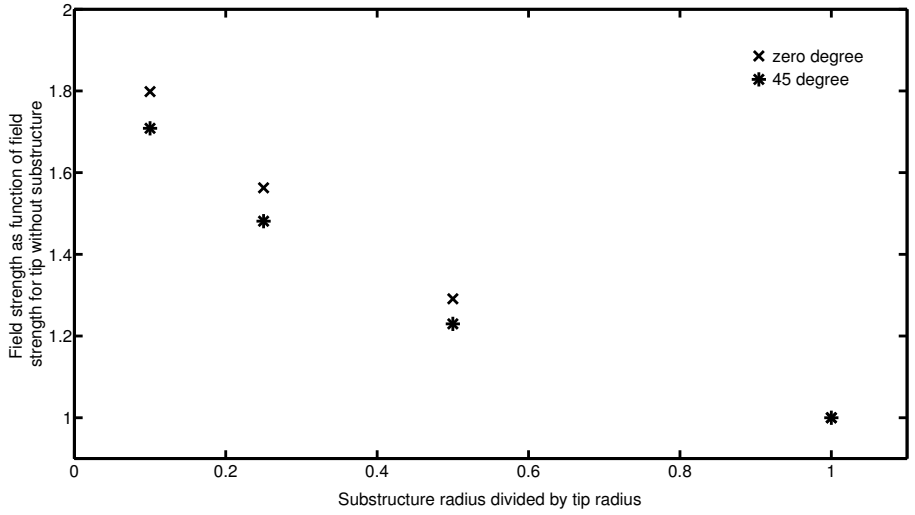

Fig. *1.28: Tip substructure field enhancement, relative field strength as function of substructure radius.*

1.5.4 Tip arrays

Tip specifications for an array were also calculated. The tips with fixed geometry are mounted opposite a large, "infinite" metal cathode charged to 100 kV. The tips themselves are set to ground potential. Their spacing is being varied. The tip length used was 1 µm, the distance to the high voltage face was 2 µm, so that the calculation finishes in finite time. The field strength was obtained from the calculation at zero degrees and at 45 degrees with respect to the high voltage surface. The further the tips move away from each other, the more every one of them approaches the field strength of a single tip. An exemplary visualization of the result of one calculation is shown in fig. 1.29. Fig. 1.30 shows the relation of the tip spacing on the array for a fixed single tip geometry. It can clearly be seen that larger spacing will support full field enhancement towards that of a single tip with approx. $5{\cdot}10^9$ V/m. Tip distances in the order of the length (or more) of the tip will allow for full field enhancement without influence on other tips. A 10% systematic error of the acquired values is assumed due to grid spacing uncertainties. The second investigation focuses on the field enhancement factor as a function of the tip base length in the array at fixed tip spacing. The other simulation parameters are the same as before. The result of the calculation depicted in figure 1.31 clearly shows a strong correlation of field enhancement with the tip length, however, by a factor of 1000, so not as strong as expected by the models of Edgcombe and Valdrè [21],[24]. This is a result of the limited calculation resolution as well as of the model simplification by using a two dimensional

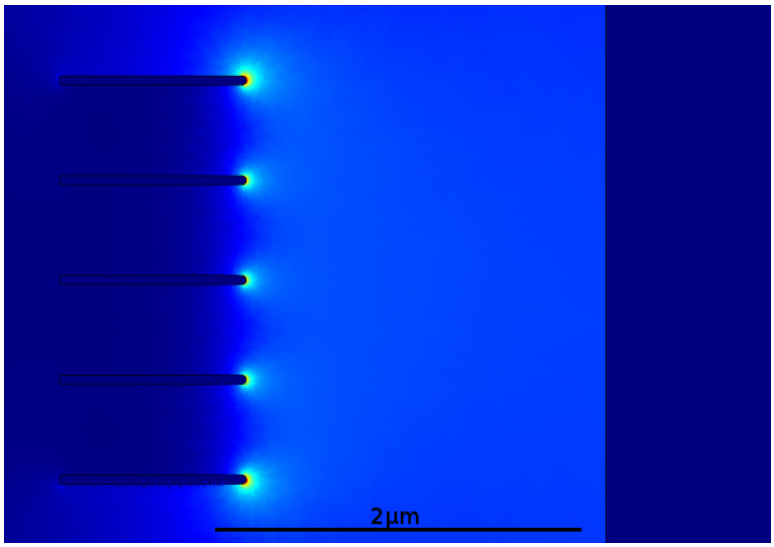

Fig. *1.29: Exemplary FEM calculation of electric field strength of tip array facing high voltage potential in 2 µm distance with 500 nm tip spacing. Field strength measured at center tip. Field strength increasing from blue to red.*

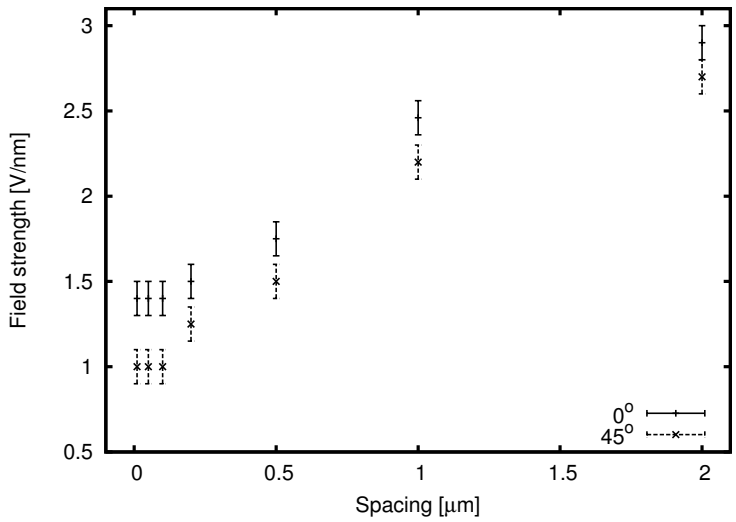

Fig. *1.30: Tip array dependency on tip spacing, tip radius 50 nm, 100 kV bias voltage, tips grounded, high voltage face distance 3 µm and tip length 1 µm*

geometry. For comparison, the L/R of a single tungsten tip as used in this work is larger than 40000. An additional 10% error is being assumed from the size of the finite elements for the values obtained. In summary the optimal tip array

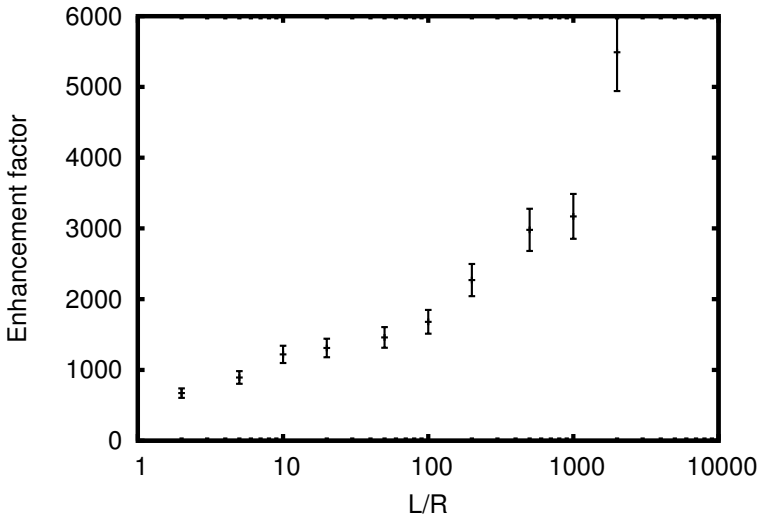

Fig. *1.31: Tip array field enhancement dependence on tip base length, tip radius $R = 50\,nm$, $100\,kV$ bias voltage. Tip spacing $2\,\mu m$. L/R is the fraction of base length L divided by tip radius R.*

would tips whose radius is as small as possible, a maximized L/R and a distance of the tips of double a tip length. Very good ionization properties is expected from a wafer which has equally distributed tips which are 1 mm long, a spacing in between the tips of at least 1 mm and a tip radius of 25 nm. It was not possible to acquire such tip arrays, not even with similar specifications within the timescale of this work.
However, the nanoscience community came up with the idea to use carbon nanotubes for ionization which are easier to produce in a wider range of parameters. Carbon nanotubes can also be used for field enhancement and field ionization of gases. Their ionization properties are similar to those of the tips which is why no dedicated calculation was performed for the nanotubes. The advantage of the nanotubes is, that the nanotube radius, their spacing and their length can be controlled very accurately. An L/R of 50 to 1000 is possible relatively easy. Also the production arrays of single upright carbon nanotubes is possible.
Both options - the tip arrays as well as single nanotube arrays - provide excellent ionization probabilities if they can be obtained.

2 Experimental Setup and Detector Systems

"In physics, you don't have to go around making trouble for yourself - nature does it for you."

- Frank Wilczek

Experimental Setup

The external and internal structure of the setup, technical and design problems are being discussed in this section. At first an overview of the vacuum system, gas handling system and detector modules will be given. Afterwards the target, crystal, support structures and sensors will be discussed.
There were three different experimental phases defined during this work, for which larger changes in the setup and the detectors were made. The different settings will be discussed regarding each experimental phase. This sections focuses on the internal changes made for the different phases. The external changes, such as more or different neutron detectors are discussed in the next chapter.
At first however, general specifications relevant for all phases will be described.

2.1 External structure and vacuum specifications

The crystal, the tip and the target, which represent the internal setup, are encased in a vacuum chamber to prevent accidental discharge of the crystal. Deuterium is fed into the chamber via the gas handling system, which can also be evacuated. The detector systems for X-rays and neutrons are mounted outside the vacuum chamber to trace and monitor the reactions inside when the crystal is charged.
Working in a low pressure environment allows the use of the charges available from the crystal if a temperature change is being applied. At atmospheric pressure the charges are immediately masked by molecules from the air which makes any application of pyroelectric charge impossible. The vacuum system consists of a main experimental chamber which has a volume of about 22 Liters and is evacuated by a turbomolecular pump. The system is tightened via the ISO-K and ISO-KF standards which uses viton o-rings and is not gas tight. The leakage is in the order of 10^{-8} mbar·L/s. The base pressure can reach values smaller than 10^{-6} mbar. A gas handling system is necessary in order to fill the vacuum

chamber with a defined amount of deuterium or purge the system with dry nitrogen gas. To remove contaminants and remaining air, the gas handling system can be evacuated as well. A scheme of the whole gas handling system including pumps is shown in fig. 2.1. The performance of the accelerator is very sensitive to

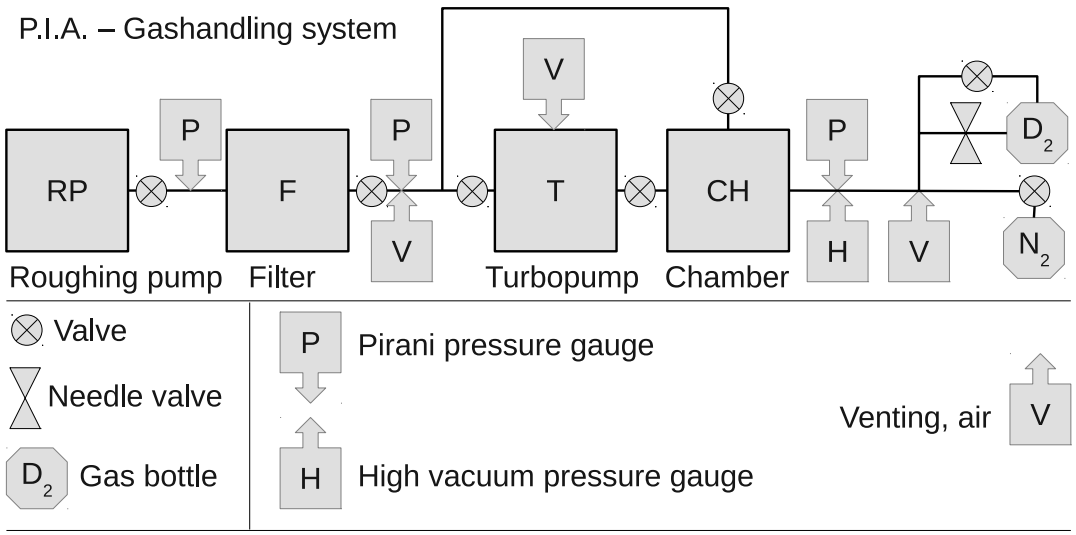

Fig. *2.1: PIA current gashandling system*

the pressure conditions. By increasing the pressure within the vacuum chamber, more deuterium molecules will pass the ionization volume around the tip and the ionization probability rises. However the probability for electrons scattering off nuclei also rises and with it the electron amplification, leading to a faster discharge of the positively charged crystal. The X-ray yield rises due to the fact that more electrons are being accelerated and decelerated which allows a better determination of the high voltage on the crystal surface due to better X-ray statistics. One has to find a good compromise to measure both, ions and X-rays. The working pressure is chosen in a range from $1.0{\cdot}10^{-4}$ mbar to $1.0{\cdot}10^{-3}$ mbar deuterium pressure where the discharge probability is low and very good high voltage performance was achieved. Lower pressures are decrease the amount of deuterium molecules entering the ionization region for a given time span. Higher pressures will increase the probability for a discharge by triggered ion collisions with gas molecules, and therefore reduces the amount of ions reaching the target. The interesting pressure ranges are within the transition of the sensitivity ranges of the two vacuum gauges, the pirani gauge and the cold cathode gauge. The reading of both vacuum gauges depend on the gas type, and the reading is calibrated to nitrogen or air. Therefore, the reading of the pressure must be corrected for deuterium gas. The gas type dependent response diagrams for both vacuum gauges are shown in the appendices F and G.

Apart from the vacuum system, detectors are needed to detect reaction products. Since the best commercially available mass spectrometers are not sensitive enough by a factor of 1000 in order to detect helium-3 or tritium, the only detectable reaction particles left are neutrons. The neutrons can be detected using liquid scintillator counters. A side product of high voltage application is the generation of bremsstrahlung by decelerating electrons. The X-ray continuum can be used to calculate the high voltage at the crystal surface, the fluorescence radiation can be used to determine the polarity of the high voltage.
The neutron detectors are described in chapter 3, the X-ray detector in section 2.3. In the next section, the internal parts of the experiment such as the crystal for high voltage generation, the ionization tip and the target are presented.

2.2 Internal structure

The internal structure consists of two main parts - the crystal part and the target part. The crystal has to be instrumented with heating and cooling devices as well as at least one temperature sensor. In this section a short overview about several development stages is given.

2.2.1 Crystal part

As introduced before, it is distinguished between different phases of this work, defined by larger changes of the experimental setup. Sketches and pictures of the different phases for a direct comparison are shown in figs. 2.3 to 2.8.

Crystals used

The crystals used in this work were two Z^-cut $LiTaO_3$ crystals with 30 mm diameter, one with 10 mm height the other one with 20 mm height. They were glued onto a very fine lapped copper holder. A polished copper disc is mounted on its face to prevent surface charge trapping. The crystal is heated or cooled with a temperature change between 0.01-0.1 K/s. The crystal is mounted with the Z^+ face towards the target, charging positively while heating. The crystals are cleaned several times before mounting to suppress leakage currents at the surface.

Crystal heating, crystal cooling and temperature sensors

The crystal is glued onto a copper holder by using silver conductive paint for thermal and electrical coupling. The crystal was cooled using a copper cold finger immersed in liquid nitrogen. This setup was only used in previous work and phase I. Because it required constant refilling of liquid nitrogen and a regulation was not possible, it was changed to an electric cooling system. An internal high vacuum certified double stage Peltier element with an ΔT_{max} of about 83 K was

installed[1] and used in phase II and III. The crystal is coupled to the Peltier element by a variable copper cold finger.
For heating purposes a 1.0 Ω heating resistor was glued onto the back of the crystal holder. The NiCr-Ni temperature sensors are mounted on the cold finger, 15 mm behind the back plate of the crystal and directly on the back plate of the crystal. The temperature sensors are glued with Emerson & Cuming Stycast® epoxy (2850FT), which is electrically insulating, has good heat transfer and vacuum properties after hardening. The two temperature sensors change their reading in parallel, the absolute difference is constant at 0.3 Kelvin, which is in perfect agreement with the precision uncertainty of the temperature measurement devices. The temperature change of those two sensors is equal, which means no measurable differential heating/cooling occurs.

Phase I

During phase I, the crystal was mounted with the target exposed to a tip holder. The tip was not on the crystal so that ions should have accelerated towards the crystal. The advantage of this setup is the more convenient way to change single tungsten tips without removing the crystal. In this configuration it is impossible to suppress secondary electrons coming from the crystal if hit by ions, because a suppression grid must exceed the voltage on the crystal surface without using external power sources and without contacting the crystal. This triggered the decision to introduce a Faraday cage containing the target during the next phase. Therefore also the tip must be moved to the crystal surface.

Phase II

The tip was mounted to the crystal facing in direction to a Faraday cage around the target. Both, target and cage can be biased with voltages up to +/- 100 V. The opening area of the Faraday cage grid was chosen to be large, 88 % at maximum. A scheme of the internal setup since this phase is shown in fig.2.2. However the neutron detection efficiency during phase II was not sufficient to measure any neutrons from fusion reactions. The idea was to construct a neutron detector right into the vacuum, covering a large solid angle in order to increase the neutron detection efficiency, causing also changes to internal geometry.

Phase III

Phase III was initialized when the new neutron detector was built and mounted directly into the vacuum chamber. Introduction of this detector made changes to the internal geometry necessary. A removable Faraday cage and a new target

[1]The Peltier element was produced by Kryotherm, Saint-Petersburg, Russia, Model no. TB-2-(127-127)-1,3

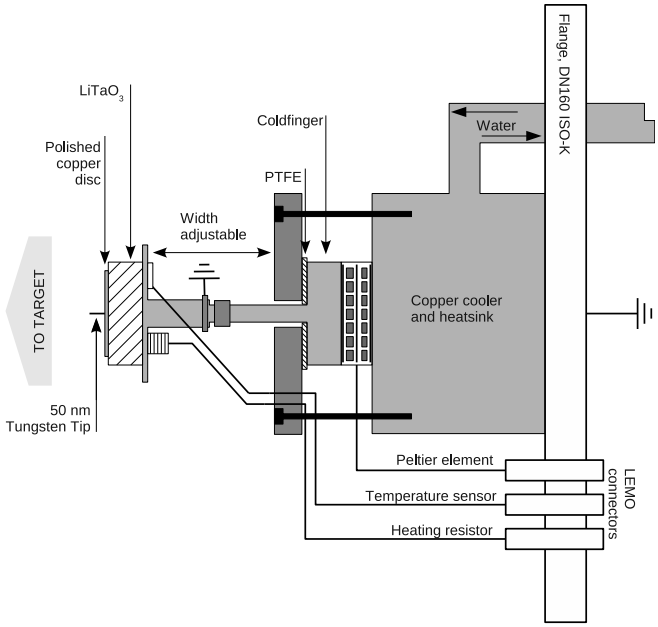

Fig. *2.2: Crystal holder structure during phase II of the experiment.*

holder were constructed and mounted directly to the neutron detector. The thermal coupling of the crystal to the cold finger was improved by enhancing the contact area.

Materials and problems

Construction materials used in the vacuum for the internal structures are copper, stainless steel, PE, PTFE and glass fiber reinforced PTFE. Electrical contact is established using common solder which in this case is believed to be the main source of outgassing. The strongest indication for outgassing is the time dependence of the base pressure, which improves slowly over time ($\mathcal{O}$1e-7 mbar/week) if regular heating and cooling of the crystal is applied.
New connectors free of solder should be used in future work.

Tip handling and tip mounts

The tips were etched from a 0.1 mm tungsten wire in 3-molar potassium hydroxide solution. The etching apparatus and process was described in previous work [16]. Scanning electron microscope (SEM) pictures of a proper tungsten tip are shown in figs.2.9 and 2.10.
Depending on the crystals polarity the tip must either face the crystal (off-crystal) or should be mounted on its surface (on-crystal). As stated above, the need to suppress secondary electrons with a grid results in a crystal mounted tip, which

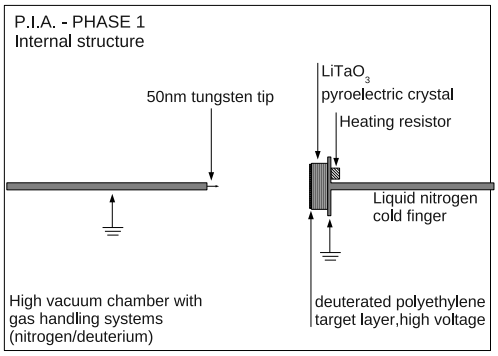

Fig. *2.3: Schematic of the internal structure of PIA during phase I*

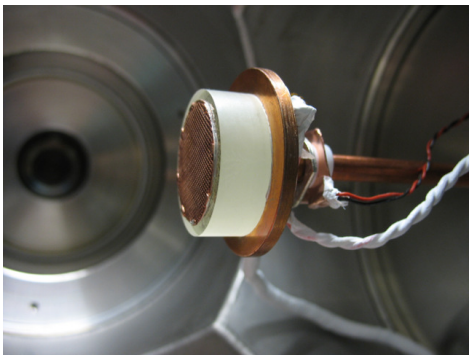

Fig. *2.4: Photo of the crystal during phase I, tip is shown in fig.2.11*

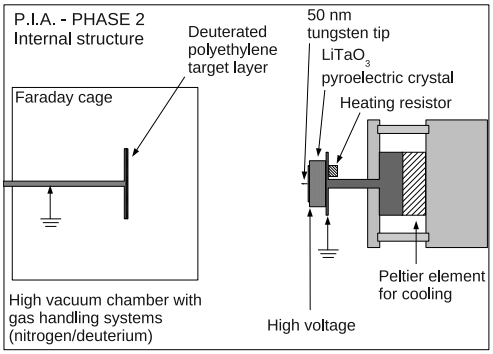

Fig. *2.5: Schematic of the internal structure of PIA during phase II*

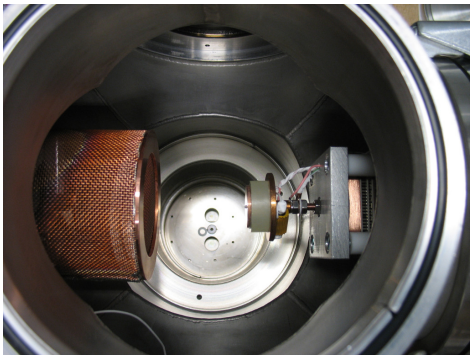

Fig. *2.6: Photo of the internal structure of PIA in the beginning of phase II*

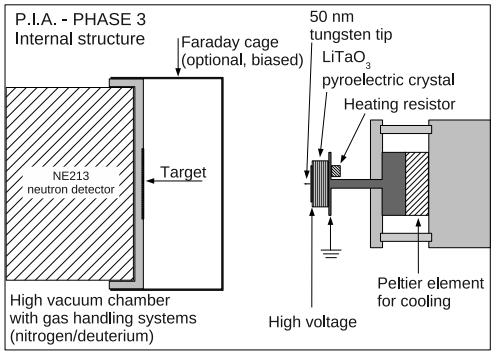

Fig. *2.7: Schematic of the internal structure of PIA during phase III*

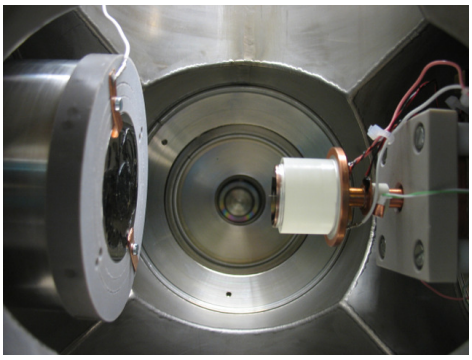

Fig. *2.8: Photo of the internal structure of PIA in the beginning of phase III*

is far more difficult to handle compared to a tip mounted off-crystal. To mount the tip off-crystal a small aluminum holder was created where the tip could be screwed into. For on-crystal mounting, a small copper disc with a 0.2 mm hole was made, and the tip glued into this hole with silver conductive paint. Mounting the tip to the copper disc requires much more precision than mounting the tip to the aluminum holder because the alignment of the tip is more difficult. In addition, the integrity of the tip cannot be checked if the tip is mounted on the crystal since the holder is too large to fit into the SEM. The tip mounts are shown in figs. 2.11 and 2.12.

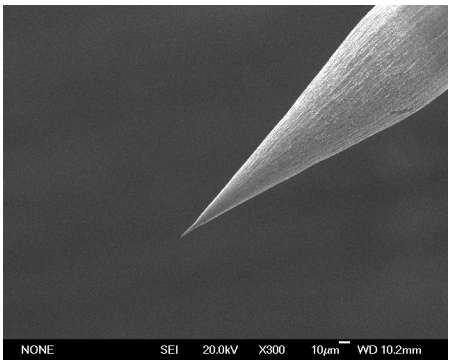

Fig. *2.9: Geometry of an etched tungsten tip*

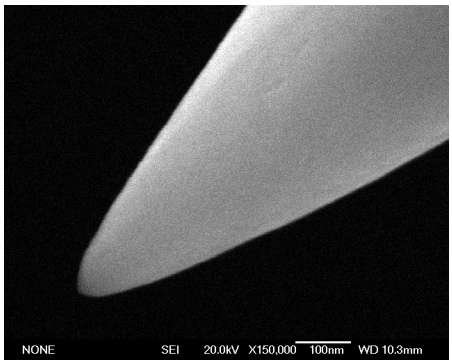

Fig. *2.10: SEM picture of the tungsten tip, tip radius $< 50\,nm$.*

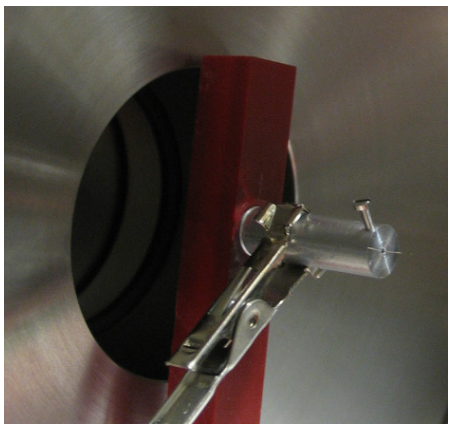

Fig. *2.11: Tungsten tip on aluminum mount, off crystal*

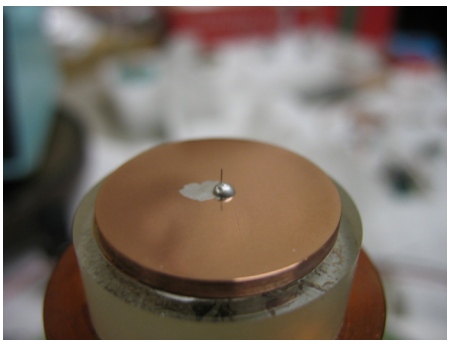

Fig. *2.12: Tungsten tip on copper disc on crystal, glued with silver conductive paint*

2.2.2 Target part

The targets are being mounted either on the crystal or at the opposite structure, vacuum chamber or neutron detector, depending on the tips location. The targets are either deposited on metal substrates, polished copper or aluminum discs or metalized with a few nm of gold. Targets were manufactured to fit two sizes used for this work namely discs with 30 and 60 mm diameter and a height smaller than one millimeter. The target is equipped with electrical contact to read the ion current.

2.3 X-ray detector system

A crucial point in this experiment is the precise knowledge of the high voltage on the crystal surface at a certain time. If the high voltage is known, periods of expected neutron production can be identified. If the high voltage exceeds the deuterium ionization voltage limit of approx. 70 kV (which depends on the tip geometry, of course.), positive ions can be created, and the cross section of the fusion reaction increases which mean more neutrons are expected.
A direct measurement of the high voltage will cause a breakdown of the high voltage due to the fixed and very small amount of available charge on the crystal. For this purpose one measures time dependent X-ray spectra. Electrons from the remaining gas as well as electrons from field emission will be accelerated by the high voltage, producing a Bremsstrahlung spectrum that ends at the maximum acceleration voltage. The available fluorescence lines show where the electrons are stopped. This can be at the crystal (charged positive) or on the target and the chamber walls (if the crystal is charged negative). They therefore give a handle on the polarity of the crystal as well.

Requirements

The X-ray detector must be able to detect X-rays up to high energies above 100 keV. It is required that the detector is able to identify X-ray fluorescence lines of silver, molybdenum and tantalum between 15 and 70 keV in order to identify the high voltage polarity. The readout must support time dependent X-ray spectra which was the reason why a charge integrating ADC was used for analysis instead of a peak sensing ADC. A peak sensing ADC and optimal filtering would have been the preferred options to read out the detector, however the available peak sensing ADCs did not provide any time information, which made the use of the QDC necessary. The optimal filter could not be applied due to restrictions of the QDC. Any attempt to use an external constant fraction trigger to integrate just over the signal maximum resulted in a worse energy spectrum compared to what was finally used.
An energy resolution of a few keV is desired for the high voltage measurement.

2.3.1 Si(Li) technical specifications

For the detection of the X-ray emissions a Canberra SL - 30165 Si(Li)[2] detector is used. The Si(Li) is a lithium drifted silicon diode with a band gap of about 1.1 eV. The diode is biased to -500 V, depleting almost the whole diode. Photons depositing energy will create electron hole pairs which drift to the corresponding contact. The charge generation statistics is responsible for the energy resolution while the total number of charge carriers is proportional to the deposited energy. The detector is equipped with a 30 L Dewar ("cryostat") to keep the diode cold at all times to prevent lithium from drifting out of the diode which would decrease the energy resolution. Some parts of the preamplifier are mounted within the cryostat to decrease the electronic noise level.
The typical X-ray energy range this detector is used for is 1-30 keV. In this work, the detector is used to detect X-rays at much higher energies. The signal processing was optimized for a linear response at high energies.

2.3.2 Si(Li) energy resolution

The resulting energy resolution was below 2 keV over the whole energy range, much worse than what usually is possible with such a detector. Luckily, achieving an energy resolution better than two keV is not important for this measurement, therefore no dedicated energy resolution optimization was performed. It was however determined on each high energy X-ray calibration with a ^{57}Co source.

Comparison of measured values with data sheet and other detectors

The data can be compared to other types of X-ray detectors such as a CdTe diode or a Silicon PIN diode. Such detectors were not available but have similar properties. In table 2.1 different detector types are compared by their nominal energy resolutions. The measured energy resolutions of the detector used in this work are also given. The energy resolution was measured by doing pulse height analysis (PHA) with a Canberra multichannel analyzer or integrating charge and digitizing the value with the CAEN v256 charge to digital converter (QDC).
The measurement of the three gamma lines of ^{57}Co as always performed the optimization for high X-ray energies. The resolution values obtained for the 6.4 keV gamma line from the QDC shows that the resolution at low energies is extremely poor if the detector is operated for high X-ray energies. To check what resolution can be achieved by optimizing the gain to low X-ray energies a QDC measurement with the ^{55}Fe source was performed. With the QDC a resolution

[2]Product datasheet:
`http://www.canberra.com/pdf/Products/SiLi-Super-Det-SS.pdf`

Isotope	Energy (keV)	Si(Li) lit.	**Si(Li) meas.** PHA	**Si(Li) meas.** QDC	CdTe	Si-PIN
^{55}Fe	5.9	159*	-	**365±3**	290[2)]	149[2)]
^{57}Co	6.4	-	**358±5**	**1089±7**		
^{57}Co	14.4	680±20[1)]	**306±6**	**590±7**	530[2)]	
^{241}Am	59.54	720±20[1)]	-	**690±8**	600[2)]	390[2)]
^{57}Co	122.0	830±20[1)]	**633±2**	**862±9**	850[2)]	

Table 2.1: Resolution (FWHM) comparison of different X-ray detectors. For the Si(Li) detector, some literature values (lit.) are given as well as measured (meas.) ones. All detector resolutions are given in eV. For a discussion of the measured values see text.
**) Value from Canberra Data Sheet*
(http://www.canberra.com/pdf/Products/Silicon-Li-Det-SS-CSP0157.pdf) ,
1) Literature values from Ahmad and Wagner [2],
2) Values from data sheets of Amptek Inc. (http://www.amptek.com)

of 365±3 eV could be achieved, compared to 159 eV which is the maximum from the data sheet. Without the use of an optimal filter and the integration gate uncertainty this value is acceptable. The optimization on high X-ray energies, resulted in very similar values from 60 keV up to 136,4 keV which are also quite good compared to the values given in the publication by Ahmad and Wagner [2] and the data sheet. For high energies both measurement methods give reasonable values and even exceed literature values.
It is not possible to access the multichannel analyzer data in order to mark each event with a time stamp, which is the reason the QDC was used for data acquisition. The data acquisition system is described in section 2.4. Nonetheless, both methods were tested and found to give similar energy resolutions for high energy measurement configuration. The energy resolutions of the measured X-ray and gamma lines are listed in table 2.1. At high X-ray energies, for which this acquisition was set up, the energy resolutions are in good agreement with published values. Over the whole energy range the energy resolution fits the requirement of a resolution in the order of 2 keV or better.

2.3.3 Si(Li) time stability

It was investigated how the properties of the detector changed over time due to possible radiation damage in the diode or charge trapping.
Dominant effects broadening the resolution are electronic noise of the research amplifier and the shaping module, as well as charge trapping in the depletion

zone of the detector occurring due to power cuts. The metal-oxide-semiconductor field-effect transistor (MOSFET) within the preamplifier, which is located in this detectors cryostat, was found to have a defective contact which may also lead to periods of questionable data taking showing up in extremely high noise. This effect was monitored closely and data taken under such conditions was never used for analysis.
The performance of the Si(Li) detector was monitored since it was put in continuous operation in 2009, by regular energy calibrations. During the first time period the data acquisition and the recording parameters were tuned until the resolution was in the order of 1 keV or smaller, sufficient for the identification of the X-ray fluorescence for polarity determination. Since that time (around 10/2009) the energy resolution seems to decrease slightly. It is still below 2 keV and can be used for high voltage determination and polarity. The time evolution of the detectors resolution with the QDC based acquisition is shown in fig.2.13. The error from calibration is small compared to the systematical and statisti-

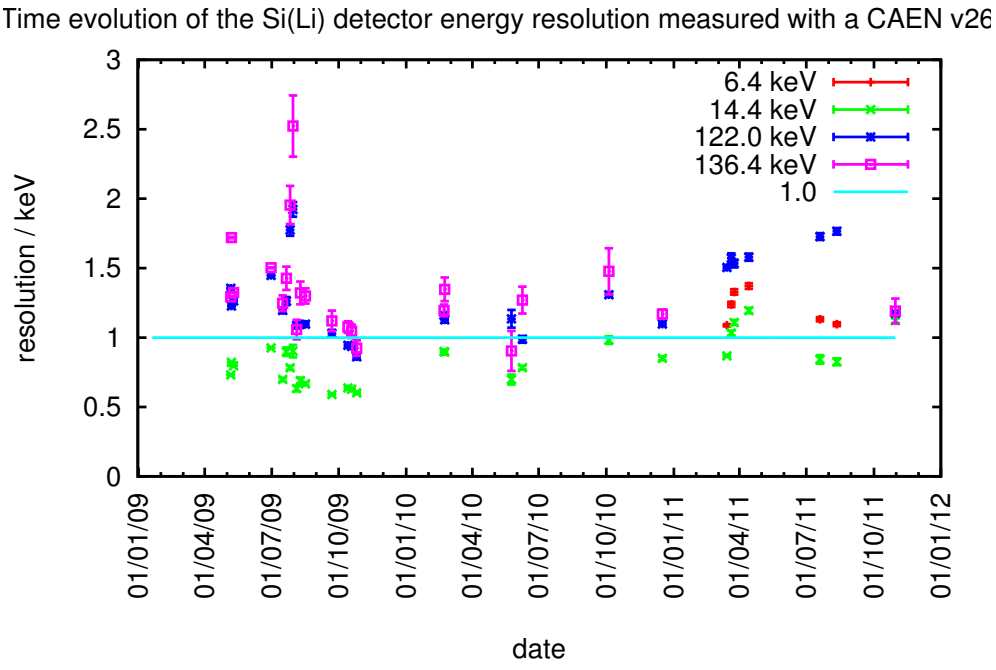

Fig. *2.13: Si(Li) energy resolution over time with QDC DAQ.*

cal errors for the Bremsstrahlung endpoint determination which is described in section 2.4.3.

2.3.4 Si(Li) detection efficiency

The lower energy detection threshold of below 1 keV is given by the thickness of the beryllium entrance window, which in this case is 8 μm thick. The upper energy detection limit of 140 keV is given by the size of the diode and the probability for a high energetic X-ray to deposit all its energy in the volume by the photo effect, multiple compton scattering or a mixture. The efficiency curve from the data sheet is shown in fig. 2.14 and ends at 100 keV. Since the high energy

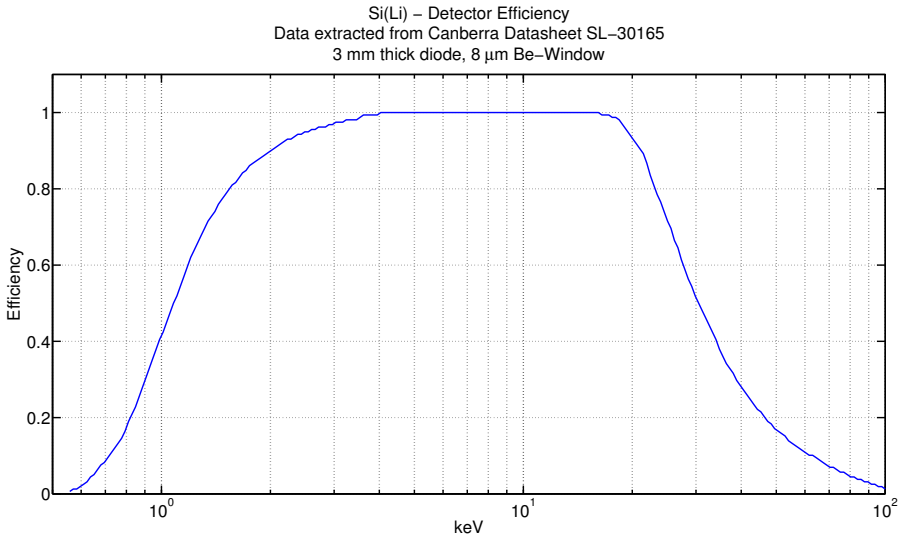

Fig. *2.14: Efficiency of the SL-30165 from datasheet* `http://www.canberra.com/pdf/Products/Silicon-Li-Det-SS-CSP0157.pdf`.

efficiency is most relevant for this project, the knowledge of the detector response at high energies was investigated. A ^{57}Co source was used which has two prominent gamma lines above 100 keV, at 122.0 and 136.4 keV to calibrate the detector at high X-ray energies. A typical calibration spectrum is shown in fig.2.16. The energy calibration is done with a linear fit of all gamma lines, the corresponding compton edges and lead fluorescence from the source shielding. The error from nonlinearities in the calibration is smaller than 2%. A linear calibration is shown in fig.2.15. The efficiency in the data sheet is only given up to 100 keV which suggests that the detector cannot be used for energies above that value. Since the photoelectric absorption cross section decreases with higher energies, the probability of observing high energetic events is dominated by the probability for multiple compton scattering and photoelectric absorption of the scattered photon.
The efficiency above 100 keV however is not vanishing, however a description of

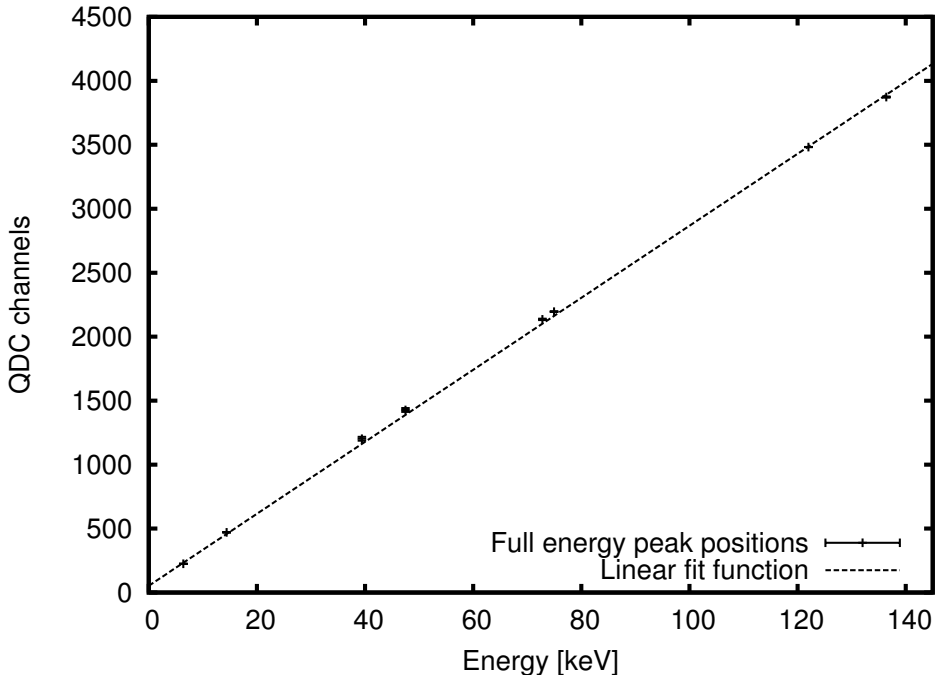

Fig. *2.15: Si(Li) linear calibration with a ^{57}Co source. The errors of the peak positions are too small to be displayed properly in this graph.*

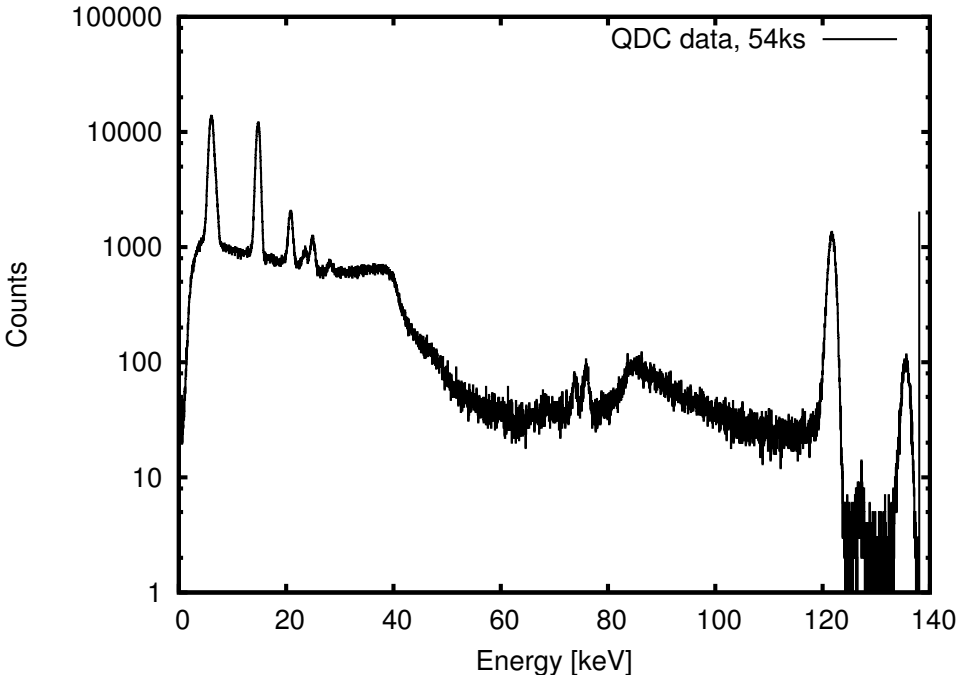

Fig. *2.16: Si(Li) calibration energy spectrum with a ^{57}Co source.*

the detectors efficiency above 100 keV can be derived. From the energy calibration with ^{57}Co one gets two data points beyond 100 keV. The branching ratio of the source is very well known so that the intensity can be determined. The detection efficiency for the 14.4 keV gamma line of ^{57}Co is 100% with a total branching ratio of 9% of the activity. The lines intensities were determined by fitting the spectrum with gaussian distributions and a suitable background. The total efficiency for the two high energetic gamma lines can be determined and is in the order of 1-2%.
Adding those two measured efficiency points to the curve obtained from the data sheet, a model function describing the high energy efficiency can be fitted to the data. The model used is the sum of two exponential functions. The exponential tail expansion of the detectors efficiency is shown in fig.2.17 and contains the values obtained from the data sheet and efficiencies obtained from the calibration. This expansion is used later on to calculate the endpoint of the bremsstrahlung spectrum with the AEDA (see 2.4.3) code.

2.3.5 High voltage polarity identification

As mentioned before, not only can the high voltage be determined at a certain time, also the polarity of the crystal facing the target. In case the electrons are

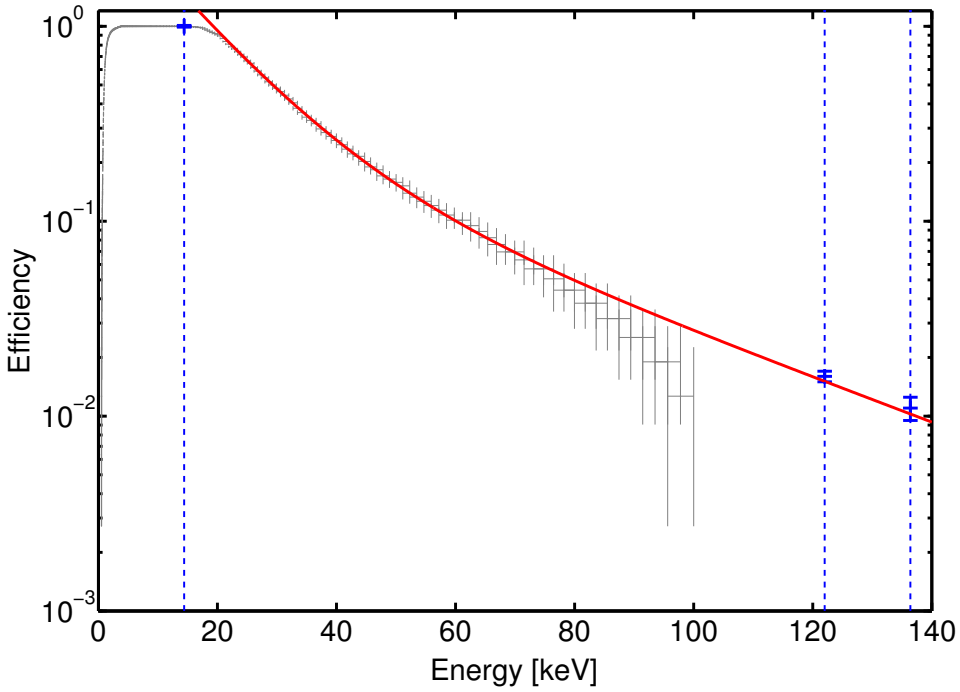

Fig. *2.17: Si(Li) exponential tail expansion of the efficiency curve. Grey, the scanned values from the datasheet, with errors in x-direction. Errors in y-direction are to small to display. In blue the measured values from a ^{57}Co source are given with errors in y-direction. The errors in x-direction are to small to display. A double exponential fit is also plotted in red to extrapolate the detector efficiency to higher energies.*

accelerated towards the crystal surface (positive polarity) one can see the silver lines emitted by the conductive glue as well as the fluorescence lines of tantalum which is present in the crystal. With negative polarity, one can clearly see the molybdenum within the stainless steel vacuum chamber walls. The lines are fitted with fixed relative fluorescence intensities and starting values. Examples of a successful fit of the silver lines is shown in figure 2.18, an example of a successful fit of the molybdenum lines is shown in fig. 2.19.

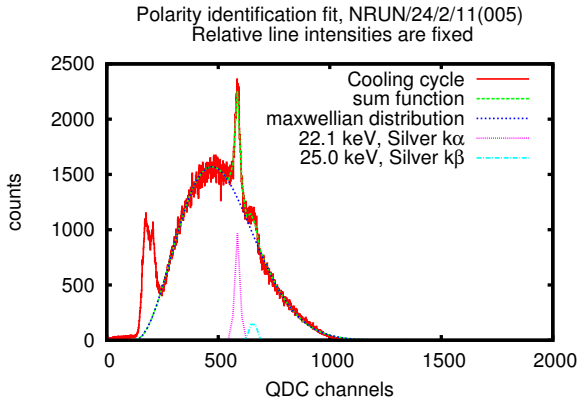

Fig. *2.18: XR fluorescence during cooling in this particular setup*

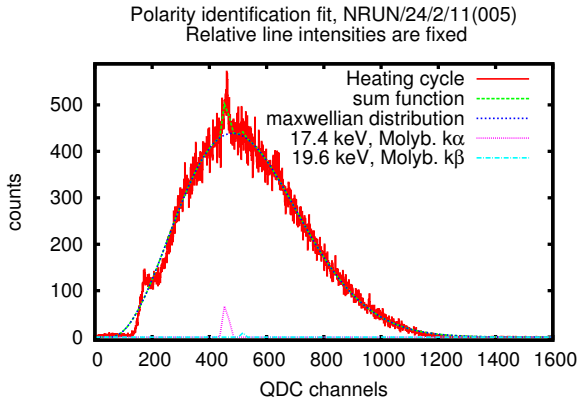

Fig. *2.19: XR fluorescence during heating in this particular setup*

2.3.6 Low energy X-ray filter

This X-ray detector does have a high efficiency towards low energies. The DAQ is slow and only supports an acquisition rate of up to 1 kHz. Therefore a low energy filter was implemented to reduce the rate in the detector. The plastics protection cap on the detector is used as well as a 0.5 mm aluminum shield to

avoid pileup in the detector at high acceleration energies. This results in an almost complete cutoff below 10-15 keV. However, low energetic compton scattered X-rays from the filter will still be seen in the detector. The high energy part of the distribution is not affected by this shielding as shown in fig.2.20 While recording

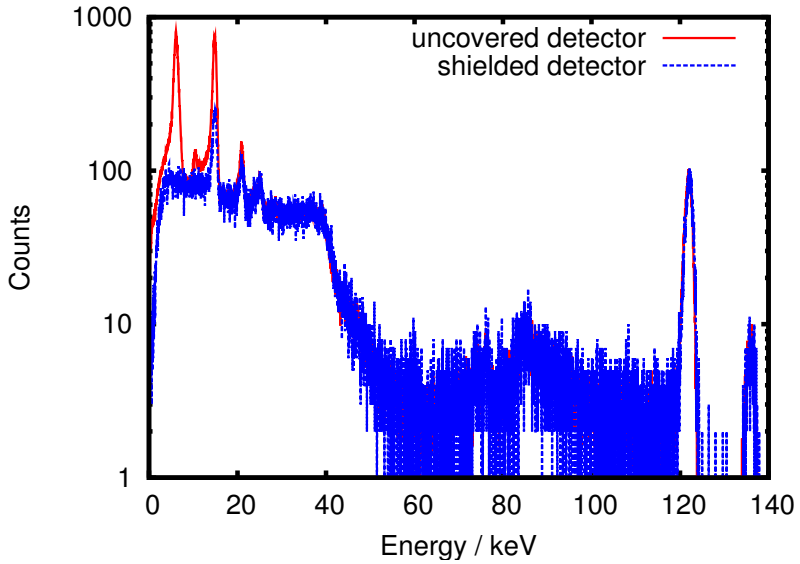

Fig. *2.20: Si(Li) low energy filter comparison with ^{57}Co source. Filter consists of plastics detector window safety cap and 0.5 mm aluminum shield.*

run data, pileup shifts the endpoint of the spectrum to higher "energies". This problem was solved by the plastic cap and the aluminum shield. A comparison of the recorded X-ray signal heights and the acquisition rates before and after the application of the filter is shown in figs.2.21 and 2.22. In these plots, the blue line indicates the maximum acquisition rate by the QDC, the red line indicates the real acquisition rate and the grey dots X-ray data points. The comparison of these two measurements show a successful reduction of the pileup due to the low energy filter. The acquisition rate stays well below the maximum rate. A measurement artifact can be found in the data around the time 1750 s. It can be removed from the data and is never present in analysis. The artifacts origin, appearance and solutions are being discussed in appendix C.

2.3.7 Safety note

The vacuum chamber is transparent for high energy X-rays (>60 keV). The chamber can be partially shielded with 3 mm lead foil. While running, the experiment does cause a radiation hazard. The total source strength was estimated to yield several GBq of activity. In a worst case scenario, the crystal supplies 40 nA cur-

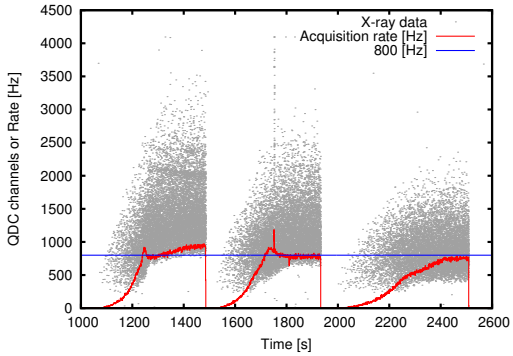

Fig. *2.21: Time vs. X-ray energy. Pileup shifts energy spectrum to higher values. The recorded event rate is also given. The vertical line at around $t \approx 1750$ is a measurement artifact (See C).*

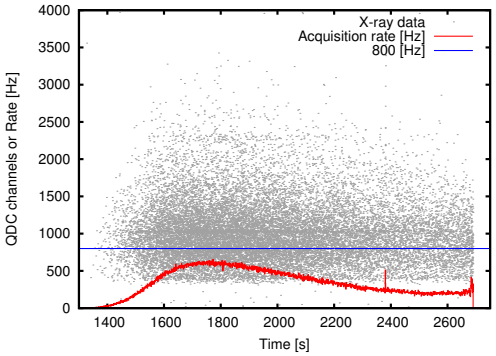

Fig. *2.22: Time vs. X-ray energy. No pileup observable. The recorded event rate at voltages similar to the ones in fig.2.21 is also given.*

rent while charged to 120 kV. The total power output - assuming high energy X-rays only - will be 4.8 mW. Full deposition on 100.0 kg of human target, this would lead to a dose of 48 µSv per second. If a more realistic mean acceleration energy such as 30 kV is assumed, the total dose per heavy standard human drops to 0.12 µSv per second. With a realistic solid angle coverage of 1/50 and a correction factor for the transmittance of the vacuum chamber walls of 1/20 the dose drops to 0.43 µSv per hour. The german radiation safety regulations allow for 0.1 µSv per hour. The X-ray dose must be monitored closely and precaution is mandatory. Portable lead shields with 3 mm thickness were installed.
The neutron radiation hazard should also be kept in mind. The human body provides the optimal target for neutrons with 2.45 MeV kinetic energy since their mean free path in water is about the thickness of a body (25 cm). Therefore the biological scaling factor for neutrons peaks at this energy. However, the expected neutron flux is extremely low and therefore no precaution is necessary if the flux is monitored closely.

2.4 Data acquisition and other control systems

The data acquisition system (DAQ) is used to record information from the detectors. The neutron detectors are being read out by flash analog to digital converters (FADC) which sample whole pulses in order to perform pulse shape discrimination. Neutron detection will be explained in chapter 3. The X-ray detector is being read out by a charge integrating analog to digital converter (QDC). Both analog to digital converters are operated with the VME bus system. The VME crate is connected to the personal computer via optical fibers and a PCI

card. The operating system for this DAQ is Linux (for info about compatibility and kernel versions see D.1).
The software for the DAQ system was written and developed mostly within the range of this work. The modules used, their properties, handling and some details about functionality will be discussed in this section as they are important to understand the data.

2.4.1 Trigger

The hardware trigger condition of the system is defined by a logical OR on leading edge discriminator modules connected to neutron detectors. If one single neutron detector exceeds a certain pulse height the trigger is released. This trigger level is chosen for each channel individually and set as close as is reasonable to the noise level. A typical value is around 10 mV on a scale up to 500 mV. The software trigger applied afterwards will have a lower effective threshold for reasons which will be explained in section 2.4.2. If the system triggers, all neutron detectors will be read out, regardless whether they contain valid traces or not[3].
A second passive trigger was applied to the X-ray detector. While waiting for the interrupt telling the system there is FADC data to read out, the QDC module is checked much more frequently. This QDC readout is a passive system where the software reads a status register, telling if there are events in the QDC buffer. This allows for QDC trigger rates up to one kHz while this still does not affect the FADC acquisition up to approx. 110 Hz. The FADC trigger is vetoed with a busy signal to block any pulses that arrive while reading out the FADC. With a conversion time of 650 μs the acquisition rate is in principle only limited by the VME-bus specification. According to the manual, an acquisition rate of about 500 Hz should be possible, but the maximum rate ever recorded by buffering blocks in the memory was approx. 220 Hz. This effect was already investigated during several diploma theses by A.Hagen, D.Dietrich, M.Pfeifer and C.Schmitt ([5],[18],[42] and [45]). The conversion time and the veto time contribute to the dead time which is discussed in section 3.10.

2.4.2 FADC: fast sampling analog to digital converter

The CAEN v1729 fast sampling analog digital converters are VME modules, designed especially to scan the time structure of fast pulses. The resolution is 12 bit, the sampling rate either 1 or 2 GS/s. A software was written, to read out these modules and preanalyze the data already during acquisition which reduces the amount of stored data. The basic features of the program are:

- Baseline determination and correction.

[3]This is a hardware limitation since the digitizing memory cannot be segmented.

- Coincidence search amongst all channels.
- Corrected pulse acquisition.
- Gate width optimization algorithm.
- Pulse height histograms.
- Pulse shape discrimination with two integration gates.
- Raw data acquisition.
- Roundbuffer and timing corrections.
- Simple pileup rejection.
- Software trigger determination, leading edge or constant fraction.
- Trace post processing.

The program was designed to be as flexible as necessary and as optimized as possible. M.Pfeifer developed a version of the program so that the module can be operated within the ACQU-ROOT framework [42]. For highly specialized experiments such as the one discussed in this work, a non-ACQU-ROOT version is still in use.
A feature to be discussed in detail is the pulse reconstruction.
The signals from the detectors are continuously written into a round buffer which overwrites itself every 1.25 μs or 2.5 μs. Upon arrival of a trigger, the continuous sampling stops and the raw data is copied into the computers memory. The first correction which must be applied is the so called "pedestal" correction which is an intrinsic property of the individual memory cells. This constant never changes for each memory cell. After subtraction of these "pedestals" the time reconstruction of the pulse is performed. The trigger information is the identification number of the cell in which the trigger was released. The absolute number of samples stored in the round buffer before and after the trigger happened can be set. The sum however must always be 2500 which is the amount of memory cells available. Each memory cell contains the pulse height at a certain time. The pulse is now shifted in time (in memory cells) so that the trigger is always at the same position.
Now the baseline correction can be applied: the baseline offset is calculate using different time intervals at the beginning and at the end of a pulse. This value will be subtracted from the pulse and adjusts the baseline to zero. The correction process is shown on a real pulse in fig.2.23. The software trigger can determine

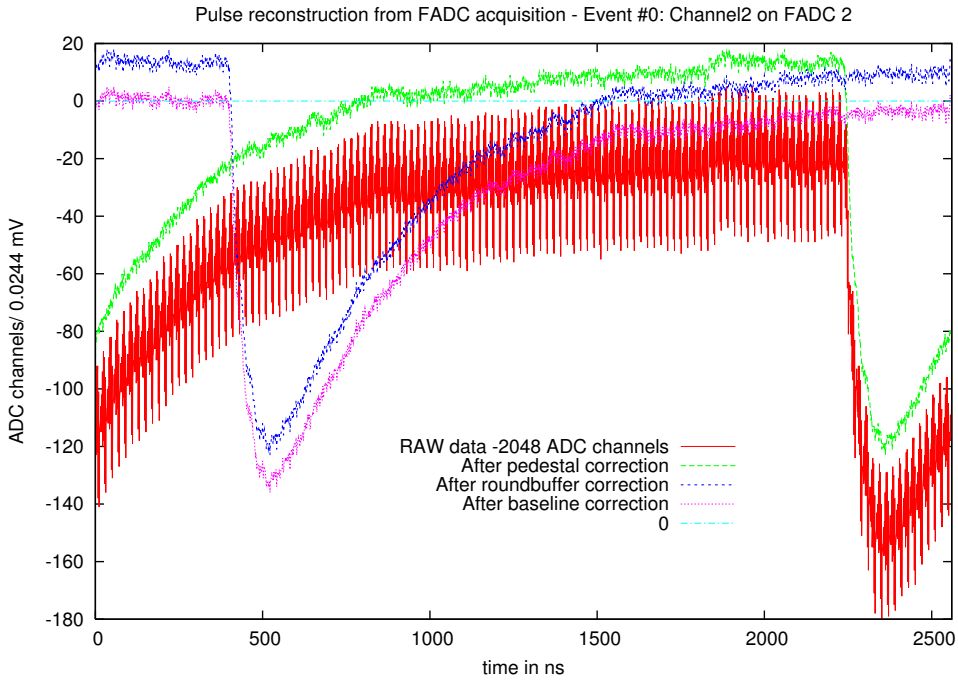

Fig. *2.23: FADC pulse reconstruction on real pulse.*

the trigger within a single pulse due to a leading edge threshold or due to constant fraction threshold independent of the external trigger. It is used to look for coincident events in different neutron detectors and it is the starting point for the pulse integration performed later on. The pulse will then be integrated over two different preset gate lengths. Valid pulses always show a ratio of the two integrals between 0 and 1 otherwise the pulses contains noise, pileup or direct hits from cosmic muons. After validation the program looks for coincident events among all channels. The software trigger threshold can be set to a lower threshold than the hardware threshold. If the noise level is still high, one can apply a software filter to smooth the data which might improve discrimination properties. This had to be done for some measurements especially at the Rosenau accelerator (see section 2.5). Much more benefit comes from the software trigger while using data from double modules. Only one photomultiplier must have released the hardware trigger for all channels to be read out. By choosing the software trigger threshold to be lower than the hardware trigger, one finds additional coincidences at low light. One can even discriminate between accidental coincidences and real coincidences as shown in fig. 2.24.
The quantities stored by the software are the time stamp, the neutron identification number, the values of the two integration gates and the pulse height.
To perform software tests on a specific data set, also the raw traces with all infor-

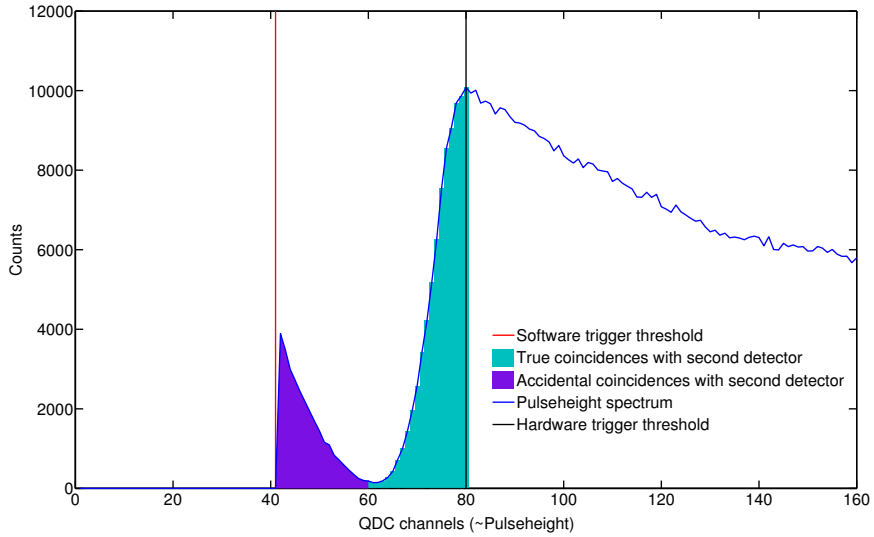

Fig. *2.24: Software trigger advantage in double modules, real data with γ-source. All events are coincident, signals from both photomultipliers (PMs) exceed the software trigger threshold.*

mation given can be stored from this program. This acquisition mode is necessary to operate the gate finding algorithm which determines the optimal settings for the neutron gamma discrimination in the case of NE-213 liquid scintillator.

2.4.3 QDC: charge integrating analog to digital converter

The CAEN v256 QDC module was used to record X-ray data. In general, this is not the preferred option for X-ray data acquisition but the timing information was necessary and there was no other option to record it. The preferred option would have been a peak sensing ADC which is able to store time information together with proper pulse shaping.
The readout software for the available QDC was written by F.Ritter[4], however modified for the current use. It is needed to record time dependent X-ray spectra to determine the high voltage on the crystal surface at a given time. The acquisition function reads out only one out of eight QDC channels available to improve performance. This integrates charge over an external gate of 200-300 ns, and digitizes the resulting value within 650 µs with a resolution of 14 bit. The acquisition program stores the QDC data in an energy spectrum and a time vs. energy file. The time resolution is one second.

[4]F.Ritter, private communication, University of Tübingen

2.4.3.1 Calculation of the high voltage

From the endpoint of the Bremsstrahlung spectrum, the high voltage was determined in two different ways. The so called standard EndPoint Algorithm (EPA) and the Advanced Endpoint Determination Algorithm (AEDA) code are codes written and developed during this work. The EPA determines the energy below which 80-99% (acquisition rate dependent) of all counts are contained. This energy is considered as the endpoint. Only time bins with more than five QDC entries are being regarded by the code. In the end a running average over five time bins is calculated where entries with zero voltage (or too view entries) are being suppressed. The endpoint calculation by the EPA is standard procedure and works very reliable.
The AEDA code was developed to correct for the high voltage underestimation by the low detector efficiency at high X-ray energies. It requires the detectors efficiency description for energies above 100 keV, the exponential tail expansion of the efficiency curve derived in section 2.17. By choosing a high efficiency energy interval as control region, the code evaluates how many counts are expected to lie within the next energy interval. An acceptance window for the counts is defined with a width of $\pm\sqrt{\text{number of expected counts}}$. If the number of counts in that window falls below this acceptance window, the values within this interval will be summed up until 90% are reached. This value is now considered the endpoint. The AEDA code corrects the underestimation of the endpoint compared to the EPA. The big disadvantage is, that it does not work below a voltage of 20 kV.
It was found, that the underestimation of the high voltage by the EPA is not as crucial as expected and that the AEDA code only works for high X-ray statistics. For analysis the EPA is being used. A comparison of both methods is depicted in fig.2.25.

2.4.3.2 Validation of the high voltage calculation

A first check of the EPA was performed by comparing the EPA results to the endpoint by just looking at the plotted spectrum. An error of 10% is assumed. The ten highest voltage values from the EPA were averaged and weighted with their statistical error. If one plots the high voltage values against each other, a very good correlation of the high voltage reading can be found. The EPA seems to work reasonably and is therefore used as the reference method to obtain the values for the high voltages. The correlation graph is shown in fig. 2.26.

2.4.4 Temperature control

Temperature measurement is done with Ni-CrNi type K thermoelements and readout with a Greisinger GMH3210. This model supplies analog and serial output and is read out via a Serial to USB converter. The temperature acquisition

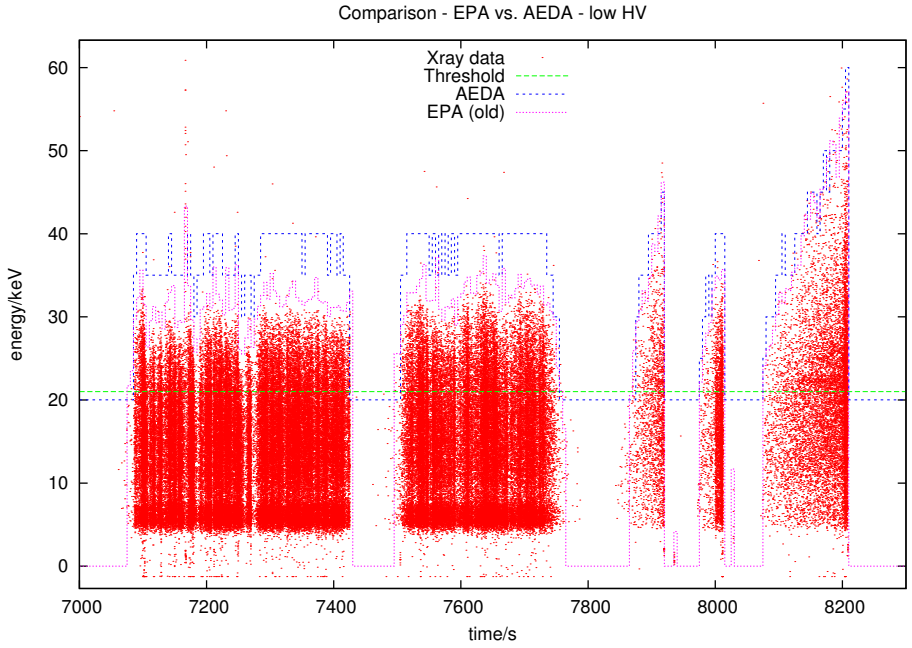

Fig. *2.25: Endpoint calculation comparison.*

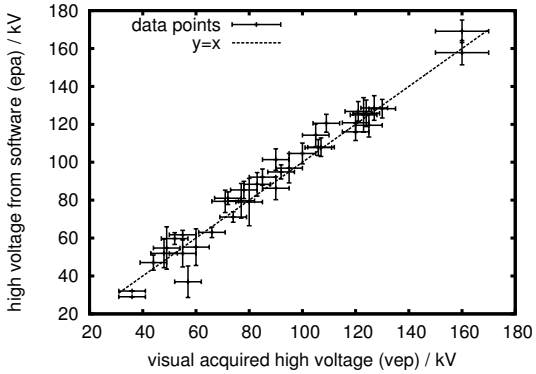

Fig. *2.26: Run parameters, correlation between visual acquired high voltage endpoint and endpoint determined by EPA.*

and regulation software for Linux was also written during this work and includes the following features:

- Record temperature response functions (see text).
- Regulation according to predefined temperature vs. time profiles.
- Regulation of temperature changes.
- Switch heater/cooler on/off until upper/lower temperature set values are reached.
- Temperature readout.
- Temperature regulation.

Regulation is being accomplished via a proportional-differential (PD) or proportional-integral-differential (PID) algorithm. For switching on/off the heater/cooler power supply, two serial port driven relays are used. The software can only turn on and off the heating and cooling, therefore it was necessary to develop a method regulation on switching time and its temperature feedback.
The temperature change as a function of heating/cooling time is determined. The acquired temperature response functions (TRF) are used as lookup tables to determine how long the heater/cooler must be switched on for a desired temperature change. The time until the temperature change is reached is being determined by the mean response time (MRT). The response times depend on the geometry and the systems heat capacity.
For example, heating for 5 seconds with a fixed power increases the crystals temperature by 1^oC starting at 20^oC. It takes 23 seconds from the end of the heating time until the maximum temperature change is reached.
The temperature response functions must be recorded again for any change in heater and cooler properties as well as for significant changes of the internal geometry. An experimentally determined TRF for heating is shown in figure 2.27, the MRT determination is shown in fig. 2.28. The TRF acquisition program is a standalone version of the Temperature control program. A concept to implement a self-monitoring PID regulator based on a robust stability metric is published in [9], which might allow for maximum dynamics of the regulation process. During regulation for a constant temperature change, the classical PID regulator is becoming unstable. A dynamical variance of the regulating parameters to stay in a stable operation mode for a wide temperature range would be preferable.

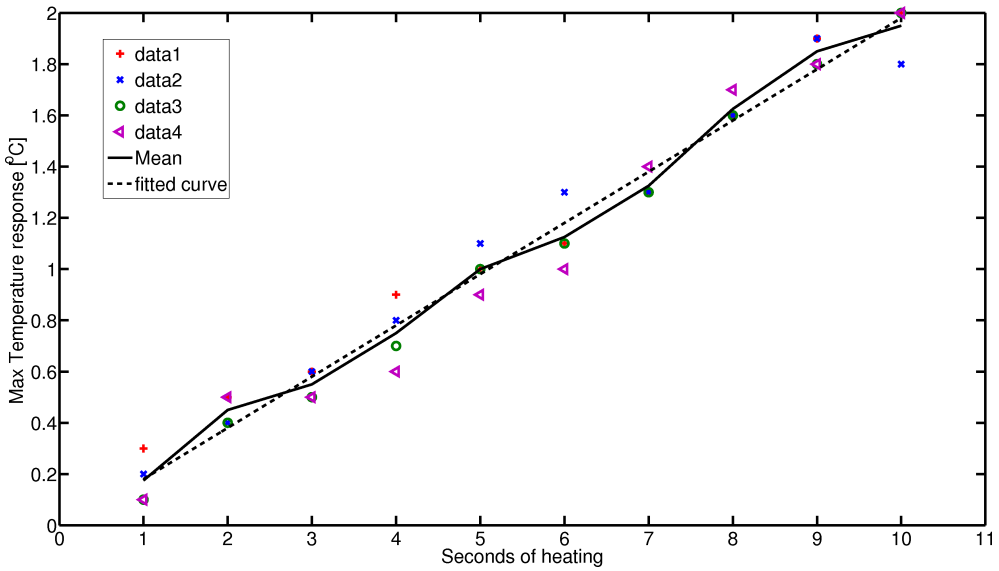

Fig. *2.27: Heating TRF for 10 W heater power. Based on four measurements. The mean values for each heating interval is given as the black line, the black dotted line is the linear best fit. The MRT is determined separately.*

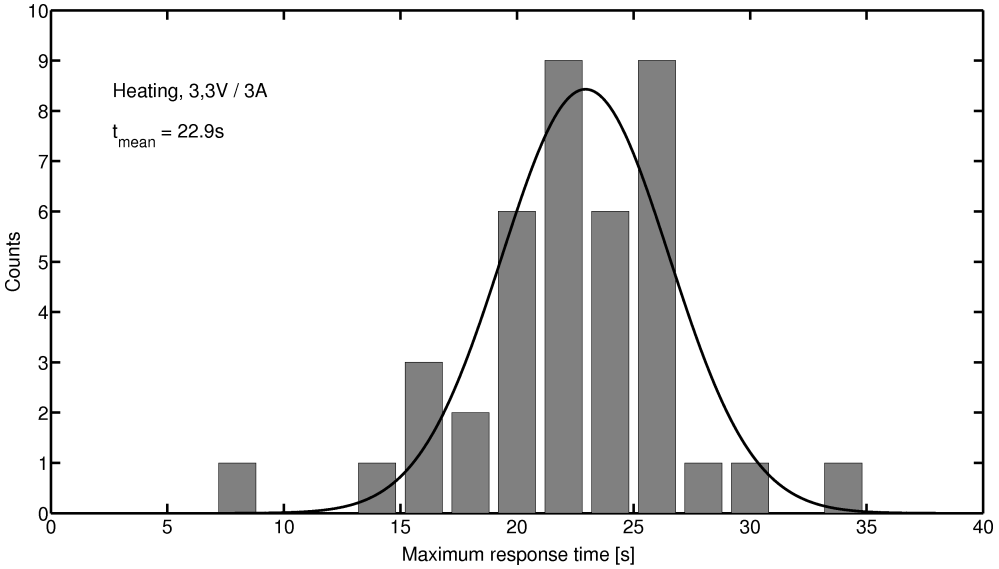

Fig. *2.28: Heating MRT for 10 W heater power. Based on four measurements. The position of the fitted gaussian gives the MRT.*

2.5 Detector and target testing at the Rosenau accelerator

Our institute operates a 3.0 MV Van-de-Graaf linear accelerator for ions with masses up to carbon. The accelerator is located in an area called Rosenau. The accelerator is being used mostly for material analysis with Rutherford backscattering and radiation hardness testing with neutrons and protons. During this work, the accelerator was mostly operated with a deuteron beam, D^+ or D_2^+ to test targets or to produce high energy neutrons via the ^{7}Li(D,nx) reactions to investigate discrimination properties of NE-213 detectors. The ^{7}Li(D,nx) reactions have the highest cross section of all ^{7}Li + D reactions. The high Q value of about 15 MeV allows for high energy neutron response tests of NE-213 detector cells. D(D,n)He fusion neutrons were used for the "low" energy response tests of the NE-213 detector cells. During detector functionality tests, whole pulse traces were stored for each detector module. With this data, the optimal gate for particle discrimination was determined as described in section 3.5.
The primary reason for target testing was the validation of deuterium content in targets. One of the plastic targets was acquired from the Jülich accelerator, the others were self made. The CD_2 usually is white, the CD_2 raw material bought for this work contains traces of a catalyst or carbon of cracked short polymer chains which leads to a black appearance. The physical properties such as melting point and density of the material did however match those of CD_2. A possibility to analyze the material would have been pyrolysis combined with gas chromatography and mass spectrometry. Unfortunately such combination of analysis tools was not available on the campus during this thesis. Therefore targets were exposed to a deuterium beam and fusion neutrons were measured to check the deuterium content. The neutron rate was compared to the rate on a target without deuterium content. The targets were prepared, cleaned and mounted to the last beam line segment, just in front of the beam dump which can be cooled with water. Electrical contact was established to measure the beam current on a metalized target. The target mounts have grooves on their surface or holes in order to allow evacuation of the enclosed volumes. The last beam line segment with the beam dump is electrically isolated from the rest of the beam line. Sketches of the target testing mounts within the beam line are shown in figs. 2.29 and 2.30. Pictures of the target mounts are shown in fig.2.31 to fig.2.34. The targets were tested on neutron yield during irradiation with defocused D^+ and D_2^+ beams, at beam energies of 700-1000 keV and beam currents in the order of some ten nA to one µA. During testing the beam is shot onto the beam line shutter in front of the target. The neutron production starts to increase slowly due to self-target effect on the shutter. When the shutter is opened and the beam reaches the target, the neutron flux instantaneously rises to a very high level which can only be explained by the targets deuterium concentration. Fusion neutrons from DD

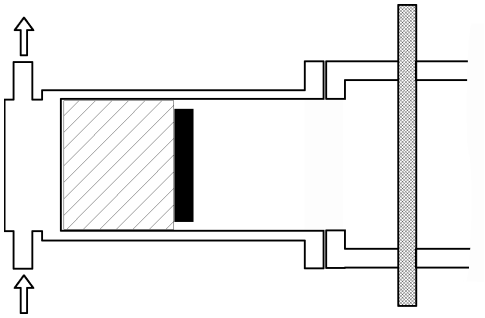

Fig. *2.29: Schematic view (Not to scale!) of target testing mount in beam line. Small target (< 30 mm) mount near cooled cup on the left side. Black is the target, black hatched is the mount. The large vertical structure on the right side represents the last shutter.*

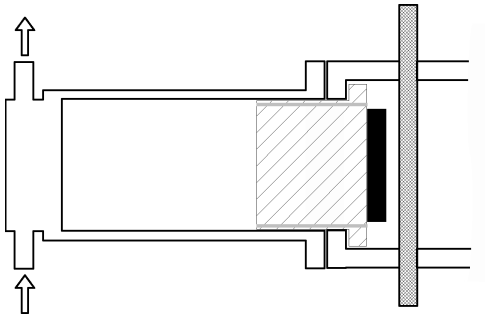

Fig. *2.30: Schematic view (Not to scale!) of target testing mount in beam line. Large target (< 60 mm) mount near cooled cup on the left side. Black is the target, black hatched is the mount. The large vertical structure on the right side represents the last shutter.*

fusion are monoenergetic so that the recoil spectrum in the NE-213 detectors ends at a defined energy. This information can be used to validate the origin of the neutrons.
All plastic targets prepared were tested and proved to contain deuterium. The metal targets tested did not contain any deuterium independent of how long they were exposed to deuterium atmosphere and independent of the deuterium atmosphere pressure up to 4 bar.
The maximum neutron flux which could be seen by the detector during these tests was limited by the data acquisition system. The DAQ can sample at a maximum of about 140 pulses per second. The neutron rate over time for one measurement is shown in 2.35. The neutron energy spectrum validates the DD fusion reaction.

2.5.1 Rutherford backscattering

The intention to metalize the plastic targets so that the ion current can be read lead to the idea to cover them with thin layers of gold foil. The gold foils thickness was investigated using Rutherford backscattering (RBS). The measurements revealed that the foils are to thick to used because the ions will lose their kinetic energy before they reach the target.
The RBS facility was used with kind support of S.Diebold[5] to determine the thickness of various gold foils to be used for metalization of CD_2 targets. The experimental setup used and details about the RBS procedure can be obtained

[5]Private communication, University of Tuebingen

Fig. *2.31: Picture of a small target mount without target. Brass holder with steel locking ring.The grooves on the surface improve evacuation.*

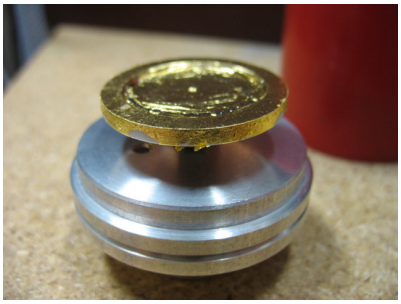

Fig. *2.32: Picture of a large target mount with one CD_2 target covered with 107 nm gold foil. Target on copper holder fixed with ceramic ring. The copper holder is screwed to the large target mount made of aluminum.*

Fig. *2.33: Picture of the disassembled small mount without target.*

Fig. *2.34: Rear view of large target mount. The centered M6 thread is used to fix the target with the copper holder. The two small M3 threads are used to safely store the mount with target and compensate pressure upon evacuation.*

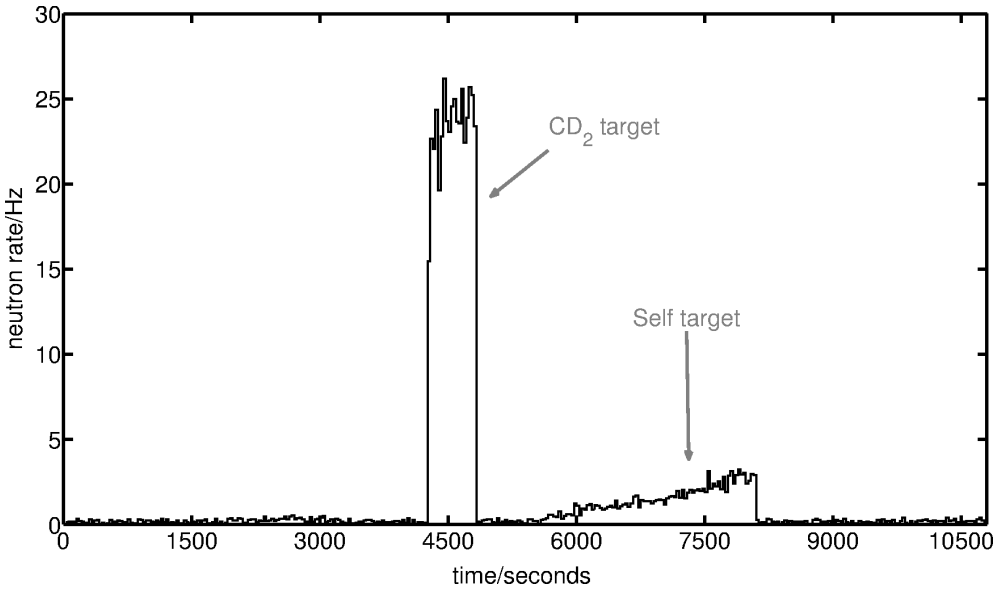

Fig. *2.35: CD_2 target test, target metalized with 10 nm gold. D_2^+ beam with 780 keV beam energy and low beam current. The time binning is 30 s, the neutron rates are mean rates. One clearly sees the difference between the fusion rate on the target and the pure self-target fusion rate.*

from the Diploma thesis of S. Diebold[17]. The energy resolution of the setup is approx. 10 keV for a 1.606 MeV alpha beam.
Thin gold foils are available for artwork or from laboratory suppliers. The thickness of the gold foils for artwork was measured to 107 nm, compared to 10-30 nm which would have been desirable. The samples were measured against a reference sample of 36.4 nm. The measurement and the corresponding fits are shown in figure 2.36. Unfortunately 107 nm of gold is a very effective deuterium ion filter at incident energies of about 100 keV. Therefore it must not and has not been used.
It was investigated if metal can be sputtered onto plastic targets. Depositing several nm of metal on a plastic surface is possible in principle however there was absolutely no experience available on that topic. Also there were concerns that unknown substances ("black appearance") of the target may evaporate during UHV environment, contaminating the sputtering equipment.
Fortunately, the GSI in Darmstadt agreed to sputter 10 nm of gold to the plastic target acquired from Jülich. This target was then used for several measurements. All other plastics target were used pure without any metalization. The deposition of aluminum or beryllium on a plastic target should also be investigated due to the lower mass and therefore less energy loss of the ions.

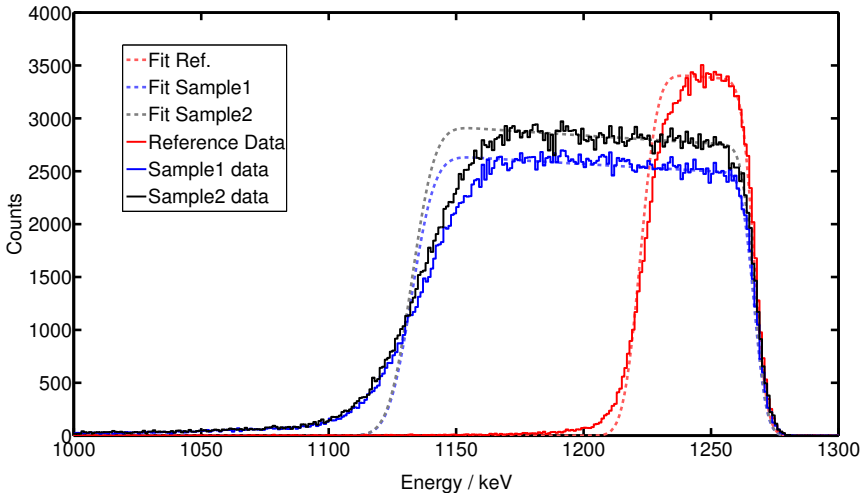

Fig. *2.36: Rutherford backscattering on Au foil vs. reference foil with 1.606 MeV alpha beam. Thickness is given by the width of the "rectangle", Reference foil thickness is 36.4 nm, Sample 1 and 2 thicknesses are 107.0 nm each. All fits were done with SIMNRA.*

3 Neutron detection

"The important thing in science is not so much to obtain new facts as to discover new ways of thinking about them."

-William Lawrence Bragg

Fast neutrons[1] are being emitted by the fusion reaction which is intended to take place within this experiment. Since none or very few neutrons were observed, improving the overall neutron detection efficiency was the main topic in this work. This chapter will explain how those neutrons can be detected, describe different detectors, discuss calibration and will show which solutions have been realized.

3.1 Neutron interaction

Monoenergetic fast neutrons from D(D,n)^{3}He fusion with 2.45 MeV kinetic energy will deposit considerable amounts of energy by scattering off protons. Compared to scattering off heavier nuclei, the energy transfer to protons is much larger. Hence, moderation in proton rich materials such as water, paraffin and organic scintillators slows neutrons down rather fast, if not the entire energy is being transferred at once. Elastic scattering off nuclei is being discussed focusing on liquid scintillator which, as will be explained, has the highest detection efficiency for fast neutrons.
For non-relativistic neutron energies E_n the recoil energy in the laboratory system is

$$E_{rec,\theta} = \frac{4A}{(1-A)^2}\, cos^2(\theta) E_n \tag{3.1}$$

with the recoil nucleus scattering angle θ and A as the mass number of the recoil nucleus. Therefore the maximum transferred energy to the recoil nucleus for a neutron scattering angle of 180^o is

$$E_{rec,max} = \frac{4A}{(1-A)^2} E_n. \tag{3.2}$$

A proton can get the full kinetic energy of the neutron, for any heavier nucleus the maximum transferred energy is much lower. For carbon which is an unavoidable constituent of organic scintillators, the maximum recoil energy is 28.4% of the

[1] Neutrons with an kinetic energy larger than 0.1 MeV are called fast neutrons.

neutrons energy or 696 keV for 2.45 MeV neutrons. The maximum carbon recoil energy is very close to a typical discrimination threshold which is explained later on. The scattering cross section is almost equal for all scattering angles so that the expected recoil spectrum for a single neutron energy is flat up to the maximum energy. The recoiling nucleus excites molecules in the scintillator which produce light. The light output of a scintillator also varies with the recoiling nucleus and can be energy dependent. The light output of nuclei is quenched compared to the light output of electrons. The light output of protons is proportional to $\sqrt{E^3}$ (Knoll, [34]) therefore the pulse height distribution is proportional to $1/\sqrt{E}$.
The size of the scintillator cell influences the pulse height distribution as well. If the cells size is small compared to the mean free path of the recoiling proton at maximum energy, the proton can escape the volume and energy will be lost. The pulse height spectrum will shift to lower energies. If the volume is large, the proton will deposit all of its energy within the cell yielding events with full energy, respective large pulse heights. As shown later, the particle discrimination works better for large pulse heights, so a larger cell increases the neutron detection efficiency. Multiple scattering of the neutron will not be distinguishable from each other because the scintillation processes are too fast in order to see a single scattering process. The resulting light output is a sum over all processes caused by the neutron. The proton recoil probability for 2.45 MeV neutrons is in the order of 20% while the detection efficiency (see section 3.10) is in the order of 5 to 15% depending on the scintillator cell geometry and the used photomultiplier to look at the scintillation light.
As mentioned before, the neutron loses energy with each scattering process. This process is called moderation. If the neutrons energy reaches thermal velocities, it can also be captured by a nucleus, leaving it in a highly excited state. The excited nucleus can emit several γ-rays with a sum energy of the excitation. By choosing a nucleus with a large capture cross section and a high excitation state, the neutron signal can be almost background free. Common capture materials are for example gadolinium which emit gammas with a sum energy of 8 MeV, lithium-6 and helium-3. All capture processes suffer from efficiency which is usually in the order of 3% for a portable device. Any energy information is also lost for a capture process. Large volumes filled with moderator and nuclei with high capture cross sections as well as very large scintillator volumes can reach almost 100% neutron detection efficiency, it depends only on the covered solid angle and the neutron cut efficiency. This will be discussed in section 3.11.
This work restricts itself to the use of NE-213 liquid scintillator which is a xylene based liquid scintillator with several constituents such as naphtalene, activators and wavelength shifters. The exact composition is a company secret.

3.2 NE-213 liquid scintillator

The NE-213[2] liquid scintillator is widely used for any kind of fast neutron identification because of its excellent neutron discrimination properties. Since photons mostly interact with the scintillator due to compton scattering[3], they produce recoil electrons. The electron recoil energy produces mainly prompt fluorescence light with a very short decay time in the order of 3.7 ns as stated in the data sheet. Proton recoils can trigger intersystem excitation between singlet and triplet states which is a slow process ($\mathcal{O}1$ ms) compared to the prompt fluorescence light. This process produces the so called delayed fluorescence light by which neutrons can be identified.
Therefore different pulse shapes for different particles can be obtained, the time distribution of the signal changes with the interaction type. Photon signals have only the fast light component, neutron signals have both, fast and delayed light components. A schematic view of the signals time structure in a scintillator is shown in figure 3.8. The photomultiplier traces are recorded using CAEN v1729

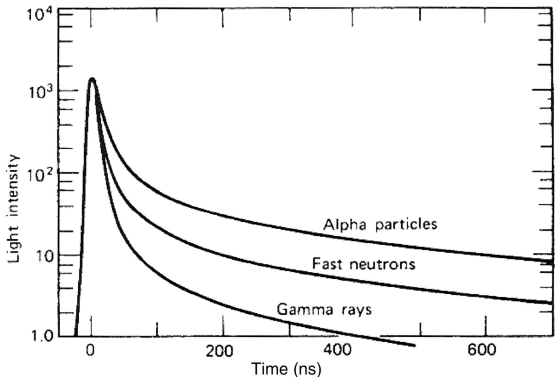

Fig. *3.1: Time dependence of scintillation pulses in stilbene when excited by different particles. From Bollinger and Thomas (1961), via Knoll (2000) [35, 34]*

fast sampling ADCs with 12 bit resolution and 500 ps timing. See chapter 2.4 for the details of the readout.
Radiationless deexcitation such as production of heat is the main cause of quenching and is different for each particle type depositing energy in the scintillator. This description of the scintillation process in NE-213 is a very simple approximation, details on the scintillation process can be obtained from literature [34].

[2]nowadays commercially available as EJ-301, which is exactly the same composition as NE-213 or BC-501A, which has similar discrimination properties.

[3]The probability for photoeffect in the scintillator is proportional to $\frac{Z^{(4-5)}}{E_\gamma^{3.5}}$ where Z is the atomic number of the material and E_γ the photon energy.

3.3 Detector modules

During this work several different types of NE-213 neutron detectors were tested and used. A short summary of their specifications, technical data and features is given in this section. The detectors can be divided into two subgroups, NE-213 detectors which are being read out by a single photomultiplier and those read out by two photomultipliers.

3.3.1 Single photomultiplier cells

A short overview with typical properties of the single photomultiplier cells will be provided here. The detailed description of the detectors, construction schemes, voltage dividers and technical data sheets are available in a technical report[1]. Most of these detectors were not only used in this project, they were also used in several accelerator experiments and are still in use in the CRESST scattering experiment at the "Maier-Leibnitz-Laboratorium" (MLL) in Garching (see refs. [12], [14] and [48]).

Type 1: First generation detectors from Freiburg.

These detectors consist of a large 1" x 7" liquid scintillator cell coupled to a Valvo XP1040 photomultiplier and were initially used for beam experiments at the accelerator in Freiburg. Pictures of the cells are shown in fig. 3.2. The voltage divider of the photomultiplier (see fig. 3.4) allows for large currents which results in signals in the order of several 10 V. Since modern day electronics accepts signals up to 1-2 V, a linear attenuator of 22 dB must be used. The bias voltages range from -2000 V to -2500 V. A construction scheme is shown in figure 3.3. These

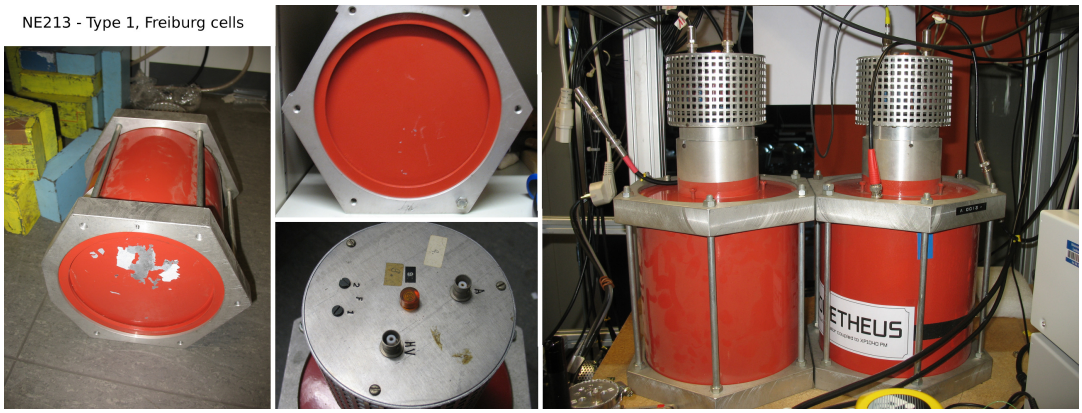

Fig. *3.2: NE-213 Type 1, Photos*

detectors, due to their large cells, provided very good solid angle coverage with typical neutron discrimination thresholds of 400-700 keVr.

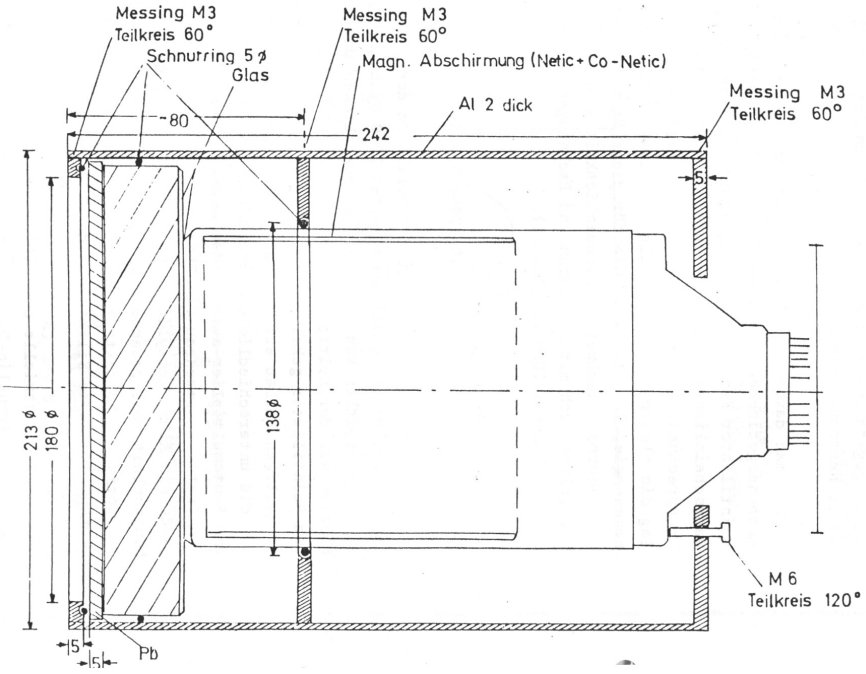

Fig. *3.3: NE-213 Type 1, construction scheme*

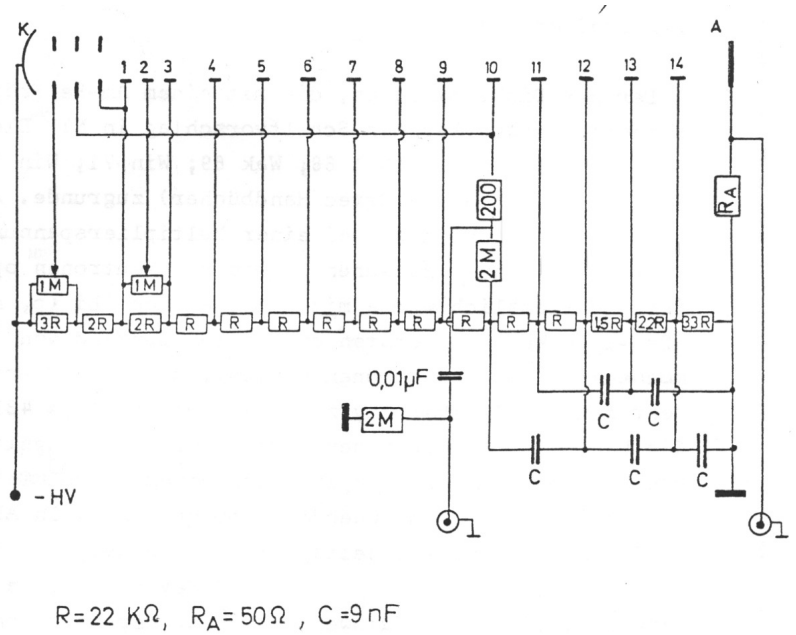

R = 22 KΩ, R_A = 50 Ω , C = 9 nF

Fig. *3.4: XP1040 voltage divider*

Type 2: First generation detectors from the Rosenau accelerator.

The detectors were built in 1981 by W. Erath (see [22]) and B. Dolderer within their work at the Rosenau accelerator. These modules consist of a 2"x 4" NE-213 cell coupled to a Valvo XP1041 photomultiplier. They are operated at bias voltages of -1700 V to -2000 V together with an Ortec Model 113 preamplifier. Such detectors were also used during the previous work. In this work they were used primarily for target testing and beam monitor measurements at the Rosenau accelerator. A picture is shown in fig. 3.5. These detectors have excellent energy

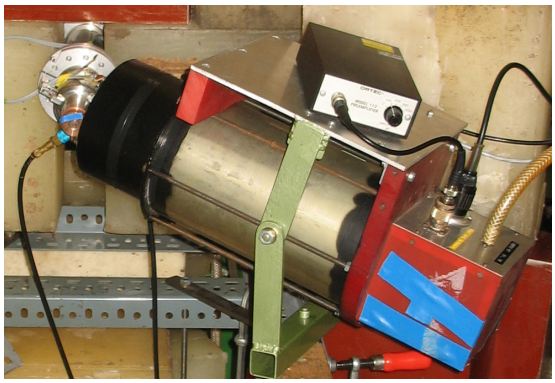

Fig. *3.5: NE-213 Type 2, photo at the Rosenau accelerator. Visible at the upper left corner is the end of beam line no.5. The black box on top of the detector is the preamplifier.*

resolutions as well as a high efficiency for low energetic neutrons. One of this detectors was used to measure the neutron flux during previous work.

Type 3: Second generation large solid angle vacuum detector.

A large solid angle vacuum detector was developed in this work. The detector is directly mounted into the vacuum chamber with the target placed on the cells vacuum face. The detector consists of a 3" x 3" cylindrical NE-213 cell readout by a Valvo XP2041 photomultiplier. The detector is directly constructed onto a stainless steel DN160 ISO-K vacuum flange. It is light tightened by deep grooves where the components fit in, black tape and mechanically stabilized when mounted horizontally. The operating voltage is set to -2450 V. It is noted here, that the stainless steel encapsulation becomes transparent for X-ray energies larger than 60 keV. The bremsstrahlung intensity decreases to higher energies so that the effective rate rises but is still within the acceptable parameters from the DAQ perspective. One might have to add additional lead shielding in order to suppress

gamma background in the future to solve the dead time problem discussed later. The detector scheme is shown in fig. 3.6.

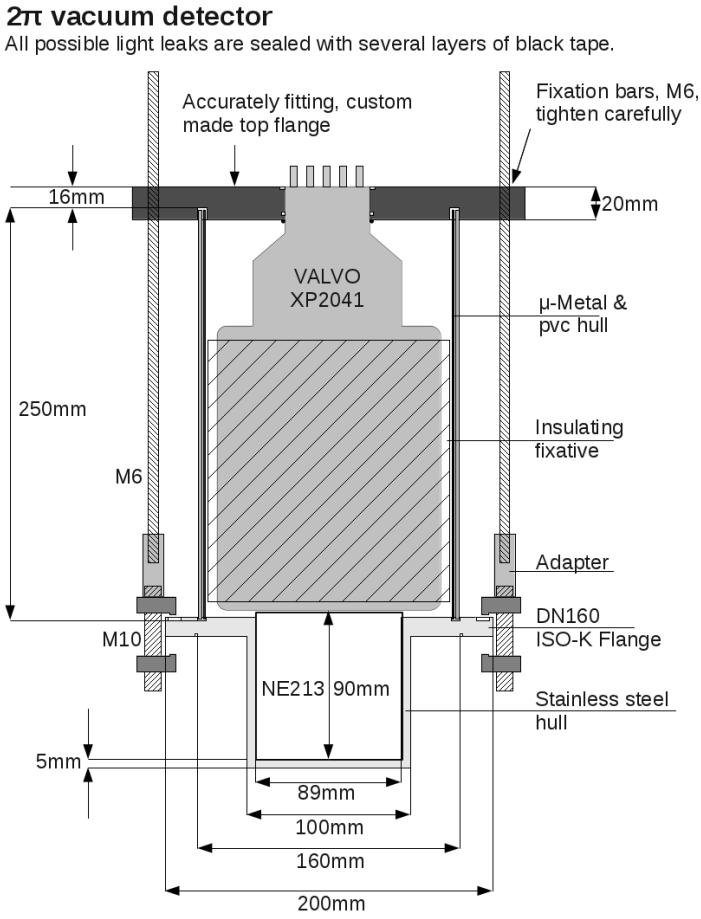

Fig. *3.6: Construction scheme of the NE-213 vacuum detector.*

3.3.2 Double photomultiplier cells

There is a set of detectors which consist of one scintillator cell sized 3"x3" or 3"x4", readout by two Valvo XP2041 photomultipliers. These cells provide excellent neutron discrimination properties if the signals of both photomultipliers are used for analysis. Due to triggering on coincident events only, the background triggering rate decreases to only 5-10 Hz compared to 50 Hz for a single detector. A picture of one of those detectors is shown in fig. 3.7.

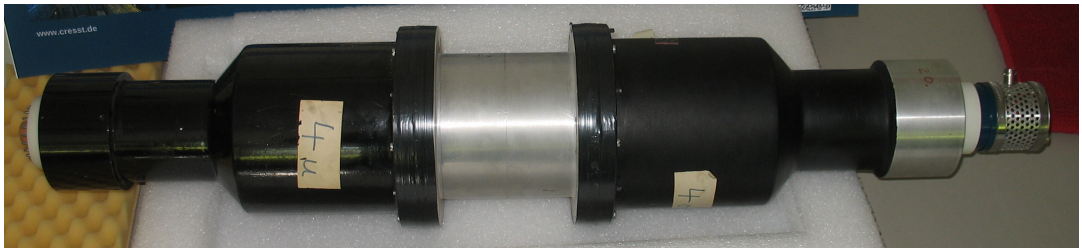

Fig. *3.7: NE-213 double module*

3.4 Neutron signal identification

The neutron signal and the gamma signal can be distinguished by the different fall times characterized by the time distribution of the scintillators light output. A convenient way to do such a pulse shape analysis is fitting with model functions, so called standard events, to the pulse and see which one fits better. The model function for the decay time of the pulse according to Jagemann [31] is

$$L(t) = A \cdot exp{-\frac{t}{t_1}} + B \cdot exp{-\frac{t}{t_2}}. \tag{3.3}$$

L(t) is the light output function over time, while A and B are interaction dependent scaling factors and t_1 and t_2 are the interaction dependent short and long fall times of the pulse. The two model functions with their starting parameters are shown in fig. 3.8, a fit on a real pulse is shown in fig. 3.9. The discrimi-

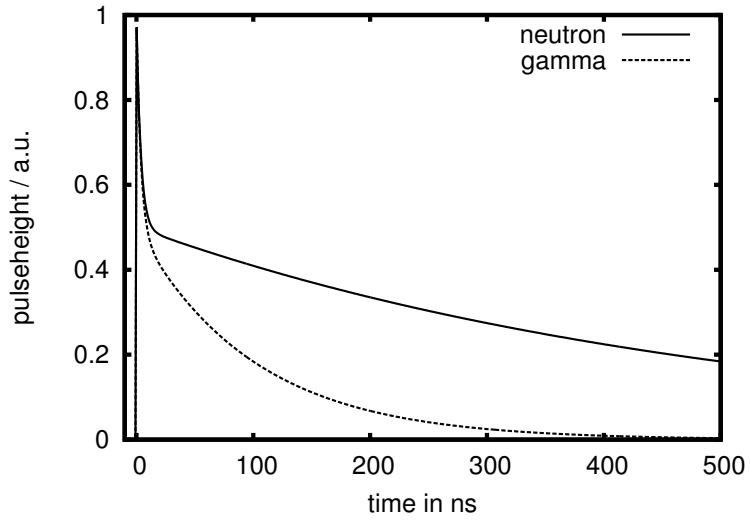

Fig. *3.8: NE-213 standardpulses, t_1 = 3.7 ns, $t_{2,neutron}$ = 500 ns, $t_{2,gamma}$ = 100 ns, A = B = 0.5.*

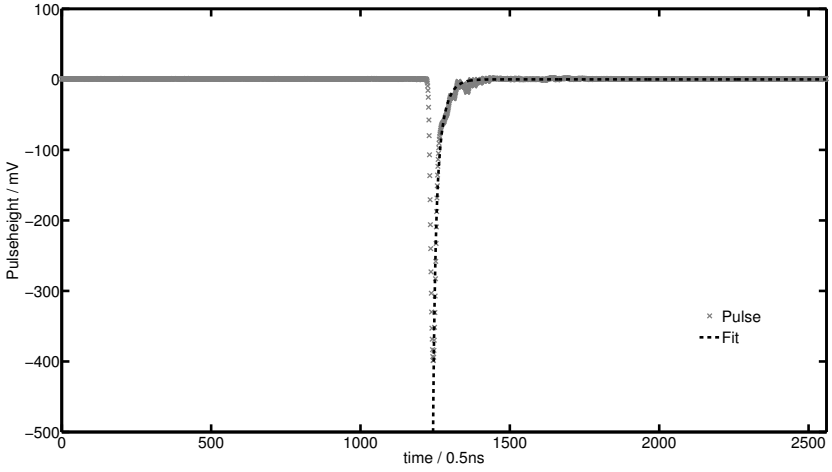

Fig. *3.9: General fit of model function to a real pulse. Typical gamma pulse of type 1 detector (see section 3.3.1), fitted with two decay times.*

nation is technically faster compared to the standard event fit, if the pulses are being integrated over a short and a long time (short gate and long gate). The ratio of those integrals is different for the respective interaction types. A similar approach, determining the 90% to 10% fall time of a pulse was also tested but suffered from electronic effects such as ringing and high frequency noise and is no longer used. Furthermore, the recorded signal is also influenced by the level of noise encountered as well as by the photomultiplier used and the electronics applied which modifies the discrimination quality. Additionally, the liquid scintillators light output and therefore its discrimination property is temperature dependent (See refs. [25, 26]). The detectors are operated in a air conditioned environment.
Typical integration values are 20-30 ns for the short integral and about 300 ns or more for the long component. The ratio short/long is a good discrimination property and is referred to as the "discrimination factor". The pulse height, which is a measure for the total light output can be plotted against the discrimination factor, as shown in the scatter plot (See fig. 3.10). The total light output can be converted into an energy by calibrating the detector with known energies. The light output is different for each particle type causing the interaction. This effect is kown as quenching. Therefore absolute energie values must be calibrated to each particle type. In this work the electron equivalent energies for gamma interaction are given as keVee or MeVee, while the neutron equivalent energies will be given in recoil equivalent energies, keVr or MeVr. In the scatter plot two branches appear. The upper branch corresponds to the gamma interactions, the

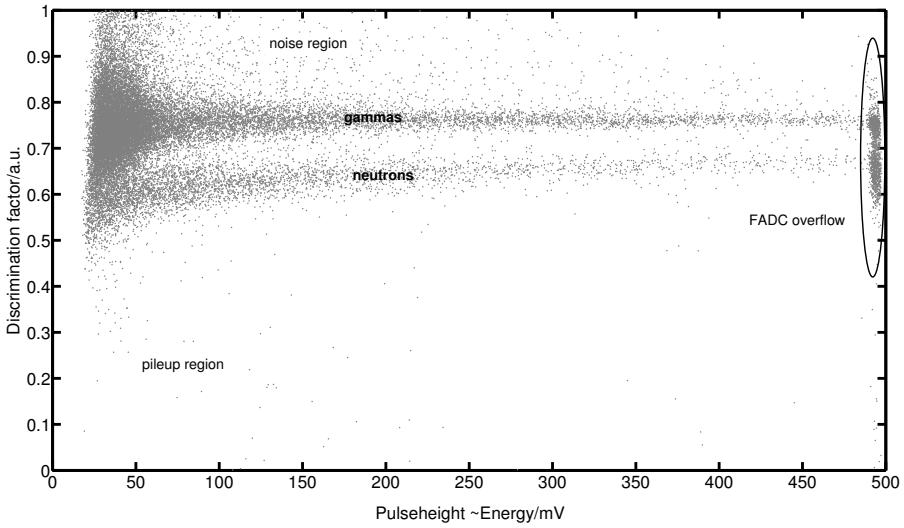

Fig. *3.10: NE-213 Scatter plot. This plot is a sum scatter plot of a beam time without any cuts. The gap at low pulse heights represents the hardware threshold. The band at lower discrimination factor corresponds to neutrons which in this case are produced by the dominant D(Li,n)X reaction and the D(D,n)^{3}He fusion reaction. For plotting purposes, only every tenth point is drawn.*

lower branch to neutron interactions. The two distributions overlap for small pulse heights. The separation of the two bands will be discussed in the next section.

3.5 Neutron discrimination optimization

In order to detect low neutron fluxes a good detection threshold is needed. This means, that a good separation of the two bands in the scatter plot is mandatory. The further the band can be separated towards lower pulse heights, the better gets the detection threshold. It is being discussed, how the discrimination threshold is defined and how it can be improved. The common discrimination threshold is usually set at the energy where a fit of two gaussian distributions on the discrimination parameter histogram is separable. For example, all events are being histogrammed over the discrimination parameter, but only within a certain pulse height or energy range, e.g. 300-400 keVee. The two distributions can now be fitted by two Gaussian distributions which is shown in fig. 3.11. The separation threshold is defined as the energy where the sum of the FWHMs of the gaussians is equal to the distance between the peaks. The ratio $P^* = \frac{D}{FWHM1+FWHM2}$ of the peak distance D and the sum of the widths is being plotted vs. the different energy intervals. A power law fit can be applied to the data points and the energy

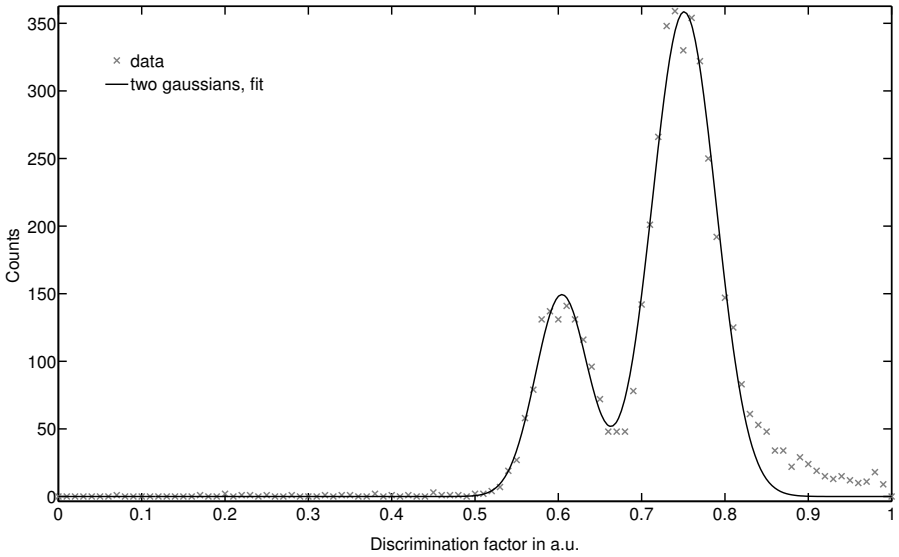

Fig. *3.11: Fit of the Discrimination parameter in a certain energy range with two gaussians, neutrons are left, gammas are right. The deviation from the fit on the far right side of the plot is caused by noise. See also fig. 3.10.*

determined where this ratio equals one. For the discrimination parameters close to one, a linear fit will give similar results. Such power law fit is depicted for an exemplary detector in fig. 3.12. This procedure was investigated in detail in the diploma thesis of M. Pfeifer [42].
The separation of the two bands can be improved by changing the integration gate widths. In the current work, an algorithm was implemented which tries to find the best discrimination settings for a specific detector. The function splits the data sets pulse height information (which is not yet converted to energy) into a specific amount of bins. For each bin the discrimination parameter histogram is calculated. Each histogram is now fitted with the two Gaussian distributions described above. By varying the integration gate widths, P^* can be maximized which results in the best gate settings. The short gate length is crucial for the separation at low pulse heights while the long gate length changes the discrimination quality almost independently of the pulse height.
This procedure requires of course a data set containing pulses (see chapter/section 2.4) with a significant amount of neutrons. The algorithm is part of the P.I.A. FADC data acquisition (see 2.4.2). The dependence of the discrimination parameter for different gate settings is shown for an exemplary data set in fig. 3.13. The neutron selection and the selection efficiency will be discussed in section 3.6.

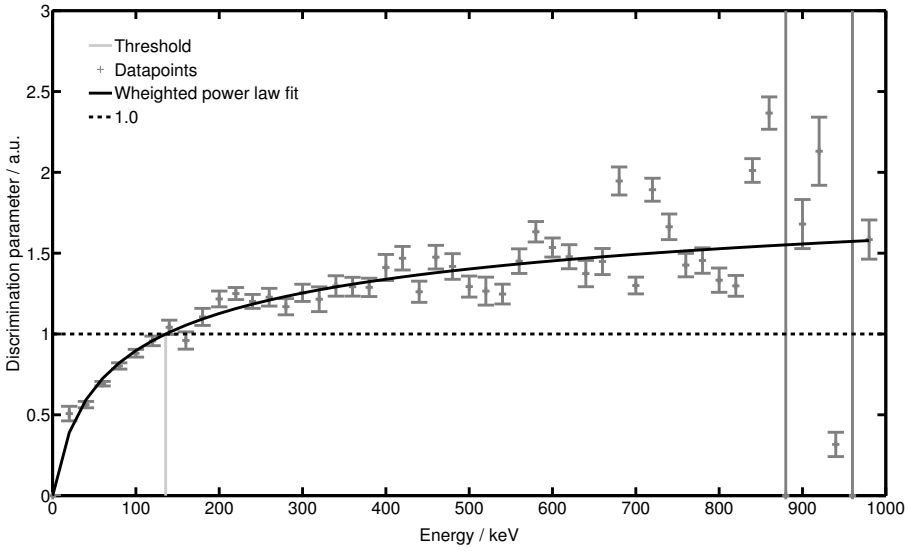

Fig. *3.12: Classical determination of the discrimination threshold. Exemplary plot on calibrated data. The low energy part from threshold up to ≈250 keVee can be fitted with a line as well.*

Definition of the n/γ cut

A byproduct of this discrimination optimization is the determination of the energy dependent widths and positions of the gamma and neutron bands in the scatter plot. If the best gates are determined, the energy binning is refined, new discrimination parameter histograms are built and the two gaussians are fitted again for each energy bin. The standard deviation σ parameter of the gaussian fits is used to determine for each energy bin the three and four σ (and even higher order) limits of the gamma and neutron bands. These energy dependent boundaries are being used to select neutrons from the scatter plot.
The boundaries can also be interpolated or fitted, which technically simplifies their application. The gamma boundaries can also be determined by using only a gamma source for calibration. Gamma calibration data was recorded using ^{22}Na and ^{60}Co sources and were also used for energy calibration of the detectors (see 3.8. Detectors were also tested at the accelerator using high energy neutrons from the D(^{7}Li,n)X reactions and low energy neutrons from the D(D,n)^{3}He fusion reaction, or calibrated by a ^{252}Cf source in the final setup.

3.5.1 Naming conventions

The energy, above which the particle bands in the scatter plot do not overlap within the three σ limit is called the **C**lassical **N**eutron **D**iscrimination **T**hreshold

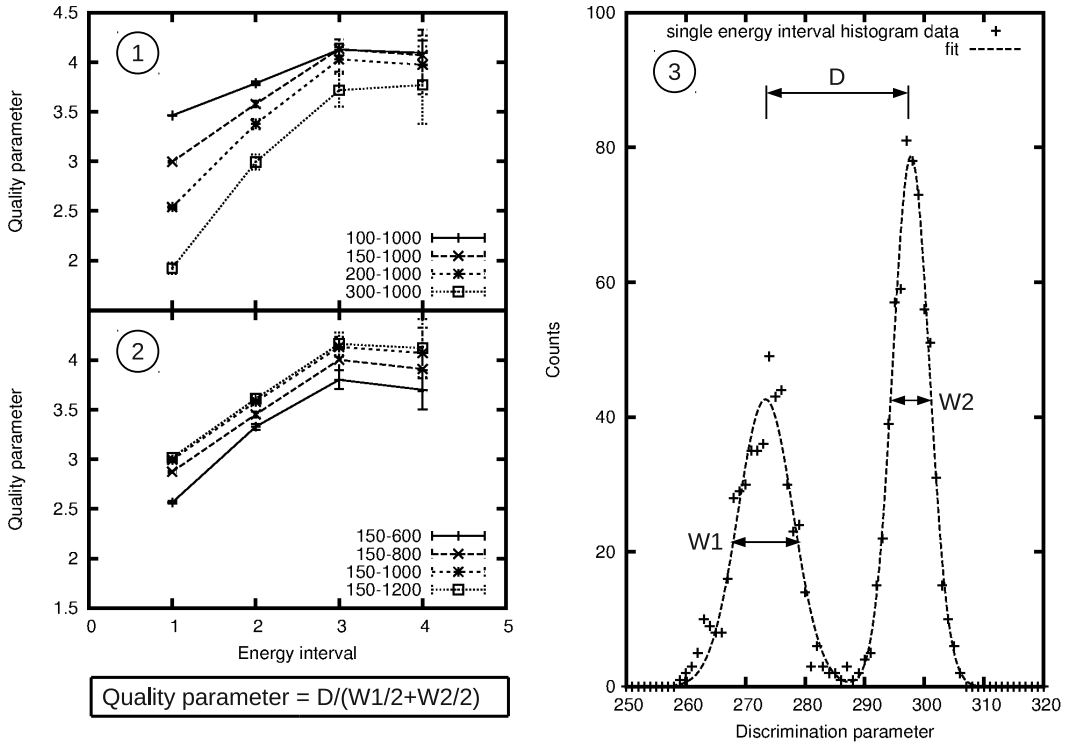

Fig. *3.13: Quality parameter for one specific data set containing neutrons with different integration gate widths. In subfigure ①, the short gate width is varied, in subfigure ② the long gate width is varied and subfigure ③ shows how the quality parameter is determined. The energy intervals are exemplary and can be chosen freely. Typical widths of a single interval are in the range of 100 keVee.*

(CNDT, (2)). The energy interval from the CNDT up to the maximum energy accepted in the neutron cut is called **F**ull **N**eutron **E**fficiency **R**ange (FNER). The energy interval from the hardware energy threshold (minimal recorded pulse height, see trigger conditions in section 2.4) up to the maximum energy accepted in the neutron cut is called **R**egion **O**f **I**nterest (ROI). A graph containing an illustration of the naming conventions is shown in fig.3.14.

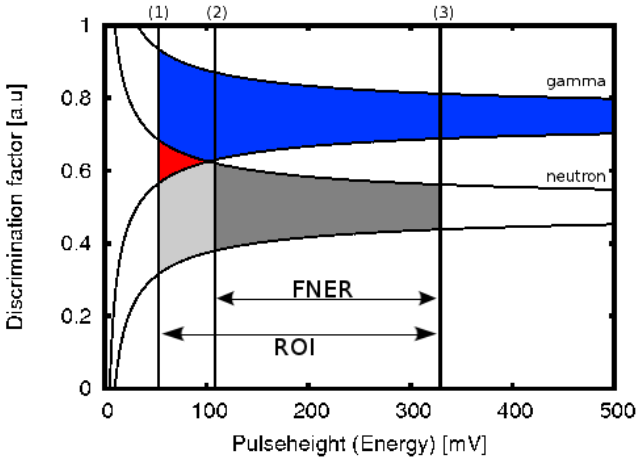

Fig. *3.14: Scheme of cut efficiency determination, the lines indicate the hardware threshold (1), the CNDT (2) and the maximum accepted energy (3). Values are exemplary and change for every detector.*

3.6 Neutron cuts

A neutron selection, also called neutron cut, defines the exact area in the scatter plot from which neutron signals are being accepted for further analysis. Modifying the boundary conditions of the neutron cut can reduce the number of accidental false neutron identifications as well as restrict the neutron energies to the region of interest.
The neutron cut has the following boundary conditions:

- Lower energy boundary:
  The lower energy boundary for the neutron cut is equal to the hardware threshold unless full neutron efficiency is desired, then the lower energy boundary condition is the CNDT.

- Upper energy boundary:
  The upper energy boundary for the neutron cut is equal to the sum of the maximum neutron energy from the nuclear reaction and the kinetic energy of the incident ion folded with the detector systems energy resolution.

- Lower discrimination factor boundary:
  The lower discrimination factor boundary is either zero, if the detector shows no pileup (for example in double modules, see 3.7), it can be set to a constant value to suppress remaining pileup, or it is the lower 4σ boundary of the neutron band in the scatter plot. The constant lower discrimination factor value is also used if only a gamma calibration of a detector during a given period of time is available.

- Upper discrimination factor boundary:
  The upper discrimination factor boundary is directly responsible for the amount of gammas leaking into the neutron acceptance region. The lower 4σ limit of the gamma band and the upper 4σ limit of the neutron band are used as upper discrimination factor boundaries for the neutron selection.
  If no neutron calibration is available only the lower limit of the gamma band to the desired gamma rejection is used as the upper discrimination factor boundary.

Neutron cut example

An example for a possible neutron cut before energy calibration is shown in fig. 3.15. The boundary conditions were obtained using only a gamma calibration. The gamma boundaries were determined, the lower boundary of the neutron acceptance region is a constant value to suppress pileup. The used boundaries are drawn in blue, the selected neutrons are identified by the red dots and the green circles. The neutron cut was later on refined with data from a neutron calibration with ^{252}Cf (see section 3.26), removing the green circled events from the cut.

Neutron cut problems

During the first stages of the experiment, problems with the stability of the high voltage power supplies of the neutron detectors occurred which influenced the neutron selection significantly. Changes in bias voltage did change the gain of the photomultipliers, therefore shifting the measured energy ranges according to the change in gain. There were two effects observed, a drifting gain and a jumping gain. These effects are being discussed in the appendix C.
For such runs the impact of the change in gain on the neutron cut prevented a clear analysis of the data. Random runs, for example a neutron run and its corresponding background run did show different gains which made background subtraction for these cases impossible. Since gamma calibration data of the neutron detectors was not available at that time, a correction and comparison of the neutron spectra was impossible. The absolute difference is smaller than 10 %.

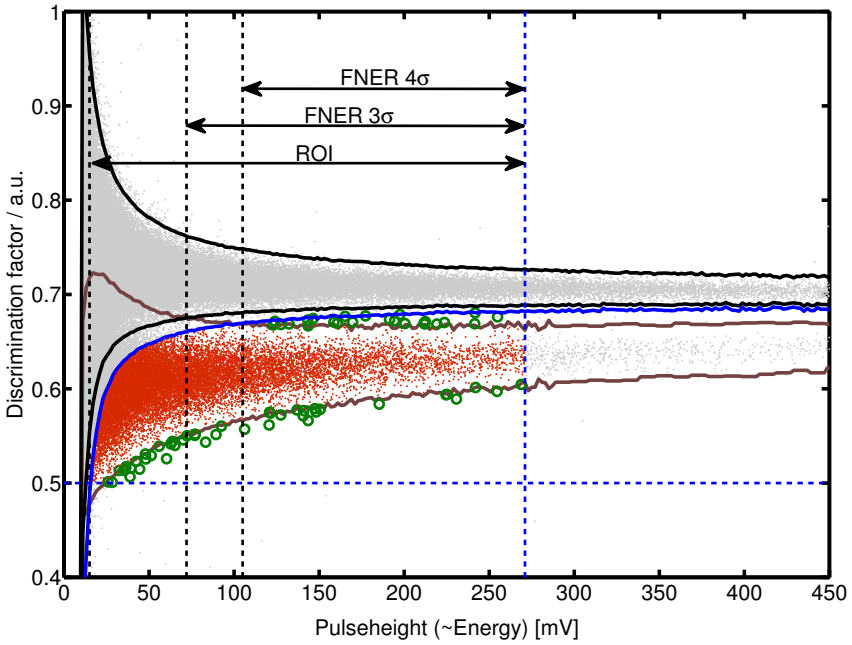

Fig. *3.15: Scatter plot from run with neutron source. The 3 and 4σ gamma boundaries were determined by a gamma calibration. The blue boundaries were used for the neutron cut, which selects all neutrons marked in red and with green circles. The refined neutron cut as introduced later with the ^{252}Cf calibration removes the green circled events from the neutron selection.*

However the neutron separation threshold shifts as well which has a crucial impact on the amount of neutrons which are accepted. An example of a neutron and background run where a gain shift happened in between the recording is shown in fig. 3.16. One of the two detectors used for this measurement showed strong gain drifting which allowed only the second detector to be analyzed. The problem has been resolved by using more reliable power supplies and performing very frequent energy calibrations on all neutron detectors.

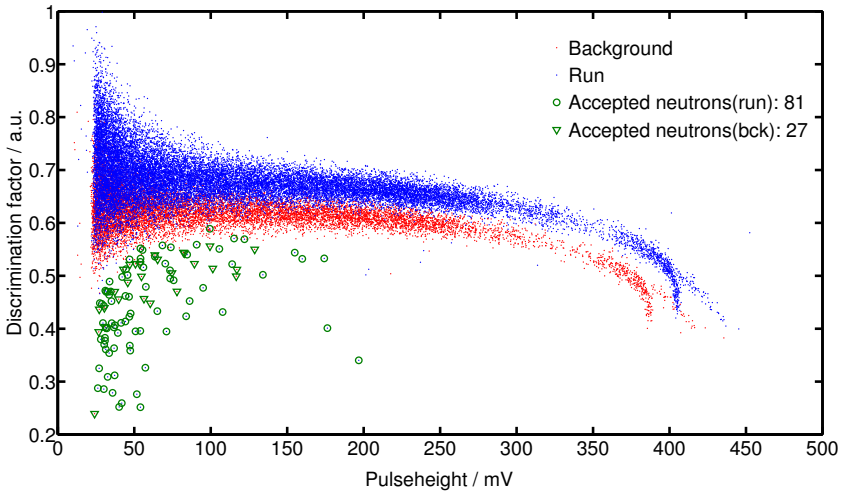

Fig. *3.16: Scatter plot of background run and neutron run with selected neutrons. Clearly visible is the detectors shift in gain in between the two measurements.*

.

3.6.1 Neutron cut efficiency

The cut efficiency describes how many neutrons are identified by the cut, compared to the amount of neutrons which deposit energy in the detector. The cut efficiency in the ROI is typically in the range of 60% for 2.45 MeV neutrons with an endpoint energy of 3.5 MeV. The neutron cut efficiency can be used to estimate the neutron detection efficiency for a complete detector.
The neutron detection efficiency is the product of the probability for a neutron depositing energy on a proton in the scintillator multiplied by the cut efficiency. The neutron detection efficiency depends on the incident angle, track length and energy of the neutron. Usually an integrated detection efficiency for a particular setup will be given or determined. The neutron detection efficiency for a single detector is typically in the range from 5-15%. The neutron detection efficiency can be determined with a neutron calibration which is discussed in section 3.10.

3.7 Measuring an absolute neutron flux

If one wants to measure an absolute neutron flux from a weak source there exist two other (related) parameters that must be taken into account. The distance from the detector to the source and possible problems with the data acquisition rate such as a large deadtime.
The solid angle covered by the detector has to be chosen to be as large as possible for detection of a weak neutron flux. For a description of the different detectors used in this work see section 3.3.

3.7.1 Solid angle coverage

Several detectors different in size were used during this work. Their position relative to the target as well as their number were optimized to cover a large solid angle fraction. In the beginning only one detector was placed in the experiments surrounding covering 1% of the solid angle. By decreasing the distance while increasing the number of detectors, 33% angular coverage was achieved. The positions of the detectors changed as well as the orientation. The setup as operational at the end of this work covers about 33% solid angle with only one detector. The various detector arrangements with their solid angle coverage are shown in fig. 3.17. Without a detector mounted directly to the target into

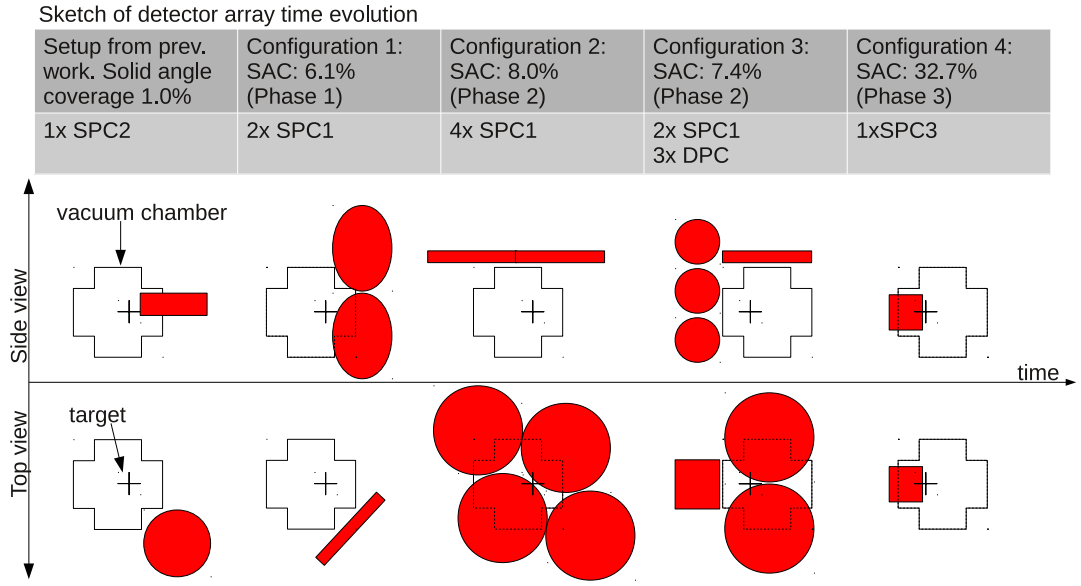

Fig. *3.17: PIA detector evolution, sketch of detector arrangement over time. The red volumes are the NE-213 cells. SPC: Single photomultiplier cell, DPC: Double photomultiplier cell, the number indicates the detector type described in 3.3.1 and 3.3.2.*

the vacuum chamber, the minimum distance to the target is fixed by the vacuum

cambers dimensions. It was attempted to increase the number of detectors as well as their efficiencies by using cells which are being read out by two photomultipliers. Since the enhancement of angular coverage and total detection efficiency was rather poor, the in-vacuum system detector was developed and built. The fusion neutrons are emitted isotropically in 4π. The true solid angle was determined using Monte Carlo methods.

Monte Carlo: Solid angle

A Monte Carlo based solid angle determination program was realized together with K.Freund[4] using Geant4. The neutron source is implemented as a cylinder with given thickness and radius. The neutrons are emitted isotropically from the disc. Starting points and directions are random. The "particles" used are so called "Geantinos" which do not interact at all. For a physics simulation see section 3.9. The code gives the primary vertex, the number of particles hitting detectors and the track length if a detector cell was hit. This track length gives the probability a neutron of a certain energy would interact. The program was executed for every setup shown in fig. 3.17. In the table 3.1 the total solid angle with systematic errors is given. The systematic errors are unavoidable due to the

Setup	Started particles	Detector hits	Solid angle in %	Lower Syst. Err.	Upper Syst. Err.	Stat. Error
Prev. Work	10 M	102499	1.025	-0.178	+0.241	0.003
Conf. 1	10 M	607840	6.078	-1.058	+1.428	0.001
Conf. 2	10 M	796779	7.968	-1.386	+1.872	0.001
Conf. 3	10 M	742861	7.429	-1.293	+1.746	0.001
Conf. 4	1 M	326521	32.652	-0.643	+1.346	0.002

Table 3.1: Solid angle determination with Monte Carlo methods. The Geant4 package was used. The solid angle is $100 \cdot \frac{Detector\ hits}{Started\ particles}$ %

remaining position uncertainties of the detector cells. The position uncertainty is in the order of ± 1 cm correspondig to 5-10% for each cell as they had to be removed quite frequently to get access to the experimental chamber. More precise position measurements were performed for detector configuration 4. The solid angle calculation for calibration sources was also determined, the sources therefore treated as point like.
Increasing the solid angle also increases the solid angle for high energetic X-rays

[4]Private communication, University of Tübingen, Physikalisches Institut 1

for which the detector hull becomes transparent above approximately 60 keV. The X-rays will also scatter in the liquid scintillator increasing the trigger rate. The data acquisition system however is designed only for very small trigger rates which will result in an increase in dead time.

3.7.2 DAQ Dead time

Dead time is the time fraction that the detector or the data acquisition is busy and cannot handle new events. The dead time in this experiment is dominated by the DAQ especially the data transfer into the computers memory. The FADC sampling time t_s is up to 2.5 μs, the conversion time t_c 650μs. During this time, no new trigger is being accepted, it is also externally vetoed using the FADCs "busy" signal. It takes another 8 ms to read out, analyze and store the pulse, called t_{daq} or data acquisition time. The t_{daq} was determined by sending pulses with variable rate to the DAQ, looking for the measured rate. There are two rates used in this context, the total trigger rate and the effective rate. The total trigger rate is the rate the FADC accepts triggers. The effective rate is the rate events are being stored. The difference between the two rate originates in an online cut applied to the data to remove very bad events. The cut conditions are chosen in a way that nothing relevant is being removed. The pulse generator sometimes produces signals containing a lot of noise which explains the deviation of the total rate compared to the effective rate. The pusle generator fires the pulses not randomly but periodically with a fixed time in between.
The measured rate increases linearly until the cutoff frequency is reached. The cutoff frequency is defined by the dead time of the system. From there to higher rates, the measured rate decreases significantly as the system does not accept triggers which appear during the veto period. This is a direct effect of the test with the pulse generator because a truly random time distribution would result in a constant maximum trigger rate. An illustration of this effect is shown in fig.3.18. If the pulsed rate is high enough, the probability for a pulse to be accepted again

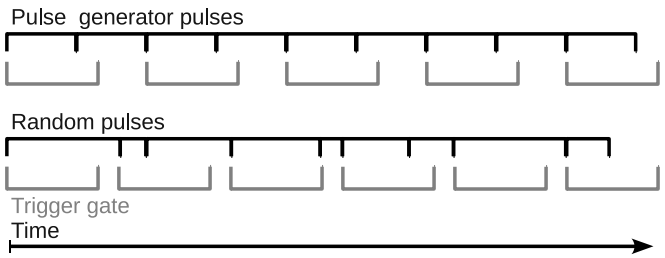

Fig. *3.18: Illustration of pulser effect compared to random pulse distribution.*

rises again until a almost full rate is achieved. The number of pulses rejected

increases with high rates. A picture of the measured rate vs. the rate of the pulse generator is shown in fig. 3.19. The sum of the sampling time, the conversion time and the data acquisition time is called blocking time $t_b = t_s + t_c + t_{daq}$. Therefore

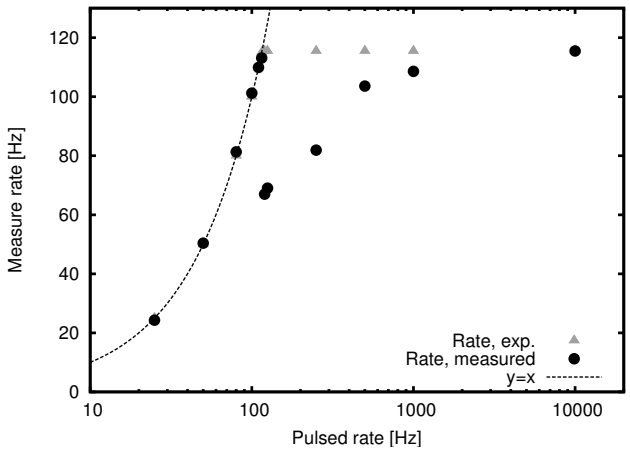

Fig. *3.19: DAQ dead time: pulsed rate vs. measured rate. The difference between expectation and measurement is an effect of the pulse generator.*

the rate dependent dead time D(f) can be calculated as

$$D(f) = \frac{t_b}{(1/f) + t_b}. \tag{3.4}$$

The rate dependent dead time for 9 ms blocked interval is shown in fig. 3.20, the blocking time dependent dead time for three different rates is shown in fig. 3.21. The total dead time for one run is being determined using the time binning given

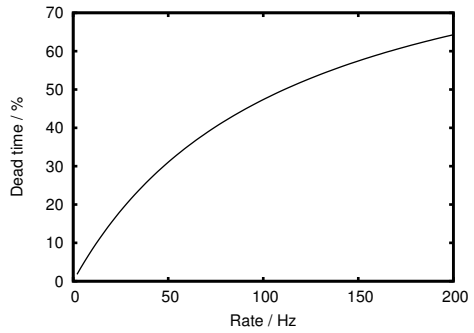

Fig. *3.20: Rate dependence of the dead time for constant blocking time of 9 ms.*

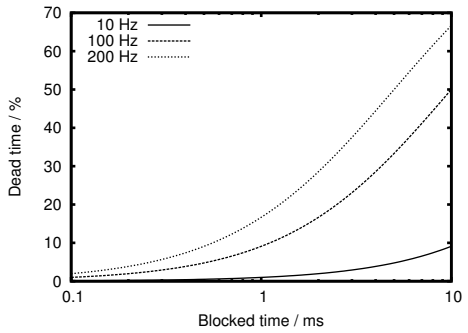

Fig. *3.21: Blocking time dependence of the dead time for different rates.*

by the data acquitition: the dead time is calculated for each time bin, the sum is

the dead time of the whole run. During most runs the native time resolution is one second.
The dead time error is being calculated assuming a 10% error for the blocking time t_b and a 5% rate error Δf:

$$dD(f) = \frac{1}{(\frac{1}{f} + t_b)^2} \sqrt{\left(\frac{1}{f} \cdot \Delta t_b\right)^2 + \left(\frac{t_b \cdot \Delta f}{f^2}\right)^2}. \tag{3.5}$$

However only the last and current detector used in phase III, which is mounted directly into the vacuum chamber and covers large solid angle is strongly affected by higher rates as it "sees" a significant amount of X-rays. In times of high voltage when the detector encounters high rates, also the dead time is high. This must be corrected for in the neutron analysis. For an exemplary run the dead time distribution throughout the run is shown in fig. 3.22. The total dead time for this

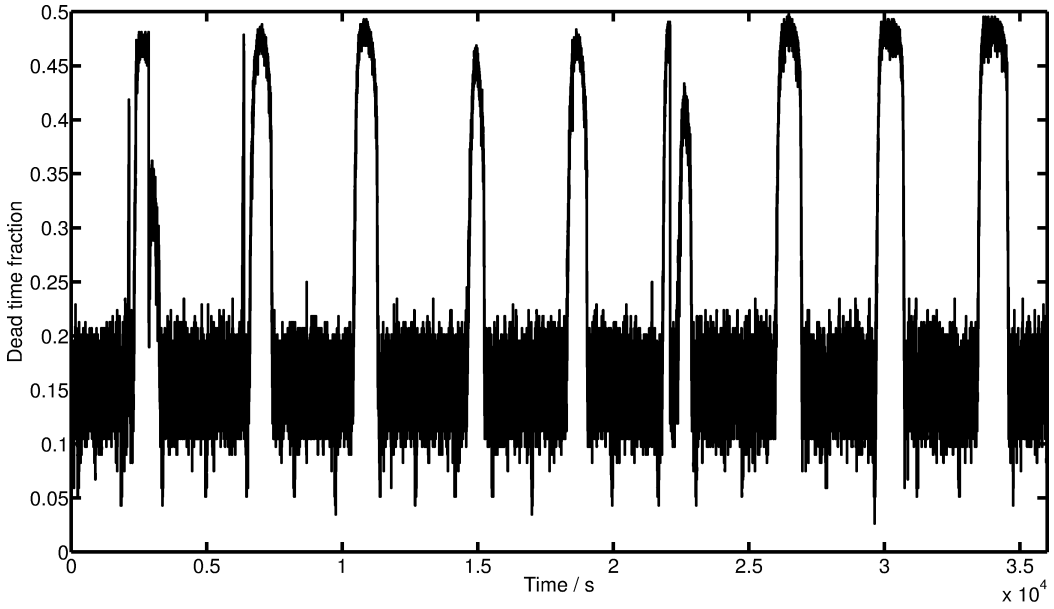

Fig. *3.22: Exemplary time distribution of dead time within one neutron run.*

exemplary run was 21.3% of the measure time. For less rate dependent detector systems as used in phase I to II, the total dead time is in the order o 5-10%. Measurements where the dead time is not constant are being corrected for that effect.

3.8 Energy Calibration

Energy calibration of a NE-213 detector is done by measuring the compton edges (CE) of various gamma sources. The energy resolution can be calculated from

this gamma calibration. With the position of the compton edges and the known response function to correct for the quenching of the neutrons, also the neutron energy spectrum can be calibrated.
Gamma spectra in NE-213 are dominated by compton scattering. If the volume would be large enough, one might also see the photopeaks of the gamma calibration sources. This is being discussed in the PIA@DODI section 3.11.
For calibration issues the position of the CE has to be determined. Fitting half a Gaussian to the CE produces reasonable results. The actual position of the edge however is calculated differently according to [31], [48], [22] and [42]. Here, the position of the CE is defined as the excess peak position of the Gaussian plus half the FWHM. Other sources use just the peak position, or position where the fit curve falls below 90%, 68% or 36,8% (1/e) of the peak value. A comparison on real data is shown in fig. 3.23. The energy resolution of the NE-213 is defined

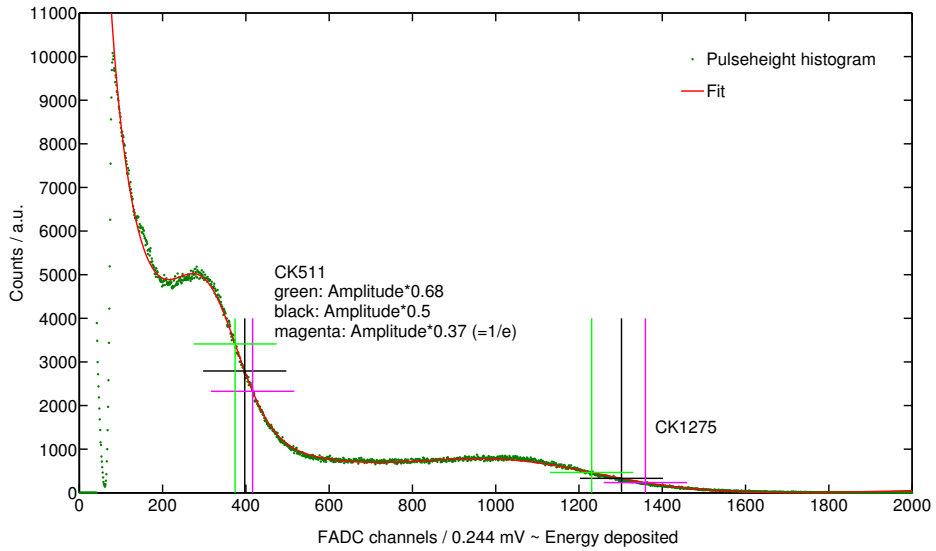

Fig. *3.23: NE-213 energy calibration with ^{22}Na source. Position of compton edges marked. DPC: single detector spectrum*

as the distance of the 90% and the 10% peak values of the compton edge at a certain energy. For the calibration depicted in fig. 3.23, the energy resolutions are 112.1 keV @ 340.7 keV and 343.8 keV @ 1062.2 keV which are the compton edge energies of the ^{22}Na source. The relative energy resolutions of 21.9% and 27.0% are in good agreement with other measurements [22].
The gamma energy calibration can be used to derive the neutron energy calibration if the scintillators response function is known. The response function describes the light output of energy deposited by neutrons compared to energy deposited by electrons, it corrects for the quenching. Response functions can

be obtained from the scintillators data sheet or using the one for low energetic neutrons up to 2.5 MeV from Lee & Lee [37] to calculate the electron equivalent energies E_e of the proton recoils E_p:

$$E_e = (0.034 \pm 0.003)E_p^2 + (0.311 \pm 0.011)E_p - (0.109 \pm 0.006). \tag{3.6}$$

The response functions given in the scintillators datasheet originate from Cecil et al. [11] for 1...300 MeV neutrons and Aksoy et al. [3] for 5...17 MeV neutrons which is mostly beyond the region of interest in this work. Response functions for the NE-213 scintillator were also published by Gul et al. in 1989. A comparison of the response functions from Cecil et al., Gul et al. [30] and Lee & Lee is shown in fig. 3.24. The energy calibration is being used to determine the threshold of the neutron cut. The total detection efficiency depends substantially on the threshold.

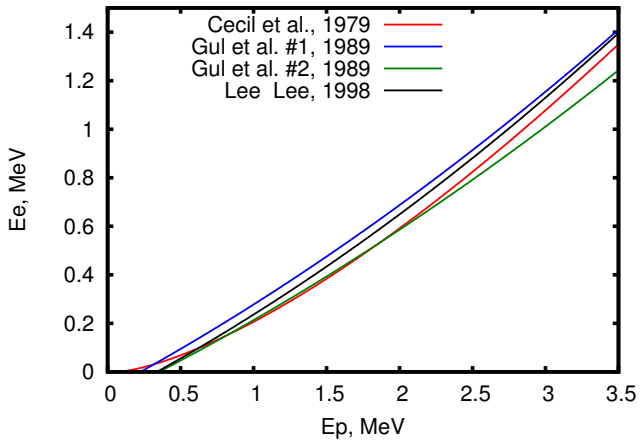

Fig. *3.24: Comparison of literature response functions for NE-213.*

3.9 Simulation of detector cell response to neutrons.

Monte Carlo simulations were performed to study the detector cell response to the neutron spectrum expected from the DD-fusion reaction. Based on the different detector designs and volumes, a 2.45 MeV monoenergetic neutron source[5] was placed near the detector and the total amount of energy deposited as well as deposited on protons was recorded. The proton recoils excite the long living molecule states which are needed for discrimination between neutrons and gammas. Table 3.2 shows the simulated energy depositions from the source for

[5]Gaussian input spectrum with a FWHM of 0.1 MeV, which corresponds to the acceleration energy.

different scintillator volumes. This simulation is missing the light output function for the scintillator however the proton recoil spectrum can be used to estimate the amount of detectable neutrons by comparing it to a measured neutron calibration (see section 3.10). The Monte Carlo codes and simulations were done in cooperation with S.Scholl and M.Röhling[6]. The last simulation (marked with ^{o} in the table) was performed analog to the ^{252}Cf calibration as will be described in section 3.10, which means that the source position was adjusted similar to the real source position and the input neutron spectrum of ^{252}Cf was used. 100 M events were simulated. Only a weak limit on the sensitivity of the neutron efficiency

Table 3.2: Proton recoil efficiencies resulting from NE-213 Monte Carlo simulations. 10 M neutrons from a point source of fusion neutrons simulated in 4π. Source position on symmetry axis of cylinder, 1 cm in front of cell if not stated differently. The cell size is given in diameter(2r) times height(h) of the cylinder. Ω is the solid angle, the percentage of started neutrons hitting the detector. E_x>0 is the number/ratio of neutrons which deposited any energy in the detector, E_p>0 is the number/ratio of neutrons which deposited energy only on protons. Width (FWHM) of the initial neutron spectrum is 100 keV (: Source positioned on edge, ^{o}: Source positioned in ^{252}Cf calibration position, 100 M started neutrons, ^{252}Cf neutron energy spectrum.).*

Cell size 2r x h	Ω	(E_x>0)/Ω	(E_x>0)/10 M	(E_p>0)/Ω	(E_p>0)/10 M
7" x 1"	37.4%	43.3%	16.2%	21.8%	8.1%
5" x 4"	38.5%	59.7%	23.0%	23.4%	9.0%
6" x 4"	40.1%	66.9%	26.8%	24.2%	9.7%
5" x 3"	37.8%	57.7%	21.8%	23.9%	9.1%
4" x 3"	34.9%	48.3%	16.9%	21.7%	7.6%
4" x 2"	35.3%	46.1%	16.3%	22.1%	7.8%
4" x 2"*	25.4%	42.7%	10.8%	20.2%	5.1%
3" x 3"	29.8%	36.7%	10.9%	17.8%	5.3%
3" x 3"^{o}	4.3%	69.0%	3.0%	27.1%	1.2%

can be given by assuming that the proton recoil must have at least deposited a certain amount of energy above the threshold to lie within the cut conditions. This will of course underestimate the amount of light produced since the fast light component of the electron interactions is not considered. However, as will

[6]Private communication, University of Tübingen

be shown, these approximations do give a realistic estimate on the detectors efficiencies if the energy resolution of the detector is being considered as well. Based on the proton energy recoil spectrum folded with the detectors energy resolution in the region of interest a value can be determined for the expected efficiency. For the 3"x3" cell in the energy range from 1 to 3.5 MeVr the estimated efficiency is $12.3^{+3.1}_{-2.4}$ %. A 20% error for the missing light output and the standard error for the solid angle are taken into account for the total error. A slight overestimation of the efficiency is expected, because the light production mechanism is not 100% efficient. As will be shown in the next section, the overestimation is in the order of 3-4% which is compatible within the errors of simulation and measurement.

3.10 Calibration with a ^{252}Cf source

The absolute efficiency calibration is usually performed using a neutron source with a known energy spectrum or even single neutrons with known energy. In this work a fast calibration is being performed, taking into account only the most relevant contributions such as the DAQ dead time, solid angle and the source strength. The obtained value will be compared with Geant4 simulations of the energy distribution of proton recoils in NE-213. It will be shown that the simulated light output is not necessarily needed for a qualitative and a quantitative estimation of the absolute neutron detection efficiency.
The detector was exposed to a ^{252}Cf source which yields fission neutrons. This isotope is needed, because the neutrons energy spectrum as well as the source activity are known. Ra-Be or Am-Be neutron sources cannot be used because the energy spectrum of the neutrons depend on many source parameters such as granularity of the source constituents and the distribution of the constituent grains within the source. A redistribution of the constituents by mechanical stress such as vibration or shock changes the alpha energy spectrum which leads to a change in the neutrons energy spectrum. This problem is being avoided by using a ^{252}Cf source. The sources neutron energy spectrum is shown in fig. 3.25. The half life of ^{252}Cf is 2.645 a[7]. ^{252}Cf is produced by neutron capture on ^{249}Bk at accelerators or reactors. ^{252}Cf decays mostly via α decay, 3.092% of the nuclei undergo spontaneous fission, producing 3.77 neutrons per fission on average. A californium source contains other Cf isotopes as well out of which ^{250}Cf contributes to the neutron emission, with a half life of 13.08 a and a spontaneous fission ratio of 0.08%. For "young" sources the neutron emission of ^{252}Cf is dominant. The isotopic composition of the source used for this calibration was 30.888% ^{250}Cf and 44.368% ^{252}Cf in percent of atoms, the rest does not emit any neutrons. At the

[7]The half life data and fission yield was obtained from the "Interactive Chart of Nuclides (Nudat2.6)" by the National Nuclear Data Center. Data retrieved 2012.
`http://www.nndc.bnl.gov/nudat2/`

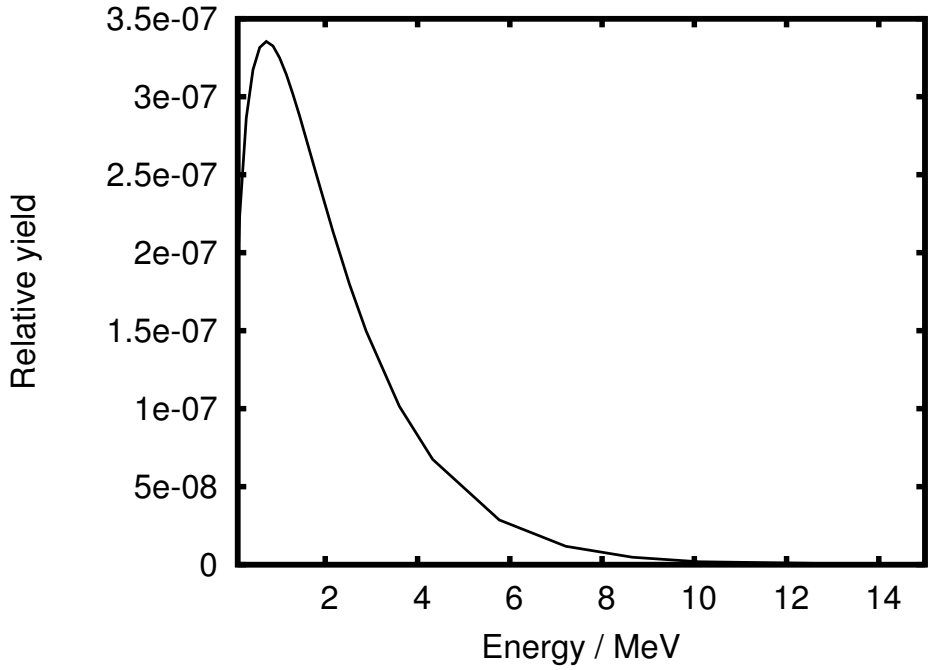

Fig. *3.25: ^{252}Cf fission neutron energy spectrum. Relative intensities given. Data from evaluated nuclear data files (ENDF) at* `www.nndc.bnl.gov/sigma/`*, library: JEFF-3.1 (Europe,2005)*

time of calibration, the source contained 27.84% ^{250}Cf and 26.563% ^{252}Cf. Weighting the fission ratios of the two nuclides, only 2.6% of all emitted neutrons come from fission of ^{250}Cf. Since the neutron energy spectrum does not differ much, the effect can be neglected in first order.
The absolute calibration was performed for the phase III detector. For all other detectors, the efficiency estimation was performed as described in section 3.9. The neutron calibration was performed with a source neutron flux of

$$\Phi_{cf} = 14,146 \pm 226\,(\text{syst.}) \pm 10\,(\text{stat.})\,\text{n/s} \tag{3.7}$$

for 43,200 seconds. The acquisition dead time was 36.18 % or 15,631.49 s. The first systematical error is determined by the precision of the absolute isotope fractions of the source which, the second systematical error is introduced by the decay of the source during the measurement. Since the first systematical error is very large compared to the second systematical error only the first systematical error is used. The statistical error is the result of the limited measure time. The solid angle for this calibration was $0.78^{+0.18}_{-0.14}\%$.
The neutron cut was applied according to the procedure described in section 3.6. The calibration scatter plot with the particle bands is shown in fig. 3.26. The

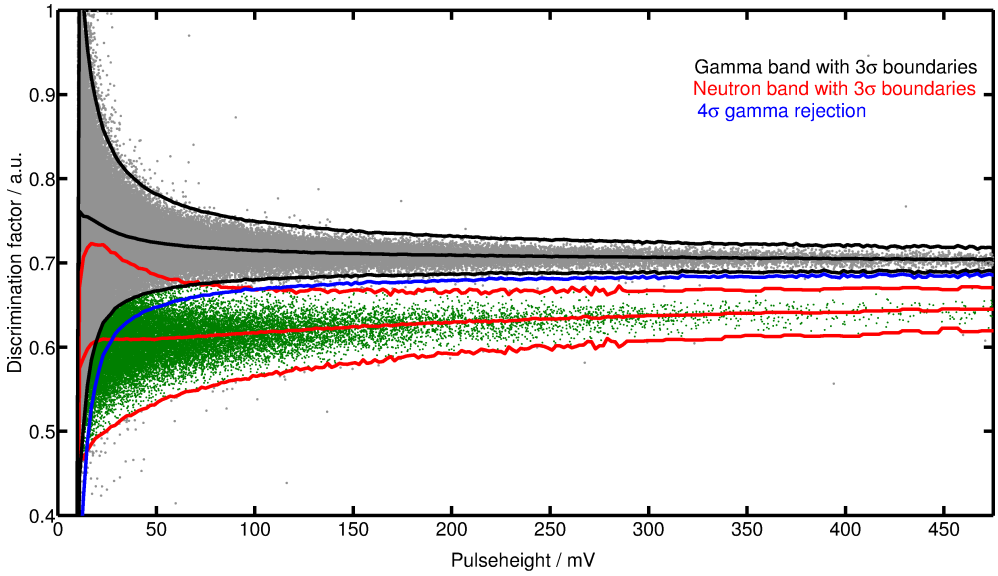

Fig. *3.26: Scatter plot of the ^{252}Cf calibration with 3σ boundaries of the neutron and gamma branches. The lower 4σ boundary of the gamma branch is drawn in blue. The green marked events pass the neutron cut. In this figure, only every 20th event is drawn.*

corresponding neutron spectra for the two different neutron cuts are shown in figure 3.27. The total dead time corrected efficiency in the recoil energy range

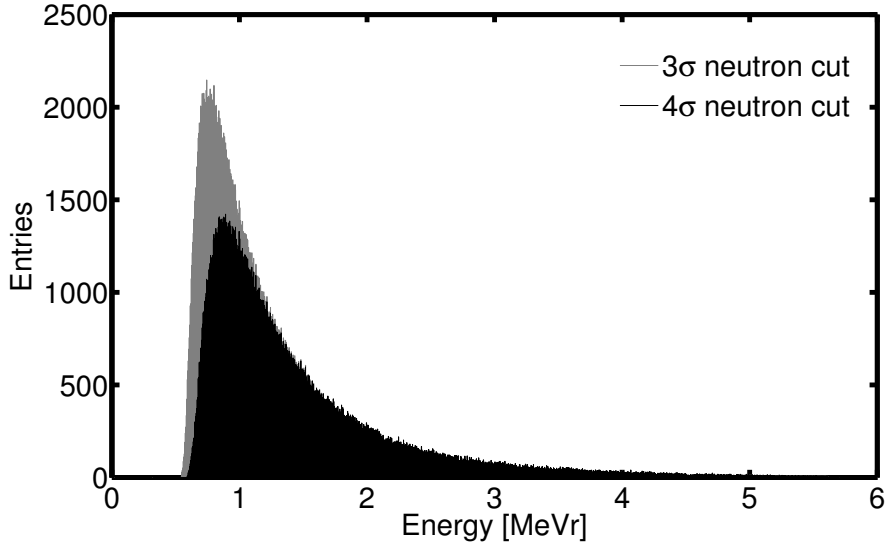

Fig. *3.27: Comparison of measured ^{252}Cf neutron spectrum for three and four sigma gamma rejection cuts.*

from 1.0 to 3.5 MeVr is

$$\mathrm{Eff}_{tot,ROI,3\sigma} = 8.09^{+1.93}_{-1.61}\% \tag{3.8}$$

for the 3σ cut and

$$\mathrm{Eff}_{tot,ROI,4\sigma} = 7.85^{+1.88}_{-1.57}\% \tag{3.9}$$

for the 4σ gamma rejection cut. The 3σ efficiency in the ROI can now be compared with the efficiency determined by the Geant4 simulation of

$$\mathrm{Eff}_{simu,ROI,3\sigma} = 12.3^{+3.1}_{-2.4}\%. \tag{3.10}$$

As expected the simulation overestimates the real value by approximately 4%, the values are almost compatible within their 1σ errors. The full neutron efficiency using the whole sensitive energy range up to the acquisition limits is

$$\mathrm{Eff}_{tot,fr,3\sigma} = 14.94^{+3.57}_{-2.99}\% \tag{3.11}$$

for the 3σ cut in the energy range from 0.62 to 5.62 MeVr and

$$\mathrm{Eff}_{tot,fr,4\sigma} = 11.85^{+1.85}_{-2.37}\% \tag{3.12}$$

for the 4σ gamma rejection cut in the energy range from 0.62 to 5.62 MeVr. The scatter plot calibrated for recoil energies with the energy acceptance limits is shown in figure 3.28. The 3σ full neutron efficiency can now again be compared

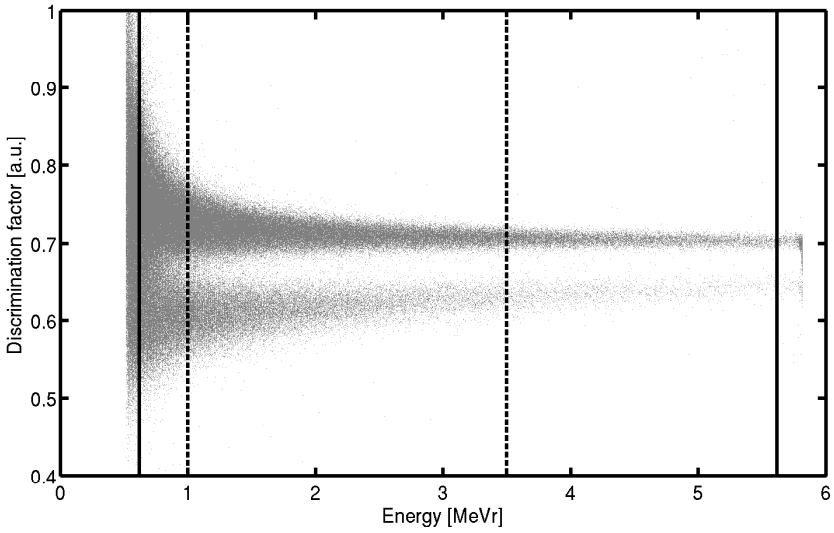

Fig. *3.28: Recoil energy calibrated scatter plot with energy acceptance windows for the ^{252}Cf calibration. Black is the full neutron acceptance, black dashed the region of interest. In this figure, only every 10th event is drawn.*

with the value from the simulation

$$\mathrm{Eff}_{simu,fr,3\sigma} = 18.4^{+5.0}_{-4.1}\% \tag{3.13}$$

which shows again that the simulation overestimates the real values by approximately 4%. The values are again compatible within the range of their errorbars. As a conservative approach, the lower simulated efficiency boundary will be used for the source neutron flux calculation. For the analysis of runs using the current (phase III) vacuum detector, the efficiency determined from the calibration is being used.
It is very important to note, that the efficiency is of course geometry dependent. For a precise determination of the detectors efficiency it must be measured as a function of energy and incident angle of the neutrons by varying the source position.
This efficiency must be multiplied by the solid angle coverage to calculate the neutron flux from the source.

3.11 4π detector concept: PIA@DODI

To further enhance the neutron detection efficiency and the solid angle, a concept for a 4π-detector was developed. The idea was based on the Tübingen liquid scintillator testing setup, a scintillator filled tank with dodecahedron shape which is observed by 11 photomultipliers, called DODI. This testing facility was built by

A. Hagen and D. Dietrich during their Diploma theses [5], [18]. By mounting the PIA device into the dodecahedron and filling the volume with gadolinium(Gd)-doped scintillator as used in the Double Chooz experiment, the emitted neutrons would be captured within this vessel. The mean free path for 2.45 MeV neutrons in mineral oil is roughly 25 cm, in Gd-doped scintillator slightly less. A capture on Gd releases several γ-rays with a sum energy of 8 MeV. The great advantage of this setup would be its extremely large solid angle coverage as well as it is impossible for the neutrons to escape the vessel. This would be equal to almost 100% efficiency compared to 10-25% in the NE-213 liquid scintillator (not regarding the neutron identification efficiency which is also expected to be better for the dodecahedron than for the NE-213 cells). Remaining background would originate only from cosmic muons and their induced showers. However, the Gd doped scintillator is extremely hard to obtain, therefore expensive and was not available in larger quantities so that geometries were discussed which need less scintillator. The performance of spheres and cylinders of Gd-doped scintillator in the center of the tank were simulated with Geant4 by C. Schmitt during his Diploma thesis [45]. The simulations show, that a suitable geometry such as half a cylindrical inner doped scintillator volume can yield a higher neutron detection efficiency as NE-213. The key property which must be optimized is the solid angle coverage. Any attempt to find a configuration which covers a large solid angle while having a neutron detection efficiency larger than NE-213 failed because of a volume limitation on the Gd doped scintillator of 10 L. Unless the dodecahedron can be equipped with a substantial amount of Gd-doped scintillator in order to cover either the full solid angle with an efficiency similar to NE-213, or cover less solid angle with a higher neutron detection efficiency, any transfer of the PIA device to DODI is not worth the effort.
Alternative liquids which have similar neutron detection capabilities such as $CdCl_2$ are similarly expensive and similarly hard to obtain to Gd-loaded scintillator.

Current situation

In the Phase III of the experiment, the type 3 neutron detector is mounted into the vacuum covering 32% of solid angle. A 4σ gamma rejection cut is used to identify neutrons. The total source neutron detection efficiency is 5%.

4 Measurements

"It is wrong to think that the task of physics is to find out how Nature is. Physics concerns what we say about Nature."

- Niels Bohr

The goal of this work is the reliable production and measurement of a high voltage and the identification of neutrons produced in a D(D,n)^{3}He fusion reaction driven by a pyroelectric ion accelerator. The expected neutron flux is in the order of 30 neutrons per second. In this section the measurements and analysis techniques will be explained and the search for a neutron signal will be discussed.
The improvements of the setup as triggered by the measurements will also be discussed in this section. The time in between two larger structural improvements of the setup, called Phase I to Phase III are discussed separately (see sections 2.2 and 3.17).
An extended discussion will follow the results, discussing the evidence for neutron production and the reasons for not reaching the expected flux.
In the end, possible future aspects aspects of this experiment are being discussed. A summary with concluding remarks will be given.

4.1 General measurement classes

The measurements can be classified into different groups for which the external conditions such as gas type, pressure, bias voltages and heating and cooling power are different. Heating and cooling power are in the region from 5-10 W for heating and 7-15 W for cooling adjusted to the respective setup. The pressure varies between lowest pressure that can be achieved in the system, where no remaining gas is present and high pressure or working pressure which is typically $5{\cdot}10^{-4}$ mbar unless stated different. This pressure corresponds to a true deuterium pressure of approx. 1.1 to $1.2{\cdot}10^{-3}$ mbar (see appendix G). The classes of different measurements are:

- X-ray run: X-ray runs are being used to optimize and check the high voltage and its polarity. A nitrogen atmosphere is applied at lowest pressure or working pressure, heating and cooling is supplied and the application of bias voltages is possible. The data recorded from the neutron detectors during X-ray runs can be used to measure neutron background.

- Neutron run: All data recorded is used to look if neutrons were produced in a fusion reaction. A deuterium atmosphere is applied at working pressure, heating and cooling is supplied and application of bias voltages to target or grid is possible.
- Background run: Due to the very low expected neutron flux, knowledge of the neutron background is essential. A nitrogen atmosphere is supplied at low pressure. Neither heating nor cooling is applied, therefore no high voltage is generated.
- Calibration run: This run is used to calibrate all the detector systems used. A nitrogen atmosphere is supplied at low pressure, no heating and cooling is supplied and no bias voltages are applied. The calibration runs are performed with one or more radioactive sources placed near the detectors. The calibration can be done for the neutron detectors and the X-ray detector with different sources.

Nitrogen gas instead of deuterium gas is used in X-ray runs for two reasons. After evacuation, the vacuum chamber is flushed with nitrogen in order to remove water from the interior. The atmosphere therefore is already nitrogen. If X-rays are measured, the neutron detector records background data. Any deuterium in the chamber may produce neutrons which falsifies the background measurement.

4.2 General data terminology

A single measurement, data set or run is always recorded at once and stored in one archive. Each run has an identification number which is used for run selection and time sorting purposes. Every run can be of any of the four classes specified above and contains all information related to that run. External parameters do not change during a run. A neutron run contains several temperature and high voltage cycles which will be explained later on.
Runs with similar or identical run conditions will be grouped for analysis to increase statistics, called analysis group. An analysis subgroup contains runs with similar run conditions and one specific identical parameter of interest. The analysis group contains the subgroup, of course. Subgroups are introduced to study parameter dependencies.

4.3 Measuring the high voltage

High voltage is the key parameter for any accelerator to work. In this work it is not only used to accelerate ions to the target, the same high voltage potential is also used to ionize deuterium from the gas phase. The high voltage must be higher than 15 kV which corresponds to the threshold of the fusion reaction, and it must exceed approximately 70 kV in order to allow the gas phase ionization

of deuterium. The high voltage polarity must be positive at the tip against the targets potential to accelerate ions towards the target. If the crystal is mounted with the Z^+ axis facing towards the target, it charges positive during heating. In this setup, neutron production is only expected during the heating cycle. In addition, the neutron flux is also expected to increase for higher voltages because the cross-section and the ionization probability increase. Therefore the optimization of the high voltage towards higher values for a longer time is desirable.
The high voltage is being measured by the X-ray spectrum as explained in section 2.3. If X-rays are observed, the high voltage on the crystal surface can be determined. As discussed in previous chapters, the X-ray production is an unwanted effect reducing the amount of charge available for ions to be accelerated towards the target. Therefore it would be preferable to minimize the charge losses by electrons. The consequence however would be the absence of X-ray radiation and therefore no high voltage information at all. Also when the X-ray intensity is very low, no high voltage can be measured. A minimal amount of X-ray counts in the detector is necessary per time bin to determine the high voltage.

Naming convention

If the voltage can be determined, a period of high voltage from a discharge to the next one is called a high voltage interval or high voltage cycle. Each high voltage cycle has a fixed polarity. There can be more than one high voltage cycle during a single heating or cooling of a crystal. Every discharge which resets the high voltage at the crystal triggers the start of a new high voltage cycle.

4.3.1 Dependence on measurement conditions

The correlations of the high voltage with the pressure and with the distance of the crystal to the target were investigated. Based on the high voltage charge model, no correlation of the distance between crystal and target is expected if the distance is larger than the crystal thickness. Measuring at distances smaller than the crystal thickness is not possible because it increases the risk of destroying the ionization tip upon mounting.
The pressure should influence the frequency of the discharges and a higher pressure should reduce the high voltage at the crystal.
At first the high voltage is measured as a function of pressure at a fixed distance. In the pressure region of interest no clear correlation was found. The results are shown in fig. 4.1. Then, the high voltage was measured as function of the distance between the crystal and the target. As expected, no correlation was found. This measurement is shown in fig. 4.2.
Any dependence on the gas type was neither expected nor seen by comparing runs with nitrogen and deuterium.

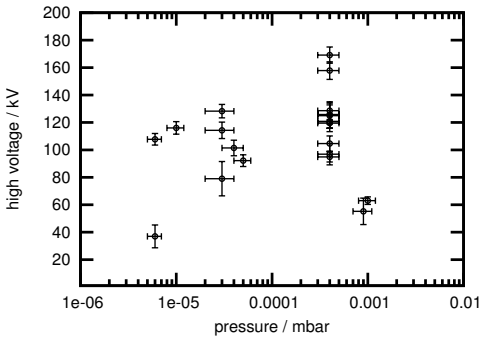

Fig. *4.1: Run parameters, high voltage as measured at specific pressures. Distance from tip to target fixed, 12 cm.*

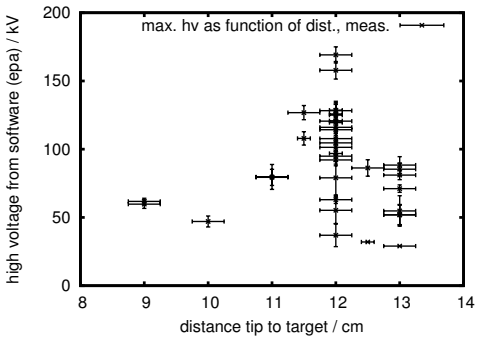

Fig. *4.2: Run parameters, the distance from crystal to target vs. the high voltage determined by EPA.*

4.3.2 Reproducibility

A high voltage of at least 70 kV is necessary to ionize deuterium. A voltage of at least this value, must be generated each time the crystal is being heated or cooled, and shall maintained for a time as long as possible. The high voltage production can be modified by adjusting the heating and cooling power for a setup. In every setup, high voltage testing was performed at low and high pressures during designated X-ray runs. The results of a successful X-ray run is shown in fig. 4.3. It

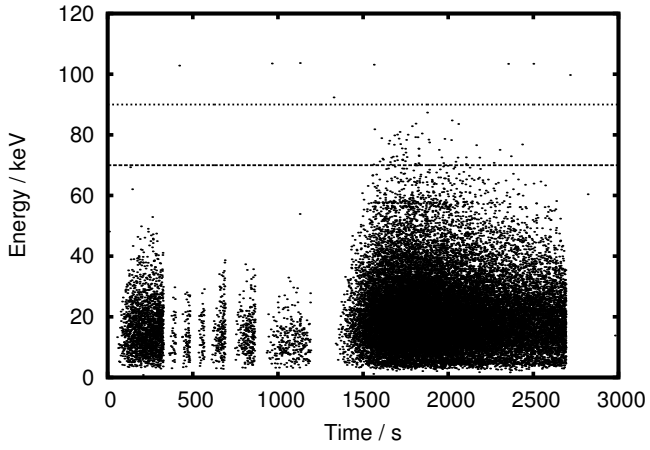

Fig. *4.3: Time vs. X-ray energy. Successful high voltage production above 70 kV. The horizontal lines indicate 70 k(e)V and 90 k(e)V.*

could be shown that it is possible to maintain voltages above 70 kV for more than 15 minutes. However the exact time span cannot be predicted since a discharge can happen at any time. The reproducibility could be adjusted to 825±125

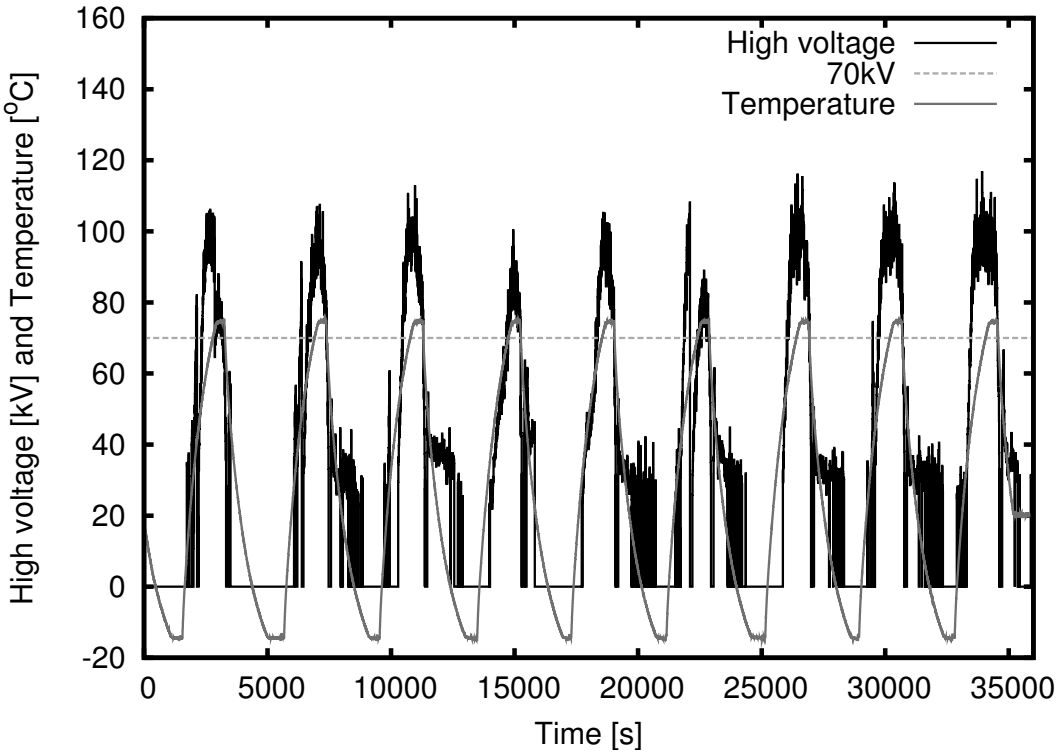

Fig. *4.4: High reproducibility of the high voltage, in every thermal cycle the necessary high voltage is reached.*

seconds above 70 kV for every thermal cycle based on the last 18 thermal cycles recorded during this work. This corresponds to a high voltage above 70 keV for 18% of the whole run time. This is the upper limit of what was achieved during this work. The fraction of run time above 70 kV is in the order of 5-20%.
The reproducibility of the high voltage for a given setup is very good.

4.3.3 Polarity determination

From recorded high voltage data the polarity can also be determined as described in section 2.3.5. It can be determined by comparing the fluorescence lines during heating and cooling. In principle, a polarity determination is only necessary once the crystal was removed and built in again, to avoid errors. An example of the X-ray spectrum showing fluorescence lines is shown in fig. 4.5.

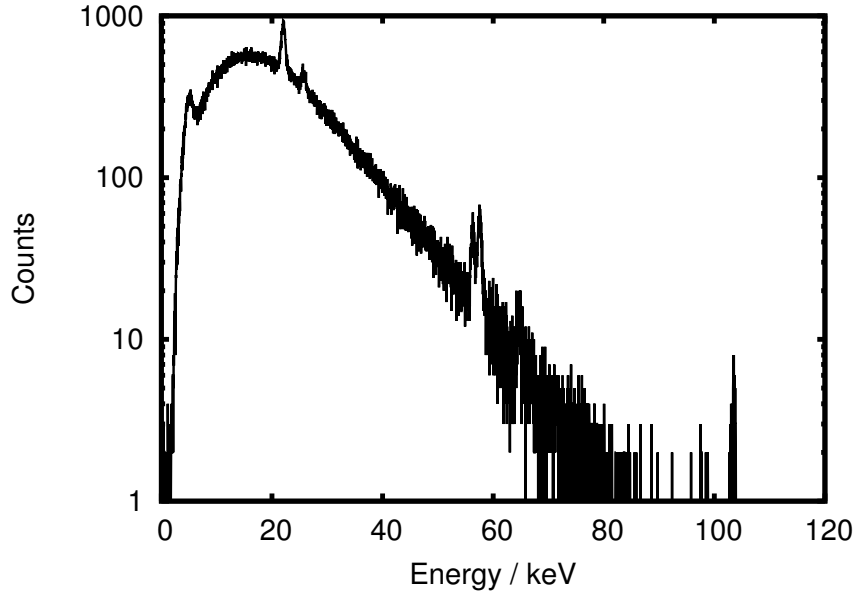

Fig. *4.5: X-ray energy spectrum with silver and tantalum fluorescence lines used for polarity determination.*

4.3.4 Correlation between high voltage and temperature change

If the high voltage cannot be measured, because the X-ray statistics is too low and most of the charge available is being converted to ions, one has to find different ways to determine whether the crystal is charged or not. An variable that can always be measured is the temperature of the crystal as well as the corresponding temperature change.

If the high voltage can be related to the temperature or the temperature change, measuring the high voltage directly would not be necessary any more. A map shown in fig. 4.6 illustrates how frequent the temperature change and the high voltage could be determined within a several runs. It describes how often these conditions ocurred within the runs. Map 4.7 shows how frequent the temperature change and the high voltage could be determined for neutrons. It shows, how the neutrons are distributed within this 2D parameter space. To see if any of those 2D parameter combination results in enhanced neutron production the two scattermaps must be divided.
However, both pictures show only times or neutron events for which both parameters, high voltage and temperture change could be measured.

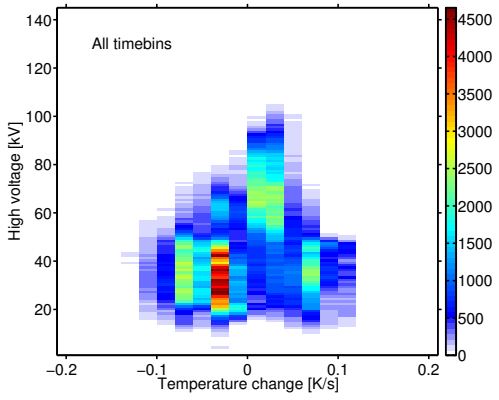

Fig. *4.6: Temperature change vs. high voltage for all* ***times*** *the determination of high voltage is possible, exemplary runs.*

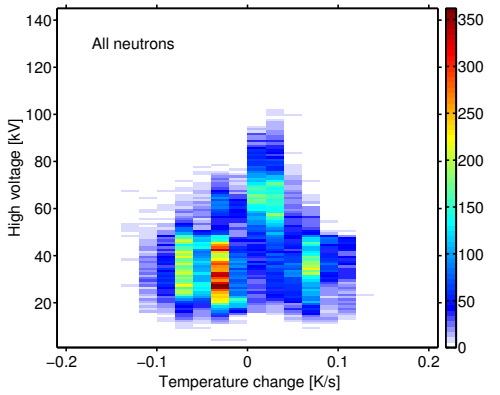

Fig. *4.7: Temperature change vs. high voltage for all* ***neutrons*** *for which the determination of high voltage is possible, exemplary runs.*

The time bins and neutron appearing in the intensity maps are only a small fraction of all available data, since most of the time no high voltage can be determined. What can be seen is, that there are temperature change regions where the high voltage is highest. These intensity map do not show any information on the polarity of the high voltage. The high voltage polarity should correspond to the heating or cooling cycle, which also means positive or negative values of the temperature change.
Splitting the neutron intensity map intp positive and negative polarities reveals however that the polarity laps into the wrong thermal cycle. This is expected, of course, since the high voltage on the crystal surface does not switch the polarity instantaneously if the temperature change switches from heating to cooling or vice versa. This is corrected for in the intensity maps shown in figs. 4.8 and 4.9 which

are now correctly splitted into polarity cycles. In fig.4.8 appear entries at negative temperature change which belong to the positive polarity as the majority of points of positive temperature change. The same effect can be seen in fig.4.9 but for negative polarity. It was found that the highest voltages at positive polarity,

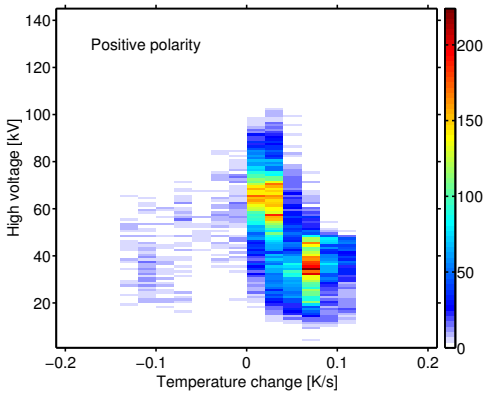

Fig. *4.8: Temperature change versus high voltage for all neutrons in appearing in* ***heating*** *cycles.*

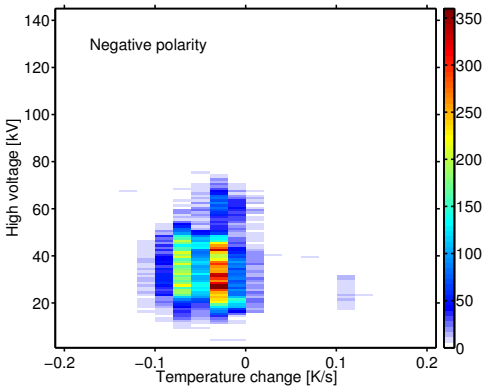

Fig. *4.9: Temperature change versus high voltage for all neutrons in appearing in* ***cooling*** *cycles.*

which in this run is needed to produce neutrons, occur at temperature changes between 0.02 to 0.05 K/s. The first order approximation, splitting the run into regions of positive temperature change and negative temperature change, can be a useful tool to split an analysis group or subgroup into parts where neutron production is expected or not. The neutron rates for each temperature change bin can also be compared which will be done in the temperature change histogram, defined and introduced in section 4.5.1.4.

4.4 Measuring neutrons

The neutrons are being measured by the detectors installed in the surrounding of the experiment. The neutrons are being selected from the raw data of all detectors and aligned to all correlated parameters which are available. These are high voltage, polarity and temperature. They must be determined and segmented into regions where neutrons are expected to be produced and regions of background measurements.

For most of the setups, the neutrons are expected to be produced in the heating cycle during which the crystal is charged to positive high voltage. Therefore the neutrons measured in the cooling cycle where the crystal is charged to negative polarity is considered to originate from neutron background. Since the high voltage and its polarity cannot be measured at all times, every run is segmented into heating and cooling cycles at first.

4.4.1 Heating and cooling

The standard temperature regulation uses two temperature set points, a lower and an upper value. The temperature is ramped up to the desired upper temperature value, then after wards cooled to the lower temperature value. For this operation mode, no temperature regulation is required. The temperature set points for a single run are stored in the temperature logfile. This logfile contains all data related to the continuous temperature measurement such as set points, regulation parameters and timestamps. By looking at the temperature set values, the run can be splitted into periods of heating and periods of cooling.

A temperature cycle is defined as a time span within a single run, starting at a minimum or maximum in temperature corresponding to the respective temperature set points. There exist several temperature cycles within one run. Due to the delay of the real temperature change to the applied heating or cooling, the set value is always exceeded. Therefore the end of the temperature cycle is given by the second crossing of the set point, the temperature cycle is shifted by the delay.
If for example the set point is 50^oC, the heating stops and cooling starts when the crystal reaches 50.3^oC which covers also the uncertainty of the temperature sensor (see section 2.4.4). The temperature still rises for the delay time. The temperature then starts to drop and crosses the upper set point again, now from above. This time marks the end of the heating cycle and is stored for further use. All temperatures and temperature changes throughout a run are recorded for each second. This information later on is used to calculate neutron rates for specific temperatures or temperature changes.

In principle, all neutrons measured in a run can be sorted into the thermal cycles, the ones that are expected to produce neutrons and the ones in which no neutron production is expected. Unfortunately this is only an approximation. One has to regard the accumulated charge on the crystal if the experiment switches from heating to cooling and vice versa. Any high voltage potential which is available at the crystal surface when the heater or cooler is switched must first be compensated before a high voltage of the opposite polarity can built up. Therefore the end of temperature cycles does not correspond to the end of the polarity cycles and must be extended until the crystal is completely discharged.
High voltage cycles whose start and stop values are completely within a temperature cycles, e.g. due to a discharge, must not be treated as they have the same polarity than all other high voltage cycles in the same temperature cycle. The new cycles are temperature cycles corrected for polarity. They can now be called polarity cycles or cycles in which neutrons are expected or not.

For a better understanding, see fig.4.10. The high voltage cycles are simplified as boxes, the temperature cycles as zigzag line. This illustration shows the case if there exists only one polarity cycle for each temperature cycle. As described

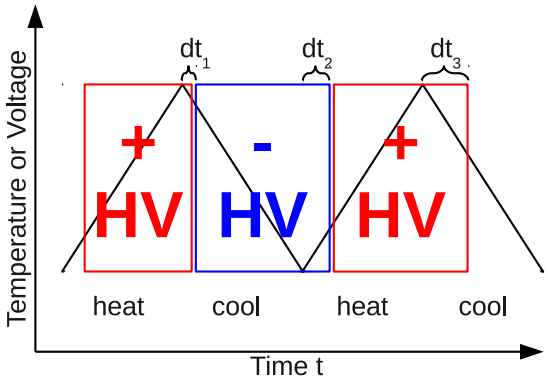

Fig. *4.10: Time correction dt_1-dt_3 for the high voltage polarity cycles. The high voltage must first be compensated unless the crystal charges with the other polarity.*

above the high voltage cycles can also lie completely within a temperature cycle. The following figure 4.11 shows the case where not all temperature cycles must be corrected for the polarity and some high voltage cycles start and end within a temperature cycle.

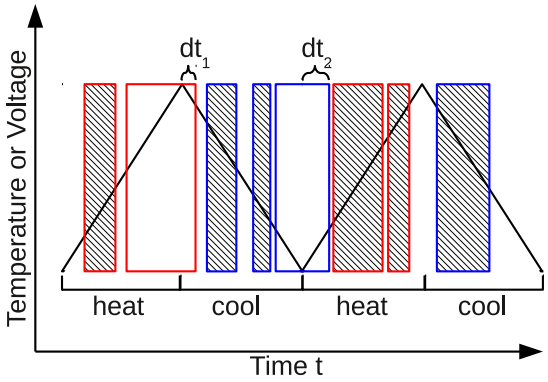

Fig. *4.11: Time correction for the high voltage polarity cycles. The high voltage cycles which lie completely within the temperature cycle are marked with a black hatching. The cycle length must be corrected only for the cases where the high voltage cycle and the end of the temperature cycle overlap.*

4.4.2 Neutron parameters

The times neutrons are measured are sorted by their occurrence in the polarity cycles which results in two neutron rates for each run: neutrons when expected, R_e and neutrons when not expected, R_n. Both rates are gross rates and contain the neutron background as well as any misidentified gammas, the so called gamma leakage ζ. They differ only in the rate of neutrons produced by the source or a correlated increase of the gamma leakage.
For each neutron all other parameters are stored and can be used for further analysis:

- Identification number and time:
  The neutron identification number contains the information in which run the neutron was measured, in which detector the neutron was seen, at which time from the start of the run the neutrons was recorded and which was the event number given by the DAQ.
  A typical information would be, that a neutron was produced during run number 122, seen in channel 1 of the DAQ, measured at second 3601 of the run, it was the 90025th event recorded during that run and was the 180th neutron identified during that run.

- Energy:
  The neutrons energy information is being stored as the primary pulse height in millivolt so that a recalibration of the detector is possible. The calibrated energies can be stored as well.

- High voltage:
  If it can be determined, the high voltage information is assigned to every neutron. It is set to zero otherwise.

- Temperature and temperature change:
  Temperature change and the absolute temperature can be determined as long as temperature data is available. The temperature change is defined as the five second average time derivative of the temperature.

- Ioncurrent:
  In measurements where the ioncurrent on the target is being recorded, the neutrons will also be assigned the corresponding ioncurrent value. Neutrons are expected to be produced when ions are being accelerated towards the target, which means an ion current can be measured. The current changes polarity if electrons are being accelerated towards the target in which case no neutron production is expected.

- Rate and deadtime:
  The data acquisition system is very slow, introducing a dead time. To study the influence of the dead time on the measured neutron rate, the acquisition rate and the corresponding dead time is being stored for each neutron as well. In times of high voltage, the acquisition rate increases when gammas leak into the detector. This is also the time period where neutrons are expected to be produced.

Systematical or random errors are treated the same as recommended by the Guide to the Expression of Uncertainty in Measurement (GUM) [40], due to the fact that systematical errors can always be reduced but not without introducing new random errors. The systematical errors in this work will shortly be discussed in the following. Based on four main measurement quantities, neutrons, X-ray, temperature and time, the systematical error for each component must be determined. The dominant systematical uncertainties of the neutron rate measurements are the calibration uncertainty and solid angle uncertainty. The calibration uncertainty as discussed in chapter 3, section 3.8 relies strongly upon the accuracy of the Compton edge positions. The fit parameters and the energy resolution are being used to determine the systematical error. The X-ray data systematical errors are dominated by the energy calibration and the endpoint determination. The systematical error of the temperature measurement is 0.3 K as determined by using different thermometers at the same time. The times systematical error is one second as it is the bin width used for all measurements.

4.4.3 Neutron background

The neutron background is measured in dedicated background runs as specified in section 4.1. The rate obtained for these runs is being subtracted from the corresponding neutron runs. The background rate for the phase three detector is 0.035 ± 0.001 n/s in the ROI.
The neutron background originates from intrinsic radioactive contamination by uranium and thorium as well as from hadronic showers induced by cosmic muons.

4.5 Analysis

The absence of a clear neutron signal above background made the development of a detailed and precise analysis necessary. By looking for correlations between neutrons and various parameters, indications of neutron production can be evaluated. Thus, the sensitivity on the occurrence of an additional neutron flux can be improved.

The analysis can be performed for a single run, analysis groups or analysis subgroups.

4.5.1 Analysis tools

The analysis tools used to look for differences between times in which neutrons are expected and times in which no neutron production is expected are described in this section. These tool will help to prove or disprove the production of neutrons for single runs or analysis groups.

4.5.1.1 High voltage correlation

For those neutrons for which the corresponding high voltage can be obtained, a histogram of the neutrons high voltages can be made. The resulting histogram then is normalized to the time span the respective high voltage occurred. This results in the observed neutron rate as a function of high voltage. It is expected that the plot rises towards higher voltages when lots of neutrons should be produced. Such a plot is shown in fig. 4.31.

4.5.1.2 Temperature change histogram

As described above, the high voltage cannot be measured at all times. Therefore the high voltage was related to the temperature change in section 4.3.4. It shows that there are temperature change regions in which neutrons are preferably produced and other where the neutron production should be zero. A histogram of the temperature change for all neutrons seen is made and normalized to the total time this temperature change happened during the run. The result is an average neutron rate per temperature change which should increase in regions where neutron production is expected. Such a temperature change histogram is shown in figure 4.30.
These rates are gross rates, of course, they do not represent a rate directly originating from the source. Therefore the background rate must be subtracted. However, the background is being subtracted for each temperature change bin, resulting in a correlated error for all bins. The error from background subtraction is represented by an offset of the net rate. It is separated from the rate error and plotted as grey shaded region.
These rates can of course be converted into the corresponding source neutron flux by applying the solid angle and the combined detector efficiency for all detectors used.
According to section 4.3.4, these temperature change histograms can also be splitted in regions where neutrons are expected and regions where no neutrons are expected. The mean values of the source neutron flux for these regions can be compared and the evidence for neutron production can be quantified. The error

from background subtraction cancels out in this case.
The disadvantage of this tool is, that the separation of the regions does not yet regard the exact high voltage polarity. For that reason the polarity cycle analysis was created.

4.5.1.3 Polarity cycle analysis

The neutrons are sorted into the polarity cycles and normalized to the amount of time the cycles cover. On these neutron rates a background subtraction can be performed, the source neutron flux can be calculated.
The resulting rates can be compared dependent on which high voltage polarity the neutrons are expected.

4.5.1.4 Time clustering

Time clustering of neutrons describes the fact that producing neutrons is much more likely for higher voltages since the reaction cross-section rises very steep. This means, in times of very high voltage the most neutrons are expected to be produced and the appearance of neutrons should cluster in time accordingly. A time binning of 30, 60 or 120 seconds can be chosen, and the bins can be aligned to high voltage or the temperature. A homogenous time distribution of neutrons throughout a run is a strong argument against the presence of fusion neutrons. How neutrons are distributed within an exemplary run is shown in fig. 4.12. An example how time clustering is expected to look like was obtained from the experiments at the accelerator and is shown in section 2.5, figure 2.35.

4.5.1.5 Ion current analysis

The measurement of the ion current was introduced to see if positively charged ions (preferably D^+) are hitting the target. The ion type can not be determined. From the measured ion current, also the amount of expected fusion neutrons produced can be calculated, assuming the current consists entirely out of D^+ or D_2^+ ions hitting the target. An ion current up to a few ten nA was expected. The target or the grid, depending on which the ion current is being measured, is connected to one pole of a DC power supply, the other pole is drawn to electrical ground. The current which the power supply must compensate because charge is deposited by ions or electrons is being measured. A bias on both the grid and the target simultaneously was not tested.
To determine the ion current on the grid or the target, a digital voltmeter was used. A pico amperemeter was not available. The used digital voltmeter has an internal resistance of 240 MΩ in the mV range and 11 MΩ in the V range. If connected in series with the bias voltage power supply, it is possible to measure the current on the internal resistance which in this case means that a 1 mV reading

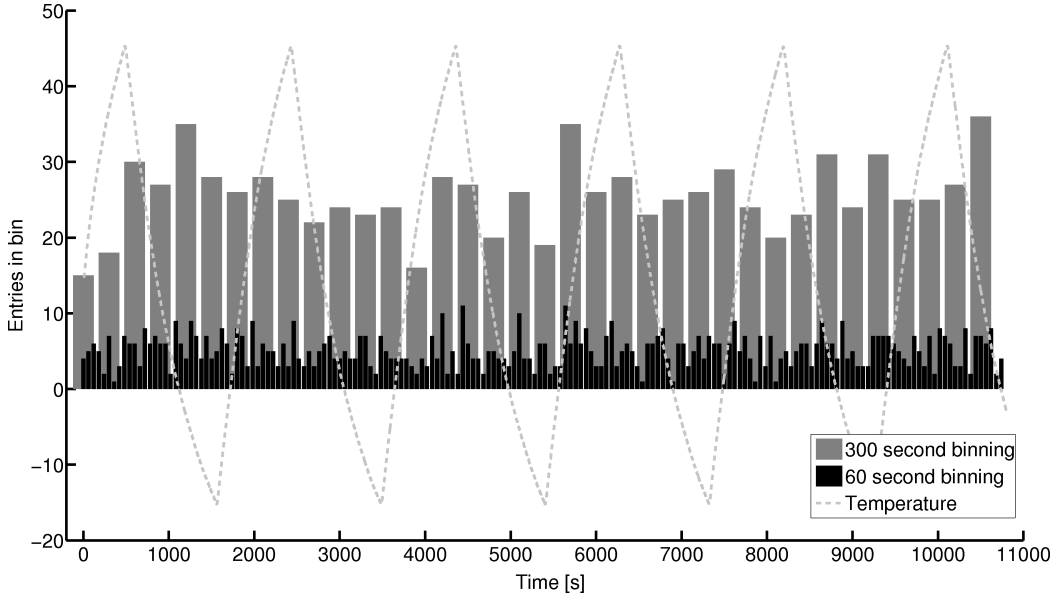

Fig. *4.12: Neutron time clustering example with two different binnings.*

corresponds to $4.1 \cdot 10^{-12}$ A, while 0.001 V correspond to 0.09 nA. The voltmeter response was checked with a ultra high precision current power supply. The digital voltmeter was found to shut down due to over voltage protection if the crystal discharges. To suppress this effect, TVS diodes have been installed whose breakthrough voltage can be selected according to the current bias voltage. As the bias voltage exceed the TVS breakthrough voltage in case of a discharge, the voltmeter is being bypassed to avoid over voltage protection lock in the voltmeter. The circuit diagram is shown in fig.4.13. The TVS diodes have very fast response times, faster than 2 ns. The bias voltage shifts the current reading by a fixed value which is the reference zero. Any current is measured to this reference zero. The reading offset shifts to a maximum constant value. The reading is not interrupted and can normally be continued if the discharge is finished. Upon a TVS breakthrough, current reading is no longer possible since only the maximum value is being read due to the fact that the power supply is shortened and already delivers maximum current which is limited to 10 mA. This behavior was tested and is shown in figure 4.14. Using the TVS diodes increased the run stability drastically, however did not solve the shutdown problem completely. Accidental over voltage shutdowns of the voltmeter still occur in rare cases which then can be solved by a reset of the device.
The measured ion current shows large fluctuations and noise especially when the source is compensating electrons hitting the vacuum chamber (ground). The reading quality increases if a bias voltage is applied. This bias voltage is identical

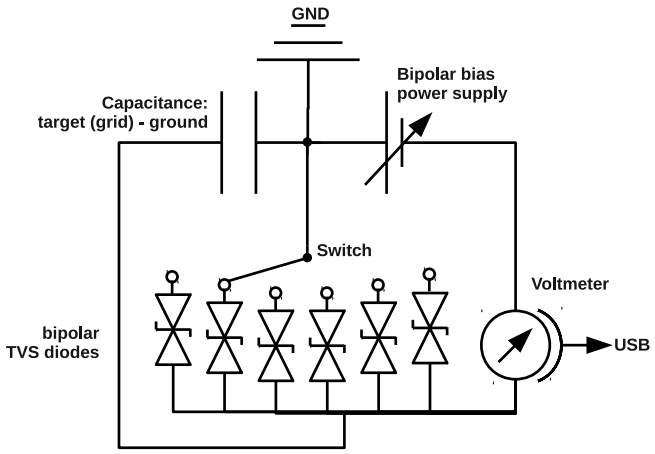

Fig. *4.13: Circuit diagram of ion current reading for either of the two cases: target or grid. The bipolar TVS diodes have different breakthrough voltages to cover the entire bias voltage range. The voltmeter reading is proportional to the ion current.*

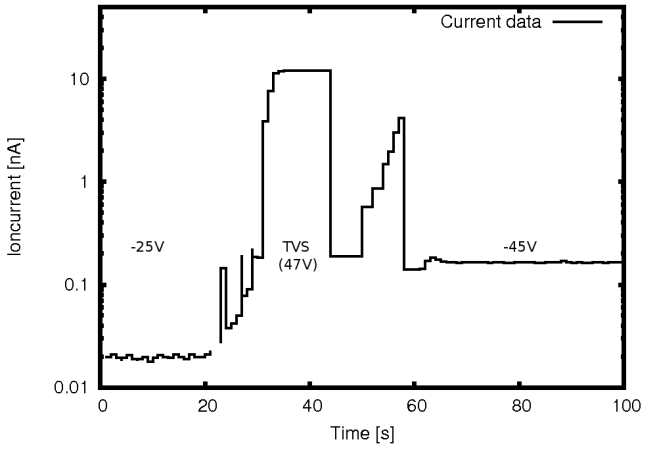

Fig. *4.14: TVS diode testing with a breakthrough voltage of 47 V. Starting bias voltage was -25 V and it was ramped up until the diode broke through. In the end the bias voltage was set to -45 V, slightly below the breakthrough voltage. Clearly visible is the changing current offset (actual zero) for different bias voltages.*

to the voltage used to suppress secondary electron emission from the target. If the current is measured on a bias voltage, the reading has a fixed offset which corresponds to the current through the voltmeter. If the capacitor represented by the target or the grid is charged to 100 V, this current is in the order of 0.5 nA. The leakage current of the source is unknown, however also expected within this order of magnitude.
The dependence of the leakage current on the temperature was checked. Two exemplary measurements are shown in figs.4.15 to 4.18, where the vacuum pressure is very low and the crystal is not heated or cooled. The temperature just fluctuates due to ambient conditions. The leakage current plotted against temperature

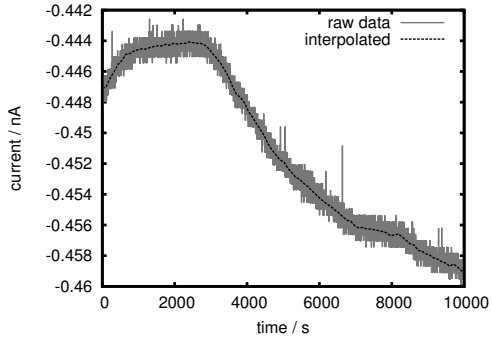

Fig. *4.15: Temperature dependence check, exemplary run 1, current data.*

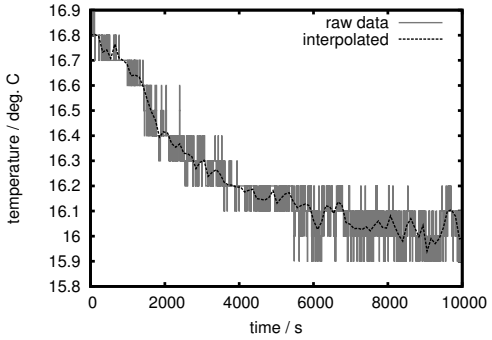

Fig. *4.16: Temperature dependence check, exemplary run 1, temperature data.*

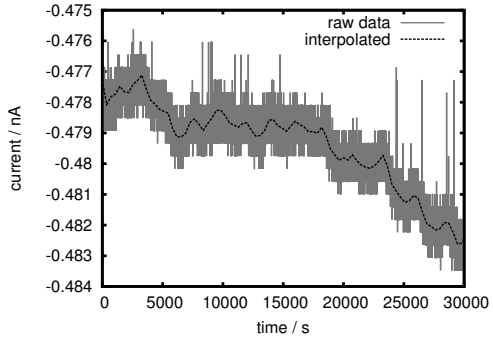

Fig. *4.17: Temperature dependence check, exemplary run 2, current data.*

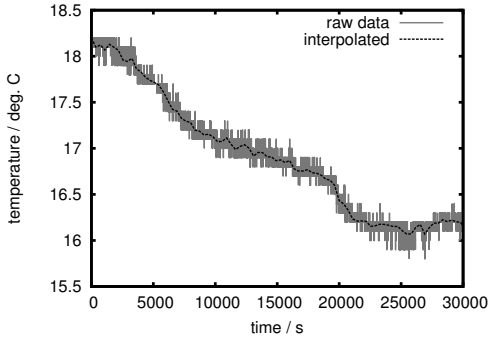

Fig. *4.18: Temperature dependence check, exemplary run 2, temperature data.*

from this data shows a correlation which is fitted for an increase in temperature

in fig.4.19. This correlation indicates that the offset must be corrected at all

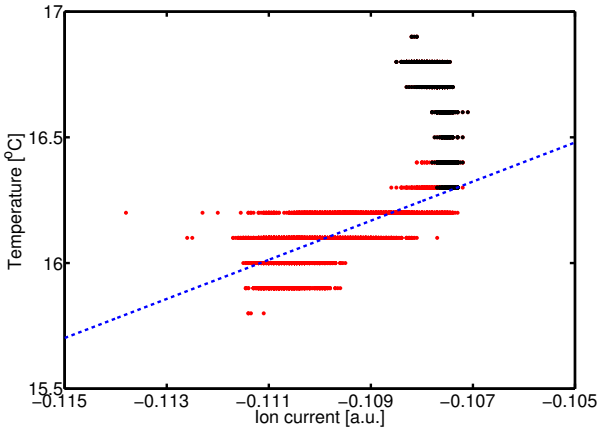

Fig. *4.19: Temperature correlation with ioncurrent. Same data as used in figs. 4.15 and 4.16. The black circled dots correspond to the first 2500s where the temperature rises. The correlation function for the decrease in temperature is fitted with a line.*

times during a long measurement. However the deviation from the average value is approx. 40 pA within 0.8 K for run 1, and 30 pA within 2 K for run 2, during 3 h and 10 h of data taking. If a higher precision is needed, the ion current measurement can be corrected at each time by determination of the corresponding offset current value. As the ion current measurement is mainly used for a qualitative check, this temperature dependence contributes to the systematical error of the ion current measurement and is not discussed further in the analysis.
Secondary electron emission and field emission of electrons cannot be distinguished from real ion current under normal conditions, because the signal looks the same.
The ion current measurements were always performed in addition to all other measurements during phase II and III. Since a reliable shutdown prevention failed, most of the ion current information was not used for analysis. It was used to qualitatively check if there are any ions reaching the target.
A typical ion current measurement shows large fluctuations in cycles where the crystal is charged negative, emitting electrons from the tip and the mounted copper disc. The current is several orders of magnitude higher than during the ion acceleration cycles.
Results of a typical ion current measurement is shown in figure 4.20 where electrons are being observed during cooling, carrying charge away from the crystal so that no high voltage can built up, and ions in the heating cycle which nicely correlate with the high voltage as expected. There are lots of electrons being

emitted by the wall and the grid due to field electron emission as well as during heating, hitting the crystal where no current can be measured. An enhanced version of the ion current measurement is shown in fig. 4.21.
The measured ion current on the target is a factor of 5-10 below expectation, which can either be explained by not covering the assumed solid angle for the ions by the target or by the ionization being too inefficient or the charge loss by electrons is to large. All possible explanations can be accounted for the lack of neutrons seen in all the measurements.
The Phase III setup was designed to measure even lower neutron fluxes in order to see if the ion current measurement is valid. It is proposed in this work that

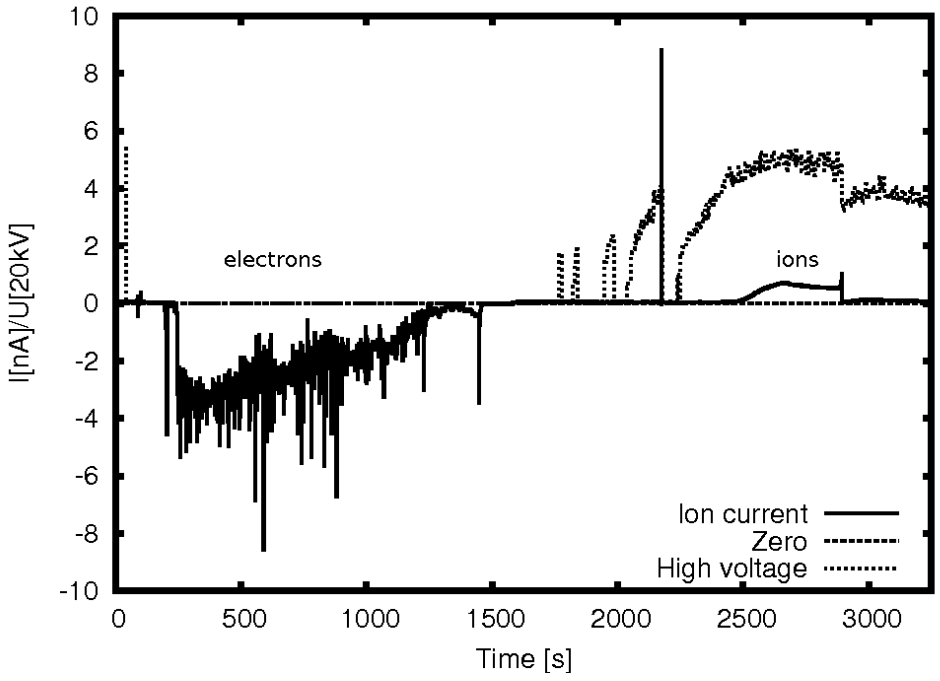

Fig. *4.20: Ion current measurement for one temperature cycle, with high voltage. During cooling, electrons are being accelerated to the target, during heating ions are accelerated to the target. The measured high voltage levels are also shown in the figure.*

the internal geometry must again be checked, it is recommended to reduce the probability of electron emission towards the crystal upon positive high voltage. Therefore the internal geometry parameters such as the grid radius and the curvature radii of the metal surfaces must be adjusted in order to reduce the field strengths at metal surfaces. Surface coating with materials having larger work functions should be considered as well.

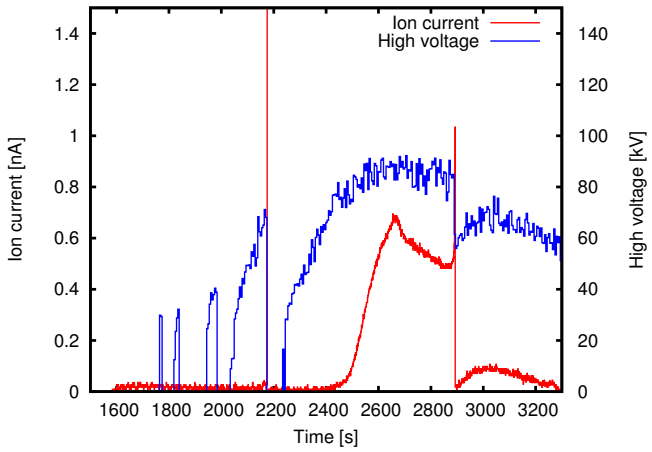

Fig. *4.21: Ion current measurement for one temperature cycle, with high voltage. Same graph as in fig.4.20 however zoomed in.*

As specified above, the ion current reading cannot distinguish between field emission and real ion current. If the target is therefore operated within a Faraday cage, field emission cannot happen on the target where the current is measured. By grounding the grid, if forms a Faraday cage with the surrounding vacuum chamber.

4.5.1.6 Deadtime correction

The dead time by the DAQ is corrected for in run data by monitoring the acquisition rate. Every neutron measured is weighted by the dead time upon the neutron rate calculation which is the same as dividing the amount of neutrons by the live time, the time the DAQ was recording.

4.5.1.7 Gamma rejection analysis

As the X-ray energies reach values of approx. 150 keV, the photons of the Bremsstrahlung can also be seen in the NE-213 neutron detector. Those X-rays can leak into the acceptance region of the neutron cut falsifying the neutron signal. To avoid low energetic X-ray photons to fall into the neutron selection region, the lower neutron cut boundary is set to 0.236 MeVee which is well above 150 keV and corresponds to a neutron deposited energy of 1.0 MeVr. The following pictures will illustrate how the neutron acceptance region is being influenced by Bremsstrahlung showing two scatter plots, one for a time period without Bremsstrahlung production 4.22 and one for a time period with high voltage 4.23. Without high voltage the recorded gamma events fill the whole energy

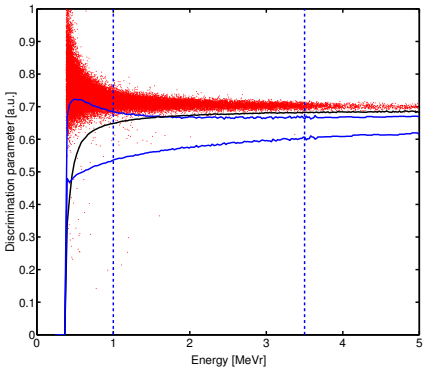

Fig. *4.22: NE-213 data scatter plot during a time period without high voltage, no X-rays were produced.*

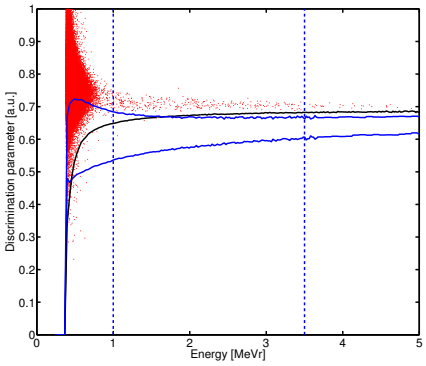

Fig. *4.23: NE-213 data scatter plot during a time period where high energetic X-ray radiation is being produced.*

range up to an neutron recoil energy equivalent of 5 MeVr. If a high voltage is present, only gamma interactions caused by Bremsstrahlung are recorded at low energies, because they occur so frequent that almost every trigger is released by a low energetic photon interaction. The large dead time causes high energetic events to die out, affecting neutrons and high energetic gammas. A comparison of the two energy (here again pulse height) spectra is shown in fig. 4.24. The

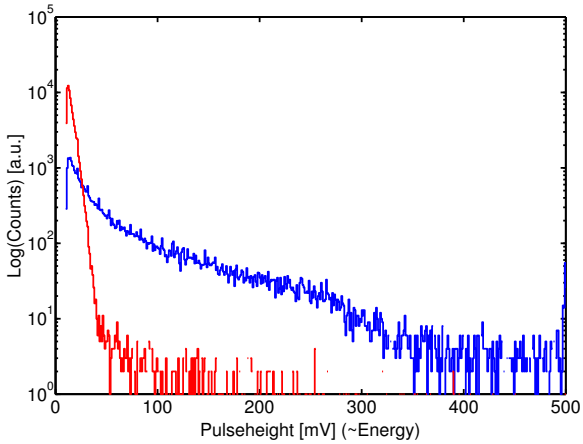

Fig. *4.24: Comparison of the energy spectra for data dominated by Bremsstrahlung and normal data.*

signals induced by the Bremsstrahlung can be removed completely with a more conservative energy threshold on the neutron cut. It cannot be applied after the data is taken, it must be applied to the hardware trigger (see section 2.4).

To further check the dependence of gamma leakage on the neutron cut, the neutron data must become dead time independent which is the same as acquisition rate independent which increases when the voltage goes up. In theory, the fraction of gammas leaking into the neutron band is being rejected and should be independent of the acquisition rate.
To check this, the gamma rejection of the neutron cut was varied. Going from a 4σ gamma rejection cut to a 5σ rejection cut does significantly remove gamma contribution however not hurting the neutron distribution by a very large factor. The 3-7σ gamma cuts are plotted against the 3σ neutron band boundary from the calibration scatterplot in fig.4.25. Increasing the gamma rejection from 3 to 5σ

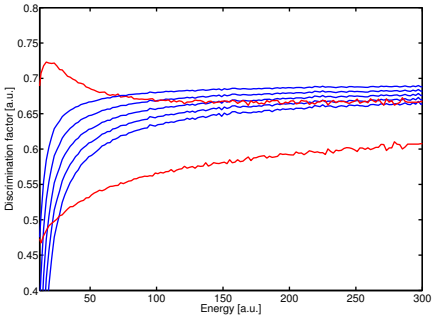

Fig. *4.25: Gamma cut boundaries, 3-7σ in blue, and the 3σ neutron band boundaries in red.*

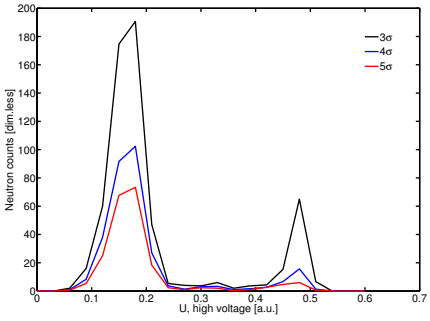

Fig. *4.26: Neutron sorted into the high voltage bins which can be correlated to the dead time. The different histograms show the distribution for different gamma rejection levels.*

decreases the neutron cut efficiency in the ROI by 21% or a factor of 5, however increases the gamma rejection capability by a factor of 110.

To correct the neutron rates for dead time, all measured events accepted by the neutron cut were sorted by their corresponding dead time which increases when the voltage U goes up. The neutrons selected with a certain gamma rejection sorted into the histograms are depicted in fig.4.26. If the whole excess seen at high voltages is only caused by gamma leakage, the ratio of two histograms must remain constant, independent of the dead time. The total measured neutron rate (Acquisition rate dependent = voltage dependent) as shown in fig. 4.26 is

$$T(U) = N(U) + B + \zeta_{cut} \cdot AR(U) \tag{4.1}$$

where T(U) is the total measured rate, N(U) is the actual neutron rate, B is the neutron background rate by intrinsic radioactivity and Muon induced neutrons,

AR(U) is the Acquisition rate and ζ_{cut} the gamma rejection level. The last term corresponds to the gamma leakage. Normalization to the acquisition rate results in the following equation:

$$\frac{T(U)}{AR(U)} = \underbrace{\frac{N(U)}{AR(U)}}_{\substack{\text{N=0, no contrib.}\\ \text{N(U)>0 exp. for}\\ \text{high U}}} + \underbrace{\frac{B}{AR(U)}}_{\substack{\to 0\\ \text{exp. for}\\ \text{high U}}} + \underbrace{\zeta_{cut}}_{\substack{\text{constant}\\ \text{fraction}}} \tag{4.2}$$

The neutron term is unknown, the T(U)/A(R) can be measured and ζ_{cut} can be varied by going from 4σ to 5σ.
The ratio of two such histograms were all events passing the neutron cut are sorted in as shown in fig. 4.26, for all data acquired with the detector of phase III is shown in figure 4.27. The acquisition rate is completely dominated by gamma rate. The

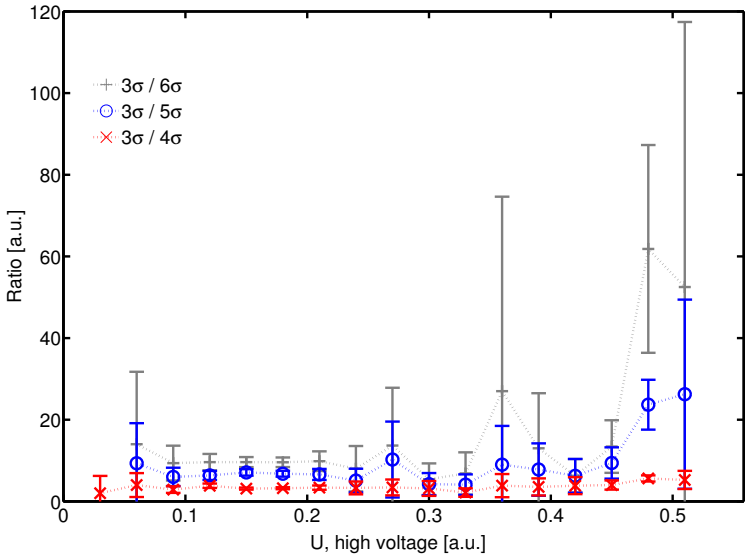

Fig. *4.27: Voltage independent fractions of gamma rejection. These fractions are the ratio of neutron histograms similar to those shown in fig. 4.26. The gamma rejection sigma levels as determined by the ^{252}Cf calibration are given in this plots legend. The cut conditions as specified in section 3.6 have been used.*

increase in fraction can either be explained by a rise in the neutron rate or by nonlinear γ and neutron bands in the discrimination plot at low energies which results in a leakage that mimics a high voltage dependence. If the distribution at low energies deviates from Gaussian shape, the symmetric cut condition from the fit is not valid for high rates. Therefore, this analysis was performed also for

the neutrons which survived the improved conservative cut with 1 MeVr energy threshold as described above. The resulting plot is shown in fig. 4.28. Clearly,

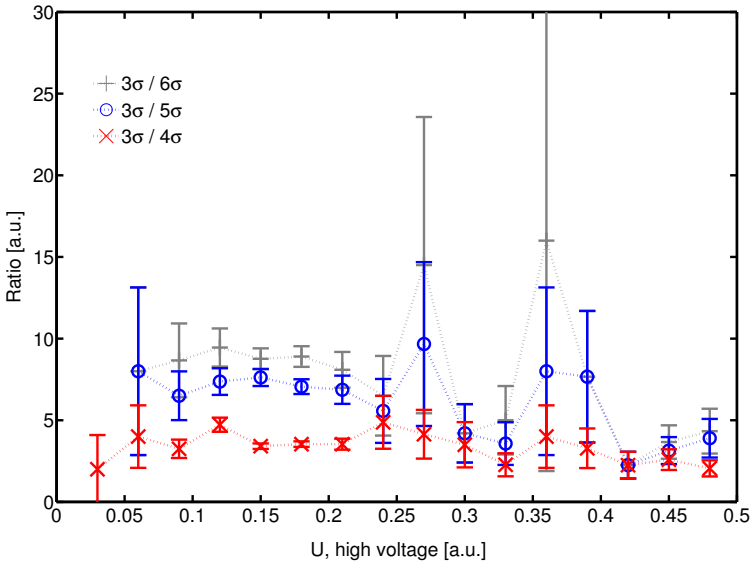

Fig. *4.28: Voltage independent fractions of gamma rejection. These fractions are the ratio of neutron histograms similar to those shown in fig. 4.26. The gamma rejection sigma levels as determined by the ^{252}Cf calibration are given in this plots legend. The changed cut conditions for a higher energy threshold as described in this section have been used.*

the indication for neutrons vanishes for the conservative energy threshold. This means, there are no detectable neutrons in those measurements.
A neutron evidence cannot be obtained from all runs performed under conditions of high dead time caused by X-rays. Adjusting the hardware threshold will solve the problem as will be shown and discussed later, in section 4.5.5.

4.5.1.8 Direct rate expectation

After a run all parameters are determined and if ion current data is available, one can calculate the expected neutron flux from the measurement.
A typical ion current in a single heating cycle was measured in the order of 0.5 nA which is small compared to the expectation of a few ten nA. The neutron times, the high voltage, the temperature and the measured ion current are shown in fig. 4.29 for a single heating cycle typical for what was achieved during the last phase of this work. Integration over the ion current from second 11820 to 12440 gives a total accumulated charge on the target of $5.1 \cdot 10^{-7}$ C in 620 seconds. If this amount of charge is completely deposited by D_2^+ ions, then

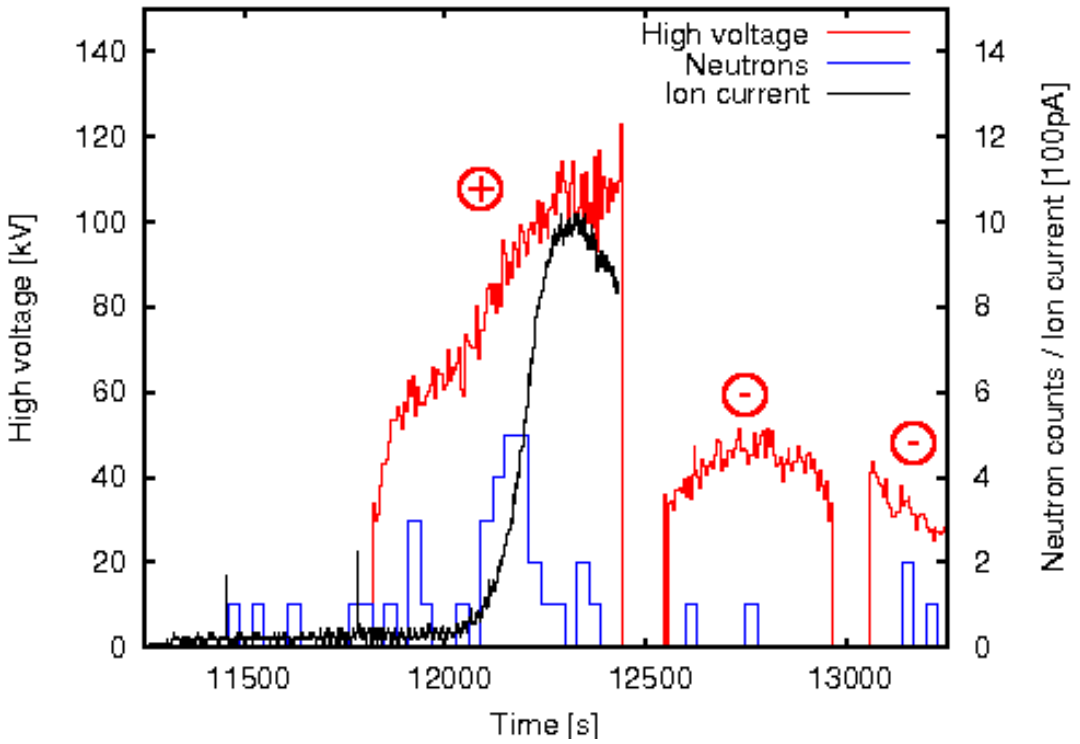

Fig. *4.29: High voltage, Ion current and Neutron rate for one heating cycle in phase III. The high voltage polarity is indicated in the red circles.*

$2.3{\cdot}10^{12}$ ions must have hit the target. Calculating the fusion rate according to section 1.3, the resulting deuterium fusion regarding only the neutron branch and using an average high voltage of 80 kV during this 620 seconds, has produced 18494 neutrons in 620 seconds. Using also the measured high voltages instead of the 80 kV to regard the high voltage fractions in detail, the average source neutron flux for this temperature cycle is 6.3 n/s for the 620 seconds the ion current was measured and 2.4 n/s for the whole polarity cycle (1639 s). This expectation can be compared to the data. However this is an exemplary cycle which should be treated as rough estimate. A deviation by a factor of two or three seems reasonable given the measured variation in ion current and high voltage.
In addition, if the high voltage would only allow the neutron production during one out of five or ten runs which are selected into the same analysis group on cannot expect an observable average neutron rate. Single runs are checked for features that indicate neutron production, such as extremely high voltage or neutron time clusters. Up to now, only the last recorded run shows a clear indication for neutron production which is still lower than the expected neutron flux.

4.5.2 Phase I

The crystal was mounted with the target glued on its exposed Z^+ face, yielding negative polarity during cooling during which neutrons should be produced by accelerating deuterium from the tip to the crystal.
The first experimental focus was the reliable reproducibility of high voltages by heating and cooling cycles. The new DAQ as described in chapter 2.4 was set up and a proper temperature measurement was installed. Searches for neutron excess above background were performed. A frequent, reliable gamma calibration of the neutron detectors was established after gain drifting (see section 3.6 and appendix C) was observed. A stable high voltage power supply and ambient temperature control were put in operation. Time, temperature and high voltage monitoring were built up. The two neutron detectors used (Detector configuration 1) covered 6% of solid angle.
Runs with stable gain were analyzed by using the time clustering analysis. However no time clustering was observed. Sorting neutrons by their occurrence in the thermal cycles and dividing by the time spans of the cycles, the rates during cooling and during heating all rates are identical with background. A measured net neutron rate average of $0.0015{\pm}0.0017$ was observed which equals an average source neutron rate of $6.5{\pm}7.4$ neutrons per second compatible with no neutrons.
The total X-ray yield increases by an order of magnitude when the crystal is charged to negative polarity, when ions should strike the crystal. From the presence of the tantalum X-ray fluorescence lines the negative polarity at the crystal

surface was confirmed. The reason for increased X-ray yield can be explained by secondary electron emission from ions hitting the target. Field electron emission from metal surfaces such as the target holder also contributes to the X-ray flux.

4.5.3 Phase II

During phase two, the tip was mounted on the crystal to be able to install a suppression grid. The suppression grid was necessary to prevent secondary electrons from compensating charge on the crystal.
After verification of the high voltage, neutron runs were performed. The settings remained almost constant at a working pressure of $5 \cdot 10^{-4}$ mbar and no grid bias voltage. The heating and cooling power was slightly adjusted, to achieve homogenous run conditions. The crystal is mounted such, that neutrons are expected to be observed during heating.
In the beginning of this particular phase, a tungsten tip was mounted to the Z^+ face of the crystal pointing to the deuterated target in a distance of approx. 8 cm. A Faraday grid was also installed. During the first operations, no bias voltages were applied. The neutron runs with the same parameters were used for a cumulative analysis.
A number of runs with the tip did not show any hint on neutron production. Therefore different nanotube wafers were tried for ionization. Upon installation of nanotube wafer W1-15, the crystals orientation was switched, so that neutron are expected to be produced during cooling contrary to all other runs without that particular wafer.

Group analysis: NTW W1-15

A series of runs with nanotube wafer W1-15 and the grid biased in most cases with negative voltages (which is an analysis subset) with a total of 70.7 h of runtime and 77.5 h of background data acquisition was recorded.
The polarity check confirms that the crystal is (not intentionally, as said before) mounted with the Z^- face towards the target so that neutrons are expected to be produced during cooling. The temperature change histogram shows no indication for an enhanced neutron flux during the cooling cycles. The difference in observed source neutron flux between heating and cooling as determined by the temperature change histogram 4.30 is $-0.02^{+0.14}_{-0.11}$ n/s with a statistical significance of only 8% as determined by a two sided t-test to the zero hypothesis that the two underlying distributions for heating and cooling are the not same which means there is only a 8% chance that those two distributions are not background. However, a correction for polarity is not yet applied.
The polarity cycle analysis of neutrons gives a source neutron flux is $0.03^{+0.62}_{-0.47}$ n/s for the positive polarity cycles and $0.14^{+0.58}_{-0.44}$ n/s for the negative polarity which

is compatible with zero. The time clustering analysis and the high voltage distribution, which is depicted in fig. 4.31, do not show any significant hint of neutrons as well. During most of those runs with the nanotube wafer W1-15, the Faraday

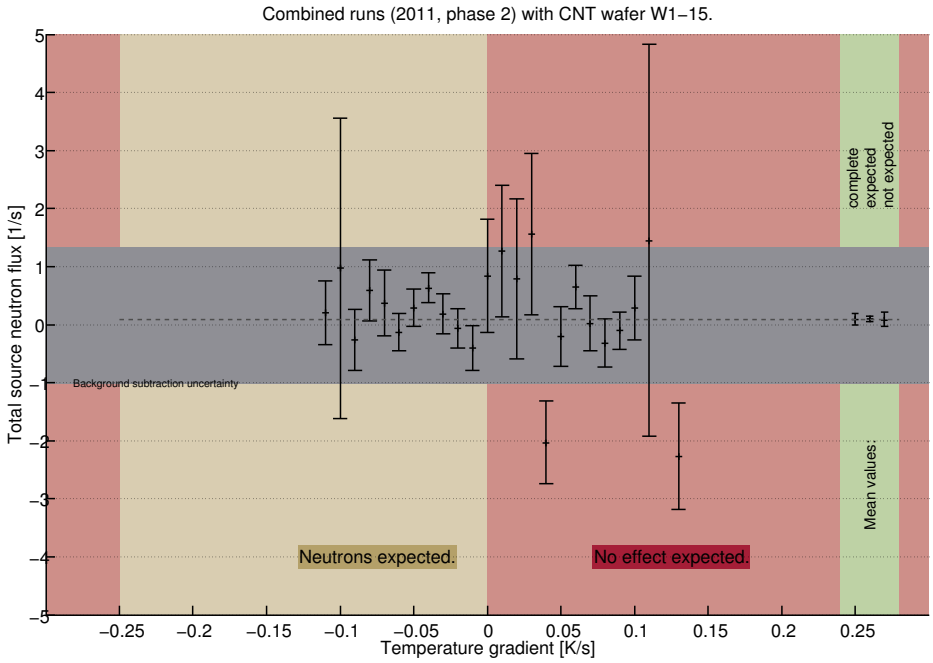

Fig. *4.30: Temperature change dependent source neutron rate histogram for 2011 runs with nanotube wafer W1-15. The errorbars are the 1σ statistical errors, the dashed line is the average value, the grey area indicates the error region from the background subtraction.*

grid was biased with negative voltage or connected to electrical ground. Regarding all runs with the NT wafer W1-15 installed, no neutrons were observed.

Subgroup analysis: negative grid bias

In order to study if the grid biasing increases the probability that neutrons are being produced, only the runs with negative biased grid were analyzed. The selected runs are now a subset of the all runs with the NT wafer W1-15.
The total source flux difference (heating-cooling) as determined by the temperature change histogram is $0.08^{+0.20}_{-0.16}$ n/s which indicates neutrons would have been produced during the "heating" cycles which is of course contrary to the expectation. This is an argument for the validity of the zero hypothesis that no neutrons have been produced. Within the error bars the rate is compatible with no effect observed.
The polarity cycle analysis however results in a neutron flux for the positive po-

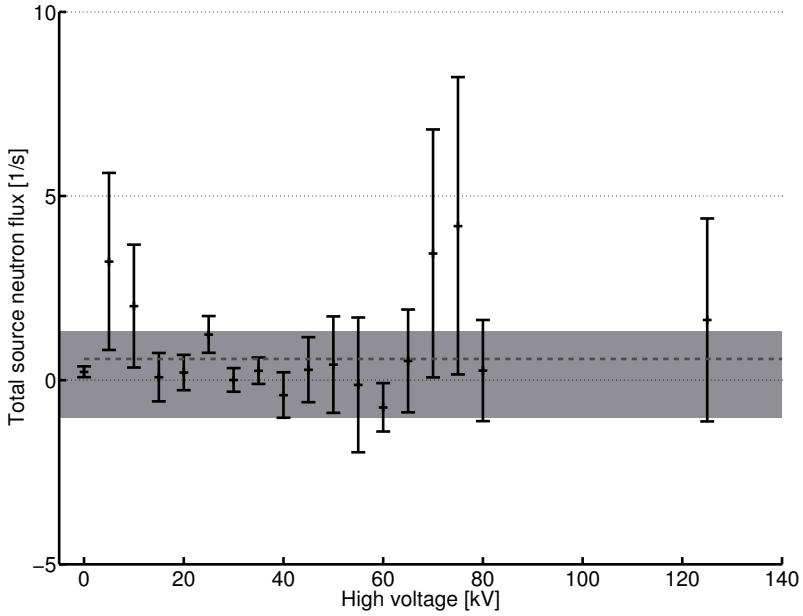

Fig. *4.31: High voltage dependent source neutron rate. The errorbars are the 1σ statistical errors, the dashed line is the average value, the grey area indicates the error region from the background subtraction.*

larity cycles of $0.23^{+0.78}_{-0.59}$ n/s and $0.36^{+0.73}_{-0.55}$ for negative polarity cycles as expected. The enhancement of the negative polarity cycle is again not significant, though. Also the high voltage distribution of the neutrons shown no increase for high voltages as shown in fig.4.33. The temperature change histogram for those runs is shown in fig. 4.32, the high voltage histogram is presented in fig. 4.33. In prin-

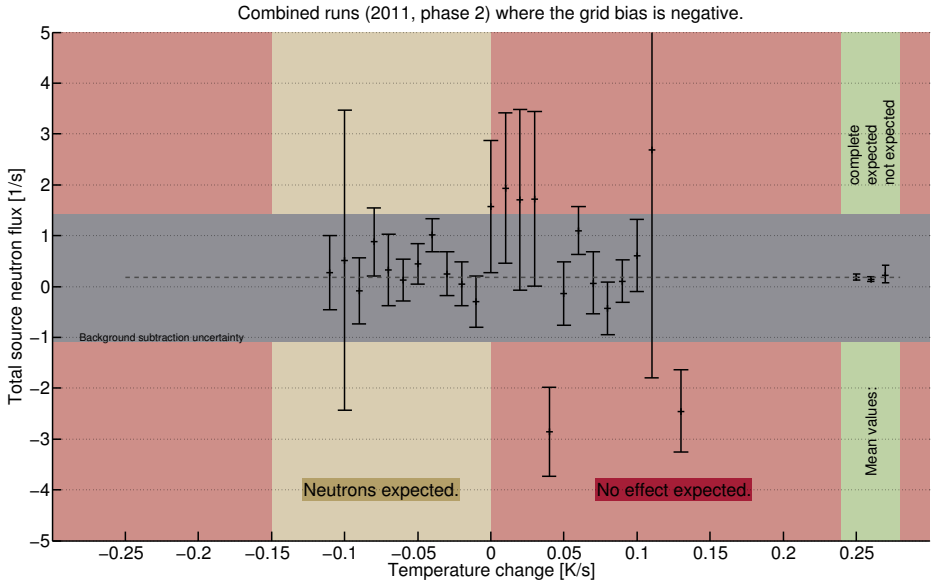

Fig. *4.32: Temperature change dependent source neutron rate histogram where the grid bias voltage is negative. The error bars are the 1σ statistical errors, the dashed line is the average value, the grey area indicates the error region from the background subtraction.*

ciple, a negative biased grid can have two effects on the internal field geometry: The field gradient is enhanced which might increase the ion focus on the target. According to the FEM calculations this effect is negligibly small. Second, the secondary electrons which are emitted by the target under ion bombardment can be repelled by the grid and therefore do not reach the crystal surface where they would take away charges. Thus the grid bias can increase the duration of the high voltage periods. Both effects will have positive impact on the fusion rate. This is in agreement with the observed indication for an increase in neutron rate if the grid is biased negatively, however the results are not significant. The result is also compatible with no observed effect.
In summary, the excess ($\text{Rate}_{notexpected}$ - $\text{Rate}_{expected}$) for the whole analysis group is -0.11 n/s and for the analysis subgroup where only runs with negative bias voltage are selected: -0.13 n/s. The results are statistically not convincing.
The runs with nanotube wafer W1-15 with a negative grid bias, did not show any dependence of the measured neutron rate on temperature change and high

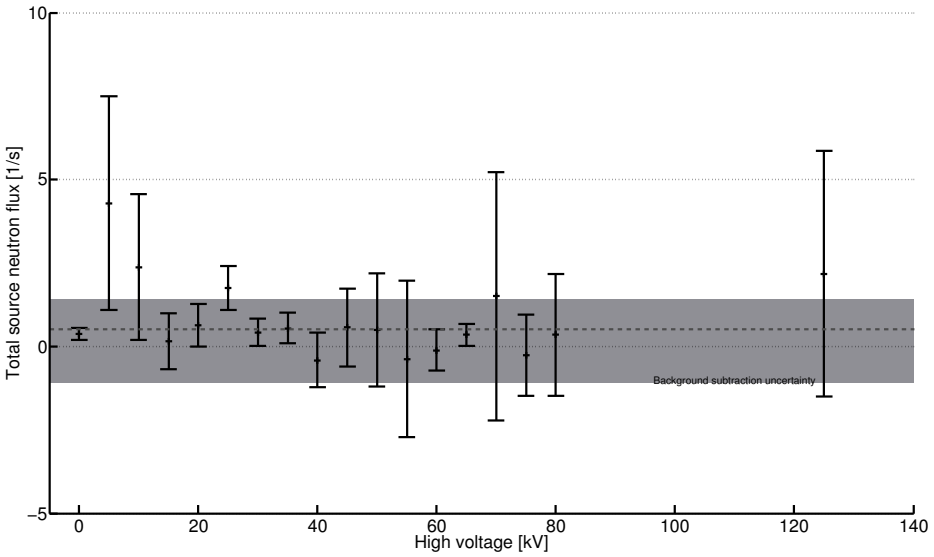

Fig. *4.33: High voltage dependent source neutron rate where the grid bias voltage negative. The errorbars are the 1σ statistical errors, the dashed line is the average value, the grey area indicates the error region from the background subtraction.*

voltage.

Group analysis: NTW W2-15

The nanotube wafer W2-15 was selected, where the structure of the nanotube forest was less chaotic compared to W1-15. The single nanotubes were also aligned more parallel compared to W1-15, standing upright with a length between 5 and 15 µm. The wafer W2-15 appears to have "sharper", isolated nanotubes sticking out of the wood. The ionization rate and therefore the fusion rate is expected to depend on the wafers structure. A total of 107 h run time and additional 241 h of background data has been recorded for this analysis group. This time the crystal is mounted with the Z^+ face towards the target, so that neutrons are expected to be produced within positive high voltage polarity during heating. The cumulative analysis of all runs by means of the temperature change histogram, fig. 4.34, shows a total source neutron flux enhancement of $0.65^{+0.26}_{-0.21}$ n/s for the positive temperature change. The statistical significance of the both underlying distributions not being identical is 94.6%. This means with a probability of 94.6% the distributions of rates during heating an cooling are not the same, which would indicate an enhanced neutron flux during heating as expected.
The source neutron flux is then determined by the polarity cycle analysis. The positive polarity source neutron flux is $0.68^{+0.30}_{-0.23}$ n/s, the negative polarity source neutron flux $0.67^{+1.39}_{-1.05}$ n/s. The source neutron flux difference is only $0.01^{+1.42}_{-1.08}$ n/s

compared to $0.48^{+0.27}_{-0.21}$ n/s from the temperature cycles which is a mismatch. Within the error bars the two values agree.
The high voltage distribution of the neutrons as shown in figure 4.35 does also not increase with higher voltages, which is expected to happen in case neutrons are being produced.

As previously discussed, the runs with the nanotube wafer W2-15 can be divided

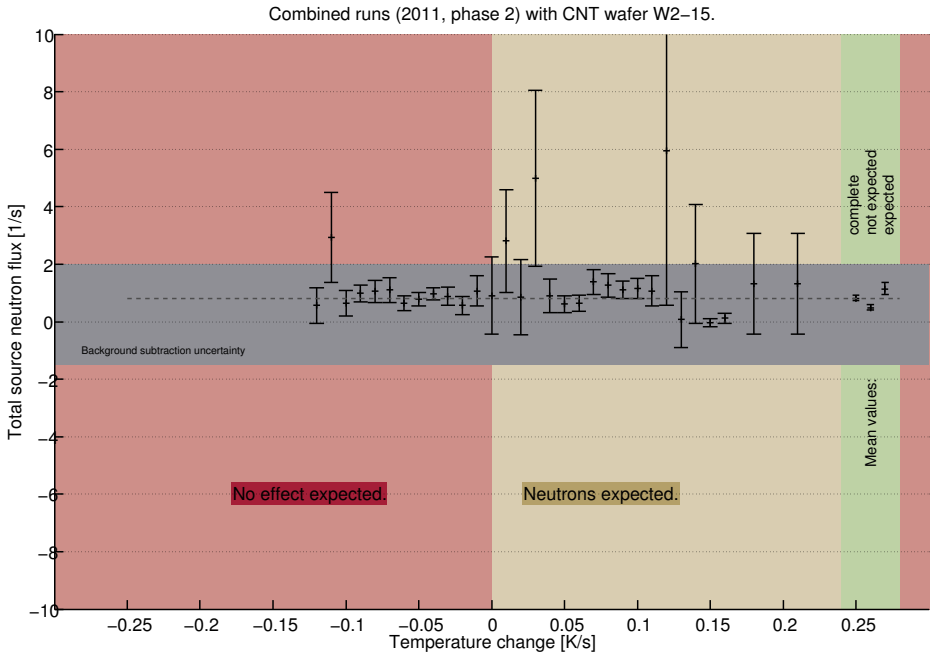

Fig. *4.34: Temperature change dependent source neutron rate histogram for 2011 runs with nanotube wafer W2-15. The errorbars are the 1σ statistical errors, the dashed line is the average value, the grey area indicates the error region from the background subtraction.*

into analysis subgroups according to the bias voltage settings on the grid of the Faraday cage and on the target.

Subgroup analysis: no bias voltages.

First, all runs where both bias voltages are zero were investigated. The default expectation is, that neutrons are produced in the cycle with positive polarity which in this case is generated by heating. The source neutron flux difference between positive and negative temperature changes (see fig. 4.36) is $1.19^{+0.37}_{-0.29}$ n/s in favor of the expected heating cycle. The statistical significance of those heating and cooling cycles not having the same underlying distribution is 98.7%. This means, the probability for those two distributions not originating from the same source such as background is 98.7%.

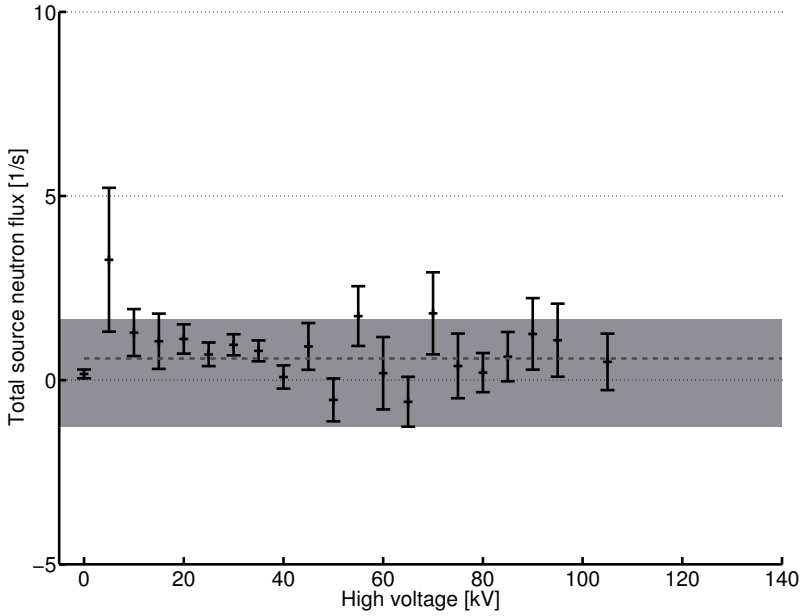

Fig. *4.35: High voltage dependent source neutron rate. The errorbars are the 1σ statistical errors, the dashed line is the average value, the grey area indicates the error region from the background subtraction.*

The source neutron flux obtained by polarity cycle analysis is $0.37^{+0.49}_{-0.37}$ n/s for the positive polarity cycles and -$0.12^{+0.45}_{-0.34}$ n/s for the negative polarity cycles. The difference in flux is $0.49^{+0.67}_{0.50}$ n/s compared to $1.19^{+0.37}_{-0.29}$ n/s from the temperature change analysis.
Nevertheless the excess points towards a rate which realistically could be expected in the order of $1.57^{+0.38}_{-0.31}$ n/s as derived in section 4.5.1.8.
The high voltage distribution of the neutrons (see fig. 4.37) however did not show any enhancement for large high voltages which is an indication that no additional neutrons have been produced and the excess is just a statistical fluctuation. The high voltage however cannot be measured at all times. A comparison of the

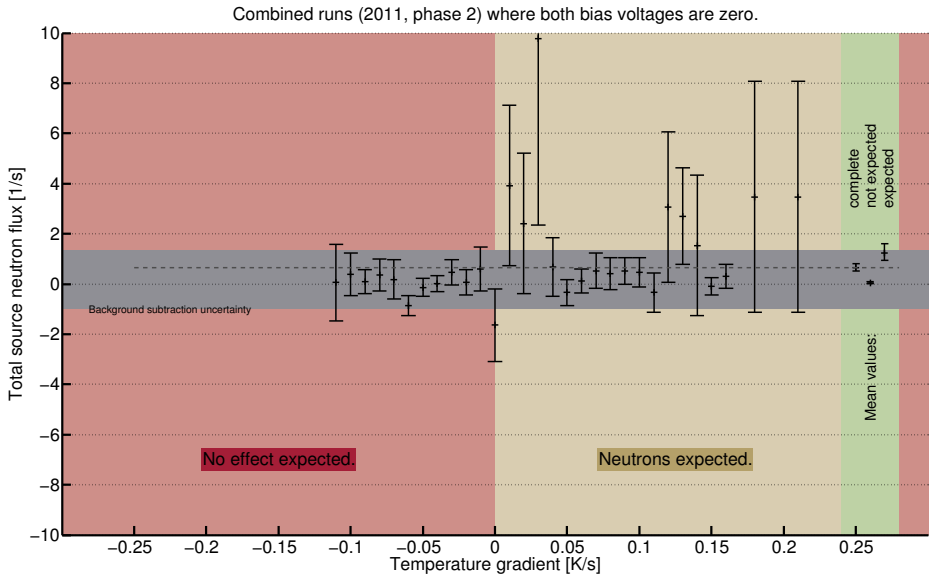

Fig. *4.36: Temperature change dependent source neutron rate histogram where grid and target bias voltage is zero. The errorbars are the 1σ statistical errors, the dashed line is the average value, the grey area indicates the error region from the background subtraction.*

neutron flux differences between the cycles for all individual runs of the subgroup is shown in fig.4.38. The pressure was almost the same for all runs, except the first one in the graph where the pressure was lower by a factor of at two. The deuterium target was changed for the last two numbers 7 and 8. The so called GSI target, CD_2 covered with 10 nm gold was used for the last two runs instead of the pure CD_2 target. The solid angle for the target got smaller, potentially reducing the neutron flux. So does the gold coating which increases the energy loss dE/dx of the ions drastically. A 100 keV D^+ ion loses 50 keV in the 10 nm gold layer. Fusion induced by D_2^+ ions is not expected to be possible any more.
None of the runs really sticks out by an increased neutron rate. Having a closer

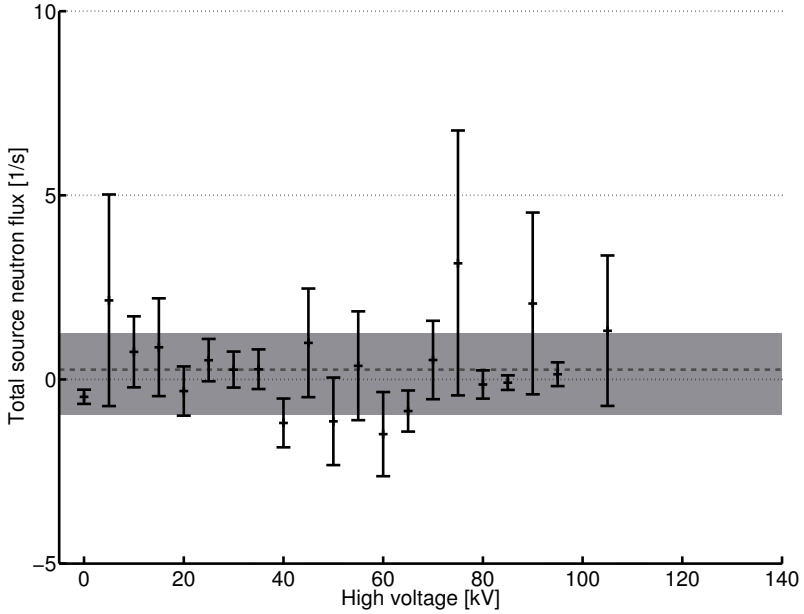

Fig. *4.37: High voltage dependent source neutron rate where grid and target bias voltage is zero. The errorbars are the 1σ statistical errors, the dashed line is the average value, the grey area indicates the error region from the background subtraction.*

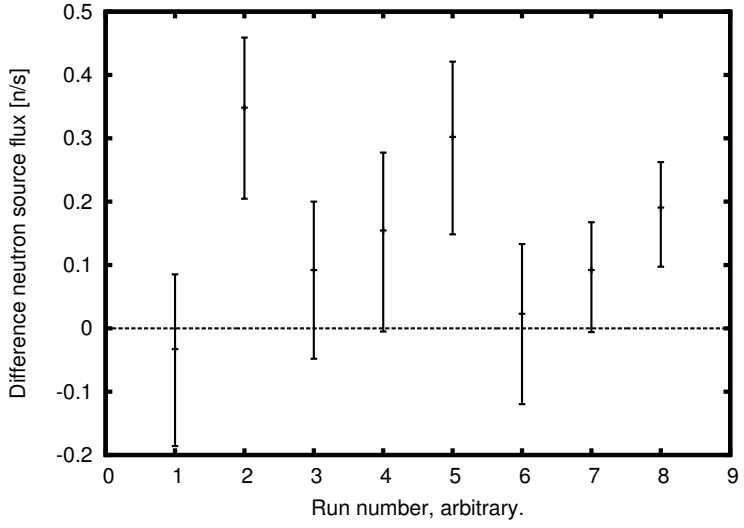

Fig. *4.38: Source neutron flux* ***difference*** *for all runs where both bias voltages are zero. The chronological run numbering is arbitrary from the first on the left to the last on the right, the neutron flux difference is s given in neutrons per second.*

look to run two, which shows the highest neutron asymmetry between the heating and cooling cycles, the time clustering analysis was performed. The time clustering plot for run two of this dataset is shown in fig. 4.39. The neutrons do

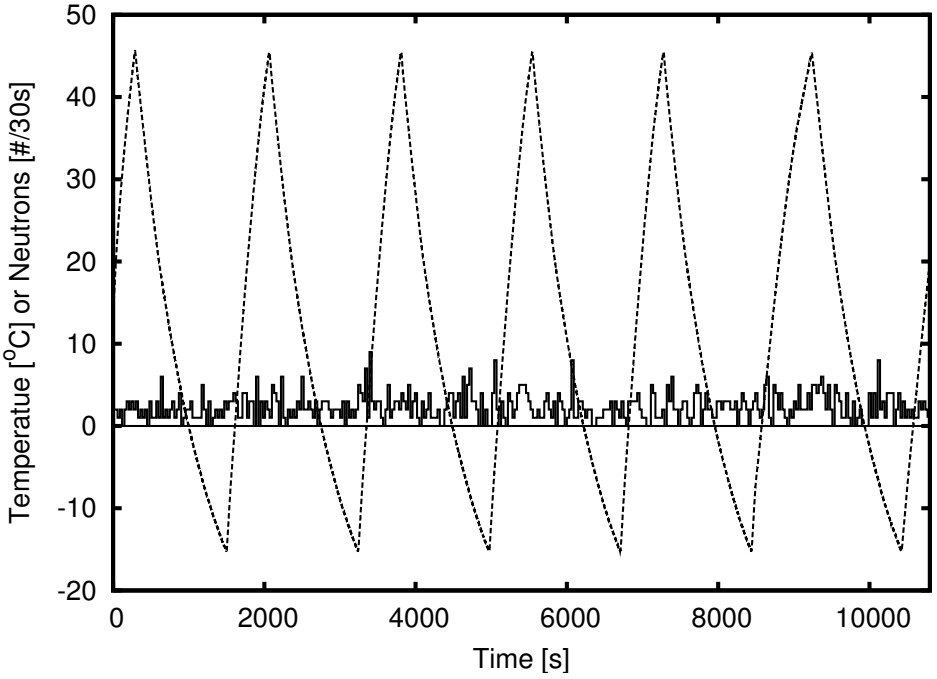

Fig. *4.39: Time clustering of a single run where both biases are zero and the neutron flux asymmetry of the heat and cooling cycles is large. The neutron time binning is 30 s.*

not cluster at specific times, the distribution of the neutrons among the time is completely random.

Subgroup analysis: negative target bias.

For this analysis subgroup, only runs were selected, for which the target was biased with negative voltages from -25 to -100 V. A negative biased target is expected to refocus the ions after passing the grid, however the effect is expected to be small since the ion velocities are a lot higher than one can usually manipulate by a weak electrostatic potential. On the other hand, a negative biased target will enhance the electron emission probability of the target upon ion hits. These electrons take away charges reducing the chance for neutron production. Since a grounded grid is installed to prevent the electron from reaching the crystal negatively biasing must not have any counterproductive effect.
A total of 6 hours of run data was recorded with these settings. The measured neutron rate difference from the temperature change histogram in fig. 4.40 is

$0.50^{+0.49}_{-0.39}$ n/s in favor of the heating cycle as expected with a statistical significance of the both underlying distributions not being equal of 58%. The polarity cycle analysis results in a total source neutron flux of $0.13^{+0.95}_{-0.71}$ n/s for the positive polarity cycles and $0.27^{+0.92}_{-0.69}$ n/s for the negative polarity cycles. The difference is $0.14^{+1.32}_{-0.99}$ n/s in favor of positive polarities like the difference obtained by the temperature change histogram. Again, the measurement is in favor of the expectation, however also compatible with zero.
The high voltage distribution of the neutrons do not show an enhancement to higher voltages and time clustering of neutron was not observed. The temperature change histogram is shown in figure 4.40, the high voltage histogram in figure 4.41. Negative biasing of the target turned out not to be as productive as

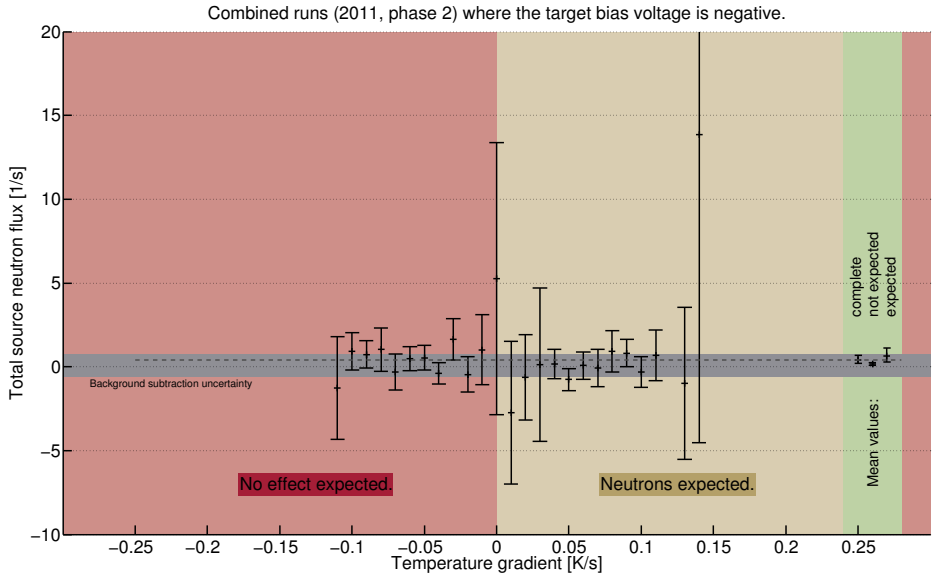

Fig. *4.40: Temperature change dependent source neutron rate histogram where the target bias voltage is negative. The errorbars are the 1σ statistical errors, the dashed line is the average value, the grey area indicates the error region from the background subtraction.*

intended.

Subgroup analysis: positive target bias: +50 V

Therefore the bias was changed to positive polarity in order to decrease electron emission probability on the target. This subgroup of the analysis group where the target bias voltage was +50 V, contains 32 h of run data.
The neutron source flux difference determined by the temperature change histogram shown in fig. 4.42 is $0.32^{+0.36}_{-0.29}$ n/s with a significance of the two sided t-test as specified above of 51.9%. This means there is no clear indication for any neu-

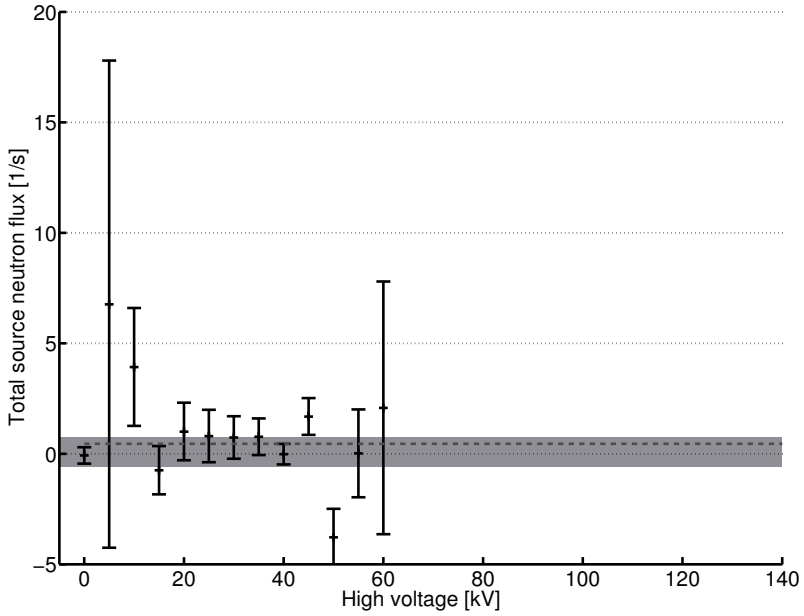

Fig. *4.41: High voltage dependent source neutron rate where the target bias voltage negative. The errorbars are the 1σ statistical errors, the dashed line is the average value, the grey area indicates the error region from the background subtraction.*

tron production for these runs. The polarity cycle analysis shows similar results, a total source neutron flux for positive polarity of $1.07^{+0.62}_{-0.47}$ n/s and $1.29^{+0.48}_{-0.36}$ n/s for the negative polarity cycles which results in a difference of -$0.22^{+0.78}_{-0.59}$ n/s. These results are only conclusive under the assumption that no neutrons have been produced. In addition, time clustering has not been observed and the high voltage histogram as shown in fig. 4.43 does again not show any enhancement at higher voltages.

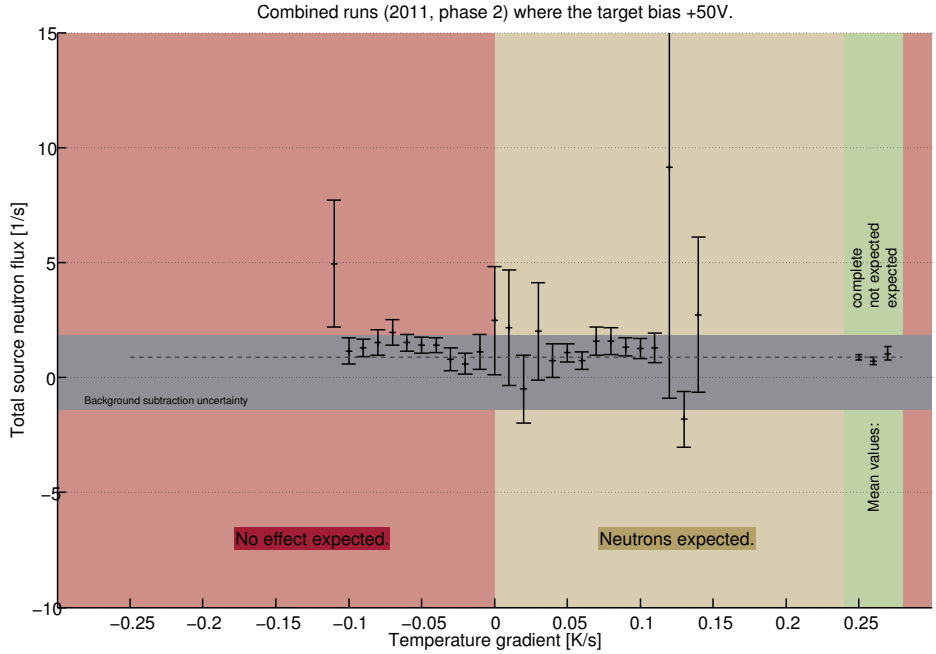

Fig. *4.42: Temperature change dependent source neutron rate histogram where the target bias voltage is +50 V. The errorbars are the 1σ statistical errors, the dashed line is the average value, the grey area indicates the error region from the background subtraction.*

Subgroup analysis: positive target bias: +100 V

As validation of the zero effect of a positively biased target, the bias was increased to +100 V. This is of course another analysis subgroup with a total of 30 h of run data.

The total source flux difference as obtained from the temperature change histogram shown in fig. 4.44 is $0.24^{+0.23}_{0.18}$ n/s with a significance of 58.8% that the underlying distributions are not equal. There is a 59% chance that the difference in flux originated from neutrons produced. The positive polarity flux from the polarity analysis is $0.40^{+0.51}_{-0.39}$ n/s, the negative polarity flux is $0.73^{+0.51}_{-0.39}$ n/s. The difference in flux is -$0.33^{+0.72}_{-0.55}$. The two flux differences are again only compatible

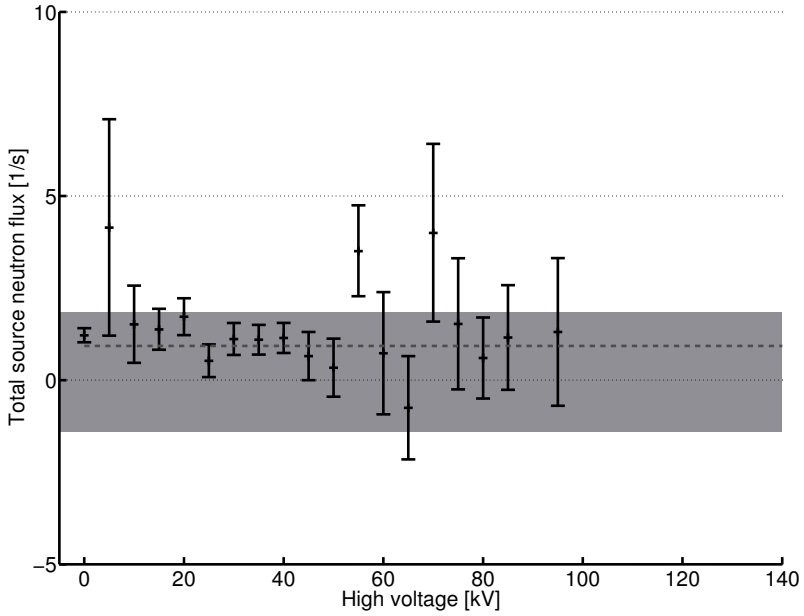

Fig. *4.43: High voltage dependent source neutron rate where the target bias is +50 V. The errorbars are the 1σ statistical errors, the dashed line is the average value, the grey area indicates the error region from the background subtraction.*

if no neutron production is assumed.
As expected from previous runs, neither the high voltage histogram shown in fig. 4.45 nor the time clustering analysis yield any indication for neutrons. A

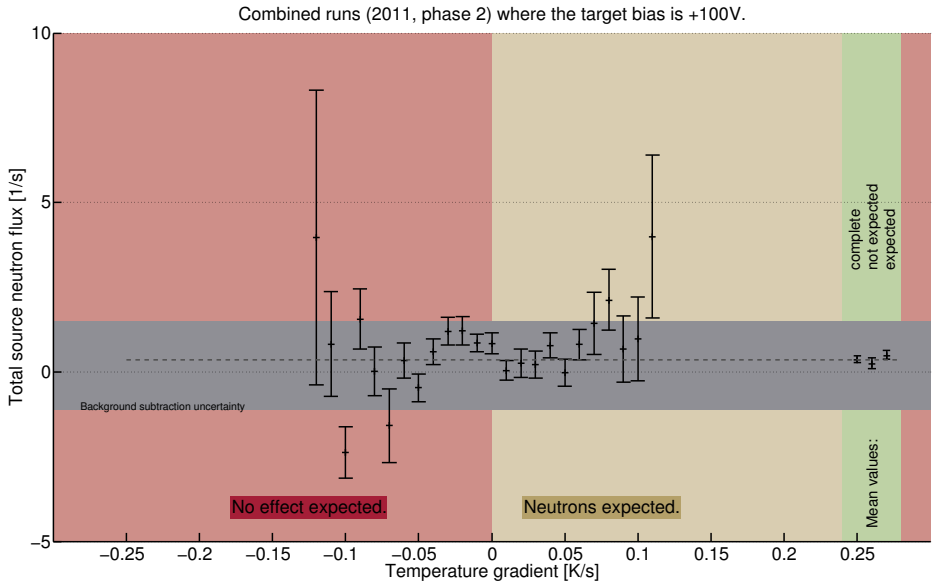

Fig. *4.44: Temperature change dependent source neutron rate histogram where the target bias voltage is +100 V. The errorbars are the 1σ statistical errors, the dashed line is the average value, the grey area indicates the error region from the background subtraction.*

possible interpretation of this behavior can be found if a positive target bias decreases the chance of an ion impact on the target, pushing ions to the grid or somewhere else. As calculated in section 1.5, this still is very unlikely since the ions should have high velocities and cannot be deflected by a 100 V electric potential. Unless the metallization of the target produces sufficient strong electric fields by field enhancement on surface structures.
Another possible explanation could be the coincidental degradation of the nanotube wafer by spark discharges with the application of positive target bias.

4.5.4 Structural damage investigation of NTW

The nanotube wafer W2-15 was removed from the experimental setup and structural damage investigated with a SEM. The wafer W2-15 did show almost no signs of degradation except some rare craters caused by spark discharges. A picture showing the uniformity of the nanotube forest after its use in this experiment is shown in figure 4.46. The other nanotube wafer used, W1-15, showed much worse degradation than W2-15. The reason is a higher spark discharge rate for the more “chaotic” wafer W1-15. Accidentally the wafer was also partially crushed

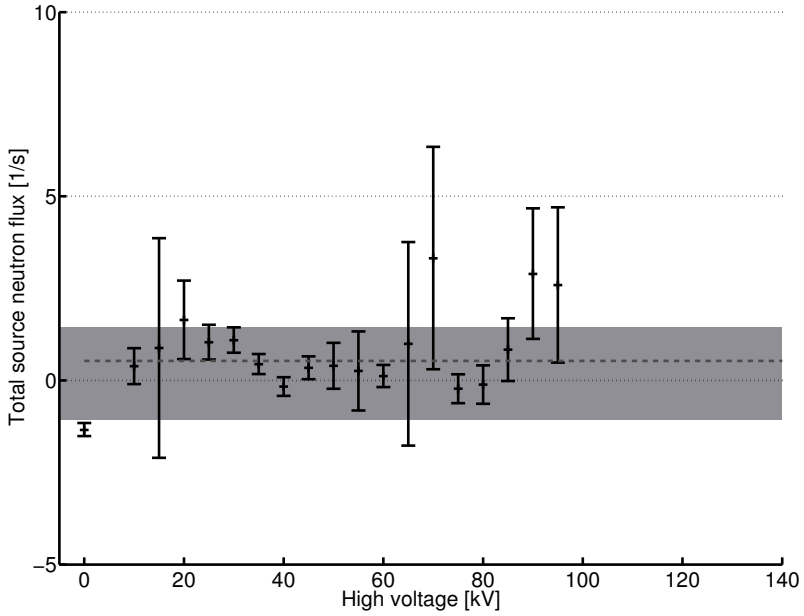

Fig. *4.45: High voltage dependent source neutron rate where the target bias is +100 V. The errorbars are the 1σ statistical errors, the dashed line is the average value, the grey area indicates the error region from the background subtraction.*

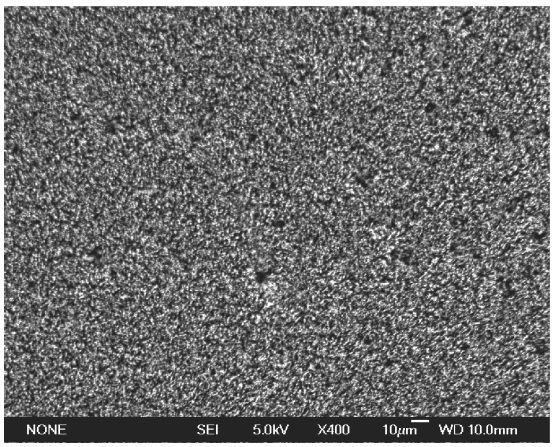

Fig. *4.46: Top view of homogenous nanotube wafer W2-15 after its use.*

by tweezers on the edge while installing it in the SEM. Also dirt particles were found, attached to the wafers surface bending the nanotubes downwards. Two pictures of the wafer W1-15 are shown in figures 4.47 and 4.48. The damage on

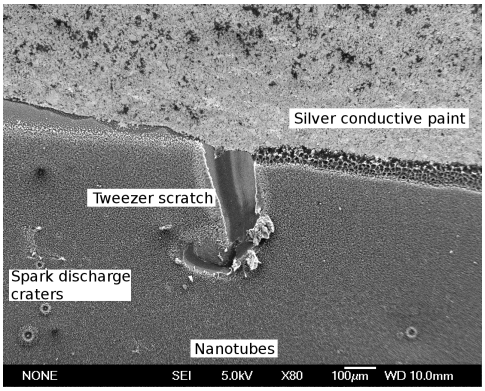

Fig. *4.47: Border of the nanotube wafer W1-15 (view from above). One can see the silver conductive paint used for electrical contact, the tweezer scratch and lots of discharge craters.*

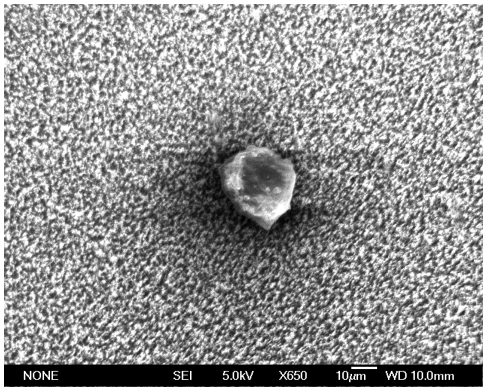

Fig. *4.48: Top view of dirt particle lying on top of the nanotube wafer W1-15, bending the nanotubes. The bending of the tubes appears as dark shade around the dirt particle in this picture.*

the wafers and the measured results indicated that the nanotube wafers do not work as expected. Of course, these wafers were not specifically produced with the intention to ionize deuterium, therefore more testing is necessary with wafers which are optimized for these ionization processes. The decision was taken to use a tip again. In addition a new detector with better solid angle coverage was installed. These actions initiated phase III of the experiment.

4.5.5 Phase III

In phase III, the vacuum neutron detector was installed into the into the experimental chamber to increase the solid angle coverage by a factor of three. This allows the measurement of even lower neutron fluxes as the total sensitivity increases by a factor of 3.5.
The new NE-213 detector was constructed and mounted into the vacuum chamber after successful discrimination testing with a deuterium beam producing neutrons at the Rosenau accelerator. After installation the detector was calibrated with a ^{22}Na source and first runs were performed in order to see if the high voltage can be reached or not.
The target was mounted directly to the vacuum side of the detector module. The distance is limited only by the holders and the targets thickness. The detector covers about 33% of solid angle and has an absolute detection efficiency in the region of interest of $7.85^{+1.88}_{-1.57}$% as determined by the absolute efficiency calibration with a ^{252}Cf source (See section 3.10). A Faraday cage around the target was not installed for the first runs, the target however biased to -100 V.
New tungsten tips were produced, three matching the requirement of having a tip radius smaller than 100 nm, one exceeding the design of 50 nm radius by a measured radius of about 30 nm. The tips were cleaned, checked with the SEM and one tip mounted on the crystal surface. The sharpest tip was installed after the testing period, during which another tip was used.
After the testing period was completed, the new tip was installed and the neutron run data collected for 67 h. During the first 50 h of record time, an strong increase in recorded rate was observed. The data was discarded for the same reasons as for the last 17 h of data taking which will be explained below. A combined polarity cycle analysis of the last runs containing 17 h of total run time yield an average dead time corrected source neutron rate for the positive polarity cycles of $0.27^{+0.07}_{-0.04}$ n/s and $0.11^{+0.06}_{-0.04}$ n/s for the negative polarity cycles. At first, this seems to fit the expectation of an increase in neutron flux during heating cycles. However the neutrons energy spectrum as described in section 4.5.1.6 reveals that low energetic events, caused by X-rays scattering in the NE-213 detectors during positive high voltage periods leak into the neutron cut region.
After refinement of the neutron cut for these runs by applying a fixed energy threshold of 1 MeVr in the software similar to what is described in section 4.5.1.6, the dead time corrected source flux for positive polarity is $-0.06^{+0.05}_{-0.03}$ n/s and $0.13^{+0.05}_{-0.03}$ n/s for negative polarity. The reason for this deficit is a statistical fluctuation due to the very small number of detected neutrons. Therefore no neutrons are observed during this time period.
This problem has been fixed in a new run temporarily by adjusting the hardware trigger threshold instead of the software threshold so that only events which

exceed 50 mV are recorded. 50 mV corresponds to to a neutron recoil energy of roughly 1 MeVr.
A run was performed using the current setup and the adjusted hardware trigger threshold. The target bias was set to +10 V, the pressure to $4.0 \cdot 10^{-4}$ mbar real deuterium pressure (see appendix G). The total source neutron flux difference was $0.26^{+0.6}_{-0.4}$ n/s in favor of the expected polarity. A time clustering analysis in fig. 4.49 shows the energy distribution of events in the ROI above 1 MeV. The red crosses are the measured neutrons with their time and energy coordinates. As can be seen, they appear especially for high voltages drawn in grey as expected from fusion neutrons. The sum of all measured neutrons in a 30 second time bin is drawn as blue histogram. It aligns perfectly with the high voltage cycles, which have positive polarity when they reach their maximum. It can also be seen that the neutrons die out after the third heating cycle which correlates to the time the deuterium supply went out. This measurement is a strong hint on a successful neutron production. By restricting the analysis to the first three polarity

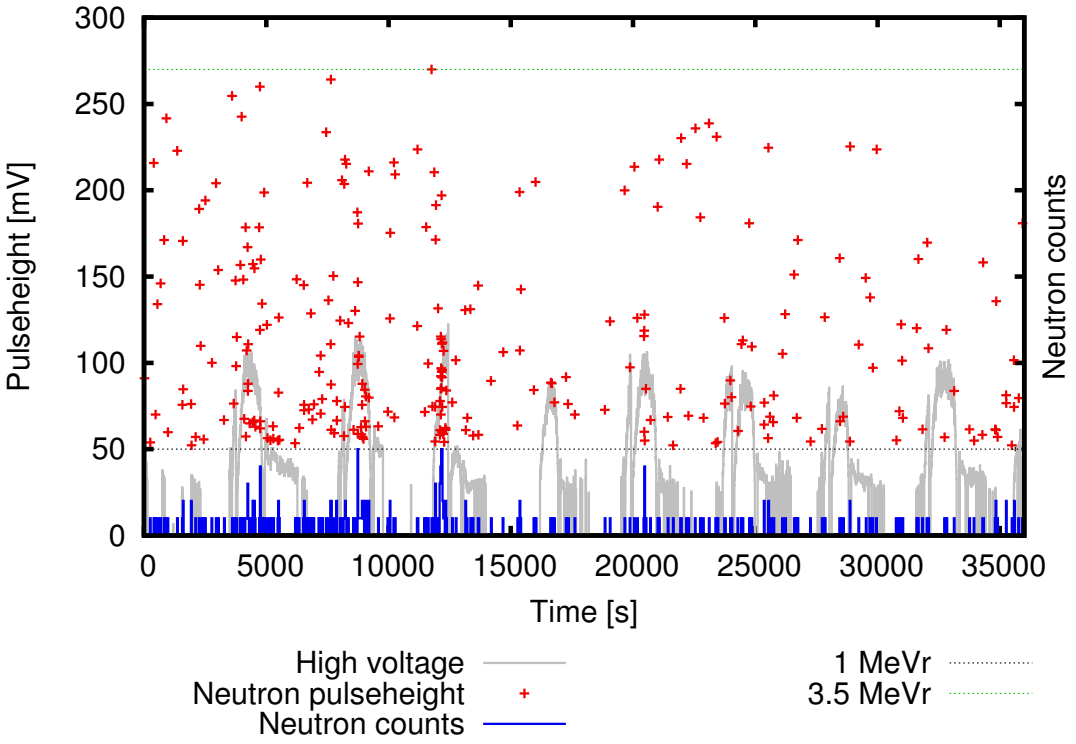

Fig. *4.49: Time clustering analysis of high threshold neutron run.*

cycles up to second 15000, the evidence for neutrons can be increased. The total

difference in source neutron flux increases to

$$\Xi_{n,avg,excess} = 0.56^{+0.10}_{-0.06}\, n/s \tag{4.3}$$

additional neutrons produced per second during positive polarity cycles.
The neutron excess also fits to the time an ion current was measured on the target. The alignment of the neutrons to the ion current is shown in figure 4.50. However it is not completely understood why the neutron rate decreases again for higher ion current. For these rates the effect is far above statistical fluctuation. A possible reason could be local charging of the polyethylene target which is also why a metalized target is preferred. For a measured high voltage of 120 kV and

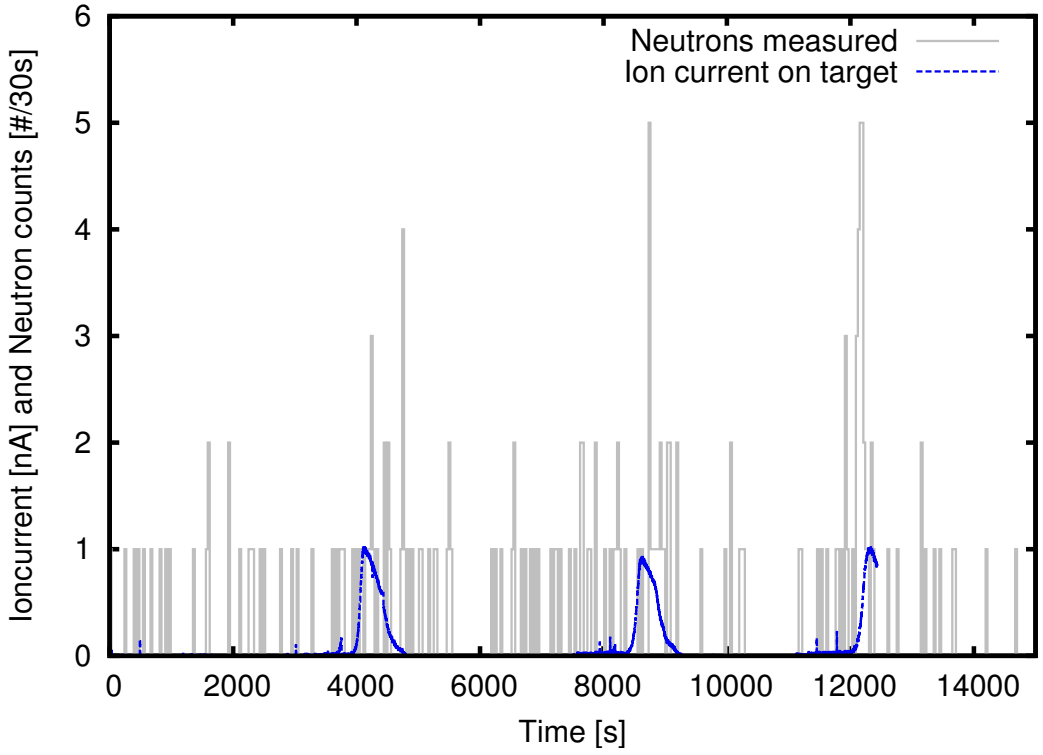

Fig. *4.50: Observed neutrons aligned to the ion current data.*

an ion current of 1 nA, the measured neutron source flux can almost be explained by fusion of D_2^+ ions, assuming a mechanism which decreases ion flux rather fast. The expected neutron flux based on a realistic calculation for these three polarity cycles is 3.4 n/s which is a factor of 7 lower than expected. A comparison with the unkown disappearance of fusion neutrons for increasing ion current as shown in fig. 4.29 suggests that the measured deficit in neutrons originate from this effect. This is the first and only measurement which shows a clear indication for neutron

production by the D(D,n)^{3}He fusion reaction. The neutrons appear when high voltage of the correct polarity is generated by the crystal. They appear over the complete expected energy range and vanish when the deuterium supply runs out. However, the correlation between the observed ion current and the detected neutrons is not yet completely understood. As the ion current further rises the number of neutrons emitted is expected to rise as well, however this was not observed.
This measurement summarizes very well all the difficulties an challenges that must be overcome to measure a low neutrons flux in this order of magnitude. The neutron flux was simply to small to be seen in any other measurement that was performed before.
Since the neutron energy spectrum in the NE-213 detector rises towards lower energies, the hardware threshold of 1 MeVr must be lowered again in order to prove this result correct with higher statistics. Since the detector is still dead time dominated for a low hardware threshold, one must get rid of the gamma background which can be accomplished by installation of a lead shield as described below.
The current experimental setup is very well suited to measure a neutron flux in even below the expectation, so that future researchers can focus on even further improve neutron detection efficiency, clarify the deficit in expected neutrons and investigate how the ion current can be increased.
This measurement must be confirmed with the lower hardware threshold after introducing a few mm of lead in between the target and the NE-213 detector. An X-ray shield would be a suitable method to prevent X-rays from reaching the liquid scintillator. The attenuation coefficient of lead is $\xi = 2.014\,\mathrm{cm}^2/\mathrm{g}$ for 150 keV X-ray radiation.The necessary thickness can be calculated using the Beer-Lambert-Law for a specific thickness of the target d, desired attenuation factor A, the lead density $\rho = 11.34\,\mathrm{g}/\mathrm{cm}^3$ and the attenuation coefficient ξ:

$$d = \frac{-ln(A)}{\xi \cdot \rho} \tag{4.4}$$

If an attenuation of A = 10^{-3} is desired for 150 keV X-rays, the lead shield must be d = 3 mm thick. The attenuation factor for 100 keV X-rays in 3 mm thick lead is $6.3{\cdot}10^{-91}$. This is an extremely conservative assumption given that the X-ray intensity at high energies drops exponentially and that the typical high voltage is in the order of 120 kV. A suitable lead shield with 3 mm thickness was prepared. A scheme of the current setup and the position where the lead shield can be built in is shown in figure 4.5.5. Given that lead is a material that should

[1]Data from NIST, National Institute of Standards and Technology.
`http://physics.nist.gov/PhysRefData/XrayMassCoef/ElemTab/z82.html`

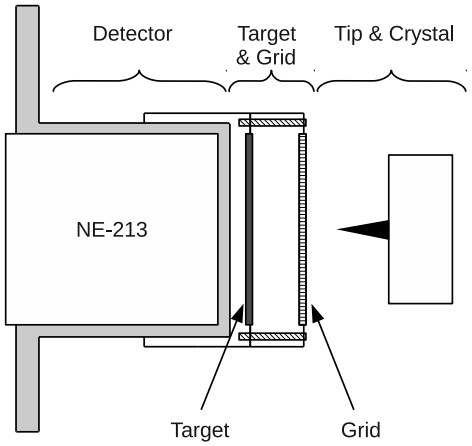

Fig. *4.51: Schematic view of the internal setup with detector mounted into the vacuuum chamber. Setup without any lead shielding.*

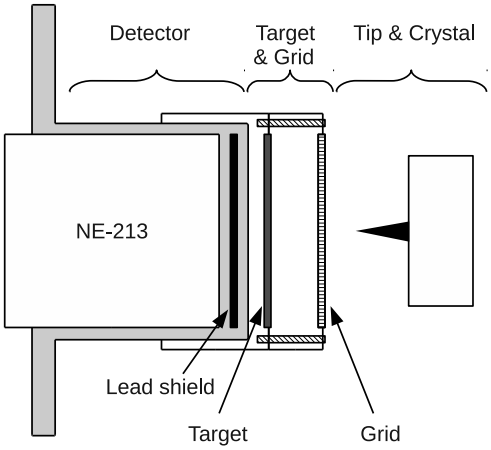

Fig. *4.52: Schematic view of the internal setup with detector mounted into the vacuuum chamber. The position where the lead shield can be installed is marked in solid black.*

be avoided in vacuum the neutron detector must be dismounted and dismantled. After installation of the lead shield the gamma suppression must be verified and the hardware threshold reset to its original value.

4.6 Application for neutron calibration of low background experiments

The PIA device is intended to be used for neutron calibration applications without any risk of radioactive contamination in low background environments. By using such neutron source for calibration, opening the radiation shielding is not necessary any more since the device can be built within the shielding. Many other low background experiments such as EDELWEISS or the future EURECA (**E**uropean **U**nderground **R**are **E**vent **C**alorimeter **A**rray) project could use such neutron source in order to calibrate their experiment remote from time to time without needing any further permit. The neutron calibration can even be done automatically, which allows detailed high statistics analysis of neutron interaction in dark matter detectors relying on SQUID technology.
To investigate how long such a device must be operated in order to replace an isotope source for calibration, some simulations were done in collaboration with S.Scholl for application in the CRESST experiment. The neutron source is possibly strong enough that it can be used for calibration within reasonable timescales.

4.6.1 PIA @ CRESST

A Monte Carlo study was performed to monitor the performance of such a neutron source at the CRESST setup. S.Scholl included the source in his Monte Carlo simulation of CRESST and located it inside the shielding. The starting volume of the neutrons was a box of 10x10x10 cm size, located in the CRESST-II setup with its center at the middle of the face of the radon box at half the height of the cold box (vertically centered). The radon box is the volume around the cold box which is constantly flushed with dry nitrogen to remove any radon from the vicinity of the cryostat. The cold box is the end of the cryostat where the detectors are located. The cold box has a vacuum shield, a liquid nitrogen shield, a liquid helium shield and the inner volume is coupled to the mixing chamber of the dilution refrigerator operating up to 33 detector modules 300 g each at 10 mK. The cold box is made completely out of pure copper to increase radiopurity.
Simulation was performed for 10^6 started neutrons in 4π, monoenergetic 2.45 MeV neutrons with a FWHM of the Gaussian distribution of 50 keV. All detector hits with a suitable lightyield smaller and an energy deposition greater than the detector thresholds were accepted. An overview about the recoils and their distribution is given in table 4.1. The calibration time is dependent on the neutron flux produced on average. If an average neutron rate of 50 n/s is assumed, the run time for this simulated statistics is 55.6 hours. With the realistic flux expectation of 5 n/s obtained in chapter 1, the calibration time rises to 550 h or 22 days. The total recoil numbers are the same order of magnitude compared to real calibration campaigns (approx. 20000 recoils in 3 days and 5000 recoils in 3 days). The scat-

Table 4.1: Simulated neutron recoils in the CRESST-II setup as in run 32, 10 M neutrons started.

Recoils on	$CaWO_4$	Oxygen	Calcium	Tungsten	Mixed
Single recoil	1202	1120	71	11	425
Double recoil	259	243	9	1	90
Triple recoil	32	29	1	0	0
Quadruple recoil	2	2	0	0	0
Higher order	1	1	0	0	0

terplot of the simulation which shows the distribution of the lightyield as function of the deposited energy is shown in fig.4.53, the neutron recoil spectrum is shown in fig.4.54. The data in the scatter plot is the pure kinetic data as obtained from simulation and not folded with the detectors energy resolution. Therefore the three recoil bands for the three different nuclei can be identified.

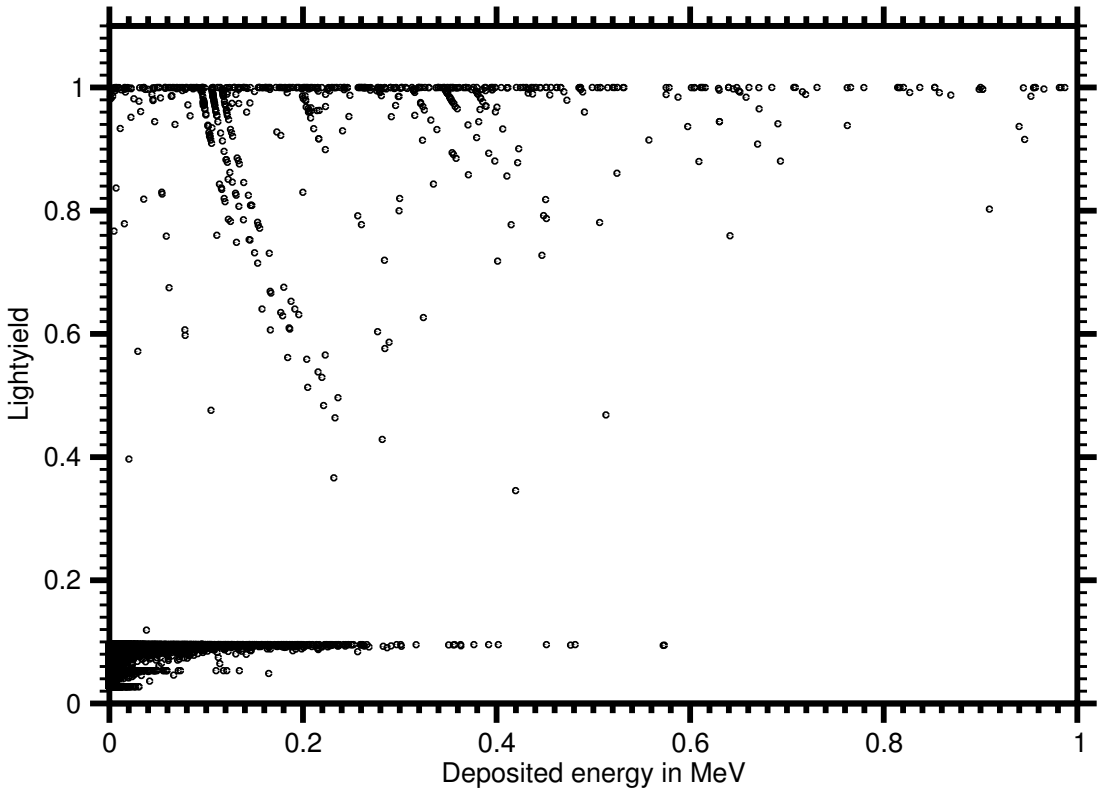

Fig. *4.53: Scatterplot of source at the CRESST-II setup. The detector thresholds and the energy resolutions are missing.*

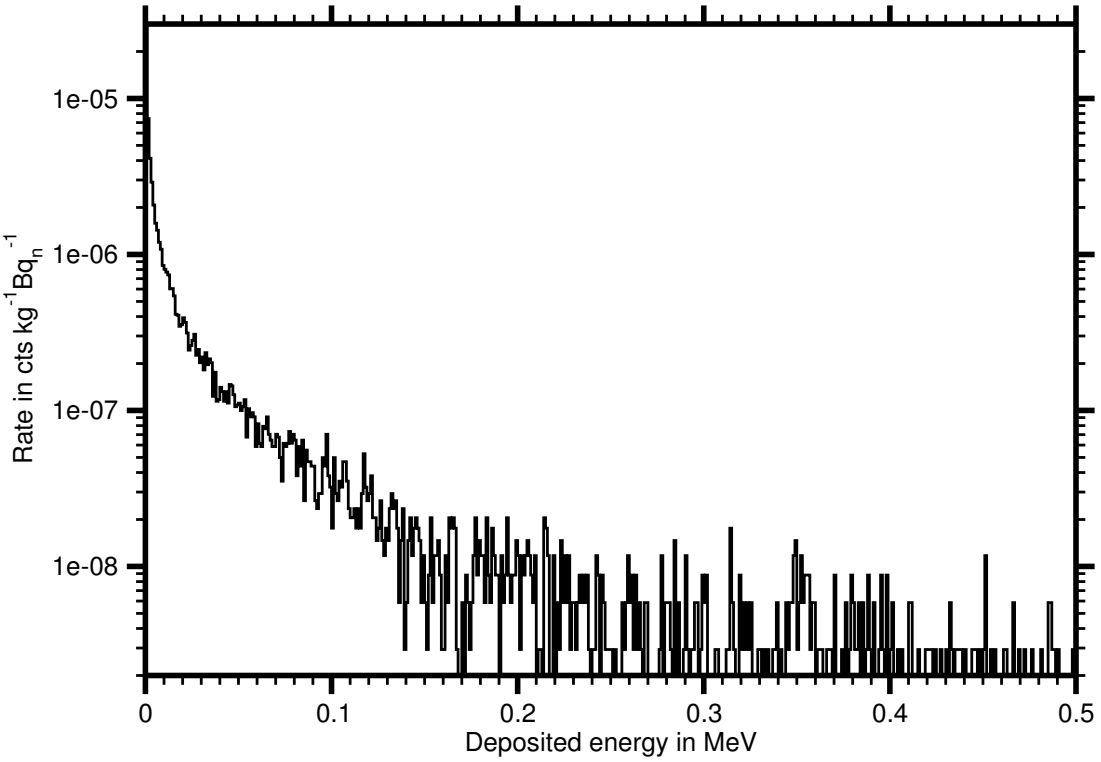

Fig. *4.54: Histogram of deposited energy in the CRESST-II setup. Cropped at 0.5 MeV.*

Tritium at CRESST

The Q-value of the tritium β-decay is 18.6 keV compared to a typical CRESST detector threshold of 10 keV. A tritium β-decay on the crystal surface will cause a low energetic recoil on the detectors constituent atoms possibly showing up right in the recoil region of interest if the electron escapes without producing any light in the scintillating housing.
If $\mathcal{O}10^7$ neutrons are being produced for a calibration, the same amount of tritium is being produced. With a half-life of $t_{\frac{1}{2}} = 12.3\,a$, the activity of the whole tritium amount for a single calibration is 17 mBq or one decay every minute.
As discussed already in previous work, tritium is not a problem if contained properly. If the whole tritium amount ever produced during a calibration would be deposited on a single one of the detector modules, the CRESST experiment would not be able to take reliable data any longer. To accumulate on a single detector module, the tritium must penetrate not only the borosilicate housing of the device itself, which is considered to be tritium tight, it also must diffuse right through the cryostats shieldings. There is no doubt that the critical amount of tritium never can reach one of the detector modules.

4.6.2 Intrinsic radioactivity

The material screening for low background environment use is ongoing topic of research. With the Tübingen low background germanium gamma detector, the radiopurity of crucial parts of the setup will be determined. The Tübingen underground germanium detector and its properties are described in the Diploma thesis of A.Hegai(2011)[4] and the PhD thesis of G.Meierhofer(2011)[27]. The detector is shielded against gamma background with ultra pure copper and lead, equipped with a radon box which is flushed with nitrogen to remove radon and it is located under about 20 m of water equivalent concrete overburden against cosmic rays. An active plastic scintillator muon veto is under construction. The main components to be checked for radioactive isotopes are the pyroelectric crystal itself, the heater and cooler unit as well as other materials used such as copper, PTFE and the target material. The greatest contribution is expected to originate from the crystal itself as well as from the peltier element because of their rare earth constituents which usually come with high uranium and thorium contamination. As a first test, the radiopurity of the heating resistor was determined by A.Hegai[4]. The total activity or upper limits for all found contaminants are given in table 4.2. The values given are already background corrected. As expected, the overall activity of the resistor is low enough that it will not cause any problems in low background experiments. No exceptional contamination was found. Apart from the natural impurities of the uranium and thorium decay chain and some barium

Table 4.2: Radiopurity screening results (95% C.L.) for the heating resistor. Sorted by gamma line energy. From Hegai, 2010 [4]. Note: some isotopes occur more than once in the table.

Nuclide	E_γ [keV]	Activity [Bq]
^{226}Ra	186.21	< 1.62
^{212}Pb	238.63	0.07±0.05
^{214}Pb	295.22	0.15±0.09
^{214}Pb	351.93	0.13±0.05
^{133}Ba	356.01	0.04±0.02
^{208}Tl	583.19	0.04±0.01
^{214}Bi	609.32	0.10±0.04
^{228}Ac	911.20	< 0.14
^{214}Bi	1120.29	< 0.26
^{40}K	1460.82	0.3±0.2
^{214}Bi	1764.49	< 0.32
^{208}Tl	2614.51	< 0.05

no other significant radioactive contribution was found in the heating resistor. The barium contamination can also be seen in the X-ray fluorescence spectrum when electrons are accelerated towards the crystal and its holder where the heating resistor is glued on. Barium, especially barium oxide is used to decrease the work function in resistors and electronics in general.
The other components to be tested are still in the queue until a measurement period is granted. A single measurement usually takes several weeks in order to see rare contaminants.

4.6.3 Miniaturization

To apply a pyroelectric accelerator to the CRESST experiment or another low background experiment, the neutron source must be as small as possible use few space within the detectors shielding. The chamber would be manufactured from borosilicate glass in order to have it as gas and especially tritium tight as possible. The electronics can be built in a compact external box connected via a multi-pole cable to the device. The necessary connections would be the following: pressure sensor data, temperature sensor data, ion current data, target bias, focus grid bias, heater power supply and cooler power supply yielding a total of 9 cables needed. All connectors and feed throughs must be sealed with borosilicate mold or a suitable epoxy in order to get it tritium tight. The heat produced by the

peltier element can be carried away by using heat pipes. The target can either be manufactured directly onto the glass, however it then must be metalized by 10 nm aluminum or another metal to measure the ion current, or the conducting substrate is mounted inside the glass tube. A metal shield which acts as Faraday cage should surround the glass cylinder to give a defined internal field geometry. The miniaturized setup can be designed in a way that refilling deuterium is possible or not. A sketch of a miniaturized PIA device is shown in figure 4.55. As

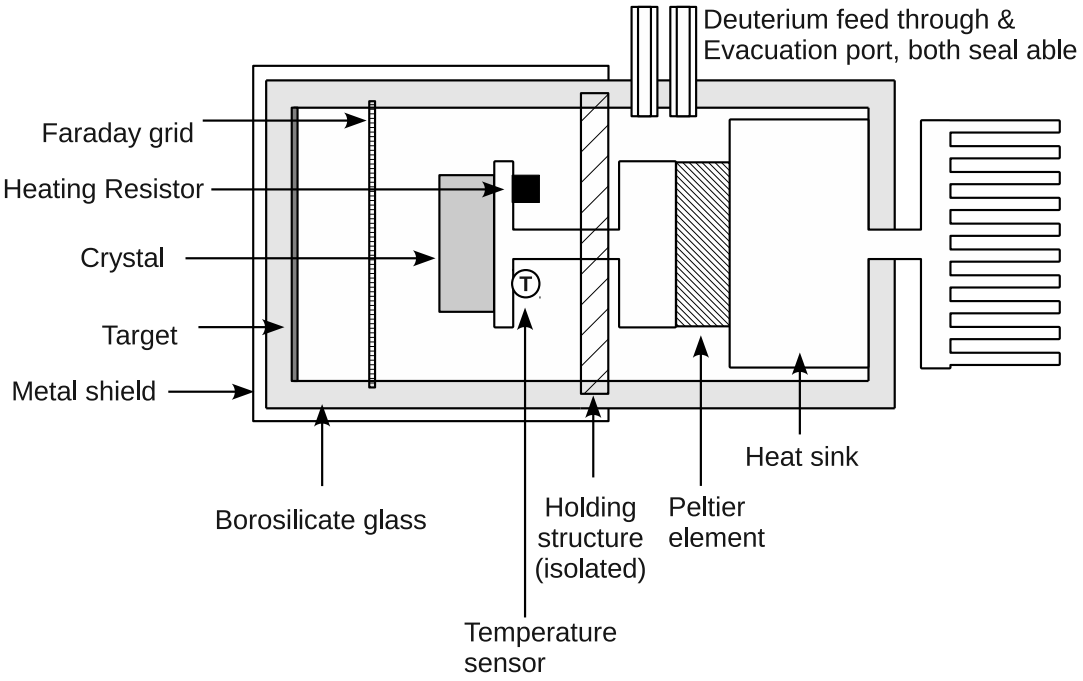

Fig. *4.55: Sketch of miniaturized PIA setup.*

the preferred option to tighten the device is glass mold, the manufacturing process can be very difficult. The gas handling system can be made refillable and not refillable. A not refillable solution is much more likely to be tritium tight, however the pressure cannot be adjusted afterwards unless a storage volume is integrated which of course needs a needle valve. The refillable solution is easier to maintenance long term since deuterium can easily be refilled, however the requirements to the valves are higher since one has to buy tritium tight ones.
For long term tritium safe operation a second shell of borosilicate glass offers the possibility to flush the volume around the source with nitrogen or simply apply a vacuum which in that case can remove any potentially leaking tritium and can be fed out of the experiments surrounding. A disadvantage is the residual heat removal from the peltier element which has to be fed through a second shell of

glass. A solution could be the implementation of a water cooling system. All feed throughs and support lines then can be guided away from the detectors for example in a flexible metal hose which is additionally used for pumping. A sketch of that miniaturized model is shown in figure 4.56.

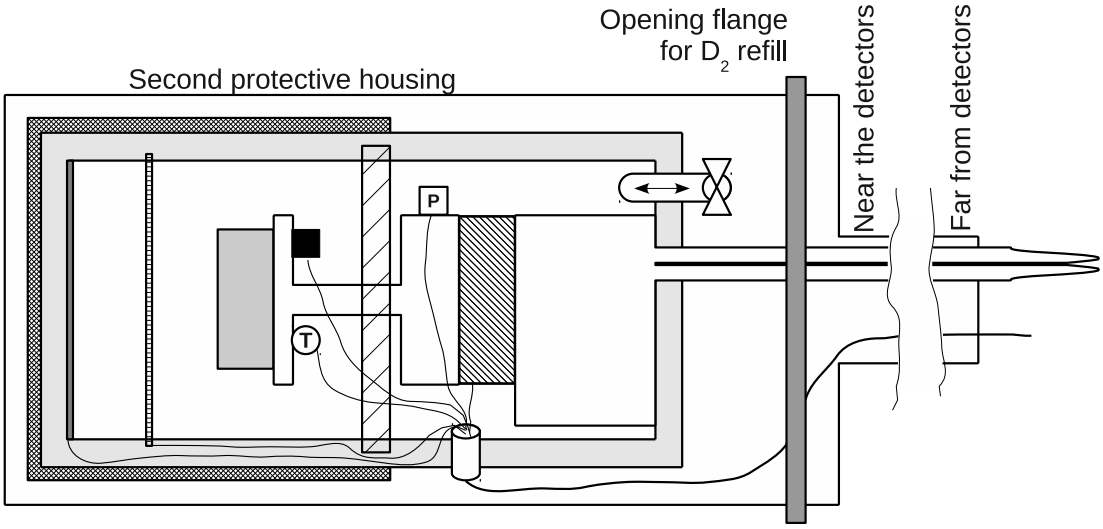

Fig. *4.56: Sketch of miniaturized PIA setup with possibility for deuterium gas refill and additional safety housing which can be pumped of flushed with protective gas.*

5 Summary

A theoretical description of pyroelectricity was given, a high voltage charge model for the used LT crystal discussed and verified. The required electric field strength to ionize deuterium from the gas phase to D^+ and D_2^+ was calculated. The necessary field strengths are about 2 V/nm in order to produce D_2^+ ions and 500 V/nm to get D^+ ions. The properties of a tip on which such a strong electric field can be achieved was determined. A tip which is 2 mm long and has a tip radius of 50 nm will generate field strengths in the order of 2 V/nm by field enhancement out of a field strength of 1 mV/nm. For properties of tip arrays, FEM calculations were performed, with the result that tip arrays can be used for field ionization.

Given known limitations, such as energy loss in the target, fusion cross section, high voltage, and ion current on the target, a realistic expectation for the expected average neutron flux during the corresponding polarity cycles was calculated, based on fusion by incident D_2^+ ions:

$$\Xi_{real} \approx \text{1-10}\,\text{n/s}.$$

Targets for the accelerator which contain deuterium were discussed, deuterated polyethylene was chosen. The experimental setup was constructed and instrumented. An X-ray detector and neutron detectors were put into operation. The corresponding data acquisition was installed, the acquisition software developed. Time dependent X-ray spectra were used to measure the high voltage on the crystal surface. The neutron detectors were characterized at the Rosenau accelerator, their discrimination performance optimized and installed close to the experiment. The total neutron detection efficiency for source neutrons was improved from 0.014% to 2.5% compared to previous work. Compared to the beginning of this work the neutron detection efficiency was improved by a factor of 3, from 0.83% to 2.5%.

It could be shown, that a pyroelectric high voltage above 100 kV can be generated reliably and highly reproducable. With this high voltage, electron and ion acceleration was performed. Electrons were measured directly on the target as well as indirectly by X-ray radiation. An ion current up to 1.2 nA was measured on the target which a factor of 3 below the expected ion current. A possible reason for this behaviour is field electron emission by the supression grid itself which causes the crystal to discharge.

Several configurations for neutron production were measured, the impact of a biased grid between the target and the crystal was studied. It turns out that the grid can prevent secondary electrons from reaching the crystal causing it to discharge faster. In the end a neutron flux of

$$\Xi_{n,avg,excess} = 0.56^{+0.10}_{-0.06}\, n/s \tag{5.1}$$

was measured which however is not in agreement with the realistic expectation of 3.4 neutrons per second. The nature of the observed deficit of neutrons for larger ion currents is still to investigate.

6 Outlook

The experiment presented in this thesis is currently in a state where it can gradually be improved to verify and further enhance the neutron production. The most urgent upgrade to be installed in the future is a lead shield for the vacuum neutron detector to suppress X-ray radiation. The lead shield is already prepared and waiting for installation. This reduces low energetic X-rays which reduces the trigger rate and therefore the dead time and the gamma leakage into the neutron acceptance region at low energies. Therefore the hardware threshold can be lowered again which should increase the statistics of neutrons significantly. As the DAQ system still suffers from high dead time losses, a suitable FADC should be equipped with 5-10 ns of sampling time such as the Struck SIS3302 FADC which is used at the CRESST accelerator experiment at the MLL in Garching. This would allow recording neutron data up to several thousand Hz of rate.
Further, the loss of ion current must be decreased by suppressing the secondary electrons, for example by properly chosen magnetic fields. However, this will cause problems with the high voltage determination, since the absence of accelerated electrons will lead to a lack of X-ray radiation. However, if enough neutrons will be produced this does not matter any more since the neutron output can be optimized without knowing the exact high voltage. If the electrons can be suppressed by magnetic fields, the grid used for suppression might not be neccesary any more. If not, the grid wire radius can be changed to check if this also increases the neutron flux by reducing the field electron emission of the grid. The disadvantage might be a decrease in ion flux since the opening angle of the grid will be smaller.
One can also further improve the ion current reading on the target by installing a dedicated readout and metalizing the target. The sputtering of aluminum thin films onto deuterated polyethylene with a final thickness of 10 nm could be investigated. This will increase the precision of the ion current measurement.
As already discussed during this work, the ionization yield can very likely be increased by using tip arrays made of tungsten or diamond, which are much easier to handle which decreases the possibility of structural damage at the tip(s). In addition the use of single carbon nanotube arrays or carbon nanotube forests can be investigated again, since they should be easier to produce and therefore easier to obtain with similar ionization properties compared to a tip array.
Due to the increase in the cross section, each kV of additional high voltage will increase the neutron flux significantly. Therefore is is suggested to use the second LT crystal for additional acceleration voltage. A second crystal must be installed in such way, that the two high voltage polarities charging opposite which provides up to double the high voltage than currently available. The target must then be mounted on one crystal, the tip on the other. This modification would however

cause severe changes in the experiment. The neutron detector must be mounted differently to install a second heating and cooling system for the second crystal. This is either a long term modification or can be done completely independently in a new setup which is optimized for neutron production and detection. This means, a UHV chamber with smaller dimensions as the ones currently used can be chosen in order to increase the gas purity by less leakage, and optimizing the geometry to the neutron detectors which then might be placed outside the vacuum again.
A second crystal also needs a temperature controller, which in future can also be modified to reliably provide a constant temperature change.
The pressure of the vaccuum chamber and the deuterium purity can be increased by using UHV seals or an UHV chamber and new internal sensor and power connectors to reduce outgassing. By increasing the deuterium purity, it is more unlikely that remaining gas such as nitrogen will be ionized and accelerated towards the target, not causing any fusion reaction.
In the long run, the setup must be miniaturized in order to be either portable or to fit into the shielding of low background experiments. A prototype must be developed and tested under real conditions such a a running cryostat at an underground laboratory as available in Tübingen and München. After a successful test the prototype can be operated at the Gran Sasso test cryostat.
The device can then be tested and used to calibrate dark matter searches or can be used as portable low flux neutron gun. A successful test at future stages of the CRESST experiment would qualify this source for a use in EURECA - the future European cryogenic direkt Dark Matter experiment with a target mass of one ton or larger.
Related to this work, the pryoelectric coefficient remains unmeasured for LT below 0^oC. Given the availability of the necessary equipment and the crystal, this would be a good opportunity to study pyroelectric behaviour at low temperatures.

A Mean free path

The mean free path for particles of diameter d in gas phase at a given temperature T and a pressure P is given by the expression

$$\lambda = \frac{kT}{\sqrt{2}\pi d^2 P} \tag{A.1}$$

where k is the Boltzmann constant. The factor $\sqrt{2}$ originated in the average relative velocity of the molecules, the number of collisions is $\sqrt{2}$ times the number with stationary targets[1]. The mean free path for deuterium molecules in vacuum at common temperatures as function of pressure is shown in fig.A.1. Within this

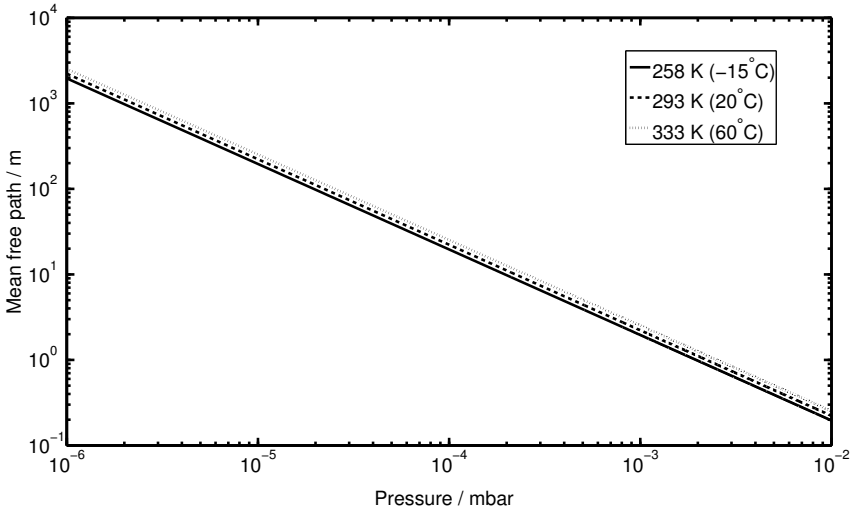

Fig. *A.1: Mean free path of deuterium molecules at certain temperatures as function of pressure.*

experiments pressure and temperature range, the mean free path is always larger than the internal geometry sizes (few cm) which means that ion collisions can be neglected.

[1] "Mean Free Path, Molecular Collisions". `hyperphysics.phy-astr.gsu.edu`

B Cleaning a beryllium X-ray window

The X-ray detector looks into the vacuum chamber through a beryllium window which has a high transmission for low energetic X-rays. In the rare case there is an oil spill into the vacuum, also the beryllium window will be contaminated. In case of an "oil film"-type contaminant this will be a guide how to clean a beryllium window of micrometer scale thickness.

B.1 Security considerations

Beryllium is toxic by incorporation and will most likely lead to a lethal pulmonary embolism when its dust is inhaled. Therefore the necessary security options should be considered before starting a cleaning procedure. It is recommanded to do the procedure within an adequate extractor hood. For your safety it is recommanded to use gloves, safety goggles (in case it bursts) and a fine dust mask or a filtered breather. It can be useful to have a moistened cloth right beside you to prevent the beryllium from spreading in case of destruction. A crossection of the windows geometry is shown in fig.B.1.

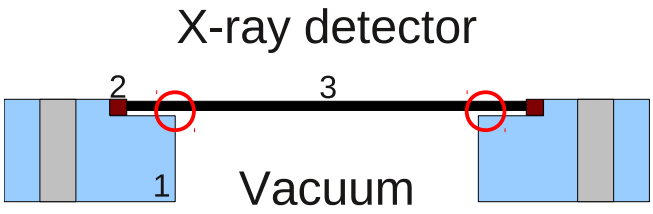

Fig. *B.1: Cut through the flange, 1: CF Flange, 2: Soldering, 3: Beryllium, the critical points are marked with red circles.*

B.2 Requirements, preparation and procedure

Concerning the stability of the window one has to focus on two crucial points. The window is slightly bent towards the vacuum side and needs to be supported from atmosphere side. One can use some layers of lint-free tissue for stabilization. This bending is the reason why immersing in cleaning liquid will most likely destroy the window due to hydraulic stresses and cannot be used here. The second much more critical stability problem occurs on the vacuum side. The window is soldered onto the flange, leaving a small gap from inside. If a particle or lint happens to be at that gap, it will be a predetermined breaking point on reevacuation. It is of greatest importance not to deposit any small pieces or particles there. Recommanded for the cleaning process is the use of small pieces lint-free

clean room wipes, slightly moistened with isopropanol, methanol or acetone. Be careful that there is no dripping on the window! Use tweezers to carefully wipe the beryllium window clean. If acetone is used, a second cleaning step with isopropanol is reasonable to prevent corrosion.
The procedure as described here, has been successfully performed on a beryllium window. For different windows the cleaning procedure might be different dependent on their thickness and geometry.

C Measurement artifacts

A few words are spent to describe measurement artifacts discovered during this work and their identification as well as their treatment.

C.1 X-ray data artifact

This particular data anomaly can be seen in many dataset recorded early during this work. It is visible as vertical data "flashes" in time vs. x-ray energy plots and appears with a time constant of 1257 seconds. Due to the regular appearance it can be removed easily. The artifact does seem to depend on current acquisition rates and energies and causes strong pileup. The artifact originates in a "LeCroy 334A 500MHz" semidigital oscilloscope which was used to monitor the x-ray events live. It turned out, that the self calibration of the oscilloscope couples to the signal resulting in the observed artifact. Removing the oscilloscope from the circuit solves the problem completely.
The software removal of the artifact uses the endpoint algorithm discussed in 2.4.3. By comparing the RMS of the high voltage running average, the artifact can be clearly identified. To compensate for the information loss for this time bin, the time bins before and after the artifact are used to extrapolate the high voltage information. A histogram of all artifacts did not show any structure.

C.2 Gain jumps

C.2.1 Si(Li) preamplifier

The preamplifier of the Si(Li) detector is coupled directly to the cryostat of the diode. Unfortunately the feed through from non-cooled parts of the preamplifier to the parts in the cryostat does have a bad contact. This bad contact is reason for sudden change in amplification and increase in noise, by at least one order of magnitude. A pseudo-stable state was achieved by opening the preamplifier and adjusting every pin at the feed through carefully at very low bias voltages to see whether there is an effect or not. Up to date this effect does show up rarely. This fault in the preamplifier might give additional reason to the detectors bad resolution at low energies.

C.2.2 NE-213, high voltage power supplies

The NE213 detectors did show strong gain jumps over time. It was found that such jumps are mostly the result of failures and instabilities of the high voltage power supplies. These instabilities were mainly caused by power grid fluctuations. In addition, erroneous photomultiplier bases and even broken photomultipliers were found as well. An example of a gain jump is shown in fig.C.1. Drifting behaviour is shown in fig.C.2. To find out where exactly the jump occurs, a

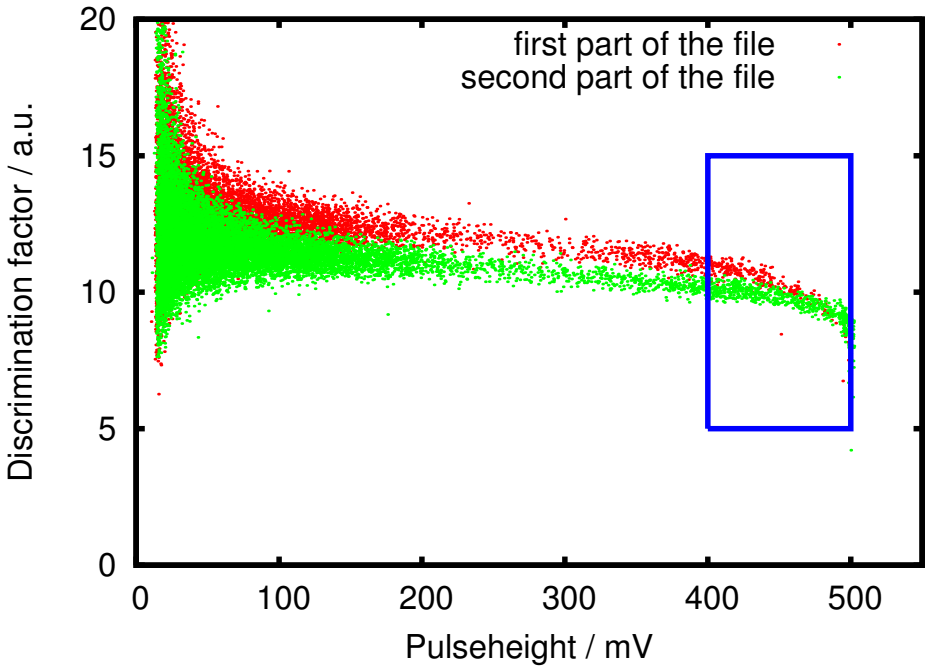

Fig. *C.1: The two scatterplots from one single datafile. Data is already cutted in two pieces and the amount reduced for plotting purpose. The eventrate in the blue marked region can be used as indicator for such spontaneous changes in gain, if no calibration source is used.*

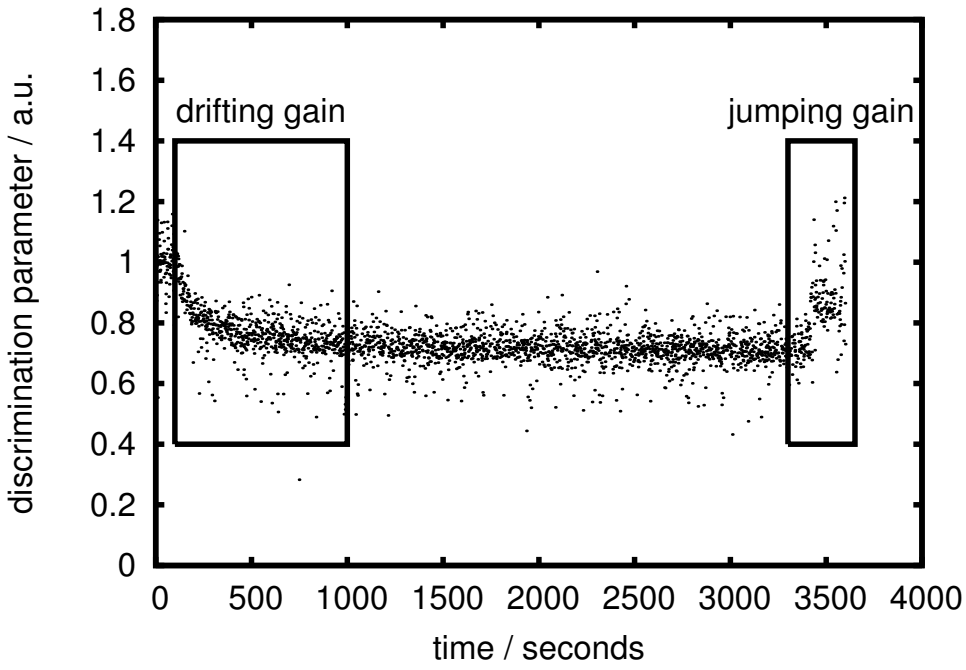

Fig. *C.2: Discrimination parameter drifts during runtime. It corresponds to a drift of gain.*

time binning is introduced and the rate at very high pulseheights is determined. A running average of the rate is done, the RMS of the average calculated. The element before the current timebin and the elements afterwards are being averaged as well, their RMS calculated. By dividing the total RMS by the difference of the two, one in advance one after the current timebin, the position can be determined with an accuracy of the time bin width. The files are separated, the time bin where the jump occurs is being cutted out, and treated separately for analysis. This determination of the gain jump position is depicted in fig.C.3. If a

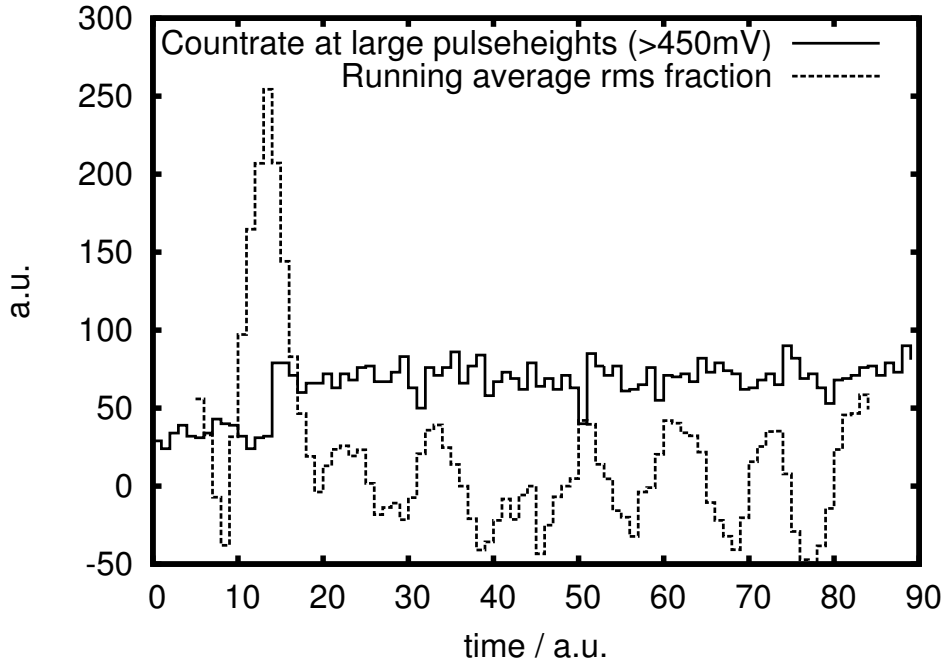

Fig. *C.3: Rate at large pulseheights is histogrammed, a running average is calculated. The RMS fraction as discussed in the test is plotted as well. The change in gain is clearly visible.*

calibration source is used, on can determine gain shift by monitoring the position of the calibration lines as done with X-ray data.
The gain jumps in the NE-213 detectors can be avoided by stabilizing the power supply. The scintillator response is also dependent on ambient temperature.

C.3 Noise levels

C.3.1 At P.I.A. setup

At the P.I.A. setup, the electronic noise is dominated by strong VHF radio frequency senders near the building and 50 Hz noise. The 50 Hz noise can be reduced

by grounding every part of the experiment carefully to the same ground potential, avoiding loops. A star like structure is achieved. The VHF radio frequencies at around 100 MHz are less important since their impact on signals with large amplitude is negligible ($O(2\,\mathrm{mV})$ of $O(5\,\mathrm{V})$ signals). This issue is also being discussed in the works of [18] and [45].

C.3.2 At the rosenau accelerator

At the Rosenau accelerator, the noise level varies from day to day. The reason for this behavior is still unknown. It is believed however that the power supply to the accelerator laboratory may cause the problem. One always has to take care on proper grounding. Also, switching power supplies on DAQ side does help occasionally.

D Software & algorithm properties

D.1 DAQ software

The DAQ software was developed to readout the CAEN v1729 fast sampling analog digital converter. In this section, special properties and details of algorithms will be provided. A general description is already given in chapter 2 section 2.4. The modules discussed are VME based unless stated otherwise. The communication with the VME bridge is not being discussed and can be obtained from the works of F.Ritter [23] or M.Pfeifer [42].

Trigger modes

The v1729 supports several trigger modes. However the trigger functionality is strongly dependent on the firmware version used and the driver version of the VME bridge. There is no 64 bit driver available. A random internal trigger that is released by a pseudo random code which uses the internal clock. This trigger is used to acquire module properties such as the pedestal. The pedestal is a constant, a non changing hardware offset of the flash memory cells. The external trigger needs a logical signal between 3 and 5 Volt and can be set to trigger on the rising or falling edge. The external trigger signal must be at least 100 ns long. Each module is equipped with an internal discriminator which can release a trigger if a value is exceeded.

Acquisition & storeage modes

The software written can record either preanalyzed pulse properties or the full traces. In full trace record mode, the program can store raw data, corrected data and corrected data plus analyzed data. The full trace files can also be compressed to zip format. If the data can be compressed on the fly, a very powerful computing system has to be used, otherwise the DAQ is slowed down. If trace data is stored, the I/O operation must be minimized. A memory buffer is filled with events and stored to file if the event buffer is full. A typical event buffer contains 2500 traces, 4 channels each and needs a memory size of 100 MiB.

Preanalysis

The pulses are being corrected for the hardware pedestal, trigger position and baseline offset. The position and value of the minimum and the maximum of the pulse are being determined and stored. The pulse is being integrated and derived in order to do a simple pileup cut and enable a constant fraction trigger. The RMS of various baseline intervals in the beginning and the end of the trace is also being calculated. By comparing these RMS, erroneous triggers and nonlinear

baselines can also be identified. During integration, the values for a long and a short integration width beginning at a leading edge or constant fraction trigger are being stored in order to do pulse shape discrimination. The corresponding gate widths can be set for each channel independently. Invalid pulses are being discarded. The preanalysis also checks for coincident events amongst all channels, however an event is treated as 'coincident' if it appears in the same trace which is up to 2.5 µs long. The coincidence data is stored in separate files. The times between the pulses is being put into a histogram and shows very few random coincidences. In principle every other pulse parameter can be determined as well.

Experimental features

One of the main experimental features of the preanalysis software is the muon identification. This is highly experimental and was not used for this work. A muon deposits about 2.5 MeV per cm traveled in the scintillator. For the least thick cells of type 1 a muon hit would produce light in the gamma band of about 6.1 MeV. This will shift the pulse mostly to the high energy part of the pulseheight distribution. A high energy cut can be applied. It is assumed that some muons can also trigger hadronic showers in the direct surrounding of the detectors, causing coincidences. This is topic of current investigations and was not finished by the end of this work.

Compatibility, tested Kernel versions

Compatible, tested (32 bit OS necessary!):
Kernel 2.6.18.8 - openSuse 10.2 - pipc74
Kernel 2.6.31.12 - openSuse 11.2 - pilr07
Also works with Ubuntu.

D.2 Analysis software

The analysis software was done in order to analyze all recorded files at once regarding all file formats used within the range of this work. As described in the following sections, some of the necessary data corrections are far from trivial.

Feature overview

The supported features are file and run identification with number of files, structure of files, date of files if available and list management such as black- and whitelists for partial analysis. The program calculates the neutron cuts for each channel, determines the X-ray cycles and its polarity, the heating and cooling periods and assigns each neutron the according parameters. In the end every measured neutron has an energy, discrimination factor, timestamp, temperature change, high voltage (with polarity) and channel information and all statistical

errors. The neutron cut application is rather simple, however strongly dependent on the individual properties of the detector module. The neutron cut on double read out modules is slightly different than the neutron cut on single detector modules. Concerning double modules, the neutron identification can be accomplished by just one of two detectors or both at the same time. Since the overlap is small, the neutron cut was set to an inclusive OR. If a neutron is identified as neutron in one of both detectors it is treated as neutron. The discrimination factors of the two detectors are depicted in fig.D.1. This plot shows, that the separation of the

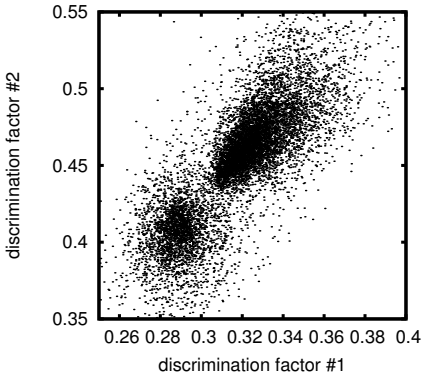

Fig. *D.1: Discrimination factor scatter plot of double module. The events at low discrimination factors correspond to neutrons, the others are gammas. The absolute values do differ due to the different detector properties. The separation between the two particle types is quite clear. This data does not contain any pulseheight or energy information which will be used in addition for the neutron cut.*

particles works quite nice in the double detector modules without even regarding any energy information at all.
One of the most challenging parts of the analysis software is the identification of the detectors individual properties and especially for early runs the individual correction functions for the gamma band nonlinearities. Care must be taken if a cumulative analysis is performed, not to accidentally mix different detector systems with different thresholds and sensitivities. This was checked and should be avoided in recent versions of the program.
After identifying neutrons from the detector files, it is checked for availability of temperature and high voltage data. The variance of the temperature as well as run naming conventions determine whether a run is an actual run, a calibration or a background run.
The timestamps of the files as well as the timestamps in the logfiles are being compared and a common time is set. If high voltage and temperature data is available, the data is segmented in high voltage and temperature cycles, the minimal and maximal values as well as the high voltage values and their polarity are

being determined.

Global analysis

In order to increase statistics as much as possible to enhance very small effects, the program was given the option to analyze all data 'ever' recorded. This functionality however is restricted to the last phase of the experiment or to be more precise the introduction of unique run identification numbers. These are necessary in order to compare the different analysis steps and do time dependent analysis such as chronologically monitor background rates over long time periods. Also, a global file is created which contains all available properties of all neutrons measured in all channels for further analysis access. One has to keep in mind that not all of this data is easily comparable since measurement conditions might have changed. This data can be used to look for any neutron correlations.

File and dataset indexing

The current program version looks for new data sets on the hard drive upon execution. The run numbers and run type is identified and stored. Black- and white listing is supported and will be regarded at that point. File indexing relies on the availability of data files and the naming conventions of run directories. If the run contains no temperature data files or no high voltage data files, this also indicates a background run. Even if temperature files are available, the temperature however does not change significantly during the run time this also indicates a background run. Similar constraints are implemented for high voltage data files.

X-ray calibration data

The high voltage determination needs the linear x-ray calibration function. One can run all data sets with a single calibration or do the high voltage calculation for each run separately with the last measured calibration. The calibration slope does not change significantly for long time periods with same amplifier gain. Therefore the systematical errors are small. The automated calibration acquisition is under development. The calibration slope over time is shown in fig.D.2.

Single dataset operation

The current analysis software version can operate single analysis steps on single datasets and has the possibility to force its execution if it was already performed in the past, or the current analysis procedure was adjusted. The analysis steps performed are stored for each dataset individually so that the analysis must not performed again on old data sets for the global properties.

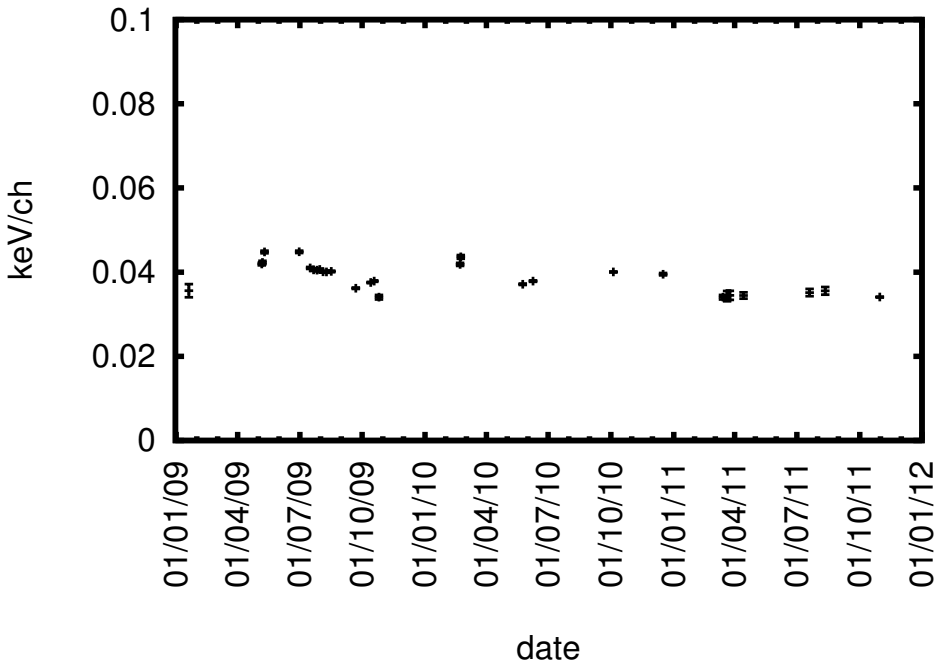

Fig. *D.2: Slope of the linear X-ray calibration over time. All values given with three sigma fit error.*

D.3 Other programs

For some purposes, programs were written to enhance useability of other programs or enhances the functionality.

Math

This library type program section covers a variety of useful functions. It includes correct rounding of floats and doubles in C++ to any number of digits within the common 64 bit variable precision. In addition inclusive and exclusive gaussian and poisson probabilities can be calculated. Additional functions such as the correct approximation of the factorial for large numbers are also implemented.

Z-lib interface

The z-lib[1] allows the decoding and encoding of file streams. A wrapper was written to provide a C++ conform library interface. Additional functionality was implemented such as decoding the unzipped file length and reserving the exact amount of memory which drastically increases the decoding performance.

Data format converters

Data converters for different purpose are available now. Converters for data to gnuplot[2] compatible format were written, as well as converters for ASCII files from the LeCroy oscilloscopes.

[1] `http://zlib.net/`

[2] `http://www.gnuplot.info/`, scientific plotting program

E Serial port relay switch

A serial port relay switch has been constructed to regulate the heating and cooling voltages. High level and low level voltages on the serial port bins execute the relay switches. A picture of the relay box is shown in fig. E.1, the positions of the relays are marked in red.

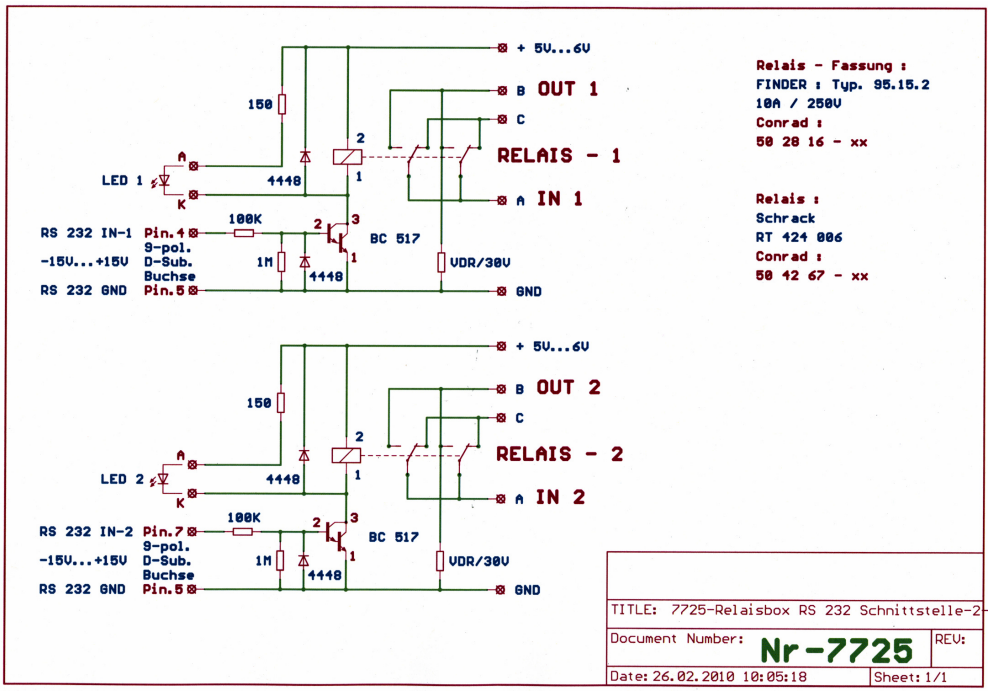

Fig. *E.1: Circuit diagram of the relay box.*

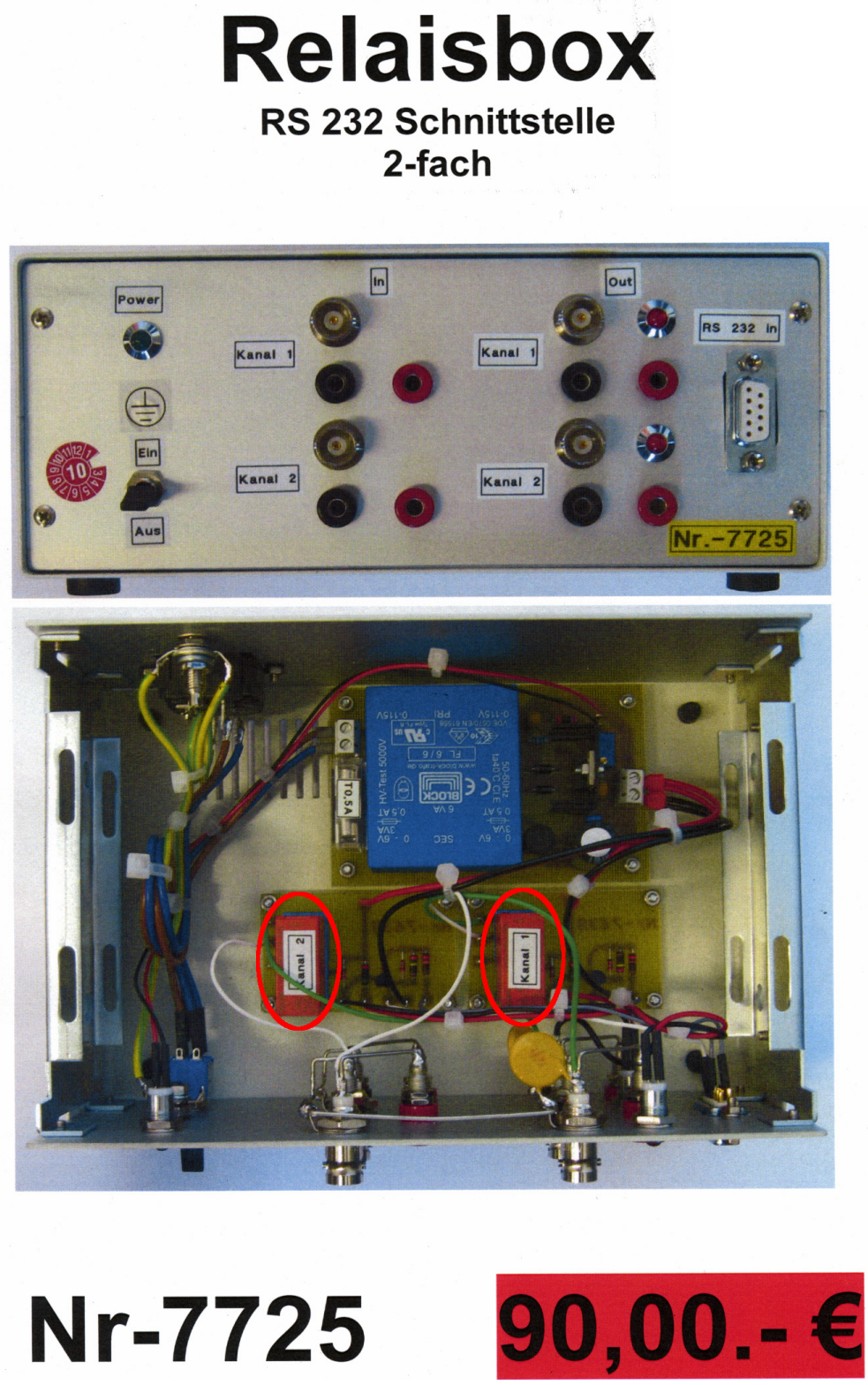

Fig. *E.2: Picture of the relay box.*

F Pirani gauge gas type dependence

The pirani gauge has different response for different gas types. Those values were measured by K. Jousten [33]. The indicated pressure p_{ind} is plotted against the true pressure p for different gas types in fig. F.1. For hydrogen/deuterium the indicated pressure is larger than the true pressure by a factor of roughly two according to this graph.

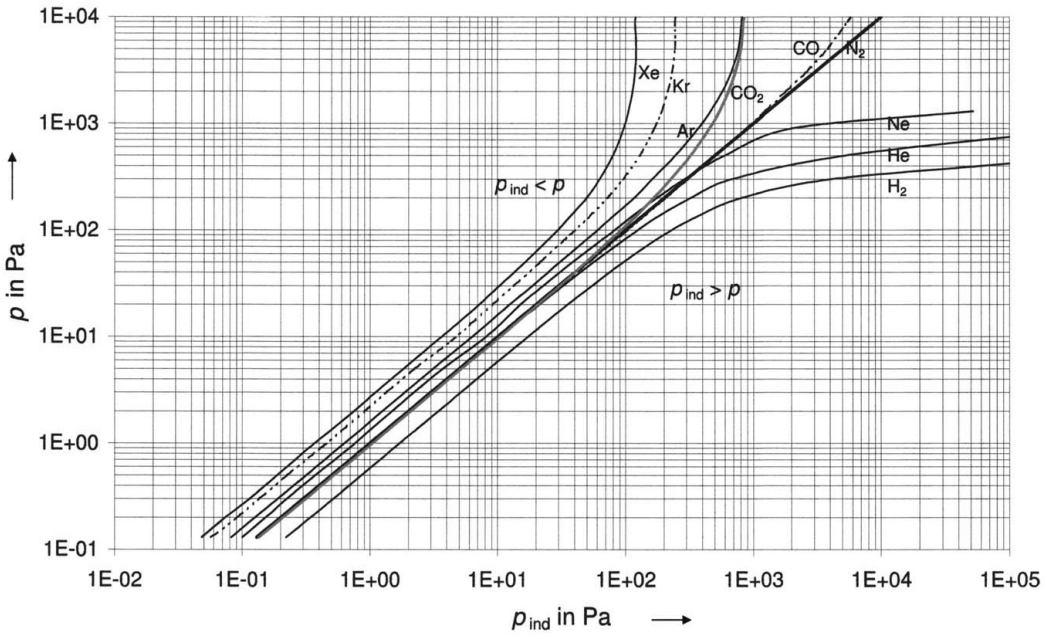

Fig. *F.1: Gas dependent response of a pirani vacuum gauge. p_{ind} is the indicated pressure by the gauge versus the true pressure p.*

G Cold cathode gauge gas type dependence

The cold cathode gauge gas type depencendence is exaclty the opposite compared to the pirani gauge. Depending on the source, the indicated pressure is 2.4 to 2.8 times larger than the true pressure for deuterium. In case of a gas mixture the partial pressures must be measured with a mass spectrometer in order to determine the pressure correction factor.

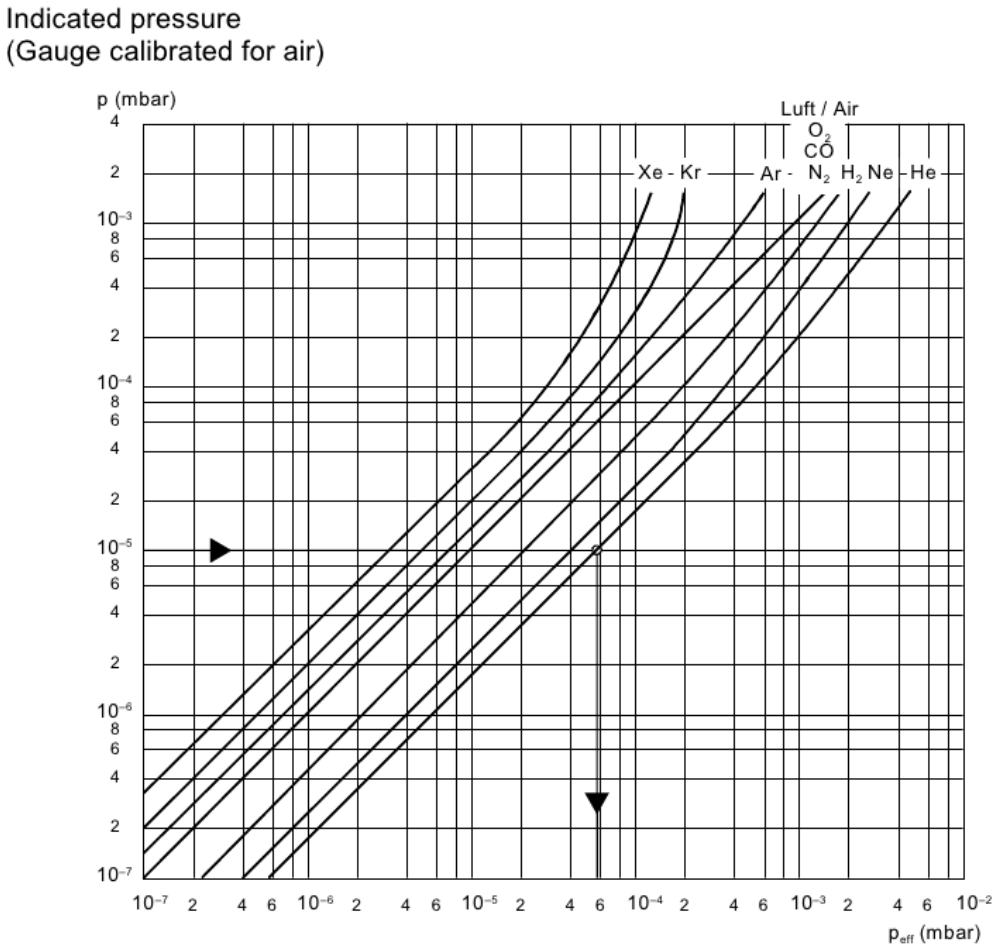

Fig. *G.1: Gas dependent response of a cold cathod vacuum gauge. p_{eff} is the true pressure versus the pressure indicated by the gauge. From Pfeiffer IKR 270 datasheet:* `http://mmrc.caltech.edu/KratosXPS/accessories/PfeifferColdCathGageIKR270.pdf`

List of Figures

List of Tables

Bibliography

[1] Technical report on NE213 detectors available in Tübingen, 2011-12.

[2] Irshad Ahmad and Frank Wagner. A simple cooled Si(Li) electron spectrometer. *Nuclear Instruments and Methods*, 116(3):465 – 469, 1974.

[3] A. Aksoy et al. Response-function measurement of an NE213 scintillator using the 2H(d, n)3He reaction. *Nuclear Instruments and Methods in Physics Research Section A: Accelerators, Spectrometers, Detectors and Associated Equipment*, 337(2-3):486 – 491, 1994.

[4] Alexander Hegai. Gammaspektroskopie mit Germaniumdetektoren. Master's thesis, Eberhard-Karls-Universität, Tübingen, 2010.

[5] Andrea Hagen. Aufbau eines Flüssigszintillator-Testdetektors. Master's thesis, Eberhard-Karls-Universität, Tübingen, 2008.

[6] G. Angloher et al. Limits on WIMP dark matter using scintillating CaWO4 cryogenic detectors with active background suppression. *Astroparticle Physics*, 23:325, 2005. arXiv: astro-ph/0408006.

[7] G. Angloher et al. Commissioning Run of the CRESST-II Dark Matter Search. 2008.

[8] G. Angloher et al. Results from 730 kg days of the CRESST-II Dark Matter Search. 2011.

[9] Jeffrey E. Arbogast, Brett M. Beauregard, and Douglas J. Cooper. Intuitive robust stability metric for PID control of self-regulating processes. *ISA Transactions*, 47(4):420 – 428, 2008.

[10] Barbara Grüner. Detektion von Rubidium durch Feldionisation an Kohlenstoffnanoröhren. Master's thesis, Eberhard-Karls-Universität, Tübingen, 2009.

[11] R.A. Cecil et al. Improved Predictions of Neutron Detection Efficiency for Hydrocarbon Scintillators from 1 MeV to about 300 MeV. *nim*, 161:439–447, 1979.

[12] Christian Ciemniak. *Setup of a Neutron Scattering Facility for the Measurement of Scintillation Light Quenching Factors of Low-Temperature Detectors Used in the Direct Dark Matter Search Experiments CRESST and EURECA*. PhD thesis, Technische Universitaet München, 2011.

[13] Douglas Clowe, Marusa Bradac, Anthony H. Gonzalez, Maxim Markevitch, Scott W. Randall, Christine Jones, and Dennis Zaritsky. A direct empirical proof of the existence of dark matter. 2006. arXiv: astro-ph/0608407.

[14] Chiara Coppi. *Quenching-Factor Measurements for Cryogenic Dark Matter Detectors* . PhD thesis, Technische Universitaet München, 2009.

[15] Davide D'Angelo. Seasonal modulation in the Borexino cosmic muon signal. 2011.

[16] Gerhard Deuter. Untersuchungen zur Anwendbarkeit eines pyroelektrischen Ionenbeschleunigers als Neutronenquelle zur Kalibrierung von Tieftemperaturdetektoren. Master's thesis, Eberhard-Karls-Universität, Tübingen, 2007.

[17] Sebastian Diebold. Bestimmung der Stöchiometrie supraleitender Proben mittels Rutherford-Rückstreu-Spektrometrie . Master's thesis, Eberhard-Karls-Universität, Tübingen, 2010.

[18] Dennis Dietrich. Aufbau, Inbetriebnahme und Messungen mit einer Myonenveto-Testversion der Experimente Gerda und Double Chooz. Master's thesis, Eberhard-Karls-Universität, Tübingen, 2010.

[19] Jeffrey A. Geuther Becky Marus Brian McDermott Donald J. Gillich, Yaron Danon. Deuterium ionization for pyroelectric crystal accelerators. 2007.

[20] Yaron Danon Donald J. Gillich, Andrew Kovanen. Deuterated target comparison for pyroelectric crystal D-D nuclear fusion experiments. *Journal of Nuclear Materials*, 405:181–185, 2010.

[21] C. J. Edgcombe and U. Valdrè. Microscopy and computational modelling to elucidate the enhancement factor for field electron emitters. *Journal of Microscopy*, 203(2):188–194, 2001.

[22] Wolfgang Erath. Aufbau einer Streuanordnung zur Messung von differentiellen Wirkunsquerschnitten mit schnellen Neutronen. Master's thesis, Eberhard-Karls-Universität, Tübingen, 1981.

[23] Florian Ritter. *The GERDA muon veto - first light.* PhD thesis, Eberhard-Karls-Universität, Tübingen, 2012.

[24] Richard G Forbes, C.J Edgcombe, and U Valdrè. Some comments on models for field enhancement. *Ultramicroscopy*, 95(0):57 – 65, 2003. IFES 2001.

[25] R.B. Galloway and J.M. Sharaf. The temperature dependence of pulse shape discrimination with ne213 scintillation counters. *Nuclear Instruments and Methods in Physics Research*, 224(1-2):181 – 184, 1984.

[26] D. Gehman, M. Smith-Nelson, K. Ianakiev, D. Dinwiddie, and B. Rooney. Temperature dependency analysis of light output from an NE-213 liquid sintillator. 2:1432 –1435, 26 2007-nov. 3 2007.

[27] Georg Meierhofer. *Neutron Capture on ^{76}Ge.* PhD thesis, Eberhard-Karls-Universität, Tübingen, 2010.

[28] Jeffrey A. Geuther and Yaron Danon. High-energy x-ray production with pyroelectric crystals. *Journal of Applied Physics*, 97(10):104916, 2005.

[29] A. M. Glass. Dielectric, Thermal, and Pyroelectric Properties of Ferroelectric $LiTaO_3$. *Phys. Rev.*, 172(2):564–571, Aug 1968.

[30] K. Gul, A.A. Naqvi, and H.A. Al-Juwair. Relative neutron detector efficiency and response function measurements with a 252cf neutron source. *Nuclear Instruments and Methods in Physics Research Section A: Accelerators, Spectrometers, Detectors and Associated Equipment*, 278(2):470 – 476, 1989.

[31] Thomas Jagemann. *Measurement of the Scintillation Light Quenching for Nuclear Recoils induced by Neutron Scattering in Detectors for Dark Matter Particles.* PhD thesis, Technische Universitaet München, 2004.

[32] J.F.Nye. *Physical Properties of Crystals.* Clarendon Press, Oxford, 1957.

[33] Karl Jousten. On the gas species dependence of pirani vacuum gauges. *Journal of Vacuum Science and Technology A: Vacuum, Surfaces, and Films*, 26(3):352–359, 2008.

[34] Glenn F. Knoll. *Radiation Detection and Measurement.* John Wiley and Sons, 2000.

[35] L. M. Bollinger and G. E. Thomas. Measurement of the Time Dependence of Scintillation Intensity by a Delayed-Coincidence Method. *Review of Scientific Instruments*, 32(9):1044–1050, 1961.

[36] Sidney B. Lang. *Sourcebook of Pyroelectricity.* Gordon and Breach, New York, 1974.

[37] J. H. Lee and C. S. Lee. Response function of NE213 scintillator for 0.5-6 MeV neutrons measured by an improved pulse shape discrimination. *Nuclear Instruments and Methods in Physics Research Section A: Accelerators, Spectrometers, Detectors and Associated Equipment*, 402(1):147 – 154, 1998.

[38] B. Naranjo, J. K. Gimzewski, and S. Putterman. Observation of nuclear fusion driven by a pyroelectric crystal. *Nature*, 434:1115–1117, April 2005. DOI 10.1038/nature03575.

[39] Nicholas M. Jordan and Y. Y. Lau and David M. French and R. M. Gilgenbach and P. Pengvanich. Electric field and electron orbits near a triple point. *Journal of Applied Physics*, 102(3):033301, 2007.

[40] Working Group 1 of the Joint Commitee for Guides in Metrology(JCGM/WG 1). *Evaluation of measurement data - Guide to the expression of uncertainty in measurement.* Bureau International des Poids et Mesures.

[41] M. A. Olivo and G. M. Bailey. Low cost deuterated polyethylene targets of controlled thickness for high current accelerators. *Nuclear Instruments and Methods*, 57:353–354, 1967.

[42] Marc Pfeifer. Aufbau einer Root- basierten Datennahme und Datenanalyse für VMEbus- gestützte Experimente mit dem System AcquRoot. Master's thesis, Eberhard-Karls-Universität, Tübingen, 2010.

[43] F. Proebst et al. CRESST: First results with phonon light technique. 2005. Talk at Workshop "Current Topics in Astroparticle Physics".

[44] L. Thuesen K. N. Leung R. L. Fink, N. Jiang and A. J. Antolak. Carbon Nanotube Based Deuterium Ion Source for Improved Neutron Generators. *AIP Conf. Proc.*, 1099, 2009.

[45] Christopher Schmitt. Nachweis von myoneninduzierten Sekundärteilchen in einem Szintillationsdetektor. Master's thesis, Eberhard-Karls-Universität, Tübingen, 2011.

[46] Stefan Scholl. *Neutron Background Simulation for the CRESST-II Experiment.* PhD thesis, Eberhard-Karls-Universität, Tübingen, 2011.

[47] J. C. Slater. Atomic radii in crystals. *The Journal of Chemical Physics*, 41(10):3199–3204, 1964.

[48] Raimund Strauss. Quenching Factor Measurements of $CaWO_4$ at mK Temperatures by Neutron Scattering for the Dark Matter Experiments CRESST and EURECA. Master's thesis, Technische Universitaet München, 2009.

[49] L. Volders. Neutral hydrogen in M 33 and M 101. *Bulletin of the Astronomical Institutes of the Netherlands*, 14:323–334, 1959.

[50] H. Wulandari et al. Neutron flux at the Gran Sasso underground laboratory revisited. *Astroparticle Physics*, 22:313–322, November 2004. DOI 10.1016/j.astropartphys.2004.07.005.

‘Leider läßt sich eine wahrhafte Dankbarkeit mit Worten nicht ausdrücken.’
- Johann Wolfgang von Goethe (1749-1832), dt. Dichter